Magnetised winds in transition discs

Étienne Martel

THÈSE

Pour obtenir le grade de

DOCTEUR DE L'UNIVERSITÉ GRENOBLE ALPES

École doctorale : PHYS - Physique
Spécialité : Astrophysique et Milieux Dilués
Unité de recherche : Institut de Planetologie et d'Astrophysique de Grenoble

Vents magnétiques et disques de transition

Magnetised winds in transition discs

Présentée par :

Étienne MARTEL

Direction de thèse :

Geoffroy LESUR CHARGE DE RECHERCHE, Université Grenoble Alpes	Directeur de thèse

Rapporteurs :

HELOISE MEHEUT
Chargé de recherche HDR, CNRS DELEGATION COTE D'AZUR
OLIVER GRESSEL
Professeur assistant, Leibniz - Institut für Astrophyzik

Thèse soutenue publiquement le **27 septembre 2022**, devant le jury composé de :

HELOISE MEHEUT Chargé de recherche HDR, CNRS DELEGATION COTE D'AZUR	Rapporteure
OLIVER GRESSEL Professeur assistant, Leibniz - Institut für Astrophyzik	Rapporteur
BARBARA ERCOLANO Professeur, Ludwig-Maximilians- Universität München	Examinatrice
JONATHAN FERREIRA Professeur des Universités, UNIVERSITE GRENOBLE ALPES	Président
GUILLAUME LAIBE Professeur des Universités, ENS DE LYON	Examinateur

Invités :

CLEMENT BARUTEAU
Chargé de recherche HDR, CNRS DELEGATION OCCITANIE OUEST

MAGNETISED WINDS IN TRANSITION DISCS

ÉTIENNE MARTEL

September 2022

I dedicate my thesis to the loving memory of Renée Martel,
Jean-Louis Chamard, Lyne Lenhof.

Je souhaite dédier ma thèse à la mémoire de Renée Martel,
Jean-Louis Chamard et Lyne Lenhof, qui n'auront connu de ce
travail que le début.

ABSTRACT

The formation of stars and planets occurs during the collapse of gigantic molecular clouds. A dense core appears at the center of the collapsing cloud, surrounded by an enveloppe of infalling gas. Because of the conservation of angular momentum, the remnants of the neighbouring matter shape themselves into a protoplanetary disc (PPD). Considering the solar system, PPDs disappear in a few million years after most of their mass concentrated in the central star. This last property makes PPDs being part of a more general class of objects known as accretion discs.

Protoplanetary discs are thought to be the birth cradle of planets and are therefore extensively studied. They are cold and magnetised objects among which stand the transition discs (TDs). These peculiar PPDs are characterised by a dust cavity in their inner regions and centred onto the host star, whose typical widths vary from a few AU up to a few hundreds AU. Interestingly, not only are such cavities seen in the dust profiles of TDs, but they are also detected in their gas density profiles. However, the formation of these objects remains yet unexplained.

A striking observation states that despite their diminished surface density profile, TDs accrete at a rate similar to the accretion rates of full PPDs, suggesting a fast inward motion of matter in their cavity. This result deeply challenges the current evolutionary model of PPDs. Moreover, TDs are observed with very large cavities together with strong accretion rates. The combination of these properties questions the viscous model of PPDs.

A possible explanation for these high accretion rates is the presence of magnetised winds launched with the Blandfold & Payne mechanism. Such winds can efficiently remove angular momentum from the disc, which allows matter to fall down onto the star at high radial velocity. This paradigm shift from the viscous model to magnetic wind outflows in PPDs is promising as the fast-accreting cavities of TDs could be sustained by a magnetic wind.

My thesis is devoted to the study of TDs harbouring magnetic winds with global non-ideal magnetohydrodynamics numerical simulations with the PLUTO code.

The ionisation fraction of TDs is similar to the one calculated in full

discs, so that ambipolar diffusion is the main non-ideal effect at stake. I simulated TDs with an initial vertical magnetic field and a cavity in the initial density profile.

With a set of 2.5 D simulations, I showed that TDs with magnetic winds are long lived and stable discs. The magnetic torques in the cavity trigger a fast radial motion of the gas, hence a strong accretion rate. 2.5 D simulations enable to catch the secular evolution of the disc and especially the transport of magnetic field in the disc.

I also studied 3 D simulations to check the stability of the cavity edge under various instabilities. I detected the formation of spirals inside the cavity rotating at a constant speed with respect to the radius. Additionally, the structure of the cavity shares similarities with magnetically arrested discs (MADs).

Finally, I studied the secular evolution of a TD on a very long period of time (300000 orbits at the internal radius). I showed that the magnetic field transport has a complex behaviour in the disc, encountering diffusion as well as advection phases. The flux of the magnetic field eventually intensifies in the cavity sustaining the disc for long period of time.

I performed the first simulations of transition discs sustained by magnetic winds. This model needs to be related to observations and kinematics predictions are good properties to test. In particular, my work shows that the cavity is sub-keplerian and threaded by a transsonic accretion flow. I could eventually compare my simulated discs to observations by building some synthetic images, which proved promising.

RÉSUMÉ

Les étoiles et les planètes se forment lors de l'effondrement gravitationnel de gigantesques nuages moléculaires. Au cours d'un effondrement, un coeur dense entouré d'une enveloppe de matière apparaît. Du fait de la conservation du moment cinétique, le gaz environnant s'organise sous la forme d'un disque protoplanétaire. Le système solaire étant dépourvu d'un tel disque, on en conclut qu'il doit disparaître (en quelques millions d'années), une fois que l'essentiel de sa masse a été accrétée par son étoile hôte. En conséquence, les disques protoplanétaires font partie d'une classe d'objets plus large : les disques d'accrétion.

Les disques protoplanétaires abritent la formation planétaire, ce qui en fait des objets particulièrement étudiés et observés. Ces disques sont essentiellement composés de gaz sous la forme d'un plasma froid et magnétisé et d'environ 1% de poussière. Certains d'entre eux se distinguent par la présence d'une cavité interne dans leur profil de densité de poussière, il s'agit des disques de transition. La taille de ces cavités est variable, s'étendant de quelques UA à la centaine d'UA. Tout comme le profil de densité de poussière, la répartition du gaz présente également une cavité. La formation de tels disques reste encore assez méconnue.

La faible densité de matière dans la cavité suggère une accrétion affaiblie dans cette région. Cependant, de nombreuses observations rendent comptent de forts taux d'accrétion impliquant une vitesse d'accrétion très élevée. Par ailleurs, certains disques de transition présentent des cavités très étendues. Ces propriétés remettent en question le modèle visqueux standard d'évolution des disques protoplanétaires.

La présence de vents magnétiques, lancés via le mécanisme de Blandford et Payne, pourrait rendre compte de ces observations. En effet, de tels vents peuvent prélever le moment cinétique du disque et permettre à la matière de tomber rapidement sur l'étoile. Ce changement de paradigme est prometteur puisqu'il pourrait expliquer l'existence de disques de transition accrétant fortement.

Le travail que j'ai conduit en thèse consiste à étudier un modèle de disque de transition munis de vents magnétiques via des simulations numériques globales en magnétohydrodynamiques non-idéale avec le code PLUTO.

La fraction d'ionisation des disques de transition a une structure similaire à celle des disques pleins, ainsi la diffusion ambipolaire est l'effet non-idéal prépondérant dans mes simulations. J'initialise ces dernières avec un champ magnétique vertical continu et une cavité imposée à la main.

Un premier jeu de simulations $2,5\,\text{D}$ m'a permis de montrer la stabilité du modèle. De plus, les couples magnétiques enclenchent une accrétion rapide dans la cavité avec un taux d'accrétion considérable. Ces simulations permettent d'étudier efficacement l'évolution séculaire du disque, notamment vis-à-vis du transport de champ magnétique. J'ai également effectué des simulations $3\,\text{D}$ pour étudier la stabilité de la cavité vis-à-vis d'instabilités magnétohydrodynamiques. Il s'avère que des spirales se forment dans cette dernière, avec des vitesses de rotation constante en fonction du rayon. La structure générale de la cavité est de plus tout à fait similaire à celle des disques MAD dans le contexte des trous noirs.

Enfin j'ai étudié plus en détail l'évolution séculaire, sur 300000 orbites au bord interne. J'ai ainsi mis en évidence l'existence de plusieurs régimes de transport de champ (diffusion et advection), le flux magnétique de la cavité s'intensifiant au cours du temps.

J'ai réalisé les premières simulations de disques de transition soutenus par des vents magnétiques, présentant une cavité en rotation sous-képlérienne traversée par un flot de gaz supersonique. Ces prédictions cinématiques m'ont permis de construire des observations synthétiques, déterminantes dans le but de comparer simulations et observations.

ACKNOWLEDGEMENTS

The work that I present in this manuscript is the result of three years at the IPAG in Grenoble. This was a great adventure though the pandemic and some hospitalizations made it quite complicated from time to time.

I want to thank all the members of my jury: Héloïse Méheut, Oliver Gressel, Barbara Ercolano, Jonathan Ferreira and Guillaume Laibe. I thank in particular Héloïse Méheut and Oliver Gressel for reviewing my manuscript and Jonathan Ferreira for being the president of my jury. I also thank Guillaume Laibe for all his advice, back in the time when I was looking for a thesis. Eventually, I thank Clément Baruteau who accepted to take part in my defence and in my CSI with François Ménard.

Je souhaite remercier mon directeur de thèse, Geoffroy Lesur, qui a cru en moi et qui m'a guidé pendant la thèse. Ses conseils ont toujours été pertinents et j'ai été très bien encadré à chaque instant. J'ai beaucoup appris, tant sur la physique que sur les simulations numériques à ses côtés.
Je remercie aussi toute l'équipe SHERPAS qui m'a accueilli et avec qui j'ai passé de très bons moments, même si les circonstances ont fait que je n'ai pu participer qu'à une seule vraie session de Sherpiades !

Je veux prendre le temps de remercier tous les doctorants et postdoctorants que j'ai croisés à l'IPAG pendant ces trois années : Jonatan, Samuel, Ceyhun, Ileyk, Antoine, Andrès, Clément, Benjamin, Marc, Gaylor, Jonah, Adrien, Joanna, Dilruwan, Thomas, Julien, Aurélia.

Je remercie également toutes les personnes avec qui j'ai travaillé lors des enseignements que j'ai donnés à l'UGA, en particulier Hadrien Mayaffre et Catherine Quilliet.

Je remercie aussi tous mes amis, dans le désordre, Jérémy, Val, Jojo et ma filleule Alba arrivée en cours de route de cette thèse, Victor et Alina, Antoine et Elina, Guillaume, Allan, Laura et Louis, Thibault (TIEM !) et Laurane, Florie, Grégoire, Arnaud, Guillaume et Charlotte, Camille, Alizée et Yan, Alexandre, Nassim et Çiçek. Je remercie aussi tous ceux que j'ai oubliés, de l'ENS de Lyon, de l'ENS de Cachan ou d'ailleurs !
Naturellement, je remercie toute ma famille pour son soutien depuis toujours, et en particulier mes parents et ma sœur Lisa.

Rien n'est éternel, pas même les étoiles,

"[...] comme je sais que la consolation ne dure
que le temps d'un souffle de vent dans la cime d'un arbre,
je me dépêche de m'emparer de ma victime.
Qu'ai-je alors entre mes bras ?
Puisque je suis solitaire : une femme aimée ou un compagnon de voyage malheureux.
Puisque je suis poète : un arc de mots que je ressens de la joie et de l'effroi à bander.
Puisque je suis prisonnier : un aperçu soudain de la liberté.
Puisque je suis menacé par la mort : un animal vivant et bien chaud, un cœur qui bat de façon sarcastique.
Puisque je suis menacé par la mer : un récif de granit bien dur."
Puisque je suis physicien : l'illusion d'un monde perméable à la raison.—

Stig Dagerman, *Notre besoin de consolation est impossible à rassasier* (1952)

LIST OF FIGURES

ACRONYMS

ALMA Atacama large millimeter/submillimeter array

AU Astronomical unit

UA *Unité astronomique*

CNM Cold neutral medium

DSHARP Disk substructures at high angular resolution project

EUV Extreme ultra-violet

FUV Far ultra-violet

GRMHD General relativistic magnetohydrodynamic

HD Hydrodynamic

IR Infra-red

IRAS Infra-red astronomical satellite

JED Jet emitting disc

MCAF Magnetically chocked accretion flow

MDW Magnetised disc wind

MHD Magnetohydrodynamic

MIR Mid infra-red

MRI Magnetorotational instability

NIR Near infra-red

PPD Protoplanetary disc

SAD Standard accretion disc

SED Spectral energy distribution

SPH Smoothed particle hydrodynamics

TD Transition disc

UA Unité astronomique

UV Ultra-violet

YSO Young stellar object

Part I

INTRODUCTION, CONTEXT AND NUMERICAL TOOLS

The first part of my thesis aims at giving the physical context of my work. I start by reviewing general results regarding protoplanetary discs, based on observations. The second chapter gathers theoretical results of the non-ideal MHD framework with the numerical setup I used.

1

OBSERVATIONAL CONTEXT AND TRANSITION DISCS

"When you consider things like the stars, our affairs don't seem to matter very much, do they?".

— Virginia Woolf, *Night and Day* (1919)

INTRODUCTION

Stars and planets are commonly observed and constitutive of anyone's daily life. There are countless examples of historic observations such as the epicycles of Hipparchus (second century b.c.) and Ptolemy (second century a.d.) or the discovery of Uranus in 1781, which act like as many landmarks in the philosophy of science. More recently, the first detection of an exoplanet in 1995 was awarded the Nobel prize in 2019. Astrophysics and planetary formation shape our understanding of the world and it comes as no surprise that among all of the missions of the recently launched James Webb Space Telescope (JWST), one is designed to study stars and planets formation. The study of protoplanetary discs is intimately linked to planet formation and is definitively key to understand how the solar system and the exoplanets were formed.

In this introductory chapter, I will start by giving some information regarding the observational context of protoplanetary discs, with a focus on some of their properties that I will talk about throughout all this work (namely accretion, ejection, sub-structures and magnetic fields).

The aim of my thesis is to work on a model of transitional protoplanetary discs or transition disc (TD) whose accretion is sustained by magnetic winds. I will therefore devote the next two sections of this chapter to this category of objects before ending with a description of magnetic wind launching in protoplanetary discs. Since I do numerical simulations of protoplanetary discs, I will also refer to previous numerical results in this text.

INTRODUCTION

Les étoiles et les planètes accompagnent la vie quotidienne de quiconque, de leur observation à l'œil nu la nuit aux références littéraires, filmographiques et artistiques de manière générale.
On ne compte plus les observations déterminantes qui jalonnent l'histoire des idées. Des épicycles d'Hipparque (deuxième siècle avant J.C.) et Ptolémée (deuxième siècle après J.C.) à la découverte d'Uranus en 1781, la conception du monde a été continûment chamboulée et remodelée par l'astronomie et l'astrophysique.
Plus récemment, la première détection d'une exoplanète en 1995 a été récompensée par un prix Nobel en 2019.

Considérant le rôle et la perception de l'astrophysique, il n'est pas surprenant de voir l'engouement généré par le lancement du James Webb Space Telescope (JWST), dont une des missions est consacrée à la formation planétaire.

Concernant les observations de disques protoplanétaires, qui sont les objets centraux de ma thèse, on ne peut que rappeler l'avancée déterminante effectuée grâce aux observations d'ALMA. Cet instrument donne à voir des détails fins dans ces disques, révélant des structures diverses comme des anneaux, des sillons, des spirales.

Dans ce chapitre d'introduction, je commence par donner quelques informations générales relatives à l'observation des disques protoplanétaires, en me focalisant sur des propritétés clés, telles que l'accrétion et l'éjection de matière.

L'objectif de ma thèse est de travailler sur un modèle de disque protoplanétaire dit de transition, muni d'un vent magnétique permettant à la matière de s'en échapper.
Je consacre ainsi une part significative de ce chapitre à ces notions (disques de transition et vents magnétiques). En particulier, je définirai le terme de disque de transition et je détaille le mécanisme responsable de l'éjection par vent magnétique.
Dans la mesure où mon travail est basé sur des simulations numériques, je ferai également référence à des travaux antérieurs de simulations de disques protoplanétaires.

1.1 OBSERVATIONAL CONTEXT: FROM THE MOLECULAR CLOUD TO PROTOPLANETARY DISCS

1.1.1 *Clouds collapses and protoplanetary discs*

1.1.1.1 *Observations of molecular clouds*

The interstellar medium is filled with many gigantic molecular clouds made of cold matter, which is supposed to be turbulent and magnetic (Chevance et al., 2022). These clouds experience many perturbations whose most common origin is supernova (McKee and Ostriker, 1977). When a perturbation is strong enough (a criteria regarding the cloud mass is given by Jeans and Darwin, 1902), the cloud starts collapsing which is the first step of stars and planets formation. Dense cores emerge from this gravitational collapse, surrounded by an envelope of infalling material. Because of the conservation of angular momentum, the falling matter ends up forming a disc around the central object. Detailed additional information regarding core collapses can be found in Lequeux (2012). These discs are named protoplanetary discs since it has been admitted that these structures are the birth cradle of planets. The overall object is called a young stellar object (YSO) and several classes of these objects are to be distinguished, labelled from class 0 to class 3. The definition of these classes was initially based on the slope of the spectral energy distribution (SED) between 2 and 25 µm (Williams and Cieza, 2011). This ranking is due to the fact that protoplanetary discs were first detected with the infrared excess in the spectra of their harbouring YSO.

Hydrodynamical simulations of cloud collapse (Bate, 2009) as well as many observational surveys (Cazzoletti et al., 2019; Tazzari et al., 2021; Otter et al., 2021) strongly suggest that the formation of protoplanetary discs around young stars is a common process. In particular, star forming regions are often crowded with an overwhelming population of YSO as seen in fig. 1, taken from Otter et al. (2021).

The study of molecular clouds collapse is interesting in many ways, because one can expect a protoplanetary disc to inherit some of the properties of its host cloud, such as its chemical composition or its magnetic field which is a key topic. It is well known that the atomic cold neutral medium (CNM) which is the progenitor of the molecular gas, is strongly magnetised (Crutcher and Kemball, 2019). However, the scenario that tracks the behaviour of the magnetic field from the interstellar medium down to the scale of the protoplanetary disc remains unclear (Ching et al., 2022). The most direct method to measure the magnetic field strength uses Zeeman effect, but the lack of suitable probes makes such measurements challenging for PPDS. Reliable direct observations remain sparse and if the molecular clouds and discs are known to be magnetised, the topology of the field is hardly known.

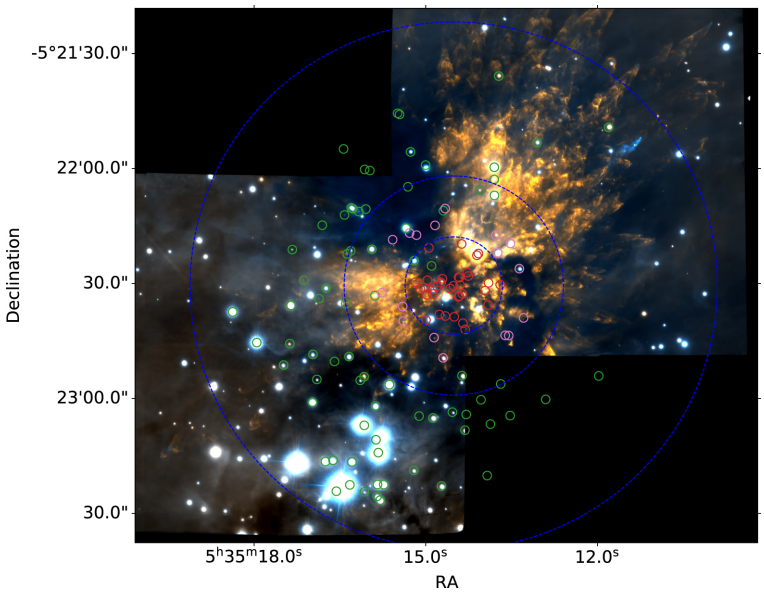

Figure 1: Infra-red (IR) mosaic images of disc hosting stars from a survey in the orion nebula. The Trapezium cluster is located at the bottom left corner. Each circle is a source of the survey, image taken from (Otter et al., 2021).

From the numerical simulations point of view, the magnetic field has been demonstrated to play a major role related to stars and planets formation. In particular, purely hydrodynamical simulations render protoplanetary discs that are way too big compared to observations, while taking into account the effects of the magnetic field reduces their size due to magnetic braking (see Hennebelle et al., 2016 for an analytic justification of this result). Non-ideal MHD processes such as ambipolar diffusion (see chapter 2 for more details on this topic) tend to regulate the accumulation of flux in the disc up to ~ 0.1 G (Masson et al., 2016). The work of Masson et al. (2016) in particular dwells on the necessity to take into account diffusing effects in the treatment of magnetic fields.

Now that I have gathered a few properties of the environment inside which protoplanetary discs form, I will give some observational results regarding protoplanetary discs themselves.

1.1.1.2 *Discs observations*

Because of the angular momentum conservation, protoplanetary are now thought as inevitable remnants of the could collapse and star formation process. They are cold objects whose temperature ranges from 1000 K close to the star (at $R \lesssim 1$ AU) down to 10 K (at $R \gtrsim 100$ AU) and made of gas and dust, with a standard ratio of 1 % of dust. These sources emit strongly in the infra-red (IR) domain so that

instruments that cover milli- and micrometer range wavelengths are convenient to study protoplanetary discs.

The infra-red Astronomical Satellite (IRAS) performed the first statistical studies of discs in the IR domain (Strom et al., 1989). Time have now passed since the first historical detections of discs and new instruments such as the Atacama Large Millimeter/Submillimeter Array (ALMA) render breathtaking observations of protoplanetary discs as well as numerous statistical studies (Long et al., 2018). The emblematic picture of the disc around HL Tau (Brogan et al., 2015) paved the way to a new epoch in the observations of discs. The Disk Substructures at High Angular Resolution Project (DSHARP), introduced in Andrews et al. (2018), is an example of such state-of-the-art observations of the field, the panel of discs being shown in fig. 2.

Protoplanetary discs are now undoubtedly understood as inherent to star formation. The aims of studying these objects are no longer to find evidences of their existence nor to check a possible link with planetary formation. The quantity and precision of all the observations of discs call for refined theoretical models and predictions regarding their composition, evolution and the detailed origin of the structures they harbour. Numerical simulations help to achieve these objectives as they make predictions to be confirmed by observations or give them a theoretical background to understand the physical processes at play.

1.1.2 *Protoplanetary discs*

1.1.2.1 *Accretion*

The Sun contains more than 99.8 % of the total mass of the Solar System but only 1 % of its total angular momentum. Based on the general picture of star formation, the primordial discs are massive and orbit with a Keplerian rotation profile around a protostar which has only 1 % of its final mass. Therefore, it stands clear that as long as a protoplanetary disc nestles around a young star, the surrounding mass should be accreted towards the central object while the angular momentum is removed outwards. In this general picture, protoplanetary discs are considered as accretion discs and the rate at which matter is moving inwards is called the accretion rate and denoted with the generic notation $\dot{M} = dM/dt$.

At the innermost radii of protoplanetary discs ($R \lesssim 0.1$ AU), the disc is made of hot gas and subject to intense magnetic fields (I will come back to this point in sec. 1.1.2.3). The matter coming from the disc is supposed to follow the stellar magnetic field lines that form loops from the stellar surface and eventually falling on it in a free fall motion. In this accretion mechanism, the gas forms accretion columns and produces an accretion shock at the star surface, that is

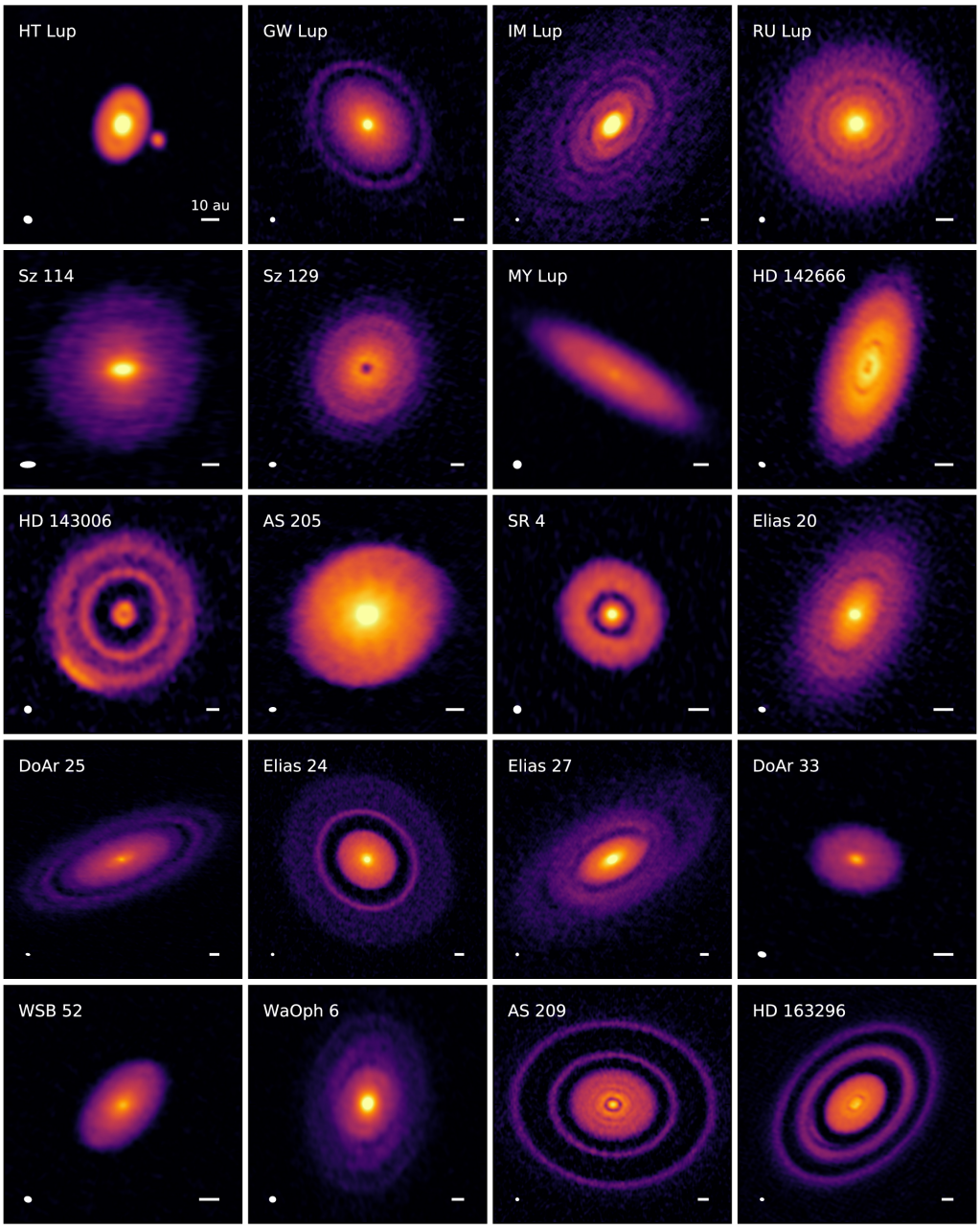

Figure 2: Panel of the 20 protoplanetary discs in the DSHARP sample (1.25 mm continuum emission). Figure taken from Andrews et al. (2018).

observed in the ultraviolet (UV) bands of discs spectra. Such a mechanism is named magnetospheric accretion (Bouvier et al., 2006) and the UV excess gives access to accretion rate estimates. Hartmann et al. (1998), Dullemond et al. (2006) or Li and Xiao (2016) give orders of magnitude regarding the accretion rate of protoplanetary discs around T Tauri stars. The most common estimation given in Hartmann et al. (1998) is $\dot{M}_{PPD} \sim 10^{-8\pm1}\ M_\odot\,yr^{-1}$, for T Tauri stars of mass $M_\star \sim 0.5\ M_\odot$, where $1\ M_\odot$ is the mass of the Sun.
This order of magnitude implies that PPDs disappear on a time scale of a few million years. Detections of discs around young stars as a function of their age corroborate this characteristic dispersion time scale for the PPDs.

1.1.2.2 *From accretion to ejection*

Accretion discs are ubiquitous objects and compose a wide class of diverse astrophysical discs. Not only are they detected in YSO, but also around black holes and neutron stars (Lynden-Bell, 1969), white dwarfs (see the review of Verbunt, 1982, for example) or late-stage stars (Kluska et al., 2022). All these discs share the same fundamental property: matter is accreted towards the central object and angular momentum flows outwards. These conditions are fulfilled when angular momentum is removed from the rotating fluid that composes the disc. This can be achieved with a radial stress $W_{r\varphi}$ or (and) a surface one $W_{\theta\varphi}$. I will give more detailed definitions and properties of these quantities that appear in the angular momentum conservation equation in chap. 2. For now, it is enough to state that the radial stress accounts for the radial removal of angular momentum (through its radial derivative) and the surface stress for the vertical one. Figure 3 illustrates the role of the stresses with a schematic and local view of an accretion disc.

An intuitive way of generating a radial stress is to take into account the viscosity ν of the fluid due to its inter-molecular forces. However, doing so leads to PPDs that live for more than the age of universe, which is in total contradiction with the orders of magnitude presented in sec. 1.1.2.1. Another source of radial stress is therefore needed.
A solution was proposed by Shakura and Sunyaev (1973) in the context of accretion around black holes. Shakura and Sunyaev (1973) showed that turbulence can be interpreted as an effective viscosity capable of generating a radial stress. The resulting normalised radial stress is labelled with the letter α and defined as

$$\alpha \equiv \frac{\overline{\rho\, v_\varphi\, v_r}}{\overline{P}}\,, \tag{1}$$

$\bar{\cdot}$ *is a vertical integration procedure defined in chapter 2.*

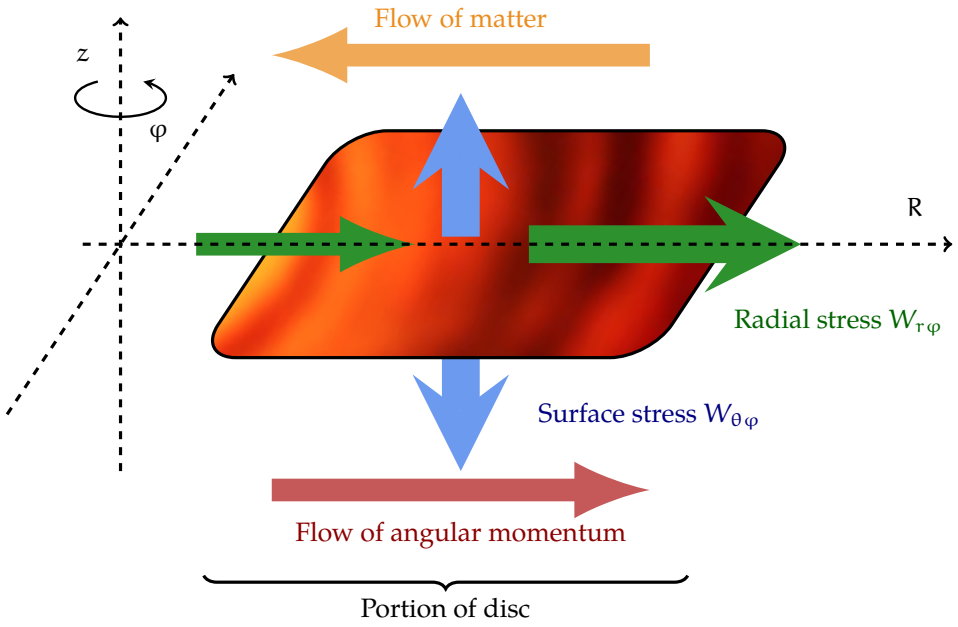

Figure 3: Schematic view of a portion of an accretion disc. The blue arrows represent the vertical loss of angular momentum via the surface stress $W_{\theta\varphi}$. The green arrows account for the radial flux of angular momentum due to the radial stress $W_{r\varphi}$. The back image is the disc HL Tau, taken from Brogan et al. (2015) as an illustration.

with ρ, P and $v_{r,\varphi}$ respectively the density, the pressure and the velocity components of the fluid. The associated effective (or turbulent) viscosity then reads

$$\nu_t \equiv \alpha\, c_s^2\, \Omega_K\,, \tag{2}$$

where c_s is the sound speed.
This way of proceeding laid the first stone to a general paradigm regarding accretion discs, under the name of α−disc model or viscous disc model. This model can be applied for the case of PPDs for which typical values of α are of the order of $\alpha \sim 10^{-2}$ (Calvet et al., 2000). The α parameter embodies a constitutive equation that links the accretion rate to the local sound speed and surface density of the discs and comes together with a characteristic time scale for the viscous evolution that can be compared to the Keplerian frequency $\Omega_K = \sqrt{G\,M_\star/R^3}$ ($M_\star$ is the mass of the central star)

$$\tau_{\text{viscous}} \sim \frac{R^2}{\nu_t} = (\alpha\,\Omega_K)^{-1} \left(\frac{h}{R}\right)^{-2} \gg \Omega_K^{-1}\,. \tag{3}$$

This ordering suggests that any viscous evolution of an accretion disc occurs on long time scales compared to the dynamical one. This model is a convenient and useful framework to address the question of accretion in long-lived accretion discs and many works use this model as a starting point.

A question still left unanswered at this point is the origin of the turbulence needed to generate the effective viscosity. Hydro and magnetohydrodynamics instabilities are fruitful topics to find sources of turbulence (the major ones being listed and detailed in Lesur et al., 2022). In particular, the magnetorotational instability (MRI, Velikhov, 1959; Chandrasekhar, 1961; Balbus and Hawley, 1991) has long been a good candidate. This instability arises from the competition between orbital inertia and magnetic tension in the ideal MHD picture and a consensus was once reached regarding its key role to generate turbulence in PPDs. However, this paradigm is now challenged by various observations in the context of PPDs.

Firstly, the dominant processes accounting for the discs dynamics strongly vary with the physical properties and therefore with the location in the disc (see fig. 6 in Lesur et al., 2022). The MRI is therefore supposed to be triggered in the innermost region of discs ($R \lesssim 1$ AU) only.

Moreover, PPDs happen to be weakly magnetised objects so that non-ideal MHD is at play with Ohmic, Hall and ambipolar diffusivities and the MRI is modified in these regimes where discs are weakly ionised (Wardle, 1999). I detail some general properties of MRI in the non-ideal MHD regime in the upcoming paragraphs. I recall that additional information are to be found in chapter 2 regarding the driving equations and origins of the non-ideal effects. I will only focus on orders of magnitude in these paragraphs as I want to extract the main physical arguments that are used to justify the way MRIis described in PPDs.

OHMIC DIFFUSION AND DEAD ZONES: I first consider the Ohmic diffusivity only that I denote with η_O. One can build the magnetic Reynolds number $\mathcal{R}_\mathcal{M}$ for a given characteristic velocity U and length L as

$$\mathcal{R}_\mathcal{M} \equiv \frac{U\,L}{\eta_O}\,. \tag{4}$$

I recall that $\mu_0 = 1$ with CGS units.

In order to trigger MRI, one must satisfy

$$\mathcal{R}_\mathcal{M} > 1 \qquad \text{INSTABILITY.} \tag{5}$$

Following Armitage (2017), the magnetic Reynolds number can be recast as

$$\mathcal{R}_\mathcal{M} = \frac{\alpha^{1/2}\,c_s^2}{\eta_O\,\Omega_K}\,, \tag{6}$$

$$\approx 1.4\times10^{12}\,\xi\left(\frac{\alpha}{10^{-2}}\right)^{1/2}\left(\frac{R}{1\text{ AU}}\right)^{3/2}\left(\frac{T}{300\text{ K}}\right)^{1/2}\left(\frac{M_\star}{M_\odot}\right)^{-1/2}, \tag{7}$$

with ξ the ionisation fraction and T the temperature of the disc. $\alpha = 10^{-2}$ corresponds to the standard order of magnitude in PPDs previ-

ously mentioned. This simple calculation implies that $\xi \sim 10^{-12}$ is the minimal ionisation fraction demanded for MRI to occur at $R = 1$ AU in PPDs. Such a criterion is not fulfilled near the disc midplane for $R \gtrsim 1$ AU, so that a dead zone (i.e. a zone in which MRIis inactive) spans in the disc as shown by Gammie (1996).

AMBIPOLAR DIFFUSION: There is a broad literature on the interplay between non-ideal processes and MRI (see Balbus and Terquem, 2001 and Kunz and Lesur, 2013 for the Hall effect for example). I want to focus on the impact of the ambipolar diffusion on MRI (Blaes and Balbus, 1994; Kunz and Balbus, 2004). A linear analysis of the MHD equations with ambipolar diffusion allows to find a stabilising criterion for MRI (Kunz and Balbus, 2004) so that ambipolar diffusion quenches the MRI. Hawley and Stone (1998) and more recently Bai and Stone (2011) showed that in the non-linear regime, the MRI is inoperative when the ambipolar Elsasser number Λ_A is below 100. The analysis of Bai and Stone (2011) shows that in presence of a mean vertical magnetic field, some modes of the MRI survive and generate a momentum transport corresponding to at most $\alpha \sim 10^{-4}$. This value is still 2 orders of magnitude lower than the one deduced from observations of PPDs. In short, MRI can hardly account for all of the momentum transfer in protoplanetary discs and another mechanism must be found.

The transfer of angular momentum through a radial stress with turbulence (whatever its source) is itself challenged. Indeed, the level of turbulence deduced from observations (Flaherty et al., 2018; Flaherty et al., 2020) are pretty low and hardly renders sufficiently high values of α (that would account for the accretion rates measured in PPDs). Therefore, an alternative to momentum transfer with a radial stress must be found.

EJECTION AND VERTICAL STRESS: Keeping in mind fig. 3, it looks natural that astrophysicists proposed to take into account the vertical or surface stress (sometimes even called a laminar stress). A credible possibility is that discs have outflows so that matter leaves their surface and extracts angular momentum. The Blandford & Payne (or magneto-centrifugal) process (Blandford and Payne, 1982) allows the launching of an MHD or magnetic wind as long as the disc is threaded by a vertical magnetic field with sufficiently bent field lines. Observations of MHD winds are challenging (Stephens et al., 2014; Whelan et al., 2021) and it is difficult to disentangle outflows in discs of various natures (de Valon et al., 2020) and origins (from the star or from the disc). Still, ouflows from YSO are observed (see fig. 4) and remain

Figure 4: Image of the Herbig-Haro object HH24. Credits: NASA and ESA.

a good candidate to account for angular momentum transport. In the world of numerical simulations of protoplanetary discs, magnetic winds are now commonly studied (Béthune et al., 2017; Jacquemin-Ide et al., 2021; Lesur, 2021b; Cui and Bai, 2021) so that this paradigm shift seems promising.

1.1.2.3 *Magnetic fields*

Either regarding MRI or magnetic wind launching, magnetic fields play a major role. It is obviously mandatory to have information on the magnetic field topology and intensity in protoplanetary discs. As said in sec. 1.1.1.1, it is perfectly fine to assume that protoplanetary discs are magnetised. However, direct detections of magnetic field remain sparse and challenging so that the topology and intensity of the magnetic fields in PPDs are both poorly constrained.
In the same spirit as for molecular clouds, Zeeman effect could be used to get access to the intensity of the magnetic field in protoplanetary discs. However, such observations were tempted (Donati et al.,

2005; Vlemmings et al., 2019; Harrison et al., 2021), but are very difficult so that we currently only have access to upper limits. As an example, Vlemmings et al. (2019) found an upper limit of $B < 30$ mG at 42 AU.

Spinning dust grains are supposed to align in a way that their short axes are perpendicular to the surrounding magnetic field (Lazarian, 2007). Hence, thermal dust polarisation is also expected to be detected perpendicular to the magnetic field, as it is the case in molecular clouds (Seo et al., 2021) or protostellar envelopes (Girart et al., 2006; Rao et al., 2009). Such measurements were also tempted for protoplanetary discs. The first attempts to measure dust grains polarisation ended up with non-detections (Hughes et al., 2009b; Hughes et al., 2013), when more recent observations conclusively detected polarisation (see for example Harrison et al., 2019). However, two alternative polarisation mechanisms could also account for observations in PPDs. A first possibility is that grains have their short axis aligned with the direction of radiation anisotropy as suggested by Kataoka et al. (2017). Eventually, polarisation could also be caused by self-scattering of grains (Kataoka et al., 2015). Disentangling these mechanisms is even challenging (Stephens et al., 2017) so that mapping the topology of magnetic fields in PPDs through dust polarisation remains a very difficult and uncertain task.
In the end, one cannot be definitive on the subject of the magnetic field strength and topology which are still questions open to debate.

1.1.2.4 *Substructures*

Studies of protoplanetary discs such as the one shown in fig. 2 reveal that substructures in PPD are common. Substructures exhibit a wide variety of shapes such as rings and gaps, spirals, non-axisymmetries, vortices or central cavities. Spirals are recovered in numerical simulations (Ogilvie and Lubow, 2002) and planets are often invoked to explain these shapes, as it is the case for AB Aurigae (see fig. 5 and Boccaletti et al., 2020). Substructures suggest the diversity of the phenomena at play in protoplanetary discs and need to be recover in numerical simulations which provide explanatory processes for them.

1.2 TRANSITION DISCS

Protoplanetary discs regroup very diverse objects from young discs gravitationally unstable to debris discs. A subset of protoplanetary discs named transition (or transitional) discs (TD) stands out. This category of discs is the central topic of my work. In this subsection, I will give a definition of these objects based on their observational properties. I will then show how they are thought as a peculiar stage of

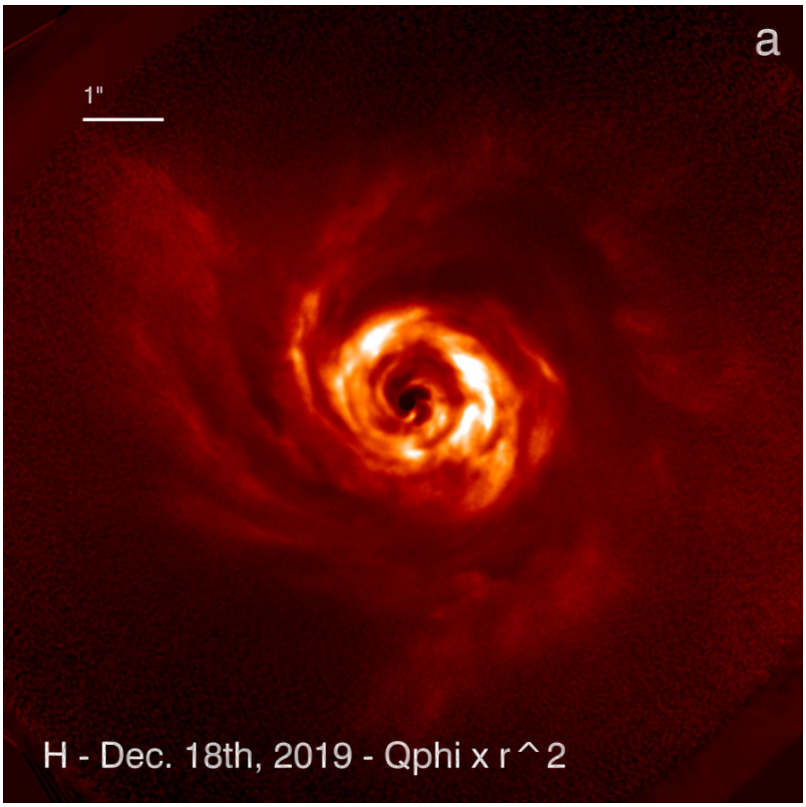

Figure 5: Image of the disc around AB Aurigae, adapted from (Boccaletti et al., 2020).

discs regarding the usual stars and planets formation picture before pointing out a few observational inconsistencies with this scenario.

1.2.1 *Definition and observations*

In this subsection, I aim to give a definition of transition discs as an attempt to have a convenient conceptual frame to work with. Finding a thing as definitive as a 'definition of transition discs' proved to be difficult.
A first conceivable definition is based on the detection of transition discs through YSO spectra. The IR excess indicates the presence of a disc and tracks the dust surface density. For some discs, this excess exhibits a lack of near infra-red (NIR) excess and a standard mid infra-red (MIR) excess, both being compared to the expected emission from a full disc. Fig. 6 illustrates this statement while some corresponding historical observations of TDs are to be found in Strom et al. (1989) and Kenyon and Hartmann (1995). A shortage of NIR excess compared to MIR suggests a loss of the hottest parts of the (still cold) disc, which implies a cavity (i. e.: a lack of dust) close the star. Therefore, transition discs are thought as a particular class of disc that is characterized by a peculiar NIR-to-MIR excess. This way of discriminating TDs amond PPDs (Owen, 2016) is efficient but says nothing with respect to any dispersal process (i. e. a process that enables the disc disappearance in a time scale compatible with observation).

Another angle of attack can be adopted to define transition discs. In particular, I emphasize that the notion of transition discs was first thought as an outcome of discs dispersal that are supposed to disappear in a few millions up to a few tens of millions years (Mamajek, 2009; Emsenhuber et al., 2021). It is then straightforward to postulate the existence of discs in an intermediate state between a full protoplanetary disc and a star left alone with no disc. Assuming that an inside-out process disperses the disc, such transition discs would exhibit an inner cavity, growing with time so that the disc would be encountering its dispersion phase. Therefore, it is possible to define transition discs as cavity hosting PPDs. This definition is made possible thanks to the actual observations of cavity in the dust radial surface density profiles (Brown et al., 2009).

Still, it is not obvious that every detected TDs are indeed dispersing PPDs.

Not only are cavities detected in the dust radial density profile but some are also observed in the gas profile of PPDs (Carmona et al., 2014; Bruderer et al., 2014; Dong et al., 2017). As an example, a drop in the gas density of 2 to 4 orders of magnitude was measured in the inner (< 3 AU) regions of the transition disc around the HD 139614 by Carmona et al. (2017) with ro-vibrational CO lines. Surveys of TDs such as van der Marel et al. (2016b) show that there exist multiple TDs with 'clean' cavities both in the dust and in the gas components.

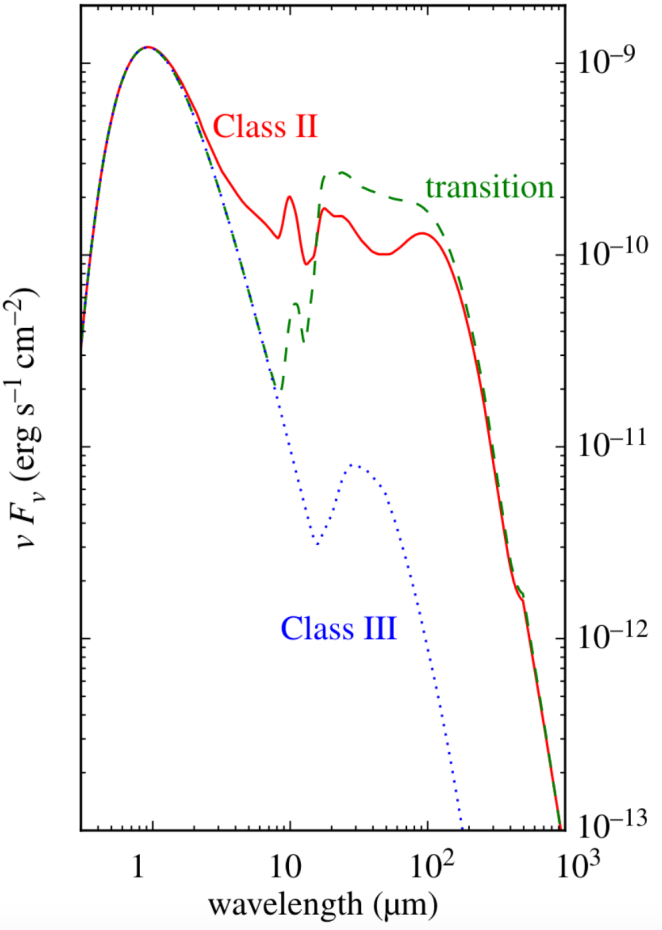

Figure 6: Spectrum of a star harboring: a full protoplanetary disc (in red full line), a transition disc (in green dashed line) and a debris disc (in blue dotted line), adapted from Ercolano and Pascucci (2020).

In this work that is based on numerical simulations, I will drop the aspects of the previous definitions related to the SED and consider that *any protoplanetary disc that exhibits a cavity in its total matter (dust and gas)) density profile is a transition disc*. In principle, this definition makes possible to have transition discs around other objects than young stars (such as late stage stars Kluska et al., 2022) and erases any differences with pre-transitional discs (Espaillat et al., 2010). However, this definition has the advantage of being easy to manipulate and remains agnostic regarding the dispersal process of protoplanetary discs.

To end this discussion on vocabulary issues, I add that I refer to protoplanetary discs that do *not* exhibit a cavity as primordial PPDS (when I refer to an evolutionary picture) or as full or standard PPDS to dwell on the absence of cavity. In particular, the word 'standard' do not refer to a viscous evolution nor to the α-disc model whatsoever and I will explicitly employ the word 'viscous' whenever needed.
Indeed, my previous comment illustrates the difficulty to get a definition of TDS, since the words 'transition' and 'primordial' are linked to an evolutionary picture that I did not addressed at all (and that I discuss in sec. 1.2.2).

Conclusively, transition discs are well known objects and many observational studies and analyses are devoted to them (van der Marel et al., 2016b; Villenave et al., 2019; van der Marel et al., 2020; Francis and van der Marel, 2020; van der Marel et al., 2022). Figure 7 displays a sample of transition discs studied in Francis and van der Marel (2020). It is worth noting that even in these discs, a wide range of substructures are detected.

1.2.2 *Evolutionary sequence*

As just said, transition discs are considered as dispersing PPDS. Disc dispersal is thought to be a combination of several processes, the most promising ones being photoevaporation (Shu et al., 1993) and planet-disc interaction (Baruteau et al., 2014). I will hereafter describes photoevaporation in short before summarising the evolutionary picture of TDS.

1.2.2.1 *Photoevaporation winds*

The central idea of photoevaporation is that the stellar radiation ionises the disc matter and heats its upper layers. The radiation to consider is highly energetic, such as far ultra-violet (FUV), extreme ultra-violet (EUV) and x-ray (Alexander et al., 2006; Alexander et al., 2014) providing as many photoevaporation regimes and covering the energetic range from 6 eV up to 100 eV. Heated material therefore encounters

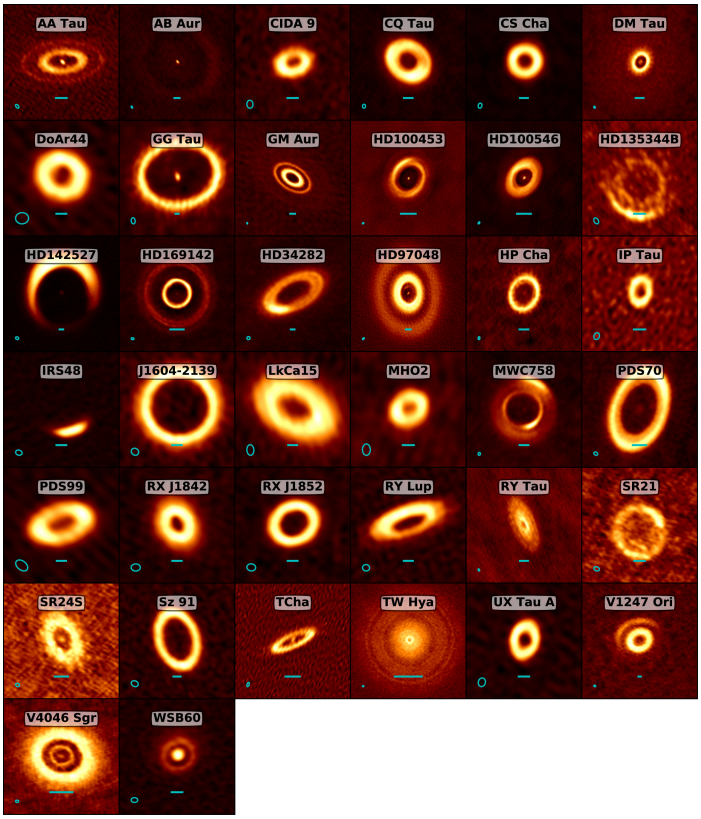

Figure 7: Images of TDs from the sample used in Francis and van der Marel (2020).

enhanced thermal agitation and the local sound speed increases.
I now consider a single layer of a PPD, ionised by the central star and characterised by a given sound speed c_s. The escape velocity in this layer decreases with the radius. At some point, the escape velocity gets lower than the thermal speed and a pressure-driven outflow is generated. Such outflows are detected (Pascucci et al., 2011) and pushed forward as promising candidates to account for the dispersal of discs (Ercolano et al., 2021). The typical mass loss rates associated with these outflows are at maximum of the order of a few 10^{-8} $M_\odot\,yr^{-1}$ (Gorti and Hollenbach, 2008).

This transsonic outflow is similar to a Parker wind.

The models of photoevaporation (Shu et al., 1993) were initially characterised by a gravitational radius R_g (the radius where the escape velocity equals the thermal sound speed) given by

$$R_g \equiv \frac{G\,M_\star}{c_s^2}\,. \tag{8}$$

This radius marks a lower limit after which photoevaporation can be effective. For a 1 $M_\odot$ star with a ionisation temperature of 10^4 K, R_g reaches 9 AU (Rodenkirch et al., 2020). However the transition is rather smooth and can occur down to a few 0.1 R_g (Font et al., 2004), at a characteristic radius $R_c \approx R_g/5$.
Photoevaporation is well studied by numerical simulations (Owen et al., 2012; Rodenkirch et al., 2020). It is commonly accepted that this process is capable of opening a gap in protoplanetary discs at approximately R_g. I detail the dispersing process associated to photoevaporation in the next subsection.

1.2.2.2 *A standard evolution scenario*

Photoevaporation winds pave the way to an evolutionary sequence of protoplanetary discs. Starting with a full disc, photoevaporation carves a gap between 1 and 10 AU. This being done, the falling matter reaching the gap from the outer disc leaves the disc in a thermal wind with a given mass loss rate $\dot{M}_w$. The mass flux $\dot{M}_{acc.}$ due to the accretion in the outer disc reaches the gap location. If $\dot{M}_{acc.} \leqslant \dot{M}_w$, the matter from the outer part of the disc leaves the disc in the photoevaporation wind and without filling in the gap. The inner disc is not fuelled by matter coming from the outer part anymore and eventually disappears because of its accretion. The disc ends up with a cavity extending up to R_g and growing with time because of the now direct enlightenment of the disc by the star. This scenario can completely come along with planet formation, that could migrate from the outer disc down to the gap. TDs undergoing photoevaporation clearing have general properties such as an inner cavity of radius $\gtrsim R_c$, little or no accretion and an outer disc with a small mass. The regions of PPDs affected by photoevaporation are very different from

one model of photoevaporation to another. As a example, EUV models of photoevaporation predict mass loss from a narrow range of radii around R_g. In the context of PPDs with external irradiation, Throop and Bally (2005) found significant mass loss rates up to 50 AU which is an upper limit for photoevaporation models. Figure 8 illustrates the dispersal scenario associated with photoevaporation winds.

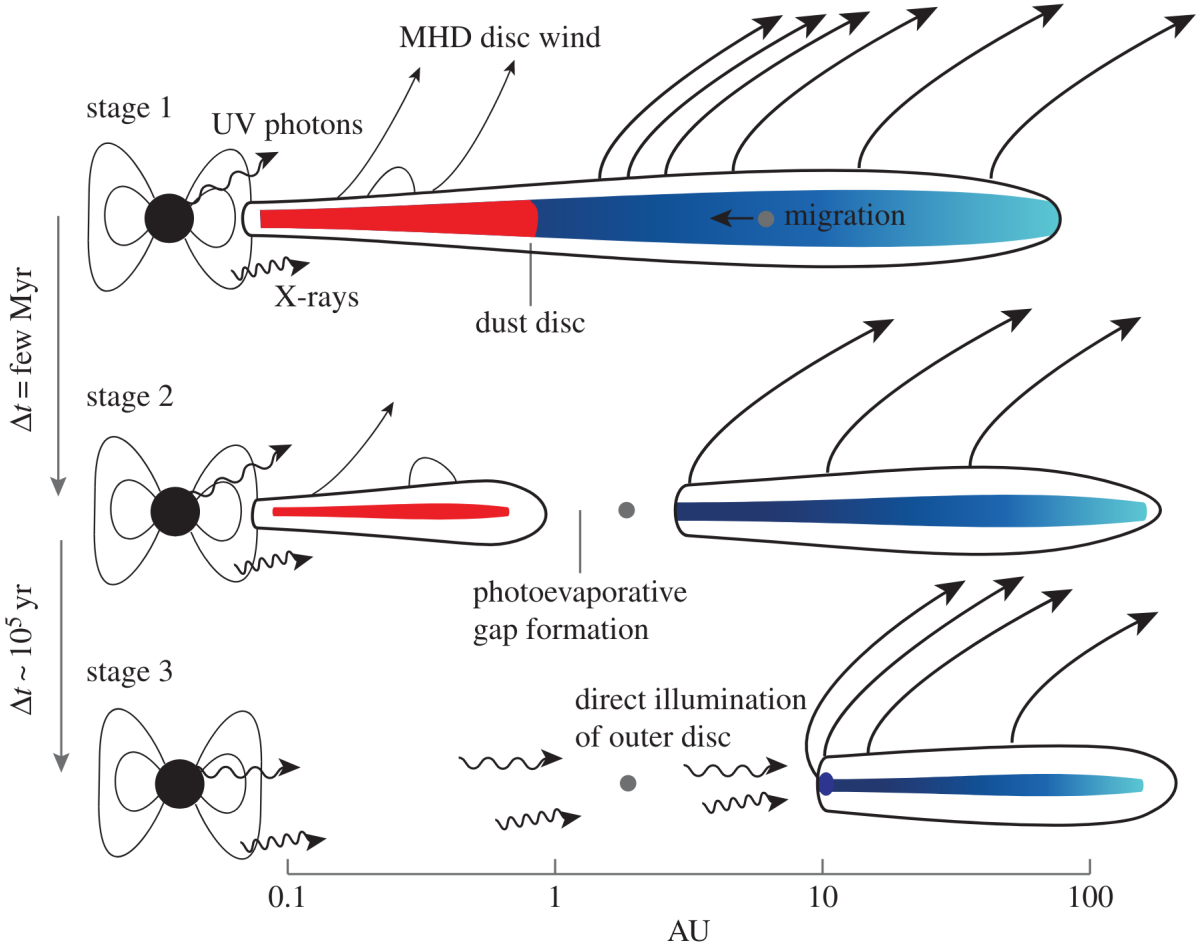

Figure 8: Photoevaporation-based scenario of protoplanetary discs evolution, adapted from Ercolano and Pascucci (2020).

A major success of this model is to give a comprehensive and appealing framework to understand the evolution of protoplanetary discs. Photoevaporation winds can be refined and completed with other processes (and I will discuss them in sec. 1.3). However, this picture encounters some observational discrepancies that I address in the coming subsection.

Anyhow, I would like to mention that this model is supported by strong evidences. Direct observations of winds compatible with photoevaporation winds favour the evolutionary sequence I just described. Still and as I am going to show in the next subsection, some discrep-

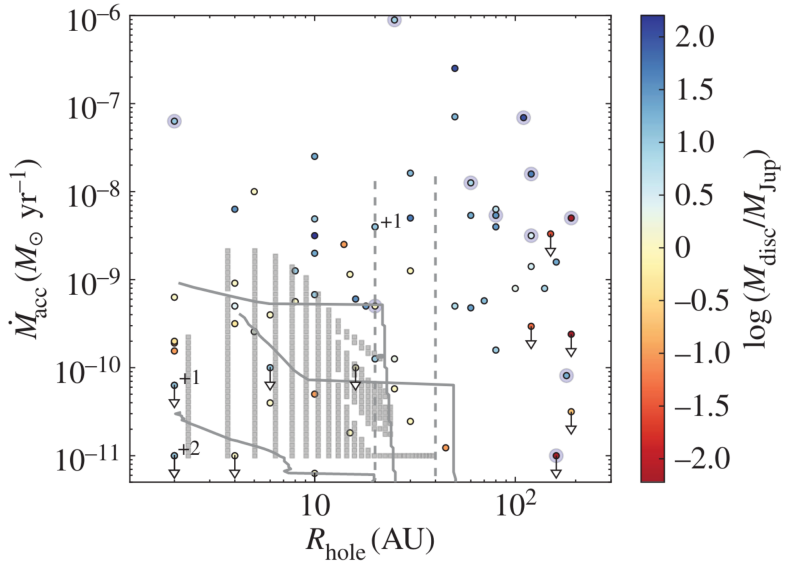

Figure 9: Transition discs in a $(R_{cav.}, \dot{M})$ plane. Each dot is an observed transition discs and the color gives its mass. The grey bars represents accessible values with an evolutionary model that includes photoevaporation as well as a giant planet embedded in the disc, adapted from Ercolano and Pascucci (2020).

ancies and limitations of this model persist. My aim is not to discard this model but rather to suggest an alternative that can work along with it (see for exemple Kunitomo et al., 2020) or at least account for the remaining observational discrepancies.

1.2.3 *A challenged paradigm*

The evolutionary model is challenged by observations when considered through the prism of photoevaporation. As highlighted in the previous subsection, photoevaporation models are effective until at most 50 AU. Moreover, in this framework, TDs should end up with weak accretion rates. Their accretion rates are of the order of the mass loss rates of the photoevaporation wind in order to get the disc clearing. Therefore their accretion rates are at most 10^{-8} $M_\odot\,yr^{-1}$ with optimistic choices regarding the star radiation properties (Owen, 2016). Such limitations are in direct conflict with observations as seen in fig. 9. Transition discs with wide cavities ($R_{cav.} \gtrsim 40$ AU) and/or encountering strong accretion ($\dot{M}_{TD} \gtrsim 10^{-9}$ $M_\odot\,yr^{-1}$) are common objects, an example of which being found in González-Ruilova et al. (2020) (and see fig.10). In particular, fig. 9 shows that some strongly accreting transition discs are still very massive, so that they seem unlikely to be outcomes of an evolution sequence.

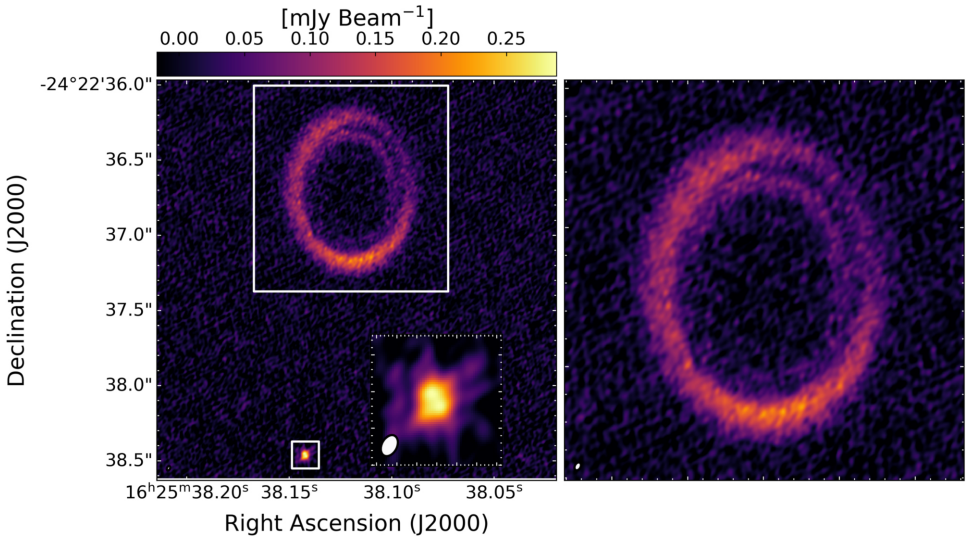

Figure 10: Transition discs observed around ISO-Oph 2 the widest one having a dust cavity of 50 AU and an accretion rate of $10^{-8.7}$ $M_\odot$ yr^{-1}. Taken from González-Ruilova et al. (2020).

From a more general point of view, Owen and Clarke (2012) perform a statistical analysis of a wide sample of 76 transition discs and get a huge fraction of sources with large mm fluxes. With the evolutionary scenario, the proportion of TDs detected with high mm flux is supposed to be lower than the ones with lower mm flux (because TDs are thought as *transitioning* objects from full hence massive discs to completely dispersed hence 'massless' discs). Owen and Clarke (2012) and Owen (2016) either suggest that at least 2 distinct families of TDs are at play to explain these results or that the evolutionary should be dropped.

I highlighted in sec. 1.2.1 that many TDs were characterised by a cavity both in their dust and gas radial density profiles. Such observations are in tension with the high accretion rates measured in TDs. As an example, this discrepancy suggests a supersonic replenishment of the inner discs for the case of IRS 48 (Bruderer et al., 2014). Such a sonic infall of gas could have been observed in HD142157 (Rosenfeld et al., 2014). Nevertheless a word of caution is to be added to the observation of this very peculiar object that is thought to possess a large warp compared to an inner compact disc (Casassus et al., 2015).

The outstanding conclusion regarding the previous arguments is that transition discs are rather unlikely to be fully described with an evolutionary scenario based on photoevaporation winds (and indeed even planet-disc interaction) and viscous discs. One is now left with two options:

- Keep the evolutionary model and add one or more mechanism(s) to account for high accretion rates.
- Discard this model (at least for the problematic TDs) and propose a new one to account for the stability of highly-accreting cavity hosting discs.

In the next section, I will discuss the first point and show that no fully convenient mechanism has yet been suggested. The final section will shed light on the model of magnetic winds sustaining the cavity that I propose and worked on.

1.3 THEORETICAL MODELS OF TRANSITION DISCS

In this section, I review some alternatives that complete the evolutionary model trying to account for high accretion rates. Two main possibilities are considered, either one has an inner mass reservoir to fuel accretion or one has a physical process that enhances accretion. Most of the models I will present rely on the viscous disc model.

1.3.1 *Photoevaporation with a dead zone*

In order to obtain high accretion rates in transition discs, a possibility is to fuel accretion with a mass reservoir located in the inner part of the disc. Such a configuration is achieved by putting a dead zone in the inner part of the disc, so that a gap opens right after. Such a configuration was first studied by Morishima (2012) and extended by Pinilla et al. (2016) and Gárate et al. (2021).

These works are both motivated by the lack of highly-accreting TDs predicted with photoevaporation winds only. With these two models, a dead zone (i. e. a poorly ionised layer characterised by a low viscosity due to the weak development of the MRI) is surrounded by layered accretion (Zhu et al., 2010). The key idea is that matter inside the dead zone is not dispersed quickly by the photoevaporation wind once a gap has been carved and maintains a strong accretion rate (concomitant with the gap, i. e. a cavity).

A definitive success of this way of proceeding is that highly-accreting TDs are indeed obtained (see for example fig. 5 in Gárate et al., 2021). However, this mechanism seems inconsistent with the observations of massive accreting TDs (see fig. 9) since discs with a small cavity radius and a high accretion rates are not obtained. In particular, most of the mass of the discs simulated in Morishima (2012) is located inside the dead zone, whereas massive TDs are observed with most of their mass located in the outer parts. More specifically, the dead zone is eventually dispersed which leads to a drop in the accretion rate, so that this model cannot generate systematic old, massive and highly-accreting TDs. Finally, it is worth noting that these works rely on the

Ohmic dead zone model (Gammie, 1996), while dead zones are now thought to be much more extended radially due to ambipolar diffusion (Simon et al., 2013).

This model is capable of generating highly-accreting TDs but fails to achieve this in a systematic way. A dead zone can act as a mass reservoir generating strong accretion, but cannot be included as a systematic step in the evolutionary scenario. This model is completely contradicted by the massive TDs with large cavity and strong accretion rates.

1.3.2 *Perturbing bodies in the cavity*

A plausible approach to cope with highly-accreting TDs is to consider that some perturbing bodies lie in the cavity. The 2 straightforward candidates are planets and/or a star embedded in the cavity.

1.3.2.1 *Planets*

Fig. 9 already concludes that taking into account planets in the cavity fails to recover the whole distribution of TDs in the $(R_{cav.}; \dot{M})$ plane. However, it is still a formative exercise to understand the very underlying explanations. The work of Crida and Morbidelli (2007) already cast doubts on the hypothesis of planet-induced cavities in TDs and this idea was confirmed by Zhu et al. (2011). The main two arguments are the following.

To start with, many planets (at least 3 to 4 planets) are needed inside the cavity to generate a gap with a sufficient density contrast compared to what is observed. This high number is also recovered by Dong and Dawson (2016) where the authors point out that such a result would imply more multiple giant planet systems in resonance as well as higher occurrence rate of giant planets at wide separation than what is observed.

A second point inferred by Zhu et al. (2011) is that planets fail to account for sufficient density contrast and high accretion rates. Indeed, the embedded planets catch a portion of the accreted material so that it is mandatory to lower the accretion on the planets to have a strong overall accretion rate onto the star which in the end reduces the density contrast in the cavity.

Therefore, planets in the cavity are unlikely to account for the observational discrepancy regarding TDs.

1.3.2.2 *Binaries*

Another model I wish to investigate is the hypothesis that cavities undergoing a fierce accretion are induced by central binary stars. A wide proportion of stars are indeed binaries. Therefore, this assumption could render systematic highly-accreting TDs.

On the one hand, discs initially labelled as transitional were eventually demonstrated to be circumbinary. This was the case for CoKu Tau/4 (Ireland and Kraus, 2008). On the other hand, some studies of TDs tend to rule out the possibility to have binary stars as central objects. The TD around GM Aurigae and studied by Hughes et al. (2009a) is an example of such discs. The binarity hypothesis was ruled out mostly because of the strong accretion rates of the disc. Hence, it seems unlikely that considering binary stars will account for highly accreting TDs.

In the work of Ireland and Kraus (2008), 'TDs' around binary stars are named circumbinary discs. With my definition, I would keep the name TDs. Such a discussion illustrates the difficulty to find a universal definition of TDs.

SPH simulations focusing on the disc MWC 758 (Calcino et al., 2020) show that with the central binaries enable the formation of a cavity. This work also shows that spirals are inherent to this model. However not all observed TDs harbour such structures.
More general numerical works (Thun et al., 2017; Chachan et al., 2019) also study the impact of binaries on a disc. If binaries seem to carve a cavity, the related accretion rates are too low (Chachan et al., 2019) so that this model does not solve the previously discussed observational discrepancy regarding TDs.

Finally, the work of Ruíz-Rodríguez et al. (2016) is devoted to the link between binaries stars and TDs. $38 \pm$ % of the TDs in their sample can correspond to a binary system. If some TDs can be reproduced with binaries, a large fraction of them have to be explained by other mechanisms. As an example, the disc J16315473 − 2503238 (part of their sample) has a strong accretion rate ($\dot{M}_{acc} = 10^{-7.2}$ $M_\odot\,yr^{-1}$) but is unlikely to have binary stars as central objects.

Lastly, I want to add that even a star among a multiple system can host its own wide and strongly-accreting TD. This is the case for the largest TD in the binary system described by González-Ruilova et al. (2020) and shown in fig. 10.

Despite being useful to account for some TDs, the binary hypothesis does not address the observational discrepancy introduced in sec. 1.2.3.

1.3.3 *Grain growth*

Leaving the viscous picture for one moment, one could think of grain growth as a potential mechanism to carve wide cavities in TDs. The efficiency of this model relies on two arguments. First, massive dust particles are known to decouple from the gas and spiral inwards (Weidenschilling, 1977). The loss of dust in the disc would reduce the dust opacities. Second, the dust opacities are also reduced by the grain growth itself since the emission of larger particles is less efficient.

This idea is of course related to the dust component of PPDs and cannot address the cavities observed in the gas profiles. Moreover, the edges of TDs are quite sharp so that the environment for dust growth should change abruptly.
Birnstiel et al. (2012) studied the hypothesis of forming cavities of TDs with grain growth (with grain growth alone and combined with a dead zone). The authors completely ruled out this model. The sharpness of the transition was not recovered, a dust-to-mass ratio lower than 10^{-4} is needed to keep enough small dust at $R \gtrsim 10$ AU and most of the mass in their 'cavity' is indeed detectable by millimetre observations.
To hammer the result home, the survey of Tazzari et al. (2021) of discs including some TDs suggests that large grains are indeed still present in the inner regions of TDs.
Despite being an interesting solution regarding the dust content of TDs cavities, dust growth is unlikely to solve the mystery of strongly-accreting TDs.

1.3.4 *Conclusion regarding the viscous picture*

All the plausible previously discussed alternatives rely exclusively on viscous accretion. It is then extremely difficult to have a strong accretion arising together with a depleted density profile. These models somehow make interesting contributions to reach an accurate description of TDs, but fail to address in a systematic way the precise issue regarding (in particular) highly-accreting TDs with wide cavities (Ercolano and Pascucci, 2020).
Let me give some orders of magnitude to illustrate this statement. The general definition of the accretion velocity is

$$v_{\text{acc.}} = \frac{\dot{M}}{2\pi R \Sigma} \,. \tag{9}$$

In the viscous model, the radial velocity of the flow is

$$v_R = -\frac{3}{\Sigma \sqrt{R}} \frac{\partial}{\partial R} \left(\Sigma \nu_t \sqrt{R} \right) , \tag{10}$$

where ν_t is defined in eq. 2. Assuming that the radial dependencies of Σ and c_s follow power laws and that the α parameter is constant, one gets

The continuity equation is needed to get to this result.

$$v_R = -\frac{3}{2} \frac{\nu_t}{R} , \tag{11}$$

which turns into

$$v_R = -\frac{3}{2} c_s \alpha \frac{h}{R} \,. \tag{12}$$

Protoplanetary discs are geometrically thin discs with $h/R \sim 0.1$ while α can reach at most 10^{-2}. With these orders of magnitude, $v_R \sim$

10^{-3} c_s. Referring to the survey of van der Marel et al. (2016b), Wang and Goodman (2017) point out that the inferred values of Σ and $\dot{M}$ for the observed TDs imply an almost-sonic accretion speed which translates into values of α greater than 8. These observations are deeply challenging the viscous model of PPDs in this peculiar context.

Interestingly, models of PPDs harbouring magnetically launched outflows (or MHD winds) seems promising. Large scale magnetic fields are known to spontaneously generate outflows Wardle and Koenigl (1993) and Ferreira and Pelletier (1995). Such magnetic winds can efficiently remove angular momentum from the disc.
Therefore, magnetised disc winds (MDW) seem capable of sustaining cavities of TDs as well as a strong accretion. This idea is based on the pioneer works of Combet and Ferreira (2008), Combet et al. (2010), and Wang and Goodman (2017) and is the very root of the work I did during my thesis.
The underlying switch of paradigm is to consider that fast accretion is possible with a strong surface stress rather the usual viscous stress.

1.4 MHD WIND LAUNCHING AS AN ALTERNATIVE

A way to maintain a cavity with a strong accretion rate is to rely on the surface stress rather than the radial stress. This can be achieved with magnetic (or MHD) winds, removing angular momentum from the gas in the disc cavity with magnetic braking. The first subsections are devoted to depict the main theoretical tools behind magnetic wind launching and the last one describes the model of magnetic winds in transition discs.

1.4.1 *Theory of* MHD *winds*

This work relies on the so call Blandford & Payne mechanism regarding magnetic wind launching that is found in Blandford and Payne (1982). I will refer to such winds as magnetic or MHD winds. Nevertheless, I note that other magnetic wind launching mechanisms do exist. As an example, a gradient of toroidal magnetic field pressure could launch a magnetic wind (Lynden-Bell, 2003).

1.4.1.1 *The magneto-centrifugal mechanism*

THE 'BEAD ON A WIRE' ANALOGY: A simple way to picture the Blandford & Payne mechanism is to consider a well ionised disc, threaded by a large-scale poloidal magnetic field and described by ideal-MHD. Matter is then tied to the magnetic field lines and accelerated because of the rotation of the disc. Angular momentum is removed by the wind as matter is expelled.

This framework is based on a force free approach just above the disc, where the magnetic field lines are in solid rotation with the disc. The matter follows the magnetic field lines (this is the 'bead-on-a-wire' analogy) and gets accelerated by the centrifugal force if the field lines are sufficiently bent. This is why this mechanism is referred to a centrifugal mechanism in Blandford and Payne (1982).

To derive the needed inclination angle of the field line, I assume that the magnetic field lines rotate rigidly at the Keplerian velocity of their basis. For a given footpoint (where a magnetic field line is anchored in the disc at radius r_0) rotating with an angular speed $\Omega_0 = \sqrt{G\,M_\star/r_0^3}$, one can write the effective potential $\Phi_{\text{eff.}}$ applied on a test particle located on the field line at a distance s of the footpoint, in the co-rotating frame. It reads

$$\Phi_{\text{eff.}} = \underbrace{-\frac{G\,M_\star}{\left(s^2 + 2\,s\,r_0\,\sin\theta + r_0^2\right)^{1/2}}}_{\text{gravity}} \underbrace{-\frac{1}{2}\,\Omega_0^2\,\left(r_0 + s\,\sin\theta\right)^2}_{\text{centrifugal term}}, \tag{13}$$

This way of proceeding hides the role of the magnetic field which is indeed fully at play when I assume that the matter follows the magnetic field lines.

with θ being the inclination angle of the field line. The critical inclination angle $\theta_{\text{crit.}}$ so that matter gets accelerated demands

$$\left(\frac{\partial^2 \Phi_{\text{eff.}}}{\partial s^2}\right)_{s=0} = 0\,, \tag{14}$$

which leads to

$$1 - 4\,\sin^2\theta_{\text{crit.}} = 0\,, \tag{15}$$

and

$$\theta_{\text{crit.}} = \frac{\pi}{6}\,. \tag{16}$$

MAGNETICALLY-DRIVEN WINDS: The previous way of understanding the wind is straightforward and gives an easy-to-read picture. However, it does not catch all the wind physics. In particular, the role and appearance of the toroidal component of the magnetic field is lost, whereas it plays indeed a key role.
Because of the toroidal component, the magnetic field lines can not behave as rigid poloidal wires as they do in the 'bead on a wire' analogy. This is why I want to detail the physics of the wind. I will support my explanations with fig. 11 in which (R, φ, z) is the cylindrical coordinates system.

At first, let me apply a purely vertical magnetic field B_z to a rotating disc (see the first panel of fig. 11). Because the magnetic field lines are anchored in the rotating disc, a toroidal magnetic field appears. This fact can be understood with the second panel of fig. 11. Because of rotation, an electric field $\mathbf{E}_{\text{ind}} = u_\varphi\,\boldsymbol{e_\varphi} \times B_z\,\boldsymbol{e_z}$ (hence an

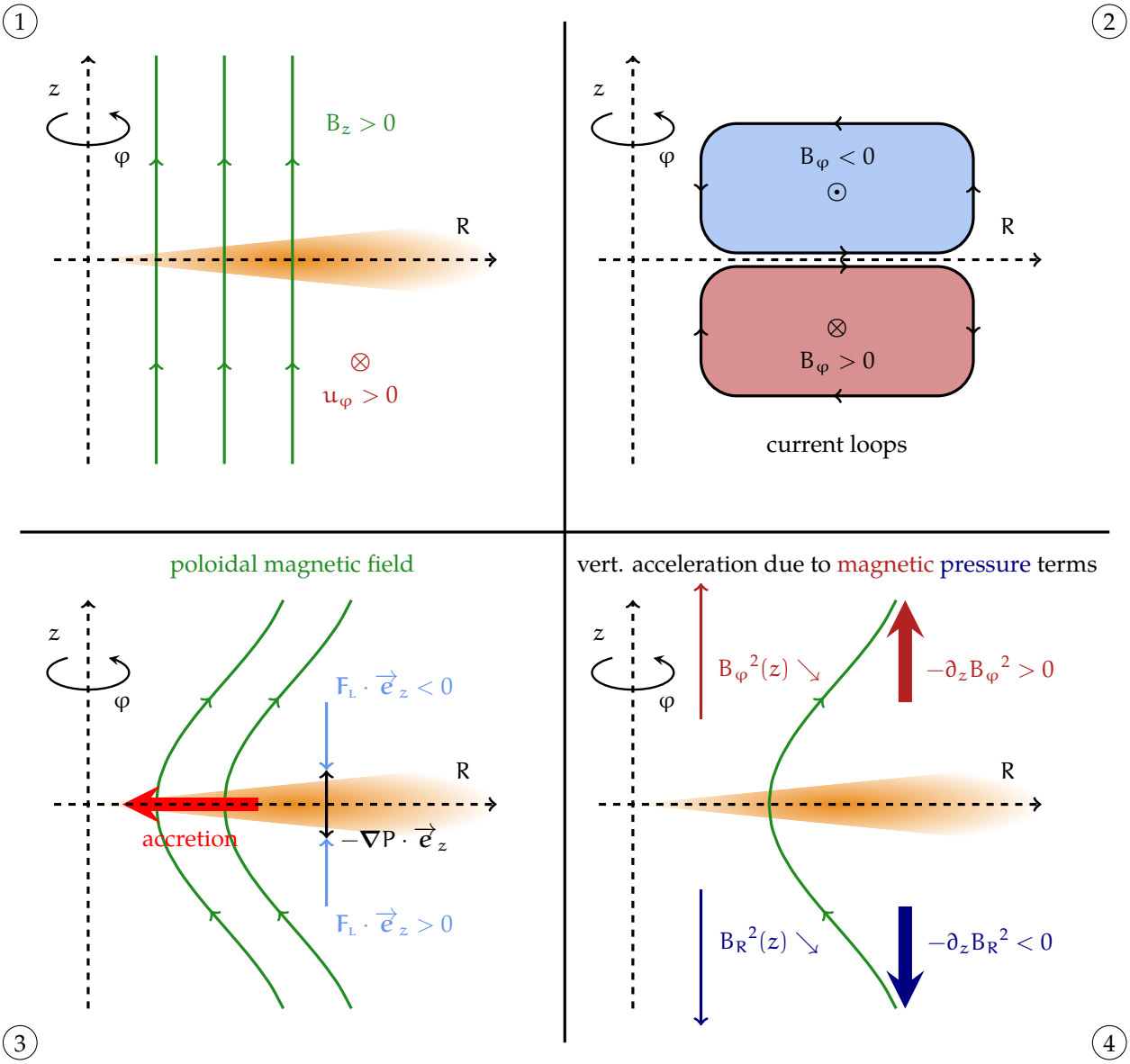

Figure 11: Scheme depicting the Blandford & Payne mechanism. The first panel describes a PPD seen edge-on (in orange) threaded by a vertical magnetic field (full green lines). The second panel shows the current loops that appear in the disc. The third panel highlights the accretion occurring in the disc as well as the role of the thermal pressure. The last panel illustrates the forces that account for the vertical acceleration of matter in the wind. See the paragraph 1.4.1.1 for detailed explanations.

electric current $\mathbf{J}$) appears. In the disc, the current is radial and directed outwards, so that the associated Lorentz force $\mathbf{J} \times B_z \, \boldsymbol{e_z}$ slows down the disc, in agreement with Lenz's law. The current must eventually close since $\boldsymbol{\nabla} \cdot \mathbf{J} = 0$, so that a current loop appears above (anti clockwise in fig. 11) and below (clockwise) the disc. The loops create a toroidal magnetic field B_φ, whose polarity depends on the location with respect to the disc midplane. Equivalently, taking the toroidal component of the Maxwell-Farady's law, with the electric field $\mathbf{E}_{\rm ind}$ leads to

$$\partial_t B_\varphi = R \, B_R \, \partial_R \, \Omega \, , \tag{17}$$

with Ω the rotation speed in the disc and where I applied $\boldsymbol{\nabla} \cdot \mathbf{B} = 0$. The shear energy is converted into magnetic energy (that is stored in B_φ).

Magnetic stresses $\propto B_\varphi$ act on the disc which are a consequence of the Lorentz force associated to $\mathbf{J}$, this is the magnetic braking of the disc. Because of the magnetic diffusivity in the disc (i. e. the non-ideal MHD framework), the matter can cross the magnetic field lines, hence generating accretion (see the red arrow in the third panel of fig. 11) and pinching the magnetic field lines at the midplane.

Matter must rise up in the disc to ensure the wind replenishment. The Lorentz force associated to B_φ (see fig. 11, panel 3) is directed toward the disc, while the gravity is of course directed toward the central star. Therefore, the only force directed upwards is the thermal pressure gradient, which enables the wind basis replenishment of matter.

The angular momentum previously stored in B_φ is transferred to the gas in the wind which is azimuthally accelerated. This is the result of the Lorentz force $\mathbf{J} \times B_z \, \boldsymbol{e_z}$ evaluated where the current loop closes (where $\mathbf{J} \cdot \boldsymbol{e_R} < 0$). As a consequence, the further up in the wind the matter, the lower the toroidal magnetic field is.

Looking at the last panel of fig. 11, one can see that the magnetic pressure term $-\partial_z {B_\varphi}^2/2$ pushes the matter away from the disc. As a result, the vertical acceleration in the wind is of magnetic origin. Because of the collimation of the poloidal field lines (due to the hoop stress), the radial component of the magnetic field also diminishes further up in the wind, with a similar consequence regarding the vertical motion of matter.

Consequently, exhibiting the precise role of the magnetic field reveals that the wind is magnetically accelerated. This why such winds are often referred to as magnetically driven winds (see for example Contopoulos and Lovelace, 1994; Ferreira, 1997). I will also use this vocabulary to refer to the wind.

1.4.1.2 *The stationary, ideal* MHD *picture and wind invariants*

The next chapter describes in depth the theoretical tools needed for this work regarding MHD. In this subsection, I will just give the wind

invariants that I will use later on when analysing my numerical simulations. In particular, I point out that they are derived assuming a stationary and ideal MHD framework. Moreover, I assume axisymmetry, anticipating on the analysis of my numerical simulations. Complete and fully detailed references derive full calculations regarding MHD winds and I refer the reader to the following reviews Spruit (1996) and Ferreira (2003) for more information.

It is however meaningful to give a few words on the becoming of Maxwell-Ampère equation under the previous assumptions (steady state, axisymmetry, ideal MHD). Indeed, one now has

$$\boldsymbol{\nabla} \times (\boldsymbol{v} \times \mathbf{B}) = \mathbf{0}\,, \tag{18}$$

so that introducing a poloidal VC toroidal projection of the fields (with a unit vector $\hat{\boldsymbol{e}}_\varphi$ alongside the rotation of the disc and a subscript X_p to indicate that X is considered in the poloidal plane), one gets

$$\boldsymbol{v}_p \times \mathbf{B}_p + v_\varphi\, \hat{\boldsymbol{e}}_\varphi \times \mathbf{B}_p + B_\varphi\, \boldsymbol{v}_p \times \hat{\boldsymbol{e}}_\varphi = \boldsymbol{\nabla} f\,, \tag{19}$$

where f is a given potential function that I assume to be axisymmetric. This last assumption (also done by Spruit, 1996) is valid for global models but is more subtle for shearing box ones. In global models, one can apply a regularity condition for the electromotive force at $R = 0$ but it is of course impossible to do with shearing box models because of the radial periodicity (see for example Lesur et al., 2013 for a case where this question is of prime interest and Lesur, 2021a for a deepest insight on this question). Taking the toroidal component of the previous equation and assuming axisymmetry, I have that

$$\boldsymbol{v}_p \times \mathbf{B}_p = \mathbf{0}\,, \tag{20}$$

where one is left with the fact that the poloidal velocitiy and magnetic field are collinear. This result drove most of my previous analysis, however, it is important to dwell on the fact that the result demands ideal MHD. This does not obviously stand with non-ideal term, so that it is rather expected to have poloidal velocity and magnetic field lines parallel above the disc surface, in the outflow, where ideal MHD is better verified than in the cold and diffusive disc.

In the following, I consider a selected poloidal magnetic field line anchored in the disc midplane at $R \equiv R_w$. The corresponding Keplerian angular velocity is Ω_w while B_w is the poloidal magnetic field. I then consider the following invariants, namely:

- The mass loading parameter which accounts for the quantity of matter that escapes the disc with the wind

$$\kappa \equiv 4\pi \frac{\rho\, v_p\, \Omega_w\, R_w}{B_p\, B_w}\,. \tag{21}$$

- The rotation parameter

$$\omega \equiv \frac{\Omega}{\Omega_w} - \frac{\kappa\, B_w\, B_p}{4\pi\, \rho\, R\, R_w\, {\Omega_w}^2}\,. \tag{22}$$

- The magnetic lever arm that accounts for the angular momentum that is removed from the disc by the wind

$$\lambda \equiv \frac{\Omega\, R^2}{\Omega_w\, {R_w}^2} - \frac{R\, B_\varphi}{R_w\, B_w\, \kappa}\,. \tag{23}$$

- The Bernoulli invariant which is energy of the wind, split into kinetic, gravitational, magnetic and thermal contributions such as

$$\mathcal{B} \equiv \underbrace{\frac{v^2}{2\,{\Omega_w}^2\,{R_w}^2}}_{\text{Kinetic}} + \underbrace{\frac{-R_w}{\sqrt{R^2+z^2}}}_{\text{Gravitational}} + \underbrace{\frac{-\omega\, R\, B_\varphi}{\kappa\, R_w\, B_w}}_{\text{Magnetic}} + \underbrace{\frac{w}{{\Omega_w}^2\,{R_w}^2}}_{\text{Thermal}}\,, \tag{24}$$

  where the thermal contribution at the curvilinear coordinate s of the field line is given by

$$w(s) \equiv \int_s^{+\infty} -\frac{\boldsymbol{\nabla} P}{\rho} \cdot \mathrm{d}\boldsymbol{\ell}\,. \tag{25}$$

I will come back to these invariants when applying the wind theory to my simulations. For now I just want to specify that these invariants are of course closely linked to the usual conservation equations of physics (mass, angular momentum, energy).

1.4.2 *Surface stress and accretion*

The essence of my work finds its roots in the work of Combet and Ferreira (2008). The authors of this article develop the JED/SAD model that connects a 'jet emitting disc' to a 'standard accretion disc' (the JED being the cavity of my TDS and the SAD the exterior of the cavity). Such an idea was recently implemented in the work of Wang and Goodman (2017), that studies the impact of a magnetic wind on the ionisation fraction of the cavity of a TD. A full section of the chapter to come is devoted to comparing these works to mine.

For now, I want to dwell on the fact that magnetic winds can disperse protoplanetary discs. This is suggested by past reviews I already cited such as Owen (2016) and Ercolano and Pascucci (2020). Similar results are shown by Suzuki et al. (2010) and Tabone et al. (2022b) who used the MRI to launch the wind, which is demonstrated to be capable of in Lesur et al. (2013). Thermal and magnetic winds could very well unite their strength to disperse discs as suggested by Kunitomo et al. (2020).

CONCLUSION

This chapter synthesizes a few observational results regarding protoplanetary discs and especially magnetic winds as well as transition discs. Magnetic outflows are now tracked by observers and pave the way to future breakthrough regarding the magnetic structures of discs and outflows.

The use of a new generation of instruments (ground based or in space), and especially ALMA renders quantitative observations of discs on which statistical tools can be applied. It now seems that the evolutionary of protoplanetary discs is deeply challenged regarding the transition disc step.

Despite previous alternatives having undeniable strengths, there is still much the need for a new tentative to address the question of highly-accreting TDs. In this broad picture, MHD winds is an appealing model of cavity hosting discs sustained by magnetic winds. This choice of paradigm also implies to lower the influence of the viscous disc model since most of the angular momentum transport relies on the surface stress. In particular, no viscosity or turbulence is considered in my work.
In the next chapter, the reader will find a detailed theoretical description of the physics at play.

CONCLUSION

Ce premier chapitre s'ouvre sur une synthèse de quelques résultats observationnels couvrant la formation stellaire et planétaire, du nuage moléculaire aux planètes. Naturellement, je m'attarde particulièrement sur les observations de disques protoplanétaires (avec ALMA notamment) et je décris les disques protoplanétaires de transition (disques de transition).
Pour ma thèse, je définis ces disques comme étant des disques protoplanétaires arborant une cavité interne dans leur profil radial de densité.

Je reprends également quelques points clés de l'évolution des disques protoplanétaires, objets voués à disparaître en quelques millions d'années. Je donne des éléments concernant le modèle standard des disques protoplanétaires, à savoir le modèle du disque visqueux. Dans ce modèle, le transfert de moment cinétique s'effectue radialement, vers l'extérieur, du fait d'un stress radial ayant pour origine la turbulence du disque. Je souligne que les estimations de turbulence dans les disques protoplanétaires fragilisent ce modèle.

Le modèle du disque visqueux permet de comprendre l'origine du terme "transition" dans l'appellation des disques de transition. En effet, ces derniers s'inscrivent dans le processus standard d'évolution des disques protoplanétaires en tant qu'étape précédent la dispersion totale du gaz initialement présent dans le disque.
Ce scénario d'évolution se base sur l'action conjointe de vents photoévaporés et du transport visqueux. Si la présence de vents photoévaporés est compatible avec les observations, il n'en reste pas moins que les observations de disques de transition avec une cavité très étendue (plus grande que 10 unités astronomiques) et/ou accrétant à des taux similaires à ceux des disques protoplanétaires pleins (soit sans cavité) ne semble pas s'intégrer dans ce modèle d'évolution.
Le problème soulevé par de telles observations est le point de départ de mon travail. En particulier, il semble que le modèle visqueux soit en difficulté pour justifier de telles observations, à cause de la densité de surface très faible au sein des cavités de disques de transition.

Pour tenter de résoudre ce problème, je passe en revue plusieurs mécanismes ayant fait l'objet d'études. J'évoque notamment l'effet de vents photoévaporés associés à une "dead zone" à l'intérieur de la cavité (jouant le rôle d'un réservoir de matière et permettant d'alimenter l'accrétion), l'influence de corps massifs dans la cavité (planètes ou étoiles) et les effets dus à la croissance des grains de poussière.

Tous ces modèles proposent autant de pistes pertinentes pour rendre compte des observations. Cependant, et malgré leurs succès respectifs, il semble que les réponses qu'ils apportent ne soient pas entièrement satisfaisantes. En particulier, la plupart d'entre eux conserve l'hypothèse du disque visqueux.
Mon travail se base sur l'hypothèse d'un vent magnétique (lancé par le mécanisme de Blandford & Payne) permettant de soutenir la cavité (d'une taille donnée) tout en maintenant un fort taux d'accrétion, grâce à une vitesse d'accrétion très élevée. Ce changement de paradigme permet de baser la dynamique de l'accrétion sur un stress de surface (et non radial comme avec le modèle du disque visqueux).

Ce chapitre s'achève avec une description du mécanisme de Blandford & Payne. Le lecteur trouvera les descriptions théoriques nécessaires dans le chapitre suivant.

2

TOWARDS THE MODELISATION OF A TRANSITION DISC

"Les jours heureux sont moins marquants
que les traumatismes, jusqu'à ce qu'ils basculent dans le passé.
"Famille je vous regretterai un petit peu"
formula Gloria songeusement.
Deux cents mètres plus loin, elle n'y pensait plus du tout."

— Virginie Despentes, *Bye Bye Blondie* (2004)

INTRODUCTION

In this chapter, I wish to give a clear description of the physics and numerical tools I need to properly describe transition discs.
I start with a general yet observation-based description of protoplanetary and transition discs. I introduce the relevant quantities needed such as the surface density and give some usual orders of magnitude. This leads me to say a word on the use of fluid mechanics in the context of protoplanetary discs.
I then introduce the ideal MHD equations for a plasma in the second section. However, the 'ideal' aspect of this set of equations is insufficient to capture the physics at stake in transition discs and calls for additional terms embedded in the non-ideal theory of MHD. Among the non-ideal processes, the ambipolar diffusion plays a major role in the physics of PPDs. The effects of ambipolar diffusion are caught by the ambipolar Elsasser number.
I establish and detail the whole set a equations needed in the framework of non-ideal MHD. I estimate the contribution of the main non-ideal process in the discs physics.
In the third section, I focus on the ionisation processes in PPDs and TDs. I develop a simple modelisation of a disc to estimate the characteristic value of the ambipolar Elsasser number in TDs.
The last section is devoted to the numerical aspect of my work. I detail the initialisation process of my simulation and describe the facilities that I used. Eventually, I give a short description of the numerical code I used to solve the non ideal MHD set of equations: the PLUTO code.

INTRODUCTION

Dans ce second chapitre, je propose une description de la physique en jeu dans l'étude des disques protoplanétaires ainsi que des outils numériques que j'ai utilisés.
Je commence par décrire quantitativement la physique des disques protoplanétaires en me basant sur des observations. Je décris les principales quantités utiles telles que la densité de surface et je donne les ordres de grandeurs associés. Cette première étape m'amène à considérer un certain nombre de quantités caractéristiques des plasmas et de la mécanique des fluides, que j'utilise pour modéliser les disques protoplanétaires. Plus précisément, je détaille les hypothèses permettant de travailler dans le cadre de la magnétohydrodynamique idéale dans un premier temps.

Je poursuis en détaillant les calculs nécessaires à l'usage de la magnétohydrodynamique non idéale, en introduisant les principaux effets non idéaux (effet Ohm, Hall et diffusion ambipolaire). La diffusion ambipolaire est particulièrement pertinente à considérer dans le contexte des disques protoplanétaires.
Il s'agit par ailleurs du seul effet non idéal que j'ai considéré dans mon travail. Ses effets sont quantifiés par le nombre d'Elsasser ambipolaire.

Dans la troisième section de ce chapitre, je me focalise sur la fraction d'ionisation dans les disques protoplanétaires ainsi que sur les processus d'ionisation (rayons X, UV, rayons cosmiques et radioactivité naturelle dans le disque). À l'aide de profils d'ionisation pour chacun de ces processus, je modélise un disque de transition, en vue de calculer le nombre d'Elsasser ambipolaire.
Ces premiers résultats me permettront de mettre au point le modèle numérique de disques de transition que j'ai utilisé dans mes simulations numériques.

La dernière section se penche sur les aspects numériques de mon travail. J'y présente le code que j'ai utilisé (le code PLUTO) de même que les infrastructures de calculs qui étaient à ma disposition pendant ma thèse.
Je présente le modèle numérique que j'ai utilisé (pour mes simulations 2,5 D et 3 D), l'initialisation et la procédure de redémarrage pour les simulations 3 D.

2.1 PHYSICAL FRAME FOR PROTOPLANETARY DISCS

2.1.1 *General properties of a protoplanetary disc*

The aim of the subsections to come is to provide orders of magnitude as well as generic dependencies of the main meaningful quantities in the physics of protoplanetary discs (density, temperature, rotation speed). Such profiles have an observational ground which implies a few hypotheses that will be discussed further out. In this prospect, I adopt a generic model of protoplanetary disc (called "standard protoplanetary discs"), whose profiles will be defined hereafter and labelled with PPD.

2.1.1.1 *Main radial profiles derived from observations*

Protoplanetary discs are commonly modelled by a cold, dense, magnetised plasma made of gas and dust grains. I will later on address each one of these properties and justify the use of plasma physics for such objects. In this subsection, I aim to give generic radial profiles for a protoplanetary disc based on observations. Referring to Andrews et al. (2009), one gets the following profile for the surface density $\Sigma_{\rm PPD}$ and the temperature $T_{\rm PPD}$

$$\Sigma_{\rm PPD} = 300\, R_{\rm AU}^{-1}\ {\rm g\,cm^{-2}}\,, \tag{26a}$$

$$T_{\rm PPD} = 280\, R_{\rm AU}^{-1/2}\ {\rm K}\,, \tag{26b}$$

where $R_{\rm AU}$ is equal to the radius R in units of 1 AU. These profiles are deduced from observations of the thermal continuum emission (at 870 µm) of 9 protoplanetary discs. The chosen samples is composed of massive discs (the masses range from 0.005 to 0.14 $M_\odot$) but is still comparable to the minimum mass solar nebula model (Hayashi, 1981). It should be noted that the model used for the surface density is $\Sigma(R) = \Sigma_c\ (R/R_c)^{-\gamma}\ \exp\left[-(R/R_c)^{2-\gamma}\right]$, with R_c a characteristic radius, $\gamma = 1$ and Σ_c is proportional to the total mass of the disc. Therefore, using a power law for Σ (see eq. 26a) increases the surface density in the outer disc. Assuming a Keplerian rotation for the disc around a star of mass $M_\star = 1\,M_\odot$, I get

$$\Omega_{K,\,\rm PPD}(R) = \sqrt{\frac{G\,M_\odot}{R^3}} = 1.99\times10^{-7}\,R_{\rm AU}^{-3/2}\,{\rm s^{-1}}. \tag{27}$$

2.1.1.2 *Vertical structure*

$\Sigma_{\rm PPD}$ expresses the radial dependence of matter inside a disc. However, PPDs are 3D objects with a vertical dependency on the height z. Protoplanetary discs appear to be flared discs (e. g.: HH30, Guilloteau et al., 2008 or HK tau c, Stapelfeldt et al., 1998). It is then meaningful

to introduce the flaring index ψ_f to build the profile of the pressure scale height $\tilde{h}$ (Andrews et al., 2009) defined as

$$\tilde{h} = \tilde{h}_c \left(\frac{R}{R_c}\right)^{\psi_f}, \tag{28}$$

with $\tilde{h}_c$ a corresponding normalisation at the characteristic radius Rc. The physical scale height h is given by

$$h \approx R\,\tilde{h} = h_c \left(\frac{R}{R_c}\right)^{1+\psi_f}, \tag{29}$$

where $h_c = \tilde{h}_c\, R_c$. Flaring controls how the stellar radiation hits the disc surface and heats its content.
The dust settling can modify the flaring of discs (Dullemond and Dominik, 2004), whose flatness can be drastically reduced (Wolff et al., 2021). Observations suggest that $\psi_f = 0.04 - 0.26$ (Andrews et al., 2009) for the dust.

2.1.1.3 *Hydrostatic equilibrium in the disc*

The hydrostatic equilibrium applied to the disc content (Dullemond and Dominik, 2004) enables to get the vertical profile of the density. I suppose that the disc is filled with an ideal gas of density ρ and pressure P. Any fluid particle is subject to the gravity potential of the host star $\phi_\star = -G\,M_\star/\sqrt{R^2+z^2}$, the pressure gradient and the centrifugal force along the radial direction (parallel to the disc midplane). In the frame of reference tied to a given fluid particle in Keplerian motion at a given radius R and using the cylindrical coordinates system (R, z), I get

A justification of this fluid modelisation lies within sec. 2.1.3.1.

$$-\boldsymbol{\nabla}\phi_\star - \frac{1}{\rho}\,\boldsymbol{\nabla}P + \Omega_K\, R\, \boldsymbol{e}_R = \boldsymbol{0}, \tag{30}$$

which gives once projected along $\boldsymbol{e}_z$

$$\frac{1}{\rho}\,\partial_z P = -\partial_z \phi_\star. \tag{31}$$

I now assume the disc is locally isothermal, so that I can use the isothermal sound speed c_s that does not depend on z and such that

An isothermal process is equivalent to a polytropic process of index $n = 1$ that leads to $c_s = \sqrt{n\,P/\rho}$, which does not depend on the ratio of specific heats γ.

$$c_s = \sqrt{\frac{P}{\rho}}. \tag{32}$$

I end up with the well known profile for ρ

$$\rho(R, z) = \rho_{\text{mid}}(R)\, \exp\left[-\frac{1}{2}\left(\frac{z}{h}\right)^2\right], \tag{33}$$

where h is chosen so that $c_s = h\,\Omega_K$. Since the disc is filled with an ideal gas, I have

$$c_s = \sqrt{\frac{k_B\, T}{\mu}}, \tag{34}$$

with $\mu \approx 2.34\,m_H$ the mean molecular weight and m_H the atomic mass. Given eq. 26b and 34 combined with eq. 27 and 29 , I get

$$c_s = 9.94 \times 10^4\, R_{AU}^{-1/4}\ \mathrm{cm\,s^{-1}}\,, \tag{35a}$$

$$h = 5.00 \times 10^{11}\, R_{AU}^{5/4}\ \mathrm{cm}\,, \tag{35b}$$

$$h/R = 0.0333\, R_{AU}^{1/4}\,. \tag{35c}$$

This gives a typical flaring angle $\psi_f = 1/4$. I define the surface density for this section as

Axisymmetry is assumed here. One could integrate over φ and divide the result by 2π to account for non-axisymmetries as it will be done for 3D simulations.

$$\Sigma_{PPD}(R) \equiv \int_{-\infty}^{+\infty} \rho(R,z)\,dz\,, \tag{36}$$

so that I find with eq. 33

$$\Sigma_{PPD}(R) = \sqrt{2\pi}\,h\,\rho_{mid}(R)\,, \tag{37}$$

and finally get, using eq. 26a and 35b

$$\rho_{mid}(R) = 2.39 \times 10^{-10}\, R_{AU}^{-9/4}\ \mathrm{g\,cm^{-3}}\,. \tag{38}$$

I eventually end up with the number density profile defined as $n_{mid}(R) = \rho_{mid}(R)/\mu$ and the pressure one with eq. 35a which read

$$n_{mid}(R) = 6.13 \times 10^{13}\, R_{AU}^{-9/4}\ \mathrm{cm^{-3}}\,, \tag{39a}$$

$$P_{mid}(R) = 2.36\, R_{AU}^{-11/4}\ \mathrm{dyn\,cm^{-2}}\,. \tag{39b}$$

The total mass of a PPD is obtained through its H_2 content or with estimations of its content in CO. Some methods can involve other species such as N_2H^+ (e. g. Trapman et al., 2022b). I now have all the basics profiles needed to dive in more detailed aspect of discs physics.

2.1.2 *Plasma parameter and magnetic fields in protoplanetary discs*

Up until now, I focused on a hydrodynamical perspective, regardless of the external forces acting on the gaseous disc and especially did not mention the role of electromagnetism. It is obvious that the gravitational potential $\phi_\star$ of the young star is central to the study of the gas dynamics. This is the dominant process which enforces the Keplerian rotation that shears the disc and on which the pressure gradient term acts as a perturbation.
Another perturbative effect emerges from the interplay between the magnetic field and the gas that are tied to each other through the Lorentz force directly acting on charged particles. It is therefore valuable to estimate the effects of the magnetic field with respect to the ones of the pressure. The so called beta plasma parameter fulfils this need by comparing the total thermal pressure P to the magnetic pressure $P_B \equiv B^2/2\,\mu_0 = B^2/8\pi$, where $B^2 \equiv \mathbf{B}^2$ and I recall that $\mu_0 = 4\pi$ in CGS units. Its definition is as follows

$$\beta \equiv \frac{P}{P_B} = \frac{8\pi P}{B^2}\,. \tag{40}$$

This definition is generic for plasma physics and commonly used. However, for the specific case of protoplanetary discs, I will consider that β is estimated at the disc midplane as a reference. Using eq. 39b, I get the following dependency of the magnetic field on β:

$$B_{\text{mid}}(R) = 7.70\, R_{\text{AU}}^{-11/8}\, \beta^{-1/2}\, \text{G}\,. \tag{41}$$

Based on the study of meteorites (Levy, 1978; Fu et al., 2014; Fu et al., 2021; Borlina et al., 2022) for which $B_{\text{mid}}(1\ \text{AU}) \sim 0.1 - 1$ G is deduced, one gets a typical value of $\beta \sim 10^{3-4}$ for protoplanetary discs. Considering the effect of the magnetic field paves the way to the use of magnetohydrodynamics (introduced in sec. 2.2).

2.1.3 *Physical modelisation of a protoplanetary disc*

2.1.3.1 *Fluid mechanics*

Based on the general properties of protoplanetary discs, I can now draw a more detailed picture of these objects. To model a protoplanetary disc, I suppose that the disc is made of classical (the typical length d between particles is way smaller than any of the Planck lengths involved) and non-relativistic (the typical speed v of any particle in the disc is by far smaller than c) particles representing the molecules. I can first assume that the properties of any kind of particles labelled by j that fill the disc are contained in a distribution function for one particle $f_j(\mathbf{r}, \boldsymbol{v}, t)$ that depends on 7 variables. This function is so that $f_j(\mathbf{r}, \boldsymbol{v}, t)\, d\mathbf{r}\, d\boldsymbol{v}$ gives the most probable number of particles that are to be found is the volume element $d\mathbf{r}\, d\boldsymbol{v}$ centred on the point $(\mathbf{r}, \boldsymbol{v})$. The moments of various orders of f_j recover macroscopic quantities, for example the zeroth order of f_j is the number density n_j

$$n_j(\mathbf{r}, t) = \int_{\mathbb{R}^3} f_j(\mathbf{r}, \boldsymbol{v}, t)\ d\boldsymbol{v}\,, \tag{42}$$

while the first order renders an average velocity $\mathbf{u}_j$

$$\mathbf{u}_j(\mathbf{r}, t) = \frac{1}{n_j(\mathbf{r}, t)} \int_{\mathbb{R}^3} \boldsymbol{v}\, f_j(\mathbf{r}, \boldsymbol{v}, t)\ d\boldsymbol{v}\,. \tag{43}$$

This averaging procedure can be generalised to any given quantity $Q(\mathbf{r}, \boldsymbol{v}, t)$ so that

$$\langle Q \rangle_j(\mathbf{r}, t) \equiv \frac{1}{n_j(\mathbf{r}, t)} \int_{\mathbb{R}^3} Q(\mathbf{r}, \boldsymbol{v}, t)\ f_j(\mathbf{r}, \boldsymbol{v}, t)\ d\boldsymbol{v}\,. \tag{44}$$

The distribution function eventually follows the Boltzmann equation which rules its temporal evolution

$$\partial_t f_j + \boldsymbol{v} \cdot \partial_{\mathbf{r}} f_j + \frac{\mathbf{F}}{m_j} \cdot \partial_{\boldsymbol{v}} f_j = \mathcal{C}\left[f_j\right]\,, \tag{45}$$

where $\mathbf{F}$ represents the external forces that act on each particle of mass m_j and $\mathcal{C}$ is the collisional operator. Given a characteristic relaxation time τ, I approximate the collisional operator with $\mathcal{C}\left[f_j\right] = -\left(f_j - f_{j,0}\right)/\tau$ (Quataert and Chiang, 2000; Narayan et al., 1994; Cook and Franklin, 1966), with $f_{j,0}$ an equilibrium distribution for particles j (such as the Maxwell-Boltzmann distribution). This peculiar expression of $\mathcal{C}$ is aims to highlight the role of τ which is the mean free time so that $-f_j/\tau$ is the rate of particles that are removed from a given phase space location due to scattering. Assuming stationarity, I write

$$\boldsymbol{v}^* \cdot \partial_{\boldsymbol{r}^*} f_j + \mathbf{F}^* \cdot \partial_{\boldsymbol{v}^*} f_j = -\frac{1}{K_n}\left(f_j - f_0\right), \tag{46}$$

where x^* refers to the dimensionless quantity of x. K_n is the Knudsen number and is defined as the ratio of the mean free path ℓ to the chosen characteristic length scale L. One of its property is to embody the role of the collision term for a given physical frame. In particular, $K_n \ll 1$ implies that the particles set is collisional so that one can use the fluid mechanics equations to get a proper description of the system. For particles of cross section σ and number density n, the mean free path reads

I assume a Maxwell-Boltzmann distribution of speed to evaluate ℓ.

$$\ell = \frac{1}{\sqrt{2}\, n\, \sigma}. \tag{47}$$

I take $\sigma \approx \pi r_{h_2}^2$ as an order of magnitude, with $r_{h_2} \approx 3 \times 10^{-8}$ cm the typical size of a dihydrogen molecule that is the predominant component of a protoplanetary disc. I eventually find that

$$\ell = 17\, R_{AU}^{9/4}\ \text{cm}. \tag{48}$$

Taking L equal to the vertical sale height h_{AU} deduced from eq. 35b gives at 1 AU

$$K_n \approx 3.40 \times 10^{-11} \ll 1, \tag{49}$$

so that protoplanetary discs are very well described by fluid mechanics.

2.1.3.2 *Hydrodynamics*

From a mathematical point of view, the procedure used is referred to as the Chapman-Enskog method (Chapman and Cowling, 1970).

The fluid equations arise from the moments of the Boltzmann equation. I define the mass density $\rho_j = m_j\, n_j$, so that taking the first moment (of order 0) of eq. 45 leads to

$$\partial_t \rho_j + \boldsymbol{\nabla} \cdot \left(\rho_j\, \mathbf{u}_j\right) = 0, \tag{50}$$

which is the usual continuity equation or mass conservation equation. The second moment of eq. 45 gives the momentum equation

$$\partial_t \left(\rho_j\, \mathbf{u}_j\right) + \underline{\underline{\boldsymbol{\nabla}}} \cdot \left(\rho_j \left\langle \boldsymbol{v} \otimes \boldsymbol{v} \right\rangle_j\right) = \mathbf{f}_j + \mathbf{R}_j, \tag{51}$$

where $\otimes$ is the outer product and $\mathbf{R}_j$ is a remnant from the collisional operator. $\mathbf{f}_j$ are the external forces per unit volume acting on the particles j. One can now repeat this procedure indefinitely, since any integration of eq. 45 of order n would generate a term of order $n+1$, so that external assumptions are needed to close the system. A first step is to decompose the total velocity $\boldsymbol{v}$ into the average term (see eq. 43) plus a random part $\tilde{\boldsymbol{v}}_j$ so that

$$\boldsymbol{v} = \boldsymbol{u}_j + \tilde{\boldsymbol{v}}_j \,, \tag{52}$$

with $\langle \tilde{\boldsymbol{v}}_j \rangle_j = \boldsymbol{0}$. Introducing the stress tensor $\underline{\underline{\mathbf{P}}}_j$ defined as

$$\underline{\underline{\mathbf{P}}}_j \left(\mathbf{r}, t\right) \equiv \rho_j \left\langle \tilde{\boldsymbol{v}}_j \otimes \tilde{\boldsymbol{v}}_j \right\rangle_j \equiv p_j \, \underline{\underline{\mathbf{I}}} + \underline{\underline{\boldsymbol{\pi}}}_j \,, \tag{53}$$

where p_j is the scalar pressure and $\underline{\underline{\boldsymbol{\pi}}}_j$ is the deviatoric stress tensor made of the off-diagonal components of the stress tensor. The elasticity theory studies in depth this tensor (from which comes the viscosity and the usual way of writing the so-called Navier-Stokes equations). However, I will neglect this term because discs are mostly pressure supported and are rather subject to an effective viscosity (due to turbulence or magnetic forces) than to a classical viscosity (Rafikov, 2017). The final equations for each set of particles j is given by

$$\partial_t \rho_j + \boldsymbol{\nabla} \cdot \left(\rho_j \, \boldsymbol{u}_j\right) = 0 \,, \tag{54a}$$

$$\partial_t \left(\rho_j \, \boldsymbol{u}_j\right) + \underline{\underline{\boldsymbol{\nabla}}} \cdot \left(\rho_j \, \boldsymbol{u}_j \otimes \boldsymbol{u}_j\right) = -\boldsymbol{\nabla} p_j + \mathbf{f}_j + \mathbf{R}_j \,. \tag{54b}$$

This set of equations however remains to be closed, in particular the expression of $\mathbf{R}_j$ is still unknown. I also did not mention the energy conservation equation to keep a straightforward physical description. I address these 3 points in sec. 2.2.

The main point to get from this section is that under a few assumptions, the matter in protoplanetary discs is accurately described by eq. 54a and 54b. Of course, one should keep in mind that this approach stands as long as the plasma is collisional enough so that the velocity distribution function remains close to the Maxwell-Boltzmann one (thermal plasma). There exists various astrophysical environments for which this modelisation is unable to render a proper physical description all alone. As an example, one can think of solar flares which are explosive events whose modelisation should include a variety of multiscale spatio-temporal phenomena. A kinetic approach (commonly used for non-thermal plasma) is then a useful alternative (Gordovskyy et al., 2019).

2.2 MAGNETOHYDRODYNAMICS IN PROTOPLANETARY DISCS

From now on, I will use the generic notion of *plasma* to refer to the matter content of the disc, with the hereafter broad definition.

A plasma is a gas experiencing density and temperature conditions such that it becomes partially or entirely ionised, with the presence of free charge carriers. Electrons together with positively charged ions are the predominant charges carriers in protoplanetary discs. Neutrals particles (of diverse origins such as grains or molecules) may be part of this mixture. Plasma physics is an absolutely huge and fundamental gear of theoretical physics. It is way beyond the scope of this work to try to address all the vastness of this topic and I refer to Rax (2005) and Piel (2010) for comprehensive pictures of this field. The aim of the sections to come is to provide a concise yet precise depiction of the physics needed to describe protoplanetary discs, namely the non-ideal magnetohydrodynamics which arises from plasma physics. The presence of electric charges in the plasma makes it particularly sensitive to the effects of electromagnetic fields, suggesting a modelisation relying both on electromagnetism and fluid mechanics, i. e.magnetohydrodynamics.

2.2.1 MHD *driving equations*

2.2.1.1 *Electromagnetic fields dynamics*

The impact of electromagnetic field on the matter is fully embodied by the Lorentz force $\mathbf{F}_L$. In a given frame of reference, a particle of charge q_j moving at velocity $\mathbf{u}_j$ immersed in an electromagnetic field is submitted to

$$\mathbf{F}_L = q_j \left(\mathbf{E} + \mathbf{u}_j \times \mathbf{B}\right), \tag{55}$$

where $\mathbf{E}$ and $\mathbf{B}$ are respectively the electric and magnetic fields. Before moving any further, one needs to get the equations that govern the dynamics of these fields, which are the well known Maxwell equations

$$\boldsymbol{\nabla} \cdot \mathbf{E} = 4\pi \rho_c, \qquad \text{Maxwell-Gauss} \tag{56a}$$

$$\boldsymbol{\nabla} \times \mathbf{E} = -\frac{1}{c}\frac{\partial \mathbf{B}}{\partial t}, \qquad \text{Maxwell-Faraday} \tag{56b}$$

$$\boldsymbol{\nabla} \cdot \mathbf{B} = 0, \qquad \text{Maxwell-Thomson} \tag{56c}$$

$$\boldsymbol{\nabla} \times \mathbf{B} = \frac{4\pi}{c}\mathbf{J} + \frac{1}{c}\frac{\partial \mathbf{E}}{\partial t} \approx \frac{4\pi}{c}\mathbf{J}, \qquad \text{Maxwell-Ampère} \tag{56d}$$

where I neglected the displacement currents in eq. 56d under the non-relativistic assumption. ρ_c is the total charge density and $\mathbf{J}$ the total current density, that are constructed as follows

$$\rho_c \equiv \sum_\alpha q_\alpha n_\alpha, \tag{57}$$

$$\mathbf{J} \equiv \sum_\alpha q_\alpha n_\alpha \mathbf{u}_\alpha, \tag{58}$$

where I used notations and definitions from sec. 2.1.3.1. The use of $\mathbf{E}$ demands a solution of eq. 56a due to the presence of charged

species all over the plasma. This is done through the Ohm's law, that is detailed in sec. 2.2.1.4 and 2.2.2 respectively for ideal and non-ideal MHD.

A plasma is subject to two opposite tendencies. A collective organisation of its constitutive particles emerges with the Coulomb interaction while the thermal agitation tends to break down this order. The competition between these antagonist processes enables to have a ionised plasma remaining globally neutral. The next paragraphs propose to obtain the spatio-temporal scales that characterizes this interplay.

PLASMA OSCILLATIONS: As just highlighted, the plasma can be considered as neutral. Nevertheless, the charge density may encounter perturbations breaking this assumption. Such perturbations are characterised by a plasma frequency, which is given for the electrons by

$$\omega_{pe} = \sqrt{\frac{4\pi n_0 e^2}{m_e}}\,. \tag{59}$$

This frequency provides a typical time-scale $\tau_{pe} \equiv \omega_{pe}^{-1}$ on which the plasma is able to recover neutrality after a perturbation occurred. The density of electrons n_0 can be replaced by ξn_n, where ξ is the ionisation fraction and $n_n = n_{mid}$ the neutrals density. A thorough study of ξ will be found in sec. 2.3, but for now I just take a standard value of $\xi \sim 10^{-13}$, so that the corresponding profile for τ_{pe} is

$$\tau_{pe}(R) = \sqrt{\frac{m_e}{4\pi e^2}}\,\xi^{-1/2}\, n_{mid}^{-1/2}\,, \tag{60}$$

$$= 7.16\times10^5 \times \left(\frac{\xi}{10^{-13}}\right)^{-1/2} R_{AU}^{9/8}\ s\,. \tag{61}$$

I also add the corresponding frequency for ions, since I will use this order of magnitude later on, I give the profile of $\omega_{p,i}$ for H^+ ions

$$\omega_{pi} = 5.44\times10^2 \left(\frac{\xi}{10^{-13}}\right)^{1/2} R_{AU}^{-9/8}\ s^{-1}\,. \tag{62}$$

DEBYE LENGTH AND SCREENING: A typical lengthscale characterizes the screening of charges accumulations that would locally break the neutrality of the plasma. This so called Debye length λ_D is valid for a hot plasma in which the thermal motion of particles challenges their screening organisation. The definition of λ_D reads

$$\lambda_D = \sqrt{\frac{4\pi k_B T}{n_0 e^2}}\,. \tag{63}$$

T is supposed to be the temperature T_e of the electrons that I consider equal to the temperature of the plasma.

Introducing ξ, I get the following profile in the disc

$$\lambda_D = \sqrt{\frac{4\pi k_B}{e^2}}\, \xi^{-1/2}\, n_{mid}^{-1/2}\, T^{1/2}\,, \tag{64}$$

$$= 4.67 \times \left(\frac{\xi}{10^{-13}}\right)^{-1/2} R_{AU}^{7/8}\ \mathrm{cm}\,. \tag{65}$$

This fundamental length embodies the capacity of the particles to organise themselves around a given charge so that if the density is high enough, many particles will screen the charge and the plasma can be considered as electrically neutral for length greater than λ_D. The Debye sphere is the underlying concept here, characterised by the adimensional number Ξ^{-1} defined as

$$\Xi^{-1} = n_0\, \lambda_D^3\,, \tag{66}$$

$$= 6.22 \times 10^5 \times \left(\frac{\xi}{10^{-13}}\right)^{-1/2} \times R_{AU}^{3/8} \ll 1 \tag{67}$$

$\Xi^{-1} \ll 1$ implies that the plasma characteristics enable the Debye spheres to be widely populated, which ensures the neutrality of the plasma at high scales.

CYCLOTRON MOTION A well-known result concerning non-relativistic charged particles in presence of a magnetic field $\mathbf{B}$ is the cyclotron motion. For a particle of mass m_j, electric charge q_j and velocity $\boldsymbol{v}_j$ submitted to the Lorentz force, the gyro- or cyclotron frequency is

$$\Omega_{q_j} \equiv |q_j|\, B/m_j\,, \tag{68}$$

to which correspond characteristic time-scales that verify $\tau_i \equiv \Omega_i^{-1} \gg \Omega_e^{-1} \equiv \tau_e$. To adopt a fluid description of the plasma, one must consider dynamical timescale before which τ_i is negligible.

CONCLUSIVE REMARKS ON THE ELECTRIC FIELD: As a consequence of the previous assumption, the plasma can perfectly be considered neutral. Subsequently and despite the presence of electrical charges, one can fairly drop the corresponding electrical field (which is neglected), as long as any studied length is greater than λ_D. However, this procedure does not mean that there is no electrical field in the plasma. Indeed, $\boldsymbol{v}_{rot.} \times \mathbf{B}$ electrical fields appear because of the rotation of the disc and non-ideal diffusivities may also translate into electric contributions to the Lorentz force. The treatment of $\mathbf{E}$ calls for a constitutive relation. The Ohm law plays this role with $\mathbf{J} = \mathbf{J}(\mathbf{E}, \mathbf{B})$. To precise this relation, the interactions between the different species in the plasma must be addressed and I refer to the sec. 2.2.2.

2.2.1.2 *Multifluid and two fluid*

At this point, one could try to solve the set of equations composed of eq. 54a, 54b as well as eq. 56b to 56d. The fluid equations should

then be resolved for each kind of particles (previously labelled with j), which very demanding in terms of numerical calculations. Such a treatment is mandatory to study plasmas in which different species could have very different dynamics (for example in solar wind in the solar magnetosphere Winglee, 1998). The use of this method has then everything to do with the dynamical coupling of the different species. This approach is called a multifluid approach and has also been used in the context of protoplanetary discs such as in Rodgers-Lee et al. (2016). Another similar method is to consider only two different species (the electrons and the ions) and to solve the equations for these species only. I refer to Goedbloed and Poedts (2004) for detailed explanations on this two fluids approach. However, as I will show in the next subsection, the use of mutlifluid can be avoided in the case of protoplanetary discs, as it is routinely done (e. g. Gressel et al., 2020).

2.2.1.3 *Single fluid approximation*

The first step toward the single fluid approximation is to define a density ρ as well as a corresponding velocity $\mathbf{u}$ in such a way that it takes all the particles j into account. Hence

$$\rho \equiv \sum_j n_j \, m_j \,, \tag{69}$$

$$\mathbf{u} \equiv \frac{\sum_j n_j \, m_j \, \mathbf{u}_j}{\sum_j n_j \, m_j} \,. \tag{70}$$

I introduce a deviation velocity $\tilde{\mathbf{u}}_j$ so that

$$\tilde{\mathbf{u}}_j \equiv \mathbf{u} - \mathbf{u}_j \,. \tag{71}$$

May this way of proceeding seem similar to what was achieved with eq. 52, it is not the same idea behind it. Eq. 52 highlights the velocity deviation between the hydrodynamic velocity of a given particle of the j specie and the averaged velocity of all these type-j particles. It shows to what extent the j-particles move in a similar fashion. In contrast, eq. 71 considers the deviation velocity between a given set of j-particles and the total velocity. This deviation highlights how well coupled the different kinds of species are. To estimate this coupling, the effects that deviates a given type of particles from the mean trajectory must be compared to the effects that impose their general trend on the global movement. Therefore, neglecting $\tilde{\mathbf{u}}_j$ demands that

$$\rho_j \, \|\tilde{\mathbf{u}}_j\| \ll \rho \, v_K \,, \tag{72}$$

where v_K is the local Keplerian speed. By saying so, I assume that gravity is the main process dynamically involved in the physics of protoplanetary discs. From now on, I will adopt a linearised depiction

of the interaction term $\mathbf{R}_{jk}$ between species j and k, which takes the form of a drag force term

$$\mathbf{R}_{jk} \equiv -\gamma_{jk}\,\rho_j\,\rho_k\,\left(\mathbf{u}_j - \mathbf{u}_k\right) \tag{73}$$

where the γ_{jk} are defined as

$$\gamma_{jk} \equiv \frac{\langle\sigma v\rangle_{jk}}{m_j + m_k}\,, \tag{74}$$

with $\langle\sigma v\rangle_{jk}$ the momentum exchange rates between species j and k. One has $\mathbf{R}_j = \sum_k \mathbf{R}_{jk}$ and since $\mathbf{R}_{jk} = -\mathbf{R}_{kj}$, $\sum_j \mathbf{R}_j = 0$. Remarking that

$$\begin{aligned}\sum_j n_j\, m_j\, \mathbf{u}_j \otimes \tilde{\mathbf{u}}_j &= \sum_j n_j\, m_j \mathbf{u} \otimes \mathbf{u} - \sum_j n_j\, m_j \mathbf{u} \otimes \tilde{\mathbf{u}}_j \\ &= \underbrace{\left(\sum_j n_j\, m_j\right)}_{=\rho}\, \mathbf{u}\otimes\mathbf{u} - \underbrace{\left(\sum_j n_j\, m_j \mathbf{u}_j\right)}_{=\rho\,\mathbf{u}} \otimes \mathbf{u} = \underline{\underline{0}}\,,\end{aligned}$$

I sum the eq. 54a and 54b for all the species and get

$$\partial_t \rho + \boldsymbol{\nabla}\cdot(\rho\,\mathbf{u}) = 0\,, \tag{75a}$$

$$\partial_t\left(\rho\,\mathbf{u}\right) + \underline{\underline{\boldsymbol{\nabla}}}\cdot\left(\rho\,\mathbf{u}\otimes\mathbf{u}\right) = \underbrace{\underline{\underline{\boldsymbol{\nabla}}}\cdot\left(\sum_j n_j\, m_j\, \tilde{\mathbf{u}}_j \otimes \tilde{\mathbf{u}}_j\right)}_{\text{neglected}} - \boldsymbol{\nabla} P + \mathbf{f} + \frac{\mathbf{J}\times\mathbf{B}}{c} + \underbrace{\rho_c\,\mathbf{E}}_{\approx 0}\,. \tag{75b}$$

I neglect the terms with $\|\tilde{\mathbf{u}}_j\|^2$ under the previously detailed assumptions, because of quasi-neutrality, the electric part of the Lorentz force is dropped. I defined P the total pressure and $\mathbf{f}$ the total forces per unit volume as the sum of all their j-counterparts. I am now left with the equations of motion under the single fluid approximation, namely eq. 56b, 56c, 56d, 75a and

$$\partial_t\left(\rho\,\mathbf{u}\right) + \underline{\underline{\boldsymbol{\nabla}}}\cdot\left(\rho\,\mathbf{u}\otimes\mathbf{u}\right) = -\boldsymbol{\nabla} P + \mathbf{f} + \frac{\mathbf{J}\times\mathbf{B}}{c}\,. \tag{76}$$

All the complexity of having a mixture of different species of various electric charges is hidden by the use of single generic fluid of density ρ and velocity $\mathbf{u}$.

2.2.1.4 *Ideal* MHD

A REVIEW OF THE PHYSICAL ASSUMPTIONS: Rather than simple algebraic manipulations, the single-fluid approximation procedure contains a fair amount of approximations. Indeed, to get the equations of the single fluid approximation, I adopted a fluid description

carrying its own set of approximations regarding the collision time-scales, before neglecting any non diagonal element of the stress tensor. Regarding the dissipative phenomena (viscosity, heat conduction between the different species), characterised by a time-scale $\tau_{\text{diss.}}$, one needs the time-scale of interest to be way smaller than $\tau_{\text{diss.}}$. This leads the pressure to be intrinsically scalar with higher order terms (such as the heat flow) being neglected. That is why I adopt a polytropic equation of state for an ideal gas to close the system of equation, with a relation between the order-0 density ρ and the order-2 pressure P, tied together with

$$P\,\rho^{-n} = C\,, \tag{77}$$

with n the polytropic index, chosen so that $n = \gamma_{\text{ideal}}$ (with γ_{ideal} the adiabatic index) to enable an adiabatic evolution of the plasma and C is a constant. The addition of electromagnetism implies another set of approximations to assume quasi neutrality and to neglect the cyclotronic motion. Goedbloed and Poedts (2004) compiled these approximations under the maximal ordering of MHD , whose typical length and time-scales verify

$$\lambda_{\text{MHD}} \gg R_i \gg R_e \gg \lambda_D\,, \tag{78}$$

$$\tau_{\text{MHD}} \gg \tau_i \gg \tau_{p\,e} \sim \tau_e\,. \tag{79}$$

In this paragraph, I want to reach the ideal MHD set of equations, therefore I consider the following Ohm equation and leave further comments to sec. 2.2.2. I am then left with

$$\mathbf{E} = -\underbrace{\mathbf{u}\times\mathbf{B}}_{\text{ideal MHD term}} + \underbrace{\mathbf{E}_{\text{NI}}}_{\text{non-ideal terms}\approx 0}\,. \tag{80}$$

I now have to give a word on the conservation of the total energy per volume unit E defined with (I drop the external forces potentials)

$$E \equiv \frac{\rho\,\mathbf{u}^2}{2} + \frac{\mathbf{B}^2}{8\pi} + \rho\,u_{\text{int.}}\,, \tag{81}$$

with $u_{\text{int.}}$ the internal energy per mass and volume units, that is equal to (under the polytropic assumption)

$$u_{\text{int.}} = \frac{P/\rho}{n-1}\,. \tag{82}$$

In the absence of any dissipative process, one is left with

$$\partial_t E + \boldsymbol{\nabla}\cdot\left[\left(\frac{\rho\,\mathbf{u}^2}{2} + P + \rho\,u_{\text{int.}}\right)\mathbf{u} + \boldsymbol{\Pi}\right] = 0\,, \tag{83}$$

with $\boldsymbol{\Pi}$ the Poynting vector. Any sources or dissipation would make this equation non zero, with supplementary terms on the right hand-side. It must be noted, that the electromagnetic and purely mechanic parts of this equation, once removed, leaves

This can be shown directly with eq. 82.

$$\partial_t P + \mathbf{u}\cdot\boldsymbol{\nabla}P + \gamma\,P\boldsymbol{\nabla}\cdot\mathbf{u} = 0\,. \tag{84}$$

IDEAL MHD SET OF EQUATIONS: I am now fully equipped to render the usual set of ideal MHD equations:

$$\partial_t \rho + \boldsymbol{\nabla} \cdot (\rho \, \mathbf{u}) = 0 \,, \qquad \text{(mass conservation)} \tag{85a}$$

$$\rho \, \partial_t \mathbf{u} + \rho \, \mathbf{u} \cdot \boldsymbol{\nabla} \mathbf{u} + \boldsymbol{\nabla} P - \frac{\mathbf{J} \times \mathbf{B}}{c} + \mathbf{f} = 0 \,, \qquad \text{(momentum equation)} \tag{85b}$$

$$\partial_t P + \mathbf{u} \cdot \boldsymbol{\nabla} P + n \, P \, \boldsymbol{\nabla} \cdot \mathbf{u} = 0 \,, \qquad \text{(internal energy)} \tag{85c}$$

$$\partial_t \mathbf{B} + \boldsymbol{\nabla} \times \mathbf{E} = 0 \,. \qquad \text{(Maxwell-Faraday)} \tag{85d}$$

$$\boldsymbol{\nabla} \cdot \mathbf{B} = 0 \qquad \text{(Maxwell-Thomson)} \tag{85e}$$

The electric field taken so that quasi neutrality is recovered is given by the Ohm law (eq. 80) so that combined with the Maxwell-Ampère equation (eq. 56d), the Maxwell-Faraday equation gives the so called induction equation

$$\partial_t \mathbf{B} - \boldsymbol{\nabla} \times (\mathbf{u} \times \mathbf{B}) = 0 \,, \tag{86}$$

which drives the dynamics of the magnetic field in the ideal MHD regime.

OTHER APPROACHES: Interestingly, the equations of ideal MHD can be recovered with a Lagrangian $L[\mathbf{u}, \rho, P, \mathbf{B}]$ (Newcomb, 1961; Zhou, 2017; Webb and Anco, 2019) and the corresponding Euler-Lagrange equations. This approach highlights the role of the energy and concentrates all the assumptions in the choice of the Lagrangian density which is not straightforward.

2.2.2 *Non ideal* MHD

In the ideal picture of MHD, the different species are strongly coupled to each other, sharing common dynamics. However and despite this coupling, charged species and neutrals appear to have slightly different speeds. In this case, the drag term is at play so that currents appear alongside with corresponding electric fields. Electro-neutrality is still valid, so that one is subsequently left with an electric field to find to fulfil this condition. This section focuses on this task which is a tremendous milestone to reach a proper description of the non-ideal MHD.

2.2.2.1 *Drag velocities and coupling*

In the ideal framework, the electric field $\mathbf{E}'$ in the fluid comoving frame is related to the electric field $\mathbf{E}$ in another inertial frame of reference with the usual Ohm's law

$$\mathbf{E}' = \mathbf{E} + \mathbf{u} \times \mathbf{B} \,. \tag{87}$$

Under the assumption that the disc is a perfect conductor, I had $\mathbf{E}' = \mathbf{0}$. However, if disparate dynamics are at play for each specy, this result does not stand anymore. Charged particles and neutrals, under adequate assumptions, reach a given speed deviated from $\mathbf{u}$ so that $\tilde{\mathbf{u}}_j \to \mathbf{cst.}$ An electric field thus appears and modifies the equations of motion in the comoving frame. All the species are coupled to each other through the $\mathbf{R}_{jk}$ forces while the electric field keeps the overall charges neutrality. I assume that a protoplanetary disc is filled with 3 kinds of species: electrons (e), ions (i) and neutrals (n). The respective drag velocities that lie behind the $\mathbf{R}_{jk}$ forces are given by

$$\begin{aligned}
\mathbf{R}_{ie} &= -\gamma_{ie}\rho_i\rho_e\left(\mathbf{u}_i - \mathbf{u}_e\right) = -\alpha_{ie}\,\left(\mathbf{u}_i - \mathbf{u}_e\right)\,, \\
\mathbf{R}_{en} &- \gamma_{en}\rho_e\rho_n\left(\mathbf{u}_e - \mathbf{u}_n\right) - \alpha_{en}\,\left(\mathbf{u}_e - \mathbf{u}_n\right)\,, \\
\mathbf{R}_{ni} &= -\gamma_{ni}\rho_n\rho_i\left(\mathbf{u}_n - \mathbf{u}_i\right) - \alpha_{ni}\,\left(\mathbf{u}_n - \mathbf{u}_i\right)\,,
\end{aligned}$$

where I define $\alpha_{jk} \equiv \gamma_{jk}\,\rho_j\,\rho_k$ as shorthand notations to ease the calculus to come. It is of prime interest to estimate the contribution of the drag velocities to $\mathbf{u}$ to know which, if any, specie dominates over the others. Protoplanetary discs are weakly ionised objects in their outer parts ($R_{AU} \gtrsim 1$). I previously estimated the ionisation fraction to be of the order of $\xi \sim 10^{-13}$, where $\xi = n_e/n_n = x\,n_i/n_n$, with $x = |q_i/q_e|$ (where I use the electric neutrality). Detailed calculations of ξ lies within sec. 2.3, nevertheless, this order of magnitude leads undoubtedly to the fact that

$$\begin{aligned}
\mathbf{u} &= \frac{n_n\,m_n\,\mathbf{u}_n + n_i\,m_i\,\mathbf{u}_i + n_e\,m_e\,\mathbf{u}_e}{n_n\,m_n + n_i\,m_i + n_e\,m_e}\,, \\
&= \frac{m_n\,\mathbf{u}_n + \xi\,x_i\,\mathbf{u}_i + \xi\,x\,x_e\,\mathbf{u}_e}{1 + \xi\,x_i + \xi\,x_e}\,, \\
&= \mathbf{u}_n + \left(x_i\,\mathbf{u}_i + x\,x_e\,\mathbf{u}_e\right)\,\xi + o_0\left(\xi\right)\,,
\end{aligned}$$

where I define $x_x \equiv m_x/m_n$, so that in the end

$$\mathbf{u} \approx \mathbf{u}_n \,. \tag{88}$$

With this result in mind, I can draw the following approximations.

1. The conclusion to get from calculation 88 is that the neutrals are predominant regarding the total velocity. They then drive the charged species which themselves experience the Lorentz force. I will make this assumption for a weakly ionised plasma.

2. Another consequence of eq. 88 and regarding the drag forces, the collisions are mostly due to neutrals so that the $\mathbf{R}_{ei}$ force is dropped before the neutrals $\mathbf{R}_{jn}$ terms.

3. I further assume that the characteristic time for any specie j to reach a terminal drift velocity, namely the stopping time $\tau_{s,j}$, is way shorter than the typical dynamical time Ω_K^{-1}, so that any advection motion ($\boldsymbol{w}\cdot\boldsymbol{\nabla}\boldsymbol{w}'$ terms with $\boldsymbol{w}$ and $\boldsymbol{w}'$ being any speeds $\mathbf{u}_j$ or $\mathbf{u}$) or external forces (gravity) shall be neglected.

4. In the same spirit, $\partial_t\tilde{\mathbf{u}}_j \approx 0$, meaning the particles reach their terminal drift velocity. This equivalent to neglect $d\boldsymbol{w}/dt$ over terms $\propto \boldsymbol{w}$ in the drag force.

5. Furthermore, any $\boldsymbol{\nabla}P_j$ or $\boldsymbol{\nabla}P$ term is also negligible assuming that the Mach number is small enough.

6. The inertia of the electrons is neglected, so that in particular $d\mathbf{u}_e/dt \approx 0$.

I hereby do not state that all these effects are negligible regarding the disc overall dynamics, I rather explicitly assume that in comparison, the dynamics at play in the deviation to ideal MHD occur on short time-scales. Note that the first two assumptions are consequence of the weak ionisation of the plasma, so that I first derive the generalised Ohm's law for a general plasma made of 3 species before adding this hypothesis. I proceed this way in order to clearly emphasise the role of neutrals particles in the disc and how the so call ambipolar process emerges. The hereafter calculations follow Braginskii (1965) and supplementary materials can be found in Elsasser (1950), Cowling (1957), and Lesur (2021a).

2.2.2.2 *Generalised Ohm's law in a three-component mixture*

Due to the presence of 3 species in the plasma, I must find the following 2 relative velocities

$$\boldsymbol{\gamma} \equiv \mathbf{u}_e - \mathbf{u}_i\,, \boldsymbol{w} \equiv \mathbf{u}_i - \mathbf{u}_n\,. \tag{89}$$

Writing down the equations of motion for each specie (and neglecting the electron intertia under hyp. 6), I get

$$-\boldsymbol{\nabla}p_e - e\,n_e\left(\mathbf{E}+\frac{\mathbf{u}_e\times\mathbf{B}}{c}\right)+\alpha_e\frac{\mathbf{J}}{e\,n_e}-\alpha_{en}\,\boldsymbol{w}=0\,, \tag{90a}$$

$$-\boldsymbol{\nabla}p_i+q_i\,n_i\left(\mathbf{E}+\frac{\mathbf{u}_i\times\mathbf{B}}{c}\right)-\alpha_{ei}\frac{\mathbf{J}}{e\,n_e}-\alpha_{in}\,\boldsymbol{w}=n_i\,m_i\,\frac{d\mathbf{u}_i}{dt}\,, \tag{90b}$$

$$-\boldsymbol{\nabla}p_n-\alpha_{en}\frac{\mathbf{J}}{e\,n_e}+\alpha_n\,\boldsymbol{w}=n_i\,m_i\,\frac{d\mathbf{u}_n}{dt}\,, \tag{90c}$$

where I used the relation $\boldsymbol{\gamma} = -\mathbf{J}/e\,n_e$ and the notations $\alpha_x = \alpha_{xi} + \alpha_{xe}$. Thanks to hyp. 5, all the pressure gradients are neglected. In eq. 90b and 90c, I use hyp. 3 and 4 to replace $\mathbf{u}_n$ and $\mathbf{u}_i$ directly by $\mathbf{u}$, so that by summation I have

$$\boldsymbol{w} = \frac{\xi_n}{c\,\alpha_n}\,\mathbf{J}\times\mathbf{B} + \frac{\alpha_{en}/\alpha_n}{e\,n_e}\,\mathbf{J}\,, \tag{91}$$

with $\xi_n = m_n\,n_s p_n/\rho$. Now that I have $\boldsymbol{w}$, I inject this velocity back in eq. 90a to end up with the generalised Ohm's law

$$\mathbf{E} + \frac{1}{c}\mathbf{u}_i\times\mathbf{B} = \frac{\mathbf{J}}{\sigma} + \frac{1-\alpha_{en}\,\xi_n/\alpha_n}{e\,n_e\,c}\mathbf{J}\times\mathbf{B}\,, \tag{92}$$

where the conductivity σ is introduced as

$$\sigma = e^2\,n_e^2\left(\alpha_{ei} + \frac{\alpha_{en}\,\alpha_{in}}{\alpha_{en}+\alpha_{in}}\right)^{-1} \approx \frac{e^2\,n_e^2}{\alpha_e}\,. \tag{93}$$

Note that the first two assumptions are not used for now, so that each specie keeps its own dynamics on the time-scale of interest. As a conclusion, I write down the electric field in the coordinate system moving with the plasma at speed $\mathbf{u}$

$$\mathbf{E}' = \mathbf{E} + \frac{1}{c}\mathbf{u}\times\mathbf{B} = \frac{\mathbf{J}_\parallel}{\sigma_\parallel} + \frac{1}{\sigma_\perp}\mathbf{J}_\perp + \frac{1}{\sigma^*}\left(\mathbf{J}\times\hat{\mathbf{b}}\right)\,, \tag{94}$$

with

$$\sigma_\parallel \equiv \sigma\,, \tag{95}$$

$$\frac{1}{\sigma_\perp} \equiv \frac{1}{\sigma} + \frac{\xi_n^2\,B^2}{\alpha_n\,c^2}\,, \tag{96}$$

$$\frac{1}{\sigma^*} \equiv \frac{1-2\,\alpha_{en}\,\xi_n/\alpha_n}{e\,n_e\,c} \approx \frac{1}{e\,n_e\,c/B}\,, \tag{97}$$

and $\hat{\mathbf{b}} \equiv \mathbf{B}/B$. I used a vector decomposition with respect to the magnetic field, so that for a given vector $\boldsymbol{x}$

$$\boldsymbol{x} = \underbrace{\frac{\mathbf{B}\cdot\boldsymbol{x}}{B^2}\,\mathbf{B}}_{=\boldsymbol{x}_\parallel} - \underbrace{\frac{(\boldsymbol{x}\times\mathbf{B})\times\mathbf{B}}{B^2}}_{=\boldsymbol{x}_\perp}\,. \tag{98}$$

In this first example, the physics that lies behind the generalised Ohm's law is more straightforward to catch. σ only involves the electron properties and accounts for the usual Ohm's law with electrons interacting with neutrals and ions. The perpendicular contribution depends on the magnetic field intensity and only on the neutrals properties. This effect needs to be understood as a perturbation to the ideal case for which the plasma follows the magnetic field. Therefore, motion of plasma across the magnetic field implies motion across the neutrals stream so that the stronger B and ξ_n, the more tremendous the effect is. Lastly, the $\mathbf{J}\times\mathbf{B}$ term accounts for the Hall effect that I will discuss in greater details as well as the other two effects in sec. 2.2.2.4.

2.2.2.3 *Generalised Ohm's law for a weakly ionised plasma*

With this peculiar case, the first two assumptions (1) and (2) come to play so that one can consider that the driving particles are the neutrals so that $\mathbf{u} \approx \mathbf{u}_n$ and therefore $\tilde{\mathbf{u}}_n \approx 0$. The one and only drag force is then given by $\mathbf{R}_j = -\alpha_{jn}\,\mathbf{u}_j$ and one is now left with $\tilde{\mathbf{u}}_j \equiv \mathbf{u}_j - \mathbf{u}$ to work with. The assumption (3) holds so that I drop the advection terms, the temporal derivatives and the pressure gradients, so that the equations of motion for particles j in the center of mass frame where the electric field $\mathbf{E}'$ is to find are

$$q_j\, n_j \left(\mathbf{E}' + \frac{1}{c}\tilde{\mathbf{u}}_j \times \mathbf{B}\right) - \alpha_{jn}\tilde{\mathbf{u}}_j = 0\,. \tag{99}$$

Since the neutrality condition is still valid, I have

$$\mathbf{J} = \sum_j q_j\, n_j\, \tilde{\mathbf{u}}_j\,. \tag{100}$$

One cannot obtain $\mathbf{E}'$ as a function of $\mathbf{J}$ as easily as in the previous case because of the $\tilde{\mathbf{u}}_j$ terms make it difficult to express the drift velocities, this is why I consider the parallel and perpendicular contributions of the vectors with respect to $\mathbf{B}$. $\mathbf{B}$ only appears in vectorial product, so that obtaining the parallel contributions is the same thing as having $\mathbf{B} = 0$. This way, I immediately have

$$\tilde{\mathbf{u}}_{j,\parallel} = \frac{q_j\, n_j}{\alpha_{jn}}\mathbf{E}'_\parallel\,, \tag{101}$$

and with a summation on j,

$$\mathbf{E}'_\parallel = \frac{1}{\sigma_o}\,\mathbf{J}_\parallel\,, \tag{102}$$

where I define

$$\sigma_o \equiv \sum_j q_j^2\, n_j\, \frac{n_j}{\alpha_{jn}} = \frac{c}{B}\sum_j q_j\, n_j\, \mu_j\,, \tag{103}$$

and

$$\mu_j \equiv \frac{B}{c}\frac{q_j}{\gamma_{jn}\, m_j\, \rho_n}\,. \tag{104}$$

For the crossed contribution, I will use the relation $\tilde{\mathbf{u}}_{j\perp} = -\left(\tilde{\mathbf{u}}_j \times \mathbf{B}\right) \times \mathbf{B}/B^2$ and the fact that $(\mathbf{x} \times \mathbf{B})_\perp = \mathbf{x}_\perp \times \mathbf{B}$. I first write from the equation of motion

$$\alpha_{jn}\,\tilde{\mathbf{u}}_{j,\perp} = q_j\, n_j \left(\mathbf{E}'_\perp + \frac{1}{c}\tilde{\mathbf{u}}_{j,\perp} \times \mathbf{B}\right)\,. \tag{105}$$

I apply $\times\mathbf{B}$ and use the equation of motion to get rid of $\tilde{\mathbf{u}}_{j,\perp} \times \mathbf{B}$ so that in the end I am left with

$$\tilde{\mathbf{u}}_{j,\perp} = \frac{c}{B}\frac{\mu_j}{1+\mu_j^2}\,\mathbf{E}'_\perp + \frac{c}{B}\frac{\mu_j^2}{1+\mu_j^2}\left(\mathbf{E}' \times \hat{\mathbf{b}}\right)\,. \tag{106}$$

I just have to sum over j to eventually get

$$\mathbf{J}_\perp = \sigma_P \mathbf{E}'_\perp + \sigma_H \mathbf{E}' \times \hat{\mathbf{b}}\,, \tag{107}$$

with

$$\sigma_P = \frac{c}{B} \sum_j \frac{q_j\, n_j\, \mu_j}{1+\mu_j^2}\,, \tag{108}$$

$$\sigma_H = \frac{c}{B} \sum_j \frac{q_j\, n_j\, \mu_j^2}{1+\mu_j^2}\,, \tag{109}$$

and the electric current is

$$\mathbf{J} = \sigma_O \mathbf{E}'_\parallel + \sigma_H \mathbf{E}' \times \hat{\mathbf{b}} + \sigma_P \mathbf{E}'_\perp\,. \tag{110}$$

I now take the vector product of eq. 107 with $\mathbf{B}$ to resume the perpendicular electric field so that the final form of the generalised Ohm's law is given by

$$\mathbf{E}' = \frac{4\pi}{c^2}\eta_O \mathbf{J} + \frac{4\pi}{c^2}\eta_H \mathbf{J} \times \hat{\mathbf{b}} + \frac{4\pi}{c^2}\eta_A \left(\mathbf{J} \times \hat{\mathbf{b}}\right) \times \hat{\mathbf{b}}\,, \tag{111}$$

with the following definition for the diffusivities

$$\eta_O = \frac{c^2}{4\pi}\frac{1}{\sigma_O}\,, \tag{112a}$$

$$\eta_H = -\frac{c^2}{4\pi}\frac{\sigma_H}{\sigma_H^2+\sigma_P^2}\,, \tag{112b}$$

$$\eta_A = \frac{c^2}{4\pi}\left(\frac{\sigma_P}{\sigma_H^2+\sigma_P^2} - \frac{1}{\sigma_O}\right)\,. \tag{112c}$$

To achieve this picture of non-ideal MHD, I just have to mention that $\mathbf{J} = \frac{4\pi}{c}\boldsymbol{\nabla}\times\mathbf{B}$, which once plugged into eq. 111, allows to recover the induction equation which gives the dynamics of the magnetic field

Because η_H and η_A depend on $\mathbf{B}$, the induction equation is non linear.

$$\partial_t \mathbf{B} = \underbrace{\boldsymbol{\nabla}\times(\mathbf{u}\times\mathbf{B})}_{\text{ideal}} - \boldsymbol{\nabla}\times\left[\underbrace{\eta_O \boldsymbol{\nabla}\times\mathbf{B}}_{\text{ohmic}} + \underbrace{\eta_H (\boldsymbol{\nabla}\times\mathbf{B})\times\hat{\mathbf{b}}}_{\text{Hall}} + \underbrace{\eta_A (\boldsymbol{\nabla}\times\mathbf{B})_\perp}_{\text{ambipolar}}\right]\,. \tag{113}$$

2.2.2.4 *Diffusivities*

Compared to ideal case, the induction equation has three non-ideal contributions. In this subsection, I give a few details regarding their physical meaning and compute the appropriate dimensionless number that control the strength of each effect.

OHMIC DIFFUSION: η_O is the most straightforward coefficient to interpret since it is found in daily life physics. It represents the usual Ohm's law of electronics that we get with $\mathbf{E} = (4\pi\eta/c)\,\mathbf{J}$ and that emerges from the Drude model of electrons. With the equations of Maxwell-Ampère (with a non-relativistic assumption), Maxwell-Faraday and Maxwell-Thomson, a few manipulations of vectors lead to

$$\partial_t \mathbf{B} = D\,\Delta\mathbf{B}\,, \tag{114}$$

with $D \equiv 1/\eta$ (I recall the use of CGS units). Such an equation is a typical diffusion equation regarding the magnetic field in a non-ideal conductor. This diffusion in particular allows matter to move across the magnetic field lines.

HALL DRIFT: The perturbation embodied by η_H is the Hall effect. In presence of a magnetic field, charges carriers moving along the electric field (hence generating a electrical current) experience the Lorentz force normal to the current vector and the magnetic field, generating a perpendicular electrical field. This happens when the ions and electrons have different motions, mainly due to the ions inertia. In the most simple case with electrons of conductivity σ and $\eta_H = c\,B/4\pi\,e\,n_e$ I write

$$\mathbf{J} = \sigma\left(\mathbf{E} + \mathbf{u}\times\mathbf{B} - \frac{1}{n\,e}\mathbf{J}\times\mathbf{B}\right)\,, \tag{115}$$

so that the induction equation is

$$\partial_t \mathbf{B} = \boldsymbol{\nabla}\times(\mathbf{u}\times\mathbf{B}) + \eta\,\Delta\mathbf{B} - \frac{4\pi}{n\,e}(\boldsymbol{\nabla}\times\mathbf{B})\times\hat{\mathbf{b}} \tag{116}$$

Introducing the Hall frequency ω_H as

$$\omega_H = \frac{e\,B\,n_e}{m\,n\,c}\,, \tag{117}$$

one can define the parameter $\ell_H \equiv v_A/\omega_H$, where v_A is the norm of the Alfvén speed given by

$$\boldsymbol{v}_A \equiv \frac{\mathbf{B}}{\sqrt{4\pi\,\rho}}\,. \tag{118}$$

The Hall effect is important on length-scales smaller than ℓ_H. For PPDS, Kunz and Lesur (2013) find $\ell_H \approx 0.4$ AU, so that this term can be neglected at $R \geqslant 10$ AU.
When this term is dominant, the ions are too heavy to follow the electrons motion and limit their influence to a fixed background field and the electrons all alone are responsible for the current. A last word on this effect is the fact that it is not a diffusion, since its energy dissipation is proportional to $(\mathbf{J}\times\mathbf{B})\cdot\mathbf{B} = 0$.

AMBIPOLAR DIFFUSION: The diffusive term at play with η_A highlights the interplay between ions and neutral particles. The ambipolar diffusion I will refer to in this work is not to be confused with another so called ambipolar diffusion which involves thermal effect that I neglect by cancelling the pressure gradient terms (see Braginskii, 1965 for more details on this). The effect I am describing is of magnetic origin and due to the drift between ions and neutrals. The drift arises from the competition between the Lorentz force and the drag force between ions and neutrals. If I neglect Ohmic and Hall effects, I am left with

$$\partial_t \mathbf{B} = \boldsymbol{\nabla} \times (\breve{\mathbf{u}} \times \mathbf{B}) \,, \tag{119}$$

with

$$\breve{\mathbf{u}} \equiv \mathbf{u}_n + \frac{\eta_A}{B^2} \left[(\boldsymbol{\nabla} \times \mathbf{B}) \times \mathbf{B} \right] . \tag{120}$$

This induction equation can be interpreted as a flux-freezing condition at a different speed than the speed of the total fluid as in ideal MHD (Masson et al., 2016). As a toy model, I consider a magnetic field of the form

$$\mathbf{B}_0 = B_0(x, y)\hat{\mathbf{e}}_z \,, \tag{121}$$

so that after a short calculation in cartesian coordinates,

$$\partial_t \mathbf{B}_0 = \eta_A \Delta \mathbf{B}_0 \,, \tag{122}$$

a diffusive process is once again at play. The radial profile for η_A in a protoplanetary disc is

$$\eta_A = 4.95 \times 10^{16} \left(\frac{\xi}{10^{-13}} \right)^{-1} \left(\frac{B}{1\,G} \right)^2 R_{AU}^{9/2} \, cm^2 \, s^{-1} \,, \tag{123}$$

where I have used (Draine, 2011)

$$\langle \rho \nu \rangle_{in} = 2.4 \times 10^{-9} \left(\frac{1}{\mu} \right)^{1/2} \, cm^3 \, s^{-1} \,. \tag{124}$$

2.2.3 *Dimensionless numbers:*

2.2.3.1 *Back to the plasma parameter*

I first wish to come back on the role β that I just briefly mentioned. It is of course a fair interpretation to use this number to quantify the effect of magnetic field in the plasma. Nevertheless, this number has a much more fundamental aspect. In the ideal MHD framework, the equations can be made dimensionless by the choice of 3 units (mass, time t_0 and length). Therefore, a quantity must tie the magnetic field to this choice of units. The Alfvén speed that appears in the equation is linked by the β parameter to the isothermal sound speed c_s

$$\beta = \frac{2\, c_s^2}{v_A^2} \,, \tag{125}$$

so that the β parameter labels the plasma and is the relevant quantity to control the effects of electromagnetism on the plasma. This is why the use of MHD ranges from galactic plasma ($B_0 \sim 10^{-8}$ T, $t_0 \sim 10^{15}$ s) up to tokamak plasma ($B_0 \sim 3$ T, $t_0 \sim 3 \times 10^{-6}$ s) despite a broad variation in the relevant physical quantities. The β plasma does not account for the strength of the non-ideal processes whatsoever, so that other dimensionless numbers are needed.

2.2.3.2 *Non-ideal effects*

The effects of Ohmic diffusion are quantified by the magnetic Reynolds number

$$\mathcal{R}_M \equiv \frac{\Omega_K h^2}{\eta_O} . \tag{126}$$

Back to eq. 114, $\mathcal{R}_M$ is so that it quantifies the magnetic field advection versus its diffusion. The strength of the Hall effect is embedded in the Hall Lundquist number

$$\mathcal{L}_H \equiv \frac{v_A h}{\eta_H} , \tag{127}$$

Note that $\Lambda_A = 1/\Omega_K \tau_s$ does not depend on the magnetic field strength.

and the ambipolar Elsasser number accounts for ambipolar diffusion

$$\Lambda_A \equiv \frac{v_A^2}{\Omega_K \eta_A} . \tag{128}$$

I now have a ready-to-use theoretical description of the physics at play in protoplanetary discs as well as in transition discs.

2.3 IONISATION FRACTION AND AMBIPOLAR DIFFUSION IN TD

2.3.1 *Radial density profile in transition discs*

To achieve this preliminary work, I need to address the specific question of transition discs to render a proper description of their inner cavity. I consider that transition discs are essentially similar to standard protoplanetary discs, so that I just need to choose a density profile for the cavity.

Several studies describe the gas and dust radial density profiles of numerous transition discs (van der Marel et al., 2016b; Francis and van der Marel, 2020; van der Marel et al., 2020) assuming inner holes (i. e. the density reaches 0) in the radial profiles. However, the observations show that the inner regions are not empty (Carmona et al., 2014) but rather depleted cavities. I will model the surface density of TDs such that Σ_{PPD} is reached in the outer part of the disc, while implementing a cavity at small radii. I do so with a 'cavity function' f defined so that

$$\Sigma_{TD} = f(R) \times \Sigma_{PPD} . \tag{129}$$

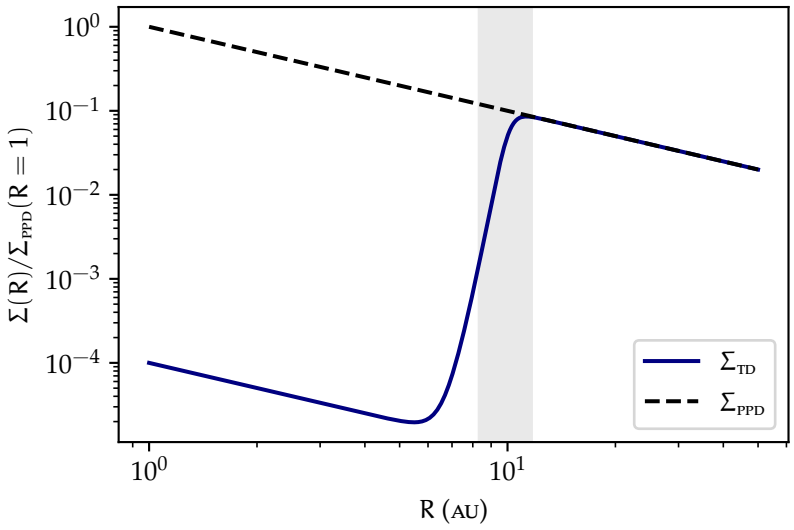

Figure 12: Radial profile of the surface density normalised by the surface density at $R = 1$ AU for a full protoplanetary disc. $\Sigma_{PPD} \propto R^{-1}$ is a standard profile for a full disc. The grey zone highlights the transition zone centred on R_0.

The explicit expression of f is

$$f(R) = a\left(1 - c\,\tanh\left[b\left(1 - \frac{R}{R_0}\right)\right]\right), \tag{130}$$

where R_0 is the outer edge of the cavity (where it connects to the full disc) and a, b and c are 3 coefficients that control the gap in density defined as $\Sigma_{TD}(+\infty)/\Sigma_{TD}(0) = 1/\Gamma_g = \beta_{out}/\beta_{in}$ and the width δR of the transition. The coefficients a and c are given by

$$\begin{cases} a = \dfrac{\Gamma_g + \tilde{b}}{1 + \tilde{b}} \\ c = \dfrac{1 - \Gamma_g}{\Gamma_g + \tilde{b}} \end{cases},$$

where $\tilde{b} \equiv \tanh b$. The last coefficient b much satisfy

$$b = \left(\frac{R_0}{\delta R}\right) \times \left(1 + \tilde{b}\right). \tag{131}$$

Assuming a sharp transition on $\delta R \leqslant 1$ AU while $R_0 = 10$ AU, I get $\tilde{b} \approx 1$ and

$$b \approx 2\left(\frac{R_0}{\delta R}\right). \tag{132}$$

This means that $\lim_{R\to 0^+} f(R) \approx \lim_{R\to-\infty} f(R)$.

The overall radial profile for Σ_{TD} is given in fig. 12 and will be used to initialise numerical simulations and as a reference for analytic calculations.

2.3.2 *Ionisation fraction*

I have already mentioned the role of the ionisation fraction which is fundamental for protoplanetary discs that are made of a poorly ionised plasma (Wardle, 2007). Hereafter is recalled the definition of the ionisation fraction ξ,

$$\xi \equiv \frac{n_e}{n_n}, \tag{133}$$

which represents the amount of free negative charge carriers n_e compared to the neutrals n_n one. This quantity is not well constrained at all and depends on the radius and altitude in the disc. Öberg et al. (2011) investigate on the vertical structure of the ionisation fraction based on observations of DM tau with the detections of a few chemical species. They give an uper averaged value of $\xi < 3 \times 10^{-10}$ for the disc midplane that corresponds to the layer where the temperature is below 16 K.
In this subsection, I estimate the ionisation fraction in a standard protoplanetary disc and check the influence of a cavity in gas radial density profile before moving to an estimation of the ambipolar Elsasser number. This procedure follows and adapt the main steps that can be found in Combet et al. (2010) or Lesur (2021a).

2.3.3 *Ionisation sources*

A first step towards the computation of ξ is to gather and describe the ionisation fraction at play in the physics of protoplanetary discs. Such discs are subject to their host star irradiation as well as the influence of the external environment (mainly with cosmic rays). Lastly, a natural ionisation source lies within the thermal ionisation. Due to the presence of "dead zones" (Gammie, 1996) in the outer parts of the disc (i. e. $R > 1$ AU), protoplanetary discs appear to be too cold to enable such process. As an order of magnitude, a temperature of $\sim 10^4$ K is required to trigger hydrogene thermal ionisation. Umebayashi (1983) gives a quantitative estimation of the ionisation fraction based on the thermal ionisation of potassium (see his fig. 7) and finds typical values of $\xi_{\text{thermal}} < 10^{-14}$ for temperatures below 800 K as it is the case in protoplanetary discs outer parts. I therefore neglect the thermal effects and focus on 4 main sources of non-thermal ionisation following Willacy (2007) that are listed below and detailled hereafter:

- Ionisation due to the stellar irradiation (x-ray and FUV photons).
- Cosmic ray (CR) due to the interstellar cosmic ray flux.
- Ionisation due to radioactive decay in the disc.

2.3.3.1 X-*ray ionisation from the star:*

Classical T Tauri stars can be very energetic sources characterized by a strong though variable x-ray emission, typically ranging from $L_x \approx 10^{28}$ up to 10^{31} erg s^{-1} (Casanova et al., 1995) and peaking around 1 keV (Feigelson et al., 2007). I model this emission following previous work (Bai and Goodman, 2009; Krolik and Kallman, 1983) by two bremsstrahlung-emitting coronal rings located at $R = 10\,R_\odot$. The x-ray photons are affected by photoionisation and Compton scattering involving secondary electrons which changes the associated ionisation rate per hydrogen molecule ζ_x. Based on Monte Carlo radiative transfer calculations displayed in Igea and Glassgold (1999) and which account for the previous processes, Bai and Goodman (2009) obtained a fitted profile for the ionisation rate due to x-ray. Therefore, I adopt the such a profile which depends in particular on the vertical column density of hydrogene

$$\zeta_x = L_{x,29}\left(\frac{R}{1\,AU}\right)^{-2.2}\left[\zeta_1\left(e^{-(N_{H1}/N_1)^\alpha}+e^{-(N_{H2}/N_1)^\alpha}\right)+\zeta_2\left(e^{-(N_{H1}/N_2)^\beta}+e^{-(N_{H2}/N_2)^\beta}\right)\right], \quad (134)$$

with $L_{X,29} \equiv L_x/10^{29}$ erg s^{-1} and $L_x = 5\times10^{29}$erg s^{-1} the x luminosity at $T_X = 3$ keV. $\zeta_1 = 4.0\times10^{-12}$ s^{-1}, $\zeta_2 = 2.0\times10^{-15}$ s^{-1}, $N_1 = 3.0\times10^{21}$ cm^{-2}, $N_2 = 1.0\times10^{24}$ cm^{-2}, $\alpha = 0.5$ and $\beta = 0.7$ are fitting parameters listed in Bai and Goodman (2009). N_{H1} and N_{H2} are the columns density of hydrogen vertically computed above and below the point of interest. It should be noted that the first exponential terms embody the x-ray attenuation due to the absorption while the seconde exponential terms account for scattering.

2.3.3.2 UV *photons ionisation from the star:*

Concerning the UV stellar irradiation, one could consider Extreme-Ultraviolet (EUV, energy ray between 13.6 and 100 eV) and Far-Ultraviolet (FUV, with 6 eV $< E <$ 13.6 eV). Despite their influence on photoevaporation winds (Alexander et al., 2006; Owen et al., 2010), EUV photons are completely absorbed out for column densities of neutral hydrogen greater than 10^{20} cm^{-2} (Hollenbach and Gorti, 2009). Their typical penetration depth are neglectible so that they do not penetrate in the disc. As a consequence, I neglect EUV photons accordingly with Wang and Goodman (2017) and only consider FUV photons whose penetration depth is larger and of the order of 10^{-2} g cm^{-2} (Perez-Becker and Chiang, 2011). FUV photons mainly affect species like carbon and sulfur inside a short layer (Bai and Stone, 2013b) whose ionisation fraction is directly of the order of 10^{-5}. Following Lesur et al. (2014),

I use an exponential model to account for the ionisation fraction ξ_{FUV} due to the FUV photons

$$\xi_{\text{FUV}} = \xi_{\text{FUV},0} \exp\left[-\left(\frac{\Sigma_\star}{0.03 \text{ g cm}^{-2}}\right)^4\right], \tag{135}$$

with $\xi_{\text{FUV},0} = 2 \times 10^{-5}$ and $\Sigma_\star$ being the matter column density computed from star up to the point of interest.

2.3.3.3 CR *from the interstellar environment of the disc*

A protoplanetary disc is embeded in the interstellar medium and subject to cosmic ray ionisation. A canonical way to model this source follows Umebayashi and Nakano (1980) in which CRs are supposed to reach the disc surface with an unattenuated flux that generates a ionisation rate $\zeta_{\text{CR}} \sim 10^{-16} - 10^{-17}$ s^{-1} with a stopping length of 96 g cm^{-2}. The profile that I take to compute the CR influence is given by

With those values, X-rays are dominant in the upper part of the disc (~ 50 g cm^{-2}) until CRs become the primary ionising source due to their greater penetration depth.

$$\zeta_{\text{CR}} = \zeta_{\text{CR},0} \exp\left(-\frac{\Sigma_{\text{col.}}}{96 \text{ g cm}^{-2}}\right) \text{s}^{-1}, \tag{136}$$

where $\zeta_{\text{CR},0} = 10^{-17}$ s^{-1} and $\Sigma_{\text{col.}}$ is the matter column density above and below the calculation point. Observations of the CR flux in ζ Persei highlights $\zeta_{\text{CR},0} \sim 10^{-16}$ s^{-1} as an order of magnitude (McCall et al., 2003).

2.3.3.4 *Ionisation due to radioactivity in the disc*

The last ionising source taken into account is the effects of radionuclides in the disc. Such elements can ionise the surrounding gas in a homogeneous manner (i. e.a spatially constant ionising rate). The greatest contributor to this ionising rate is the aluminium ^{26}Al whose half-life time is $\sim 7 \times 10^5$ yrs. The expected ionisation rate estimated from Umebayashi and Nakano (2008) is

$$\zeta_{\text{rad.}} = 10^{-19} \text{ s}^{-1}. \tag{137}$$

With all the previous ionising sources, one can now get the total ionising rate defined as

$$\zeta \equiv \zeta_{\text{x}} + \zeta_{\text{CR}} + \zeta_{\text{rad.}}. \tag{138}$$

In order to compute the ionisation fraction, one needs to study the chemical equilibrium of a chosen chemical network and therefore to develop a model for recombination processes in the disc.

2.3.4 *Recombination processes*

Contrary to the ionising processes, recombination is greatly affected by the presence of grains. Because of the previously discussed "dead

zones" (Gammie, 1996) and dust settling at the disc midplane, the dominant recombination process is expected to be the dissociative recombination with molecular ions. An example of such process is given by the reaction $HCO^+ + e^- \rightarrow CO + H$. The dissociative recombination rate δ associated to this process is (Armitage, 2017; Fromang et al., 2002)

$$\delta = 3 \times 10^{-6}\, T^{-1/2}\ \mathrm{cm^3\, s^{-1}}. \tag{139}$$

Such a model favours simplicity as well as a direct understanding rather than a high accuracy and may very well overestimate the electron density (Fromang et al., 2002). In the prospect of picturing a simple model for recombination, I mention but not include two other recombination processes, namely the radiative recombination with heavy-metal ions and the charge transfer from molecular ions to metal atoms (details can be found in Fromang et al. (2002), Armitage (2017), and Lesur (2021a). I hereby anticipate on the upcoming simplification of neglecting the direct influence of grains and metals.

2.3.5 *Chemical network*

Now that I have introduced how electrons appear and disappear in the disc, I can build a chemical network to solve the corresponding equation that will render the profile of the ionisation fraction. Astrochemistry in protoplanetary discs is a vast and thoroughly studied area of research. As illustrations, astrochemistry is combined to observations and simulations to study peculiar chemical species (e. g.: Gal et al., 2021 for sulfur molecules in discs) or used to build complex chemical networks (e. g.: Marchand et al., 2016 for core-collapse simulations with non-ideal MHD processes). It is completely beyond the scope of this work to render a detailed description of the chemistry at play. With this in mind, I precise that the aim of this section is to get orders of magnitude regarding the Elsasser ambipolar number in protoplanetary discs. In this prospect, I will assume that the chemical network is stationary and neglect both metals and grains. This is a strong assumptions which is valid as long as the chemistry time scales are shorter than the dynamical ones and seems valid according to (Woitke et al., 2009). This being said, here is the chemical network I consider

$$\mathrm{m} + \text{ionising radiation} \longrightarrow \mathrm{m^+} + \mathrm{e^-} \qquad \zeta_i\,, \tag{140}$$

$$\mathrm{m^+} + \mathrm{e^-} \longrightarrow \mathrm{m} \qquad \delta\,, \tag{141}$$

with m referring to an ion. I eventually get the ionisation fraction (Lesur et al., 2014)

$$\xi = \sqrt{\frac{\zeta}{\delta\, \rho}} + \xi_{\mathrm{FUV}}\,. \tag{142}$$

Looking at eq. 124, I have all the profiles needed to compute η_A hence Λ_A. I can use eq. 129 to mimic a transition disc or keep eq. 38 to compute Λ_A for a full protoplanetary disc.

2.3.6 *Ambipolar Elsasser number computation*

2.3.6.1 *Ambipolar diffusion and magnetically driven accretion*

I aim to perform numerical simulations of transition discs in the physical frame of non ideal MHD. Protoplanetary discs are expected to be far from the ideal regime (Lesur, 2021a), however, the relative strengths of each non-ideal process are not well known because of various uncertainties regarding the discs physics (ionisation rate, shape and structure of the disc, chemistry and composition). However, a common hypothesis is to consider that the ambipolar diffusion is the prominent process in the outermost parts of discs, where $R_{AU} > 10$ (Simon et al., 2015). This is why the ambipolar effect is commonly used in numerical simulations of protoplanetary discs with magnetic winds (Riols et al., 2020; Lesur, 2021b; Cui and Bai, 2021). Keeping up the pace with these works, I assume that the outer parts of the TDs I will study in my numerical simulations share this property with standard PPDs, at $R_{AU} \gtrsim 10$ at least. Consequently, I have to find a way of dealing with non-ideal processes inside the cavity of a TD $R_{AU} \lesssim 10$. The role of ambipolar diffusion for transition discs with MHD winds was tackled by Wang and Goodman (2017) who obtained the profile of Λ_A inside the cavity of a TD with a detailed chemical network. The accreted matter falling through the cavity needs to cross the magnetic field lines that create the magnetic wind. Following the wind solutions of Königl (1989) and Wardle and Koenigl (1993), Wang and Goodman (2017) invoke ambipolar diffusion as a good candidate to achieve this goal. Surely does this non-ideal process render an appealing solution for this problem, but it may not be the only one. According to Wang and Goodman (2017), one must have $1 \lesssim \Lambda_A \lesssim 20$ to recover a sonic accretion (as demanded by the presence of the cavity), but because of the drop in density in the cavity and the proximity with the stars which enhances ionisation, Λ_A might very well be off the grid regarding the upper boundary. An alternative solution that would allow matter be accreted while launching a wind is the presence of a small turbulent diffusivity (Blandford and Payne, 1982; Ferreira and Pelletier, 1995; Zanni et al., 2007) which could be due to the MRI (Lesur et al., 2013) despite the fact that it tends to be quenched by the large poloidal fields generated along with wind launching models (Gressel et al., 2015). Despite these limits, the ambipolar process is still a plausible option providing that Λ_A remains roughly below ~ 20 and above ~ 1. An interesting point is the fact that Λ_A being below $\Lambda_{A,crit.}$ also inhibits MRI (Bai, 2011), so that this process is expected

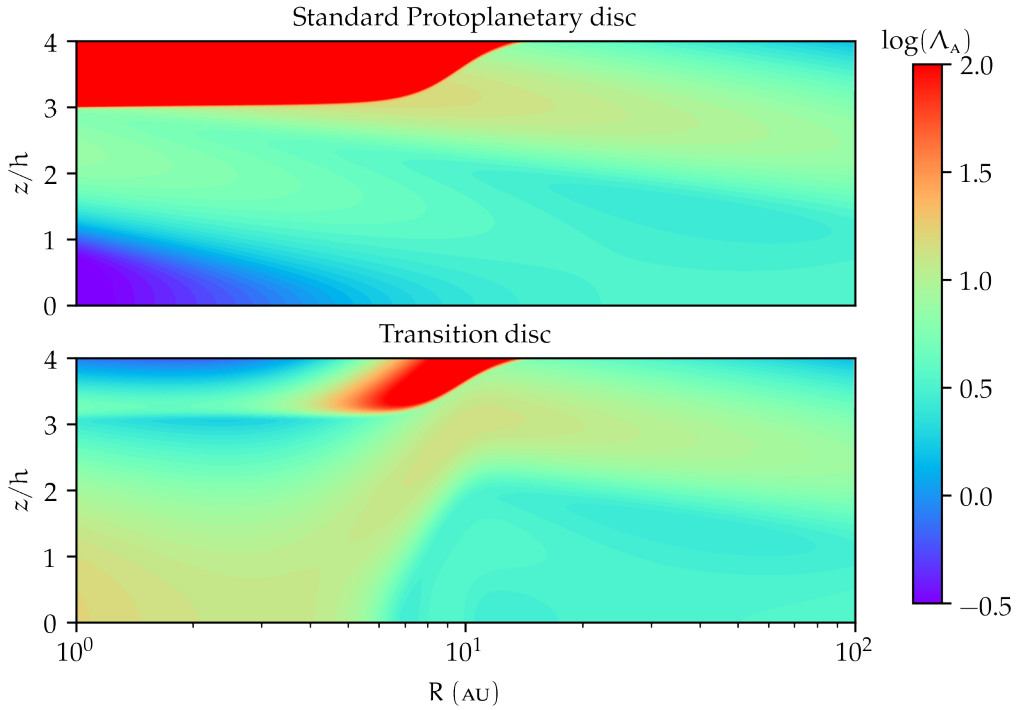

Figure 13: . Ambipolar Elsasser number Λ_A in a standard protoplanetary disc (top panel) and in a transition disc (bottom panel). In spite of these 2 profiles being slightly different, no major changes occur from one kind of disc to another around the midplane.

to control most of the physics of the cavity. I conclusively adopt this salient choice of relying on ambipolar diffusion to account for the microphysics of the TDs I study.

2.3.6.2 *Profile of Λ_A in a transition disc*

Since I will not use a chemical solver nor refined thermodynamics models, I need a toy profile of Λ_A that can mimics the non ideal process at play with ambipolar diffusion inside the cavity of a TD. Based on all the profiles I have presented up until now, I estimate the spatial profile of Λ_A in a generic transition disc to check its differences with a full protoplanetary disc.

The profile of Λ_A is given in fig. 13 both for a transition disc (bottom panel) and a standard protoplanetary disc (top panel). Though these 2 profiles look different at first glance, a deeper investigation reveals that the values taken by Λ_A in the discs remain pretty much close to unity in both cases, while the general trend of Λ_A in a standard protoplanetary disc is recovered even in the case of a transition disc (Thi et al., 2019).

Moreover, Λ_A remains fairly below the critical value $\Lambda_{A,crit.} = 10^2$ with or without a cavity so that the MRI effects are negligible (Blaes and Balbus, 1994; Bai, 2011). Regarding the bounds suggested by Wang and Goodman (2017), it seems that in a TD modelled this way, $\Lambda_A \sim 1-10$ is a good approximation everywhere at the midplane and up to a few scale height. Since I do not call for a high order precision regarding Λ_A, assuming a characteristic value of $\Lambda_{A,0} = 1$ should capture within a reasonable accuracy the physics of ambipolar diffusion.

The results I get from my simple toy model are to be compared to the more detailed work of Wang and Goodman (2017) where many chemical species are taken into account to compute the ambipolar Elsasser number inside the cavity of a wind-driven transition disc. This work highlights in particular the influence of the X-ray luminosity of the star L_X (see their fig. 2, panels 2 and 3) as well as the role of the temperature T_0 at 16 a.u. (fig. 2, panels 6 and 7). My work renders profiles similar to their models 2 (with $L_X = 10^{29}$ erg s^{-1}), 6 and 7 (where $T_0 = 30$ and 300 K). The decisive conclusion to draw from all this theoretical development, is the fact that a characteristic value of $\Lambda_A \sim 1-10$ is genuinely adequate to address the microphysics in magnetic winds emitting TDs. This choice is meaningful regarding the physical context.

2.4 NUMERICAL TOOLS: SIMULATIONS WITH THE PLUTO CODE

Protoplanetary discs are definitely out of reach regarding experiments. Observations unveil the behaviour of this object but need a theoretical background to rely on. Numerical simulations address this point and work along with observations. In this prospect, I did numerical simulations of transition discs with magnetic wind launching using the PLUTO code that I present in this section. I will also describe the setup of my simulations as well as the facilities I used.

2.4.1 *The* PLUTO *code*

All of the simulations I did are performed using the PLUTO code (Mignone et al., 2007) that solves the MHD equations with a conservative Godunov type scheme and a second order Runge-Kutta time stepping. This code comes with several modules and I exclusively used the MHD one for the numerical integration of the MHD set of equations. I will describe the code, starting with the finite volume method.

2.4.1.1 *Finite volume, time-stepping and Riemann problem*

The PLUTO code (Mignone et al., 2007; Mignone et al., 2011) with the MHD module is designed to integrate the MHD set of equations written in the following way

$$\partial_t \mathcal{U} = -\underline{\underline{\nabla}} \cdot \underline{\underline{\mathbf{T}}}(\mathcal{U}) + \mathbf{S}(\mathcal{U}) \ . \tag{143}$$

In this context, $\mathcal{U}$ is a state vector whose components are conserved quantities, $\underline{\underline{\mathbf{T}}}(\mathcal{U})$ is a rank 2 tensor and its rows accounts for the fluxes of the corresponding component of $\mathcal{U}$. Finally, $\mathbf{S}(\mathcal{U})$ represents the source terms. Of course, a given choice of geometry (e. g. spherical geometry) could lead to implicit additional source terms because of the curvature terms. With the MHD, one has

$$\mathcal{U} \equiv \begin{pmatrix} \rho \\ \rho\,\mathbf{u} \\ \mathbf{B} \\ E + \rho\,\phi \end{pmatrix} , \tag{144}$$

where ρ and $\mathbf{u}$ are respectively the density and the velocity of the fluid, while $\mathbf{B}$ is the magnetic field and E the total energy. In ideal MHD, one is left with eq. 113 where the curl of $\mathbf{E}$ is taken. I enforce the general form of eq. 143 using

$$\boldsymbol{\nabla} \times (\mathbf{u} \times \mathbf{B}) = \underline{\underline{\nabla}} \cdot (\mathbf{u} \otimes \mathbf{B} - \mathbf{B} \otimes \mathbf{u}) \ , \tag{145}$$

so that I have

$$\underline{\underline{\mathbf{T}}}(\mathcal{U}) = \begin{pmatrix} \rho\,\mathbf{u} \\ \rho\,\mathbf{u} \otimes \mathbf{u} + \left(P + \frac{1}{2}\mathbf{B}^2\right) \underline{\underline{\mathbf{I}}} - \mathbf{B} \otimes \mathbf{B} \\ \mathbf{u} \otimes \mathbf{B} - \mathbf{B} \otimes \mathbf{u} \\ \left(E + P + \frac{1}{2}\mathbf{B} \cdot \mathbf{B} + \rho\,\phi\right) \mathbf{u} - (\mathbf{B} \cdot \mathbf{u})\ \mathbf{B} \end{pmatrix} , \tag{146}$$

and

$$\mathbf{S}(\mathcal{U}) = \begin{pmatrix} 0 \\ -\rho\,\boldsymbol{\nabla}\phi \\ 0 \\ 0 \end{pmatrix} , \tag{147}$$

where ϕ is for example the gravitational potential of a central star. This calculation shows that the formulation of eq. 143 is definitely not hazardous and that the use of the divergence operator $\underline{\underline{\nabla}}\cdot$ is key to get a conservative form of the equations. This way of proceeding leads for any volume $\mathcal{V}$ of surface $\partial\mathcal{V}$ to the following equation

$$\partial_t \mathcal{U}_\mathcal{V} + \int_{\partial\mathcal{V}} \boldsymbol{\Phi}_f \cdot \mathrm{d}S = \mathbf{S}_\mathcal{V} \, , \tag{148}$$

where I used the theorem of Green-Ostrogradski and the subscript $X_{\mathcal{V}}$ denotes the integral over the volume $\mathcal{V}$. The $\boldsymbol{\phi}_f$ term account for the fluxes intercepted by the surface of $\mathcal{V}$, so that a discretised version of eq. 143 could capture the advection of $\boldsymbol{\mathcal{U}}$ by computing the fluxes passing through the surfaces of cells. This is the idea behind the finite volume methods that numerically solves partial differential equations on a grid of cells.

The PLUTO code functions in the following way to solve the equations. At each time step, the code starts with a reconstruction phase to build polynomial approximations of quantities based on $\boldsymbol{\mathcal{U}}_{\mathcal{V}}$ inside each cells.

The Riemann problem is then addressed with a Riemann solver that estimates the fluxes for each cells. See Toro (2009) for details on Riemann solvers in hydrodynamics. The Godunov scheme (Godunov and Bohachevsky, 1959) then consists of using these fluxes in eq. 148. The Riemann problem is inherent when piecewise reconstruction is used, since it creates discontinuities at each cell interface with its neighbours. I used the HLLD solver (Mignone, 2007) in all of my simulations.

Regarding the temporal evolution of my simulations, the code evolves $\boldsymbol{\mathcal{U}}$ with a Runge-Kunta method of order 2 (RK2). One must note that the time step δt is limited by the Courant-Friedrichs-Lewy (CFL Courant et al., 1928) condition that imposes

$$\delta t = C_{\text{CFL}} \min \left[\sum_d \left(\frac{\delta \ell^d_{\text{min}}}{|\lambda^d_{\text{max}}|} \right) \right] , \tag{149}$$

with $\delta \ell^d_{\text{min}}$ and λ^d_{max} respectively the smallest cell length and largest signal velocity in direction d and C_{CFL} is the Courant number. I refer the reader to Mignone et al. (2007) for greater details regarding the code.

2.4.1.2 *Constrained transport and non-ideal* MHD *terms*

In addition to the bundle of equations contained in eq. 143, one needs to satisfy the divergence-free condition for $\mathbf{B}$ or so call solenoidal constraint

$$\boldsymbol{\nabla} \cdot \mathbf{B} = 0 . \tag{150}$$

The fact that eq. 150 is not an evolution equation prevents from treating it like the others. Satisfying this condition is a demanding issue and many solutions were proposed (eigh-wave formalism Powell, 1997, hyperbolic divergence cleaning Dedner et al., 2002). In the finite volume framework, a way of satisfying eq. 150 at machine accuracy is to use constrained transport (Kane Yee, 1966; Evans and Hawley, 1988). The main idea of this method is to get the electromotive forces EMF (the $-\boldsymbol{\nabla} \times \mathbf{E}$ term in the induction equation) by computing $-\mathbf{E}$

on the edges of cells with the magnetic field being taken at the centre of their faces to evaluate its flux (the magnetic field is said to be staggered). The induction equation in the ideal regime is written once integrated and with the use of the Stokes theorem as

$$\partial_t \int_S \mathbf{B} \cdot d\mathcal{S} = -\int_{\partial S} \mathbf{E} \cdot d\ell \,, \tag{151}$$

so that the total magnetic flux is conserved in each cell. Note that with PLUTO, one can initialise $\mathbf{B}$ with a vector potential $\mathbf{A}$, with $\mathbf{B} = \boldsymbol{\nabla} \times \mathbf{A}$, so that the solenoidal condition is maintained.

Eq. 151 contains $\mathbf{E}$ which can be modified when ambipolar diffusion is taken into account. One needs to add $\eta_A \mathbf{J}_\perp$ in this equation to get the total modified EMF, so that it is present both in the evolution equation and in the solenoidal constraint. This diffusion gives a maximum value for the time step used to evolve the code which is $\tau_{lim} \sim \delta\ell^2_{min}/\eta_A$, so that the more diffusive the simulated disc is, the more time it will take to reach a given final state. This way of proceeding regarding ambipolar diffusion is described in Lesur et al. (2014) and has been used many times since (Béthune et al., 2017; Riols et al., 2020).

2.4.1.3 *Alternative numerical procedures*

Grid-based codes are not the only possibility to simulate MHD physics problem and I wish to mention a few alternatives (in a non-exhaustive way).

I would like to start by mentioning the possibility to solve the Boltzmann equation (see eq. 45) in the peculiar collisionless case. Explicitly adding the Lorentz force leads to the Vlasov equation, that evolves in a 7 dimensions space (3 for position, 3 for impulsion or velocity and 1 for time). This method uses a kinetic approach and is relevant to capture reconnection events for example. Rieke et al. (2015) renders a great example of a numerical scheme based on the Vlasov equation.

The previous example paves the way to say a word about particle in cell (PIC) simulations. This is also a kinetic approach with electromagnetic fields being evolve on a grid. Zeltron (Cerutti et al., 2013) is an example of code that is based on PIC method, which is a good tool to catch particles acceleration around black holes for example (Crinquand et al., 2019).

Another method that is widely used in astrophysics is the SPH one for Smoothed-Particles Hydrodynamics. This method is based on a Lagrangian approach of the fluid (while grid-based codes adopt an Eulerian one). It is particularly accurate to catch the physics when the thermal effect (such as pressure terms) are negligible. Phantom (Price

et al., 2018/ed) is a major SPH code used in astrophysics. Because of their Lagrangian nature, these codes can in particular easily capture the influence of other gravitational sources. Cavity-hosting discs with binaries and/or planets can be described using SPH, see for example Calcino et al. (2020) or Heath and Nixon (2020). The impact of the dust on the evolution of PPDs is also caught in SPH simulations (Laibe et al., 2008).

2.4.2 *Numerical set-up*

I ran both 2.5 D and 3 D simulations of cavity-hosting protoplanetary discs. In this subsection, I will give the numerical set-up I used for all the 2.5 D simulations as well as a few 3 D ones, and the procedure applied to (re)start most of the 3 D simulations from corresponding 2.5 D ones. I will explain the restart procedure in the last subsections so that all the previous ones have to do with the general set-up of the discs I simulated.

2.4.2.1 *Equation of state and cooling function*

As used throughout sec. 2.2, I assume that the plasma is well described by an ideal equation of state and approximately locally isothermal, i.e. $T \approx T_{\text{eff.}}(R)$ where $T_{\text{eff.}}$ is a prescribed radial temperature profile. This is achieved solving the total energy conservation equation contained in eq. 148 to which I add a heating/cooling function Λ defined by

$$\Lambda = \frac{P}{T}\frac{T - T_{\text{eff.}}}{\tau}\,, \tag{152}$$

where τ is the cooling time that equals 0.1 time code unit (see below) and $\Gamma = 1.0001$ is the polytropic index of the gas (that I previously named n as a general quantity). The role of Λ can be seen when calculating $\partial_t P$ which gives

$$\partial_t P + \mathbf{u}\cdot\boldsymbol{\nabla} P + \Gamma P \boldsymbol{\nabla}\cdot\mathbf{u} = \Lambda\,. \tag{153}$$

The target temperature profile is

$$T_{\text{eff.}}(R) = T_0\left(\frac{R}{R_{\text{int}}}\right)^{-1}\,, \tag{154}$$

where T_0 is the midplane temperature at the inner radius R_{int}. This choice of cooling function allows to enforce a chosen temperature profile which mimics the real radiative equilibrium, and avoid the development of the vertical shear instability (VSI, Nelson et al., 2013), which would appear in a strictly locally isothermal approximation.

Since the gas is ideal, I define an isothermal sound speed $c_s^2 \equiv P/\rho$. As I showed using the vertical hydrostatic equilibrium, c_s and Ω_K are related to the vertical disc thickness $h(R)$ through

$$h(R) = c_s(R)/\Omega_K(R)\,. \tag{155}$$

Assuming the disc is at thermal equilibrium ($T = T_{\text{eff.}}(R)$), I have $c_s \propto R^{-1/2}$ and hence the disc aspect ratio $\varepsilon \equiv h/R$ is constant. I choose T_0 in eq. 154 so that $\varepsilon = 0.1$.

2.4.2.2 *Computational domain*

I use spherical coordinates (r, θ, φ) for all the simulations. The radial direction is divided into 320 cells that expand from the inner radius $r \equiv R_{\text{int}}$ to the external one $r \equiv R_{\text{ext}}$ that are uniformly meshed on a logarithmically spaced grid. The colatitude domain is mapped on a stretched grid near the poles (from $\theta = 0$ to $\theta = 1.279$ and from $\theta = 1.862$ to $\theta = \pi$, with 72 cells in each zone) while the grid is chosen to be uniform around the midplane (from $\theta = 1.279$ to $\theta = 1.862$ with 96 cells) for a total of 240 that increases the precision in the region of interest. The disc scale height h is then covered by 16 points in the case where ε is fixed constant and equal to 0.1.

In 3 D simulations, the discs covers the azimuthal direction from $\varphi = 0$ up to 2π (full 2π simulations) with 120 cells equally spaced.

2.4.2.3 *Code units and notations*

The internal radius is $R_{\text{int}} = 1$, which sets the length code unit, and is chosen to be 1 AU while $R_{\text{ext}} = 50$. The time code unit is $\Omega_0^{-1} \equiv \Omega_K(R_{\text{int}})^{-1} = 1$ which is set to $1/2\pi$ years so that $G\,M_* = 1$ with $M_* = 1\,M_\odot$, $M_\odot$ being 1 solar mass. Therefore $\Omega_K(R) = \Omega_0\ (R/R_{\text{int}})^{-3/2} = R^{-3/2}$. I choose as a unit for the surface density $300\,\text{g}\,\text{cm}^{-2}$ and express the accretion rate in units of $M_\odot\,\text{yr}^{-1}$. I denote by "c.u." the use of code units and use the subscript X_0 to indicate that the quantity X is considered at the disc midplane ($\theta = \pi/2$) and the subscript X_p when X is a poloidal quantity.

2.4.2.4 *Dimensionless numbers and definitions*

I use the plasma parameter β (see sec. 2.2.3.1) to quantify the disc magnetisation, defined from the midplane properties of the disc as

$$\beta = \frac{8\pi P_0}{\mathbf{B}_{p,0}^2}\,. \tag{156}$$

When considering the initial state of a given simulation, I refer to the initial magnetisation inside the cavity as β_{in} and to the initial magnetisation in the external part of the disc as β_{out}. For the fiducial 2.5 D simulation, I choose $\beta_{\text{out}} = 10^4$ which leads to a realistic magnetic field in the disc. β_{in} is set equal to 1, as discussed in the introduction chapter and based on Wang and Goodman (2017). The second key parameter of this study is the strength of ambipolar diffusion, quantified with the Elsasser number, that is widely discussed in sec. 2.3.6.

Following Lesur, 2021a and Thi et al., 2019, I implement the profile of Λ_A so that

$$\Lambda_A(z, R) = \Lambda_{A,0} \exp\left(\frac{z}{\lambda h}\right)^4, \tag{157}$$

where λ is a parameter that controls the height where a transition between non-ideal and ideal MHD occurs (the non-ideal MHD part being the inside of the disc) and is chosen constant and equal to $3\,h$. $\Lambda_{A,0}$ remains a free parameter which is equal to 1 in most of my simulations and to 10 in a few of them. Additionally, a cutoff is used for the η_A profile so that if $\eta_A > \eta_{A,max}$, the value of η_A is replaced by $\eta_{A,max} \equiv 10\,\varepsilon^2$ in code units, such a choice being reflected on the Λ_A profile with eq. 128. This diffusivity cap prevents from getting a time step $\tau \sim \delta\ell^2/\eta_A$ too small.
I choose $\Lambda_A = 10$ in my 2.5D fiducial simulation based on my calculations detailed in sec. 2.3.6.

The disc refers to the whole part of the simulation that covers $r \in [1;50]$ and $z/R \in [-0.3;0.3]$. The cavity is the region where the surface density is reduced by a given factor in the innermost part of the disc (i. e. from $r = 1$ to $r = 10$ in most of the models). The external part of the disc or so called "outer disc" refers to the region where the disc is full and described by a standard protoplanetary disc (without a drop in the density profile) and which extends from $r \approx 10$ to $r = 50$. Finally, I call 'seed' the region defined by $r \leqslant 1$ of my disc, which is at play in my simulations through the inner radial boundary condition.

2.4.2.5 *Boundary conditions*

Outflow boundary conditions are used in the radial direction so that no matter can come from the inner radius. In addition, I add a wave absorbing zone for radii $r < 1.5$ which damps poloidal motions on an orbital timescale.

In the 2.5D simulations, axisymmetric conditions with respect to the polar axis are enough to handle the boundaries for the colatitude direction. With the aim of reducing the impact of the outer boundary conditions, I will focus on radii lower than 30 for most of the figure.

2.4.2.6 *Initial condition, wind and cavity*

The initial temperature profile is the effective temperature profile given in (154). The initial states for the density and the azimuthal velocity $v_\varphi = R\,\Omega_K$ mimic Nelson et al., 2013 to account for the hy-

drostatic equilibrium, while $v_r = v_\theta = 0$ initially. These profiles read, without taking into account the cavity yet

$$\rho(R,z) = \rho_0 \left(\frac{R}{R_{\rm int}}\right)^p \exp\left[\left(\frac{\Omega_K(R)\,R^3}{c_s(R)}\right)^2 \left(\frac{1}{\sqrt{R^2+z^2}} - \frac{1}{R}\right)\right], \quad (158)$$

$$v(R,z) = v_K(R)\left[(p+q)\left(\frac{c_s(R)}{\Omega_K(R)\,R^2}\right)^2 + (1+q) - \frac{q\,R}{\sqrt{R^2+z^2}}\right]^{1/2}, \quad (159)$$

with ρ_0 being the density at the internal radius. I choose $q = -1$ and $p = -3/2$ for eq. 158 and 159 which is consistent with self-similar stationary disc solutions (Jacquemin-Ide et al., 2021).

The initial vertical magnetic field follows a power law $B_z \propto R^{(p+q)/2}$ so that the plasma β parameter in the unperturbed disc is constant. To ensure that $\boldsymbol{\nabla}\cdot\mathbf{B} = 0$, I initialise the magnetic field using its vector potential $\mathbf{A}$ defined so that $\mathbf{B} = \boldsymbol{\nabla}\times\mathbf{A}$. Following Zhu and Stone, 2018, I choose

$$A_\varphi = \begin{cases} \dfrac{1}{2} B_0 R & \text{if } R \leqslant R_{\rm int} \\ B_0 \dfrac{R_{\rm int}^2}{R}\left(\dfrac{1}{2} - \dfrac{1}{m+2}\right) + R\left(\dfrac{R}{R_{\rm int}}\right)^m \dfrac{1}{(m+2)} & \text{if } R > R_{\rm int} \end{cases}, \quad (160)$$

where $m = (p+q)/2 = -5/4$. This results in a poloidal magnetic field which depends on the radius only

$$\mathbf{B} = B_0 \left(\frac{R}{R_{\rm int}}\right)^m \boldsymbol{e}_z\,. \quad (161)$$

The initial strength of the magnetic field is controlled by $\beta_{\rm out}$, so that $B_0 \propto \beta_{\rm out}^{-1/2}$.

To add a cavity and mimic a transition disc, I multiply the density profile by the function f that is given in eq. 130 with $R_0 = 10$ in most of my simulations. Note that while the density profile exhibit an inner "hole", the magnetic field distribution is kept as a power law (with eq. 161). As a consequence, the initial magnetisation $\beta(R)$ also exhibits a jump in the cavity since $P \propto \Sigma(R)$ and therefore $\beta_{\rm out}/\beta_{\rm in}$ is equal to the contrast in the gas surface density. In short, the function f creates a cavity in Σ but does not affect B_p. As a result, I simulate a transition disc with a strongly magnetised cavity ($\beta_{\rm in} = 1$) as shown in fig. 14.

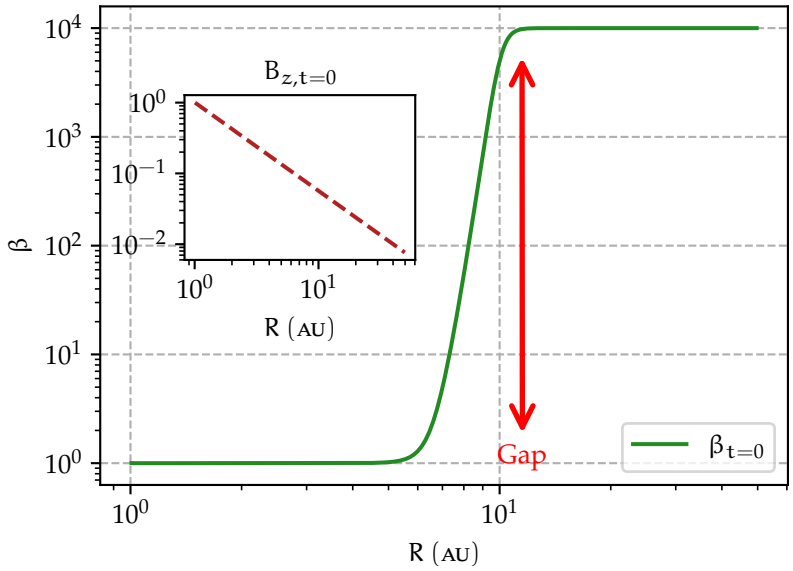

Figure 14: Initial β plasma parameter for my simulations with the initial profile of the vertical magnetic field. The magnetisation exhibits a cavity similar to the one of the density profile.

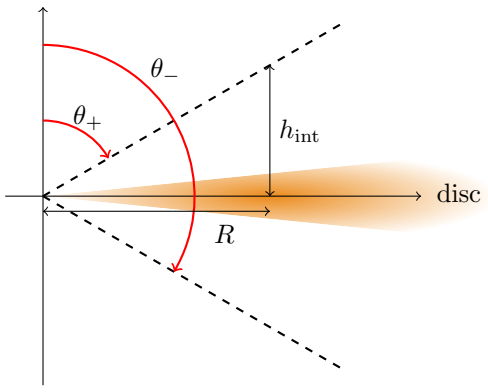

Figure 15: Schematic view of the disc which is represented in orange. $\theta_\pm$ define the vertical integration surface and $h_{\rm int}$ is the integration scale height at a given radius R.

2.4.3 *Integration and averages*

Several integrations and averages are used throughout this work. In this manuscript, I use the following proxy for the vertical integration along θ

$$\overline{X}(r,t) = r \int_{\theta_+}^{\theta_-} X(\mathbf{r},t) \sin\theta \, d\theta \,. \tag{162}$$

$\theta_\pm$ quantify the integration height as shown in fig. 15 so that

$$\frac{\theta_- - \theta_+}{2} = \arctan\left(\frac{h_{int}}{R}\right) = \arctan \varepsilon_{int} \,, \tag{163}$$

with h_{int} the integration height at radius R given by an integration effective aspect ratio $\varepsilon_{int} \equiv h_{int}/R$. Note that this integration "height" is not necessarily the disc thickness h. For 3 D simulations, I add an azimuthal average defined as

$$\langle X(r,\theta,t)\rangle_\varphi = \frac{1}{2\pi} \int_0^{2\pi} X(\mathbf{r},t) \, d\varphi \,, \tag{164}$$

and I will assume that this azimuthal average is contained in the definition of $\bar{\cdot}$ for 3 D simulations only. I introduce $\overline{\beta}$ as

$$\overline{\beta} \equiv \frac{8\pi \Sigma \overline{c}_{s,0}^2}{\sqrt{2\pi} R \varepsilon \left(\overline{B_r}^2 + \overline{B_\theta}^2\right)} \,, \tag{165}$$

Because of the axisymmetry of the 2.5 D simulations, the $\bar{\cdot}$ procedure is indeed the same for all the simulations.

which corresponds to a theta-averaged "effective" midplane β plasma parameter. It is defined so that it matches the midplane β parameter in a hydrostatic isothermal disc. This more general definition is needed when the disc midplane is displaced vertically such as inside the cavity.

Finally, I add the time-average defined by

$$\langle X(\mathbf{r})\rangle = \frac{1}{T} \int_{t_0}^{t_0+T} X(\mathbf{r},t) \, dt. \tag{166}$$

I run the 2.5 D simulations so that they reach 1000 orbits at $R = 10$ which means $\approx$ 31000 orbits at R_{int}. The 3 D simulations are run for 1000 orbits at R_{int} in order to check the stability of the cavity. If not specified, time-averages are calculated taking into account the whole simulation without the first 4000 orbits at R_{int} to suppress the transient state. Otherwise, I indicate our choice of notation when needed $\langle X\rangle_{1000}$ being the time-averaged value of X during the last 1000 orbits at R_{int} for example.

2.4.4 *Restarted 3 D simulations*

The 3 D simulations are built on the 2.5 D ones, once a steady state has been reached. All the fields from the 2.5 D (r, θ) files are interpolated on a 3 D (r, θ, φ) grid (with respect to centred and staggered

Figure 16: Logo of the mesocentre GRICAD.

Figure 17: Logo of GENCI.

variables) so that each field (scalars or components of vectors) are axially symmetrical. A random perturbation is then added to the 3 velocity components with a white noise proportional to 10% of the local sound speed.

2.4.5 *Table of* 2.5 D *and* 3 D *simulations*

All the simulations performed are listed in tab. 1. The characteristic parameters are the external initial plasma parameter β_{out}, the internal initial plasma parameter β_{in} and the initial ambipolar Elsasser number $\Lambda_{A,0}$. I do not list here the 'control' runs that I did to check some numerical (e. g. spatial resolution) or physical (e. g. size of the cavity) effects. I leave them to the app. B and C.

2.4.6 *Facilities*

During my thesis, I used different facilities regarding the kind of simulations I wanted to work on (2.5 D or 3 D).

With the mesocenter GRICAD, I had access to the machine Dahu on which I run the equivalent of $\sim 3-4\times10^6$ CPU hours for my 2.5 D simulations. For each simulation, I used from 1 to 4 nodes, each node having 32 cores.

The 3 D simulations cost much more CPU time so that I needed the HPC resources of a national centre to run them. I ran my 3 D simulations on the AMD Rome machine of TGCC, part of GENCI. Each 3 D simulation used either 2304 or 4608 cores. I had to write annual report to get access to this machine on which I consumed $\sim 25\times10^6$ CPU hours.
While using this machines, I had the opportunity to give a talk about my work at the JCAD day in december 2021.

Name	β_{out}	β_{in}	$\Lambda_{A,0}$
S2DB4BinoAmo	10^4	1	1
Initial external magnetisation			
S2DB3BinoAmo	10^3	1	1
S2DB5BinoAmo	10^5	1	1
Initial ambipolar Elsasser number			
S2DB4BinoAm1	10^4	1	10
Initial inner magnetisation for each tested value of β_{out}			
S2DB4Bin1Amo	10^4	10	1
S2DB4Bin2Amo	10^4	10^2	1
S2DB4Bin3Amo	10^4	10^3	1
S2DB5Bin1Amo	10^5	10	1
S2DB5Bin2Amo	10^5	10^2	1
S2DB5Bin3Amo	10^5	10^3	1
S2DB5Bin4Amo	10^5	10^4	1
S2DB3Bin1Amo	10^3	10^1	1
S2DB3Bin2Amo	10^3	10^2	1
S3DB4BinoAmo	10^4	1	1
Initial external magnetisation			
S3DB3BinoAmo	10^3	1	1
S3DB5BinoAmo	10^5	1	1
Initial ambipolar Elsasser number			
S3DB4BinoAm1	10^4	1	10
Initial inner magnetisation			
S3DB4Bin1Amo	10^4	10	1
S3DB4Bin2Amo	10^4	10^2	1
S3DB4Bin3Amo	10^4	10^3	1

Table 1: Simulations information. 'S2D' refers to a 2.5 D simulation while 'S3D' indicates a 3 D one. The fiducial simulations (S2DB4BinoAmo and S3DB4BinoAmo) are shown in bold font. S2DB4BinoAm1 quantifies the influence of $\Lambda_{A,0}$ while S2DB5BinoAmo and S2DB3BinoAmo are the reference runs for $\beta_{out} = 10^5$ and $\beta_{out} = 10^3$. All the runs with Bin $\neq 0$ in their label explore the role of the initial value of β at R_{int}.

CONCLUSION

In this chapter, I showed that given the observational information available on protoplanetary discs, the most relevant physics framework is magnetohydrodynamics. In particular and because they are cold and poorly ionised, protoplanetary discs are well described by non-ideal MHD.
I stressed that the ambipolar process is the dominant non-ideal process in the outer parts of PPDs, both for full and transition protoplanetary discs.

I calculated the ambipolar Elsasser number in TDs, given some radial profiles to account for a few ionising processes in PPDs. I estimated this number inside the cavity of TDs and showed that the influence of the cavity on the effect of ambipolar diffusion is modest. Therefore, I can model this non-ideal process for TDs the same way it is implemented for simulations of full PPDs.

Given this theoretical frame, I described the numerical code I used to simulate discs (the PLUTO code) and the facilities I had access to.

CONCLUSION

Dans ce chapitre, j'ai décrit le cadre de travail usuel pour étudier les disque protoplanétaires. Considérant les observations disponibles pour de tels objets astrophysiques, la magnétohydrodynamique s'avère être le modèle le plus adéquat pour capturer toute la physique en jeu dans leur évolution.
Plus particulièrement, les disques protoplanétaires sont froid et peu ionisés si bien que la magnétohydrodynamique non idéale doit être utilisée. J'ai rappelé les différentes équations régissant la dynamique d'un disque dans ce cadre de travail. J'ai également mis en lumière l'influence de la diffusion ambipolaire, dont les effets sont contrôlés par le nombre d'Elsasser ambipolaire.
Je souligne par ailleurs le rôle dominant que joue la diffusion ambipolaire par rapport aux effets non idéaux dans les parties externes des disques protoplanétaires.

À ce stade, il était alors nécessaire d'estimer l'impact de cet effet non idéal à l'intérieur de la cavtié d'un disque de transition. J'ai réalisé un tel travail en me basant sur des profils radiaux simples des principaux processus d'ionisation dans les disques protoplanétaires. J'ai ainsi montré que l'influence de la cavité est faible, et qu'il est de fait possible de modéliser le nombre d'Elsasser ambipolaire dans un disque de transition de la même façon qu'on le ferait pour un disque protoplanétaire plein.
Fort de ce premier résultat, j'ai pu ensuite détailler le modèle numérique que j'ai utilisé pour effectuer mes simulations numériques en présentant notamment leur initialisation.

Finalement, j'ai présenté le code que j'ai utilisé (le code PLUTO), ainsi que les infrastructures de calculs auxquelles j'ai eu accès pendant ma thèse.

Part II

NUMERICAL SIMULATIONS AND RESULTS

The second part of this manuscript focuses on my numerical results. I present the results I get from my 2.5 D simulations before moving to my 3 D ones.

3

2.5 D SIMULATIONS: THE STRUCTURE OF TRANSITION DISCS

"C'est par un mécanisme de désastres,
Un engrenage au volant faussé,
Que je traverse, entre des visions de potences,
Un jardin où flottent des fleurs sans tiges."

— Fernando Pessoa, *Opium à bord* (1914)

INTRODUCTION

The work I did during my thesis is based on numerical simulations of transition discs with magnetic winds. This chapter is devoted to the study of 2.5 D numerical simulations whose the main objective is to characterise the cavity of such TDs.
In particular such simulations make feasible the study of the long-term evolution of these discs especially regarding the stability of the underlying model.

I will start by presenting the results of my fiducial simulation so that I can give the most salient results before exploring the parameter space.
I focus on the time-averaged disc structure to describe the cavity. The secular evolution of the disc relies on the accretion theory. I detail this theory and define the accretion rate accordingly.
I also describe the magnetic wind through its invariants.

The temporal evolution of the disc occurs on short and long time-scales.
I link the slow evolution of the disc to the magnetic field transport in the disc and to the evolution of the transport coefficients. I focus on the fast variability of the cavity and check the possibility to have an instability triggered in the disc.

Eventually, I describe a few additional simulations with different ambipolar Elsasser numbers and different magnetisations.

The results presented in this chapter are published in Martel and Lesur (2022) that can be found in App. D.

INTRODUCTION

Mon travail de thèse se base sur des simulations de disques de transition munis de vents magnétiques. Ce chapitre est consacré aux simulations 2,5 D que j'ai réalisées et dont l'objectif premier est de caractériser la cavité interne et d'étudier sa persistence au cours du temps.

J'initialise les simulations correspondantes avec la procédure décrite dans le chapitre précédent, dans lequel je détaille les différents nombres adimensionnés contrôlant la physique de mon problème. Les simulations 2,5 D sont particulièrement adaptées à un travail portant sur la persistence d'une structure telle que la cavité. Pour un coût réduit, elles permettent de simuler les disques sur de longues périodes de temps, ce qui permet d'atteindre un état (quasi-) stationnaire et d'émettre des diagnostics robustes concernant le disque.

Je décrirai en détails la simulation fiduciaire avant de laisser la place à une exploration de l'espace des paramètres. La simulation de référence permettra d'avoir une comparaison pour le reste de mon travail (simulations 3 D et perspectives), tout en établissant des résultats importants.

Pour la simulation de référence, je débute avec une étude générale de la structure du disque. Je m'attarde sur l'évolution de la densité de surface avant de présenter tout un jeu de profils moyennés temporellement. J'établis ainsi la structure du disque (lignes de champ magnétiques, flux de moment cinétique), ce qui me permets de caractériser plusieurs sous-suctrures pertinentes, notamment une boucle de champ magnétique poloidal située au niveau de la jonction entre la cavité et le disque plein.
En ce qui concerne l'évolution séculaire du disque, je me base sur la théorie de l'accrétion. Je définis en particulier le taux d'accrétion et plusieurs coefficients de transport.
Je propose également une description du vent magnétique, en calculant les invariants MHD associés au vent pour différentes lignes de champ (émises depuis la cavité ou depuis le disque plein).

Je constate deux formes d'évolution du disque, une rapide (sur quelques orbites au bord interne) et une lente (sur plusieurs milliers d'orbites au bord interne). L'évolution lente est liée au transport du champ magnétique dans le disque ainsi qu'aux différents coefficients de transport calculés dans le cadre de la théorie de l'accrétion. C'est dans le cadre de cette évolution lente que j'interprète le lent élargissement de la cavité au cours du temps.

Pour ce qui est de l'évolution rapide, je me focalise sur la cavité et sur la possibilité que cette dernière soit sujette à des instabilités. En particulier, je décris l'apparition de bulles de gaz qui traversent la cavité de manière erratique.

Enfin, je présenterai une rapide exploration des paramètres, notamment en étudiant l'influence du nombre d'Elsasser ambipolaire et de la magnétisation imposés initialement. Cette section permet d'établir certains résultats et de dégager une structure générale pour les disque de transition que je simule.

J'enchaînerai ensuite avec quelques remarques de conclusion, en me focalisant notamment sur l'élargissement de la cavité.
Je lierai par ailleurs le modèle de disques de transition que j'utilise et à un modèle de disques d'accrétion employé dans le contexte de l'accrétion autour des trous noirs. Il s'agit du modèle des "magnetically arrested discs" (MAD). Ce modèle prédit des disques d'accrétion avec une zone interne rencontrant un fort support magnétique, s'opposant à la gravité.
Si ce modèle concerne la plupart du temps des disques étudiés dans le cadre de la magnétohydrodynamique relativiste, je montre qu'il est pertinent d'y faire référence dans mon cadre de travail.

Les résultats présentés dans ce chapitre font partie de Martel and Lesur (2022) que le lecteur pourra retrouver dans l'appendice App. D.

3.1 FIDUCIAL SIMULATION

This section is devoted to the general description of my model with the fiducial simulations, characterised by $\beta_{out} = 10^4$, $\beta_{in} = 1$, $\Lambda_A = 1$ and $R_0 = 10$. The justification for these values is given in the previous chapter, together with the description of the initial state. I wish to give the main achievements reached by this model.

3.1.1 *General overview of the disc evolution*

I start by describing the general evolution of the disc, with the spatio-temporal diagrams of both the surface density and the plasma parameter given in fig. 18. There is an initial transient state that lasts up until ~ 4000 orbits at R_{int}, after which Σ and $\overline{\beta}$ reach a quasi-stationary state.
The cavity is *stable* in the sense that on long time scales (of the order of 10^{3-4} orbits at R_{int}) the disc is in a quasi-stationary state. This state is characterised by a persistent cavity that widens slowly with time. For a more quantitative insight, I define the cavity location as the radius where the surface density equals half of its maximum value. This location is subject to a variation of $\Delta R/R = 10.3\%$ over the duration of the simulation. For now, I want to stress that this very first result is a compelling one, because it demonstrates that a cavity can survive with time. I will come back to this result later in sec. 3.1.5.1.
Two regions are observed in the disc, the cavity and the external disc. The latter exhibits a relatively smooth structure with respect to time while the cavity is striped by fast temporal variability (see the profile of Σ in the top panel of fig. 18) suggesting a fast accretion on the central star. I study in depth these stripes in sec. 3.1.5.3.

A small amount of material seems to accumulate close to the star (at $R \leqslant 1.5$). Due to its proximity with the inner boundary condition, I come back to this observation in the appendix chap. C.

The plasma parameter depicted in the bottom panel of fig. 18 overall shares the same spatio-temporal structure as Σ. In particular, the striped pattern in the cavity as well as the accumulation close to the inner boundary condition are also detected. The cavity is characterised by $\overline{\beta} \sim 1$ with some excursions down to 10^{-2}. The external disc has a typical value of $\overline{\beta} \sim 10^4$ that matches the initial one. The outer edge of the cavity varies around its initial value of 10 AU in the profile of $\overline{\beta}$.

Note that I use a different definition of β here, as detailed in chapter 2.

3.1.2 *Disc structure*

In this subsection, I describe the disc structure with time-averaged profiles in the poloidal plane of the disc. The profiles are time-averaged

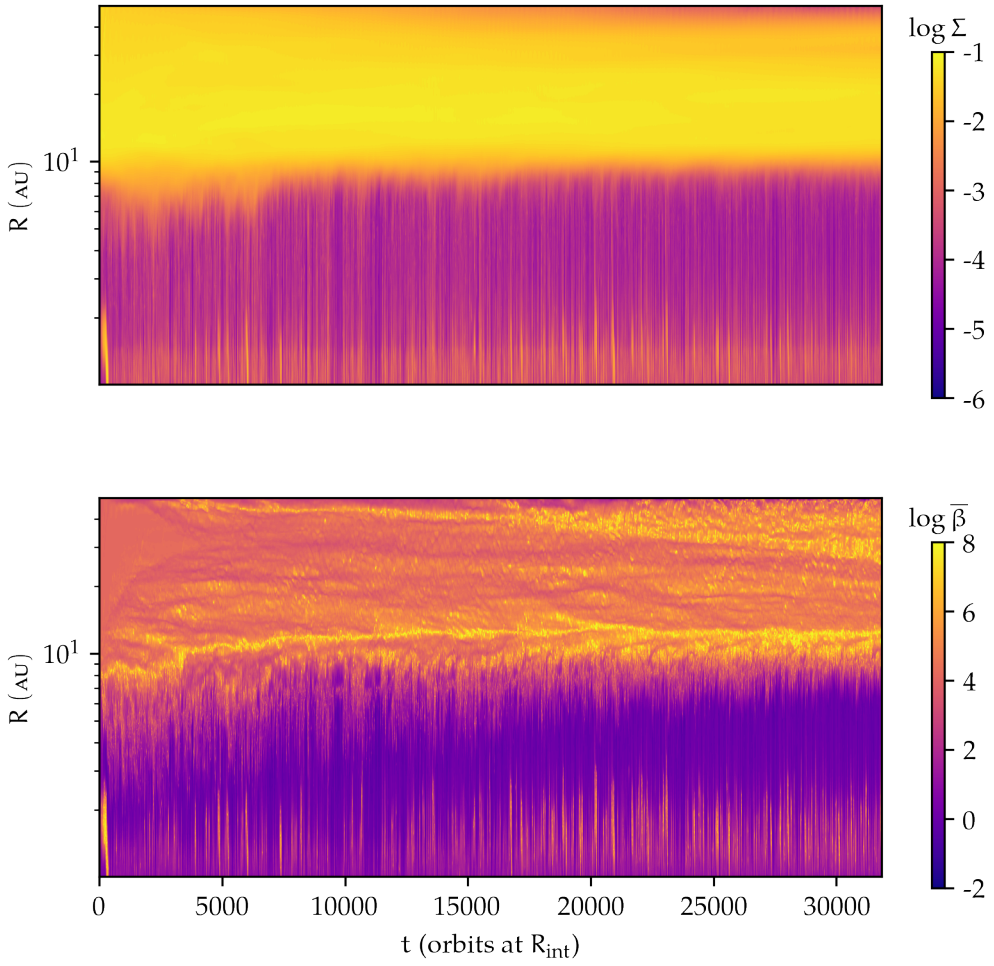

Figure 18: spatio-temporal diagrams of the surface density Σ (top panel) and of the plasma beta parameter $\overline{\beta}$ (bottom panel) for the fiducial simulation. The cavity remains during the entire simulation and keeps a relatively strong magnetisation with $\overline{\beta} \sim 1$.

on the whole simulation minus the transient state (I drop the first 4000 orbits of my simulations).

3.1.2.1 *Magnetic structure*

I start with the magnetic field structure of the disc that is shown in fig. 19. The back field is the toroidal magnetic field whose general trend is as follows. $\langle B_\varphi \rangle$ is negative above the disc and positive below. Such a structure echoes the magnetic wind launching mechanism described in chapter 1. The poloidal magnetic field lines are pinched at the midplane inside the cavity but remain vertical in the external part of the disc. These two behaviours define two distinct regions in the disc, separated by a transition zone located at the cavity edge.

This peculiar transition zone exhibits a poloidal magnetic loop inside which the polarity of the azimuthal component is reversed (with $\langle B_\varphi \rangle > 0$ in the upper hemisphere and close to the disc). The poloidal field lines surrounding the loop are characterised by an elbow-shaped structure, with significant changes of direction at $h_{\rm int}/R \approx \pm 0.3$, ± 0.6 and $\pm 0,9$ (see the straight lines in fig. 19).

3.1.2.2 *Velocity stream lines*

Fig. 20 shows the time-averaged density $\langle \rho \rangle$ over which are plotted the poloidal streamlines. This figures focuses on the cavity region and only extends up to $R = 15$ AU. The full part of the disc is clearly visible around the midplane for $R \gtrsim 10$ AU and the drop in density characterises the cavity for $R \lesssim 10$ AU.

The poloidal streamlines leaving the cavity are indicative of a wind emitted from this region. In particular, fig. 19 and 20 show that $\langle \mathbf{B}_p \rangle$ and $\langle \boldsymbol{v}_p \rangle$ are approximately collinear one with each other, as expected from ideal MHD. The previous elbow-like pattern is also observed and a closer inspection of the streamlines reveals that close to the transition zone at $R \gtrsim 8$ AU, matter is indeed falling into the cavity.

This falling material flow is fuelled by matter coming from the outer disc that follows the elbow pattern. Such matter is originally ejected from this disc, before being deflected and accreted into the cavity, hence generating the elbow-like structure. The resulting accretion stream then stays localised close to the cavity midplane down to the inner radius of the simulation. On the contrary, the motion of the gas in the outer disc is not as well organised, though it is approximately symmetric with respect to the midplane.

3.1.2.3 *Angular momentum flux stream lines*

In order to deeper the analysis of the structure of the disc, I study time-averaged angular momentum flux, defined by

$$\mathcal{L}_p = r \sin\theta \langle \rho \mathbf{u}_p u_\varphi \rangle - r \sin\theta \langle \mathbf{B}_p B_\varphi \rangle . \tag{167}$$

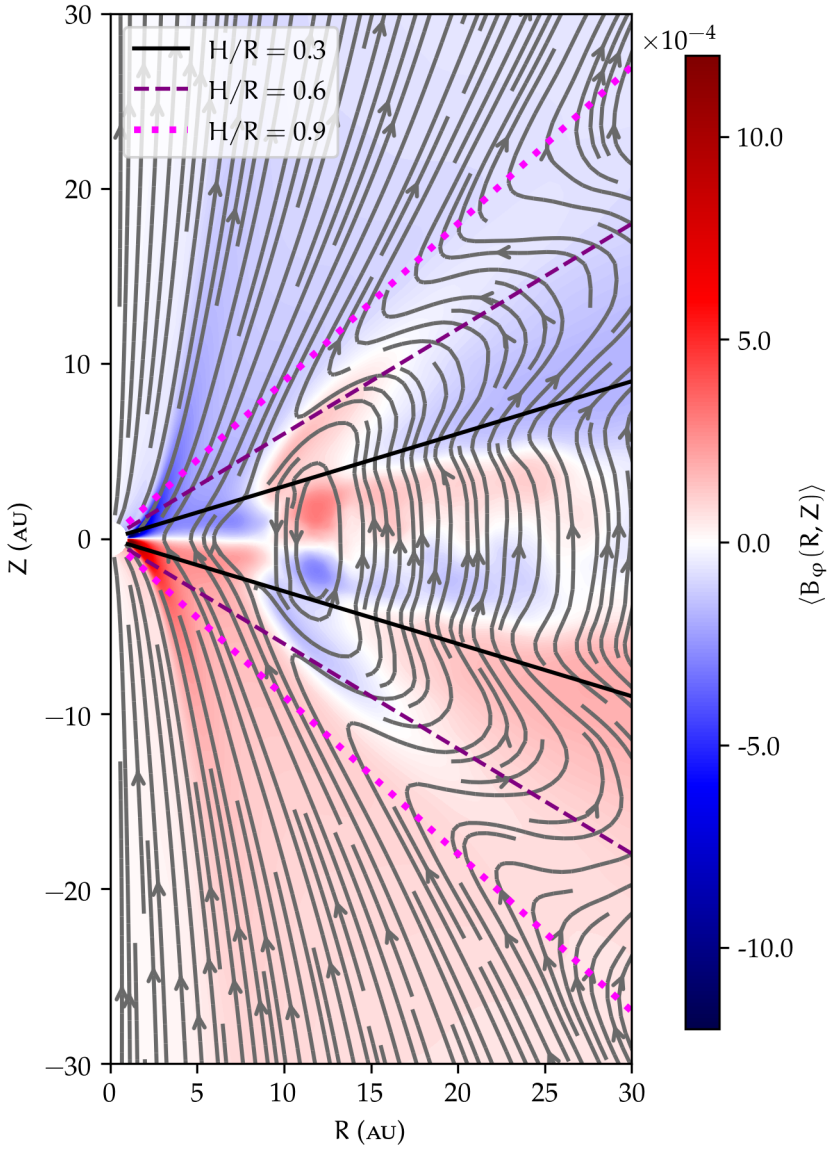

Figure 19: Time-averaged poloidal magnetic field lines and toroidal magnetic field $\langle B_\varphi \rangle$ for the fiducial simulation. Note the peculiar field topology close to the truncation radius.

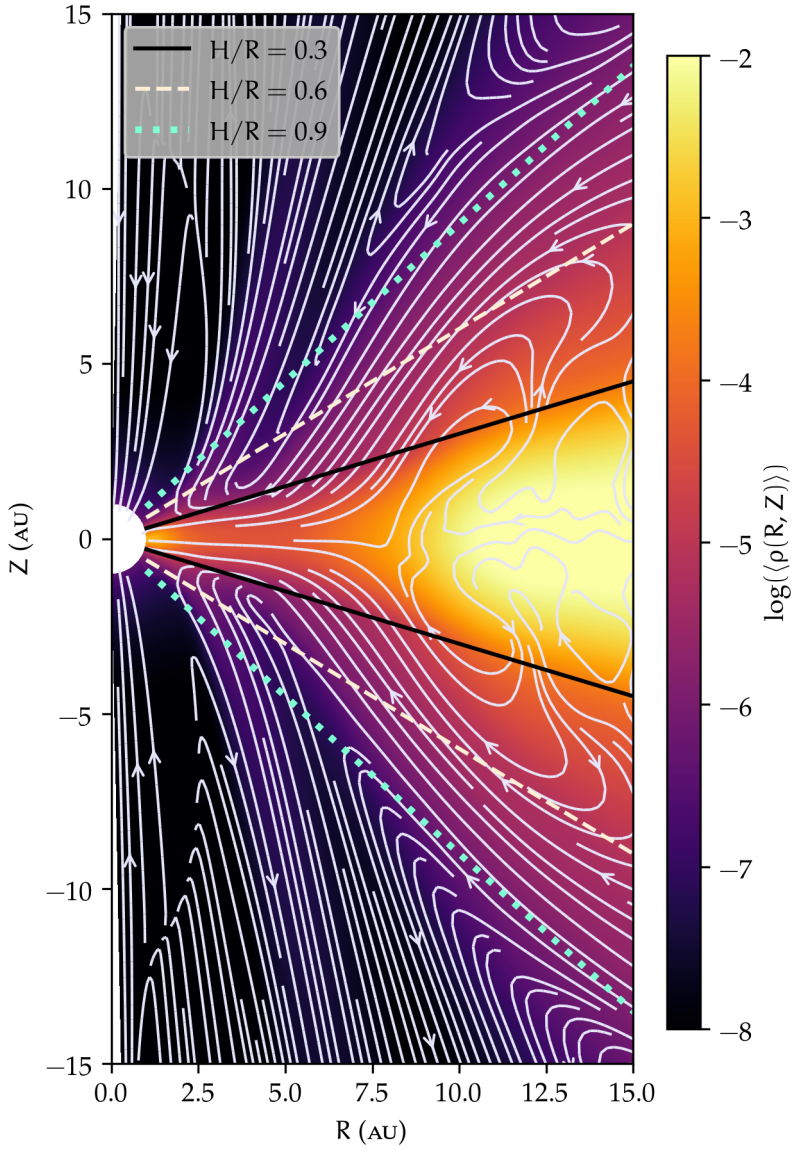

Figure 20: Time-averaged stream lines and density for the fiducial simulation with a focus on the cavity area. Note the peculiar shape of the streamlines around the transition radius.

The corresponding flux lines are shown in fig. 21. They reveal that angular momentum is extracted from the disc midplane and carried away both radially and vertically in a relatively homogeneous fashion, symmetric with respect to the midplane. In particular, no elbow-like structure is detected for the angular momentum flux. This indicates that the cavity + outer disc system has adapted its magnetic topology to transport angular momentum homogeneously, and that the magnetic loop is part of this adaptation.

3.1.2.4 *Gaps in the profile of Σ and β*

Gaps are detected in the external disc, both in the spatio temporal diagrams of Σ and $\overline{\beta}$ (see fig. 18). Such structures are detected in all of my simulations (see sec. 3.2.1.1). Back to the fiducial simulation, two gaps are seen after the cavity edge and before $R = 30$. I show the time-averaged profiles of Σ and $\overline{B}_z$ at the midplane in fig. 22. These profiles are averaged over the last 1000 orbits of the simulation for better visibility and to avoid any long-term variation of the gaps. I find that the local surface density drops by $\sim 5\,\%$ at the gaps location. In addition, their location is characterised by a sharp increase of the vertical magnetic field intensity. In short, the gaps surface density is anti-correlated with the vertical magnetic field, which matches the secular wind instability described by Riols et al. (2020).

3.1.3 *Accretion theory*

The study of the general poloidal structure of the disc states in particular that accretion is occurring inside the cavity. To address this key point quantitatively, I focus in this subsection on the theory of accretion in protoplanetary discs, in order to extract information on the accretion rate and speed. I start with the definition of the accretion rate before focusing on the conservation equations (of mass and angular momentum).

3.1.3.1 *Accretion rate and speed*

I define the accretion rate $\dot{M}$ as

$$\dot{M}(R,t) \equiv -2\pi R \overline{\rho v_r}\,. \tag{168}$$

The use of the average procedure $\bar{\cdot}$ implies that I have to choose a specific height over which ρv_r is integrated, as explained in chapter 2 and controlled by the parameter $\varepsilon_{\rm int} \equiv \tan\left[(\theta_+ - \theta_-)/2\right]$. Due to the elbow-shaped pattern in the streamlines profile, the integration height has a direct influence on $\dot{M}$. Figure 23 gives the radial and time-averaged profile of $\dot{M}$ for 3 different integration thickness. As

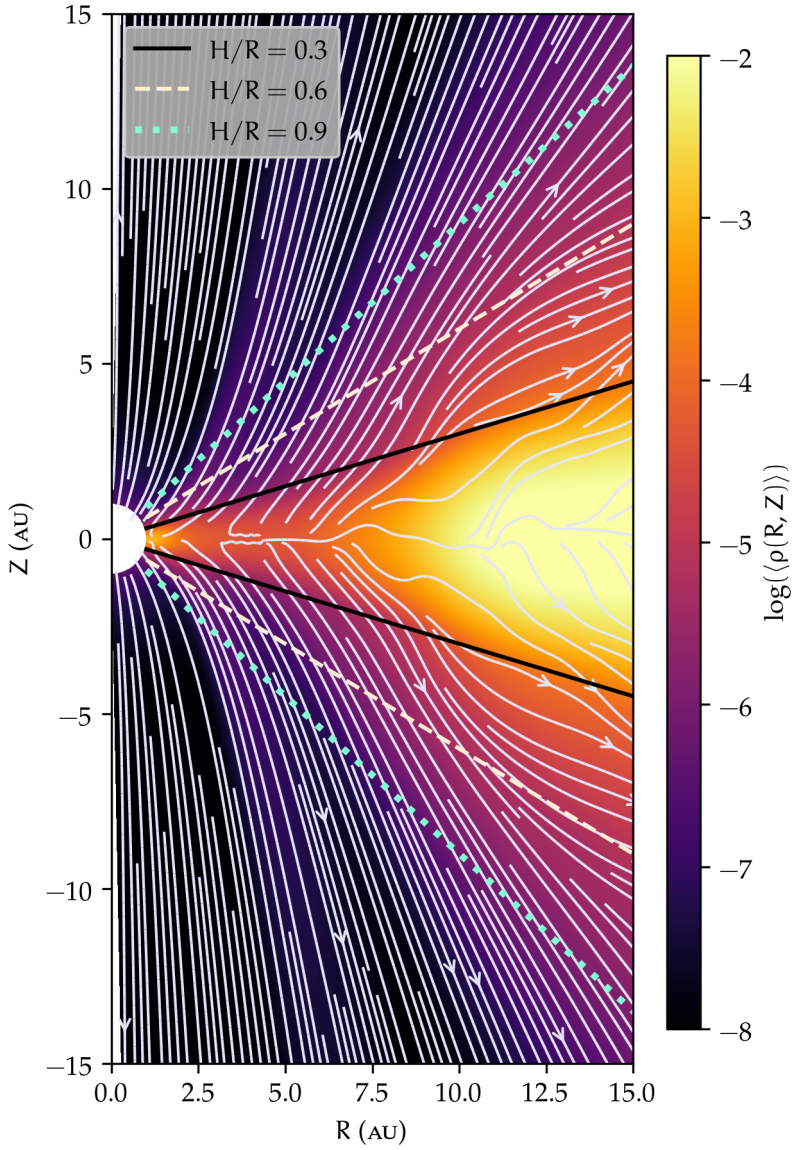

Figure 21: Time-averaged angular momentum flux stream lines over time-averaged density for the fiducial simulation. Angular momentum leaves the disc midplane because of the wind.

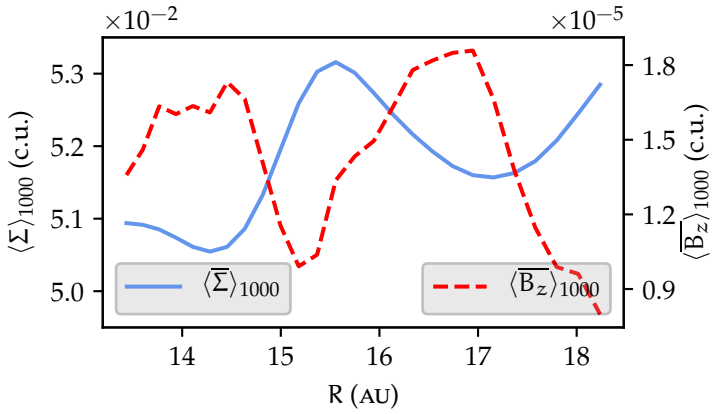

Figure 22: Time-averaged profiles of Σ and $\overline{B}_z$ on the last 1000 orbits at R_{int}. The horizontal axis is the radius and I focus on the area between $R = 12$—18 AU. Both profiles are given in code units.

expected, $\langle \dot{M} \rangle$ reaches negative values at $R \approx 10$ for low integration height. This is due to the matter leaving the disc at the foot of the elbow pattern. Such an effect is cancelled out for higher integration heights. Moving to $\varepsilon_{int} = 0.6$ and 0.9, the accretion rate reaches constant values inside the cavity and in the outer disc. The two regions match by less than 50 % despite a jump of four orders of magnitude in Σ. A striking conclusion is that the accreted material effectively 'jumps' above the transition radius, and that a steady state is reached with the whole system (cavity + outer disc) accreting at a constant rate. In particular, the accretion rate inside the cavity ($\dot{M}_{TD}$) reads

I give the accretion rate in $M_\odot\,yr^{-1}$. To do so I use the set of units detailed in the previous chapter.

$$\dot{M}_{TD} = 1.4 \pm 0.2 \times 10^{-7}\ M_\odot\,yr^{-1}\,, \tag{169}$$

so that this model of transition disc creates strongly accreting transition discs.

The accretion rate being almost constant while the surface density decreases by two orders of magnitude implies that the accretion speed should increase dramatically. This characteristic speed is defined by

$$\langle v_{acc.} \rangle \equiv \frac{\langle \dot{M} \rangle}{2\pi R \langle \Sigma \rangle}\,, \tag{170}$$

and shown in fig. 24 for $\varepsilon_{int} = 0.9$. Fig. 24 confirms the previous statement as $\langle v_{acc.} \rangle$ exhibits a well-defined transition between subsonic accretion outside the cavity with $\langle v_{acc.} \rangle \sim 10^{-3} \langle c_s \rangle$ and transsonic accretion inside with $\langle v_{acc.} \rangle \sim \langle c_s \rangle$.

3.1.3.2 *Governing equations for accretion*

Now that I have introduced the accretion rate as a characteristic quantity of a protoplanetary disc, I aim to bring a more general picture of the accretion theory, understood as the secular evolution of $\dot{M}$ and

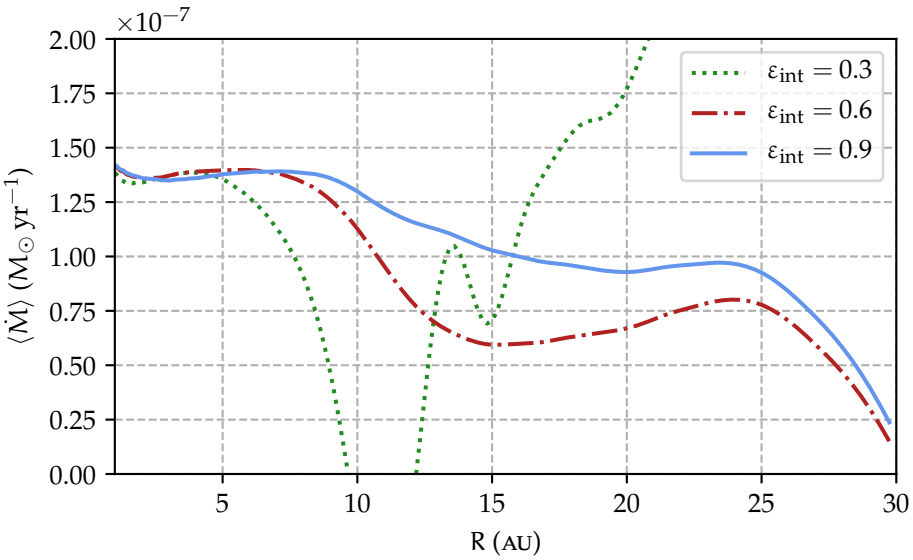

Figure 23: Accretion rate for different integration heights with respect to the radius. The higher ρv_r is integrated the closer to a constant value $\dot{M}$ is in the cavity. The average value inside the cavity (from $R = 1$ to $R = 10$) is $\dot{M} = 1.4 \pm 0.2 \times 10^{-7}\ M_\odot\ \mathrm{yrs}^{-1}$.

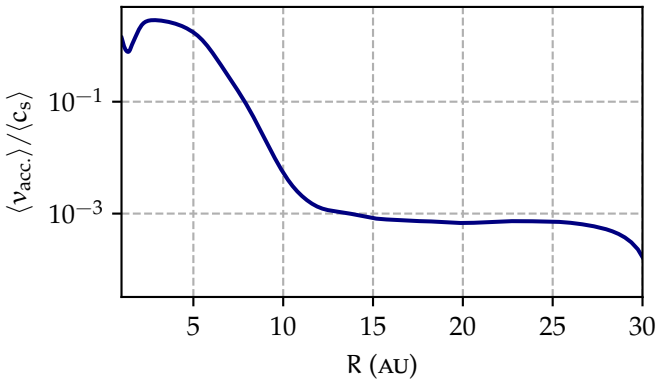

Figure 24: Accretion speed for $\varepsilon_{int} = 0.9$ in units of local sound speed c_s. The profile exhibits a clear transition between subsonic and transsonic accretion that occurs at the cavity edge.

Σ. When dealing with MHD processes, one needs an additional equation related to the vertical magnetic field threading the disc B_z and accounting for the magnetic field transport in the disc. Under the $\bar{\cdot}$ integration procedures, the mass and angular momentum conservation equations respectively read

$$\partial_t \Sigma - \frac{1}{2\pi r}\partial_r \dot{M} = -\left[\sin\theta\, \rho v_\theta\right]_{\theta_+}^{\theta_-} , \quad (171)$$

$$\partial_t \left(\overline{r \sin\theta\, \rho v_\varphi}\right) - \frac{1}{2\pi r}\dot{M}\,\partial_r\left(r^2 \sin^2\theta\, \tilde{\Omega}(r)\right) = -\frac{1}{r}\partial_r\left(r^2 W_{r\varphi}\right) - W_{\theta\varphi} , \quad (172)$$

where $W_{r\varphi}$ and $W_{\theta\varphi}$ are respectively the radial and surface stresses whose definitions are provided by

$$\begin{cases} W_{r\varphi} \equiv \overline{\rho \sin\theta\, v_r\, v_\varphi} - \overline{\sin\theta\, \frac{B_r\, B_\varphi}{4\pi}} \\ W_{\theta\varphi} \equiv \left[r \sin^2\theta \left(\rho\, v_\theta\, v_\varphi - \frac{B_\theta\, B_\varphi}{4\pi} \right) \right]_{\theta_+}^{\theta_-} \end{cases} . \quad (173)$$

The peculiar expression of the velocity deviation $\boldsymbol{v}$ is at play here and rules out any additional surface terms in eq. 172.

The vertical magnetic flux conservation equation is given by

$$\partial_t B_{\theta,0} = \frac{1}{r}\,\partial_r\left(r\,\mathcal{E}_{\varphi,0}\right) , \quad (174)$$

and takes into account the effects the magnetic wind.

3.1.3.3 *Mass conservation and mass loss rate parameter*

This subsection focuses on the conservation of mass given by eq. 171 whose contributions are plotted in fig. 25 (time-averaged and with $\varepsilon_{\rm int} = 0.9$). First of all, the cavity reaches a steady state up until $R \lesssim 8$ AU since the time derivative of the surface density is constant and equal to zero. The edge of the cavity ($R \sim 10$) is however characterized by $\partial_t \Sigma < 0$ which is to be linked to the slow expansion of the cavity with time, as discussed later in sec. 3.1.5.1. More specifically, fig. 25 shows that the negative values of $\langle \partial_t \Sigma \rangle$ at $R = 10$ AU are compensated by the divergence of $\dot{M}$. Therefore, the widening of cavity is like an erosion process due to the radial variation of the accretion rate.

In the prospect of comparing the results of my simulations to the previous one of Lesur (2021a), I use $\varepsilon_{\rm int} = 0.6$ for any calculation related to ζ. However, I will go back to $\varepsilon_{\rm int} = 0.9$ for the other transport coefficients.

The magnetic wind mostly acts on the disc for radii $R \lesssim 5$ AU. Such contribution is fully compensated by the radial derivative of the accretion rate (since the cavity reaches a steady state). The change of sign of the "wind" mass flux (which is negative at the cavity edge location) is reminiscent of the elbow-shaped pattern of the flow in the poloidal streamlines profile as previously discussed.

I construct the mass loss rate parameter ζ that accounts for the effects of the wind. This choice of parametrisation is analogous to the one in Lesur (2021a). ζ is defined as $\zeta = \zeta_+ + \zeta_-$ with

$$\langle \zeta_\pm \rangle \equiv \pm \frac{\langle \rho v_z \rangle(\theta_\pm)}{\langle \Sigma \rangle\, \Omega_K} = \pm \frac{\langle \rho v_r \cos\theta \rangle - \langle \rho v_\theta \sin\theta \rangle}{\langle \Sigma \rangle\, \Omega_K} , \quad (175)$$

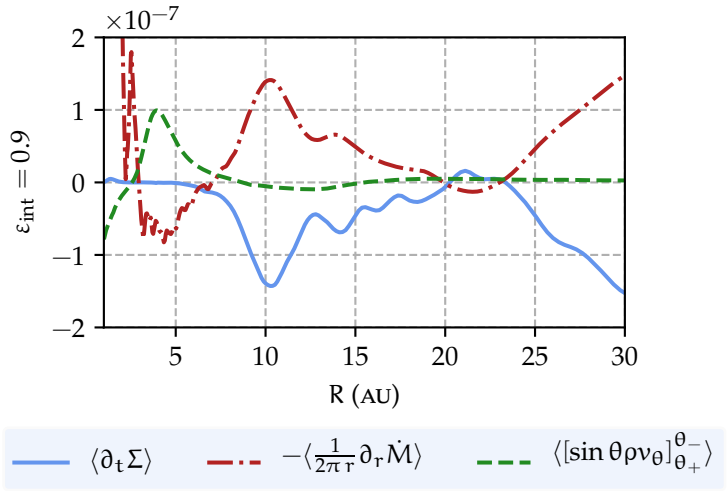

Figure 25: Mass conservation for $\varepsilon_{\rm int} = 0.9$. The three lines do not add up exactly to zero because I use a moving average for better visibility (on 10 cells) and the quantities are time-averaged on a sample selection of output files that do not contain all the time steps computed by the code.

where the corresponding quantities are time-averaged. The $\pm$ sign is chosen accordingly so that $\zeta_\pm$ being positive implies that matter leaves the disc at the surface defined by $\theta_\pm$. ζ_+ and ζ_- share a similar behaviour, so that I focus on ζ only that catches all the flux of matter leaving the disc at its surface. The corresponding time-averaged profile can be found in fig. 26. I evaluate $\langle\zeta_\pm\rangle$ with $\varepsilon_{\rm int} = 0.6$ which corresponds to an integration height $z_0 = 6\,h$ so that I compare my results with predictions from self-similar models.

I find that the mass loss rate parameter is roughly constant and equal to 6.2×10^{-5} in the outer disc around and peaks at 2.9×10^{-2} inside the cavity. $\langle\zeta\rangle < 0$ close to the inner boundary (which is likely to be a boundary condition artefact) as well as from $R \approx 5$ to $R \approx 17$ AU. In the second case, $\langle\zeta\rangle < 0$ is due to the material falling down on the disc. Such a contribution being notably stronger for $\varepsilon_{\rm int} = 0.6$.

I plot in fig. 26 a solution built from self-similar simulations of ambipolar dominated disc with a magnetic winds and derived by Lesur (2021b) (dark blue dotted line). The corresponding power law scaling reads $\langle\zeta\rangle = \zeta_{0,\rm ext}\langle\beta\rangle^{a_{\rm ext}}$, with $a_{\rm ext} = -0.69$ and $\zeta_{0,\rm ext} = 0.24$. It comes as no surprise that this scaling law cannot account for the negative values reached by $\langle\zeta\rangle$ that are not self-similar by essence and due to the presence of transition radius. $\langle\zeta\rangle$ is also significantly weaker than what is predicted from a direct extrapolation of the self-similar models in the cavity. It suggests that $\langle\zeta\rangle$ saturates when $\beta \lesssim 1$, a range of values that has not been explored by Lesur, 2021b.

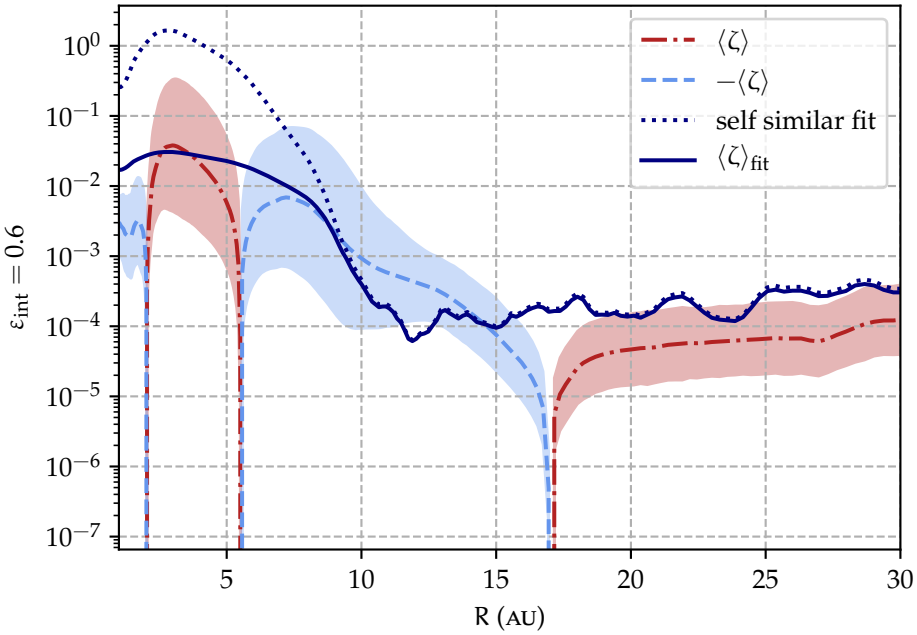

Figure 26: $\langle\zeta\rangle$ parameter for $\varepsilon_{\rm int} = 0.6$ in the fiducial simulations. The red semi-dashed (resp. light blue dashed) line represents the positive (resp. negative) values of $\langle\zeta\rangle$. The dark blue dotted line is a self-similar fit shown for comparison. The dark blue full line is a modified fit that recovers proper values of $\langle\zeta\rangle$ in the cavity.

In the outer disc, the self-similar predictions are also off by a factor of a few . This discrepancy is likely to arise from the influence of the cavity magnetosphere. This later compresses the disk magnetosphere and implies a deviation of $\langle\zeta\rangle$ from the self-similar predictions. It seems that this discrepancy is reduced far from the transition radius (where the influence of the cavity is low) so that $\langle\zeta\rangle$ better matches with the self-similar values.

In order to catch the right value of $\langle\zeta\rangle$ inside the cavity, I propose an alternative model to the self similar one. To do so, I keep the self similar scaling law in the outer disc, $\langle\zeta_{\rm ext}\rangle = \zeta_{0,\rm ext}\langle\beta\rangle^{a_{\rm ext}}$ and calculate another one in the cavity of the form $\langle\zeta_{\rm int}\rangle = \zeta_{0,\rm int}\langle\beta\rangle^{a_{\rm int}}$, with $a_{\rm int} < 0$. The final model combines the 2 profiles so that

$$\langle\zeta\rangle_{\rm fit} = \frac{\zeta_{0,\rm ext}\langle\beta\rangle^{a_{\rm ext}}}{1 + \frac{\zeta_{0,\rm ext}}{\zeta_{0,\rm int}}\langle\beta\rangle^{a_{\rm ext}-a_{\rm int}}}. \tag{176}$$

I find $a_{\rm int} = -0.20$ and $\zeta_{0\,\rm int} = 0.018$. Having $a_{\rm ext} - a_{\rm int} < 0$ allows to recover the correct values both in the cavity and in the outer disc with a reasonable accuracy. Because the negative values of $\langle\zeta\rangle$ at the cavity edge are due to the elbow pattern, I do not try to get a model that is able to catch such changes of sign. I rather expect a model that can render correct values regarding the quantity of matter that is

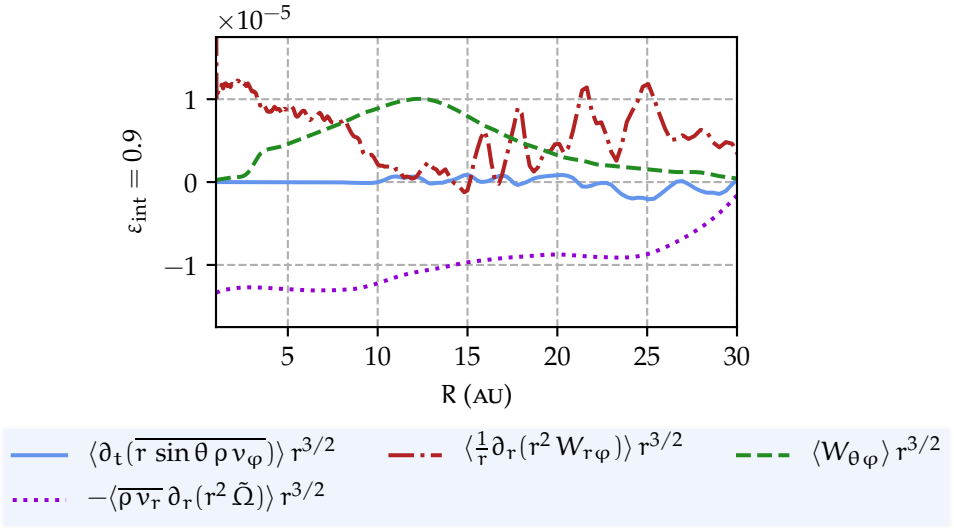

Figure 27: Angular momentum conservation multiplied by $r^{-3/2}$ and time-averaged. Full blue line is $\langle \partial_t(\overline{r \sin\theta\, \rho v_\varphi}) \rangle\, r^{-3/2}$, red dot-dashed line is $\langle \partial_r(r^2 W_{r\varphi}) \rangle\, r^{-3/2}$, green dashed line is $\langle W_{\theta\varphi} \rangle\, r^{-3/2}$ and purple dotted line is $-\langle \frac{1}{2\pi r} \dot{M}\, \partial_r(r^2 \tilde{\Omega}) \rangle\, r^{-3/2}$.

indeed ejected from the disc. The final fit has a transition that occurs at $\beta_t \approx 5$ (by construction) which is close to the lowest value of the ones used to build the self similar fit in Lesur (2021b).

3.1.3.4 *Angular momentum conservation*

I perform the same analysis steps for the angular momentum conservation equation as for the mass conservation equation. I consider the terms involved in the angular momentum conservation equation (172), time-averaged and multiplied by $r^{-3/2}$. The corresponding profiles are shown in fig. 27. The chosen integration height is now $\varepsilon_{int} = 0.9$. This choice lowers the influence of the transition radius.

Contrary to the mass conservation equation (eq. 171), the time derivative in the angular momentum conservation equation is negligible (see eq. 172). The surface stress (or 'wind' stress) removes angular momentum from the whole disc and peaks at the cavity edge location, at $R \approx 13$ AU. The derivative of the radial stress is also mostly positive with the exception of the cavity location where it is slightly negative, suggesting the existence of 2 accretion regimes in the disc. Having 2 different accretion regimes in the disc recalls the radial profiles of the accretion rate and speed shown in fig. 23 and 24.

I introduce the dimensionless Shakura and Sunyaev (1973) α parameter to quantify the radial stress. I strongly shed light on the fact that the origin of this stress is in no way solely linked to turbulence but rather due to the laminar structure of the magnetised wind, which possesses both radial and vertical components. However, I can

still use the α parameter with my wind model whose definition once time-averaged becomes

$$\langle \alpha \rangle \equiv \frac{\langle W_{r\varphi} \rangle}{\langle \bar{P} \rangle} . \tag{177}$$

I show the associated time-averaged profile in fig. 28 (light blue full line), where the integration height is still $\varepsilon_{\rm int} = 0.9$. $\langle \alpha \rangle$ peaks at $\langle \alpha \rangle = 13 \pm 5$ in the cavity and exhibits a plateau in the external part of the disc characterised by $\langle \alpha \rangle = 49 \pm 5 \times 10^{-4}$.

I adopt the same procedure to quantify the surface stress by introducing a dimensionless parameter υ_w and following Lesur (2021a), whose radial dependence is given in fig. 28 (red doted curve). As for ζ, I define one coefficient for each surface of the disc, namely $\upsilon_{w,\pm}$, which are chosen to be positive for angular momentum leaving the disc on both sides, so that

$$\langle \upsilon_w \rangle \equiv \langle \upsilon_{w,+} \rangle + \langle \upsilon_{w,-} \rangle \equiv \frac{\langle W_{\theta\varphi} \rangle}{r \langle P_0 \rangle} . \tag{178}$$

This coefficient slowly decreases in the outer part of the disc with a characteristic value of $\langle \upsilon_w \rangle = 2.3 \pm 1.1 \times 10^{-4}$ and reaches its maximum value of $\langle \upsilon_w \rangle = 1.0 \pm 0.1$ inside the cavity.

The radial profile of $\langle \zeta \rangle$ and those of $\langle \alpha \rangle$ and $\langle \upsilon_W \rangle$ share similarities. Indeed, all of these profiles look alike a step function that reaches its maximum inside the cavity, hence separating the two regimes at play in the disc. In particular, the outer disc regime is typical of wind-emitting protoplanetary discs and the transport coefficients in this region have values that are coherent with self-similar models with $\beta \sim 10^4$. This strongly suggests that the dynamical properties of the outer disc are not affected by the cavity.

On the contrary, the cavity regime is characterised by a fast accretion and high values of ζ, α and υ_W, of the order of unity. The corresponding values of the transport coefficients are gathered in table 2 for all the simulations.

3.1.4 MHD *wind*

Steady-state MHD winds in ideal MHD are known to be characterised by a set of invariants (Blandford and Payne, 1982). I gave the cor-

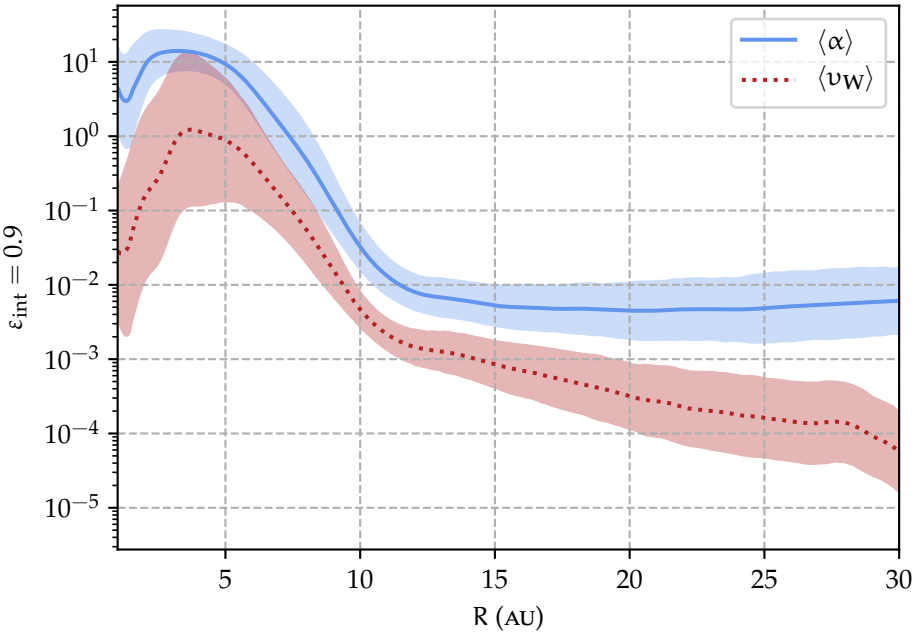

Figure 28: Time-averaged transport coefficients $\langle\alpha\rangle$ and $\langle\upsilon_w\rangle$ for $\varepsilon_{int} = 0.9$.

responding definitions of these invariants in the first chapter, still I recall their respective definitions hereafter:

$$\kappa \equiv 4\pi \frac{\rho\, v_p\, \Omega_w\, R_w}{B_p\, B_w}\,, \tag{179}$$

$$\omega \equiv \frac{\Omega}{\Omega_w} - \frac{\kappa\, B_w\, B_p}{4\pi\, \rho\, R\, R_w\, {\Omega_w}^2}\,, \tag{180}$$

$$\lambda \equiv \frac{\Omega\, R^2}{\Omega_w\, {R_w}^2} - \frac{R\, B_\varphi}{R_w\, B_w\, \kappa}\,, \tag{181}$$

$$\mathcal{B} \equiv \underbrace{\frac{v^2}{2\,{\Omega_w}^2\,{R_w}^2}}_{\text{Kinetic}} + \underbrace{\frac{-R_w}{\sqrt{R^2+z^2}}}_{\text{Gravitational}} + \underbrace{\frac{-\omega\, R\, B_\varphi}{\kappa\, R_w\, B_w}}_{\text{Magnetic}\equiv\mathcal{B}_{mag.}} + \underbrace{\frac{w}{{\Omega_w}^2\,{R_w}^2}}_{\text{Thermal}}\,. \tag{182}$$

My 2.5 D simulations are axisymmetric and a steady-state is approximately achieved above the disc, within the ideal MHD region. Therefore, I compute these invariants along selected poloidal magnetic fields lines, one attached in the cavity and another one in the outer disc. The corresponding field lines are shown in fig. 29. The first line is anchored in the cavity (referred to as "in") and leaves the midplane at $R_{in} = 3.5$ AU while the second one is in the external disc (referred to as "ext") and leaves the midplane at $R_{ext} = 15$ AU. Both lines are built on quantities that are time-averaged on the last 1000 orbits at R_{int} of the simulation.

It should be noted that the disc thickness affects the calculation of MHD invariants. The physical footpoints of the field lines are not precisely located at the midplane but slightly above. This effect is

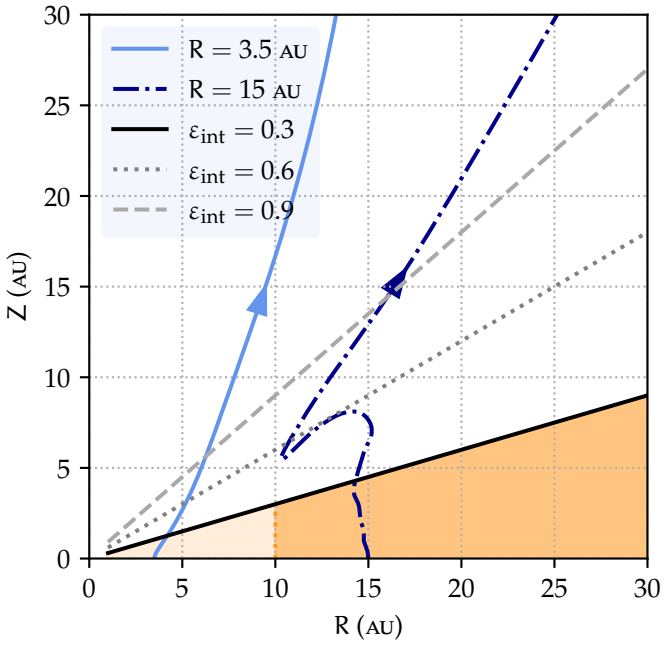

Figure 29: Selected magnetic poloidal field lines to compute the MHD invariants for the 2.5 D fiducial simulation. The disc is shown in orange with the cavity edge located at $R = 10$ AU. I add a few lines delimiting surfaces at $\varepsilon_{int} = 0.3,\ 0.6$ and 0.9.

notably stronger for the field lines leaving the external part of disc. Therefore, the values of MHD invariants are subject to caution so that I only draw general conclusions regarding the nature of the wind.

I show the corresponding invariants computed along each chosen field lines in fig. 30 while their asymptotic values are gathered in tab. 3. First of all, the invariants remain reasonably constant once high enough above the disc. The wind launched from the cavity has different properties from the one launched from the disc. In particular, the wind emitted from the cavity has a much weaker mass loading parameter and a much larger lever arm (by almost a factor 10). Moreover, its rotation parameter is significantly lower than 1. Indeed, the corresponding field lines are rotating at 80% of the local Keplerian angular speed. This result is likely due to the disc being significantly sub-Keplerian in the cavity.

Regarding the Bernoulli invariant, it appears that the greatest contribution to the invariant arises from the magnetic energy term, which is in particular way higher than the thermal one. This is consistent with the magnetic origin of the wind which is confirmed. However, the wind should end up being dominated by the kinetic term. The kinetic component rises up all along the field line, but without being the dominant term.

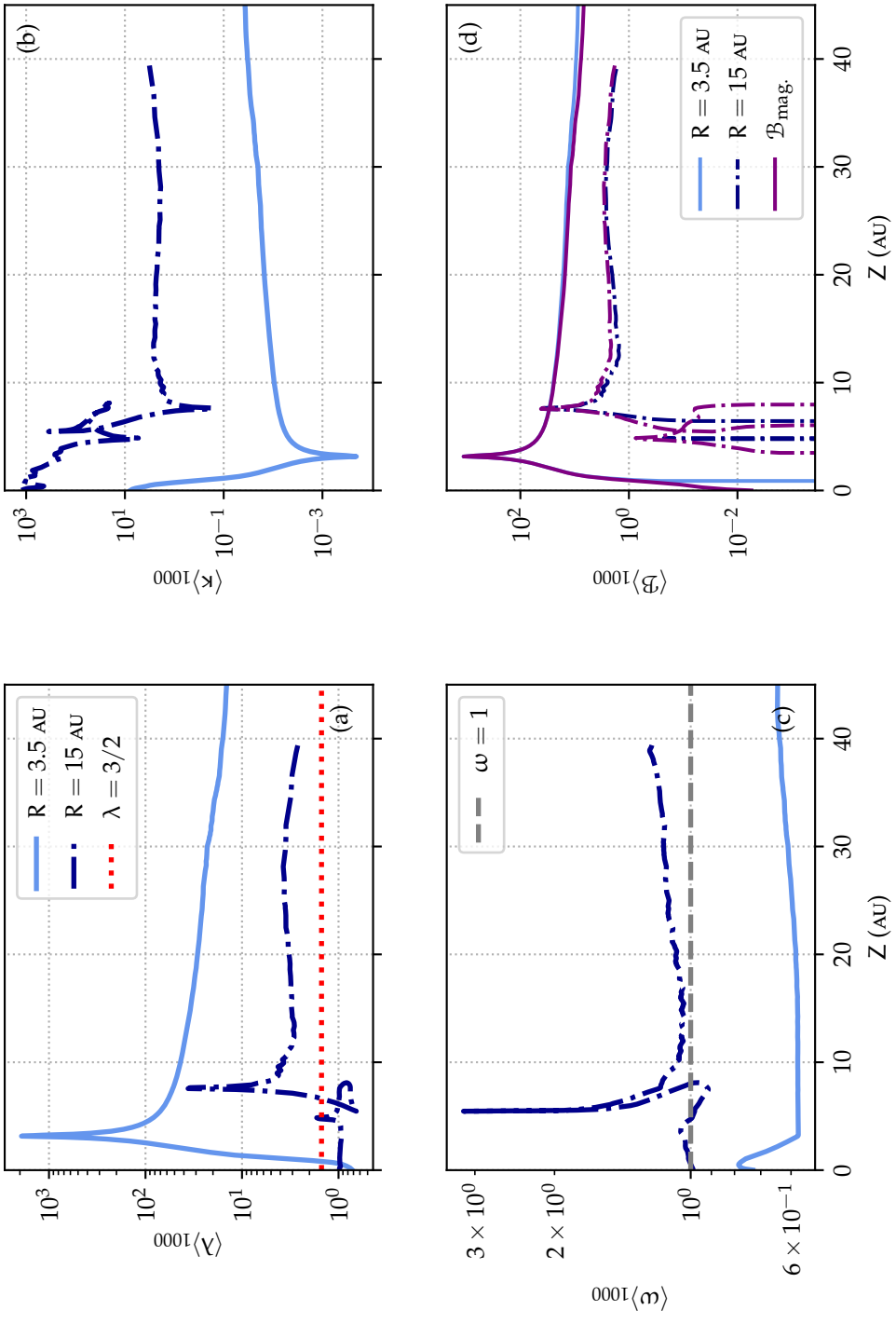

Figure 30: Panels (a), (b), (c) and (d) respectively show each MHD invariants, λ, κ, ω and $\mathcal{B}$, time-averaged over the last 1000 orbits at R_{int} for the 2.5 D fiducial simulation. The light blue full lines refer to the invariants computed for the inner selected field line while the semi-dashed dark blue lines refer to the invariants associated with the external one. In panel (d), the purple curves represent the magnetic contribution to the Bernoulli invariant for each field line.

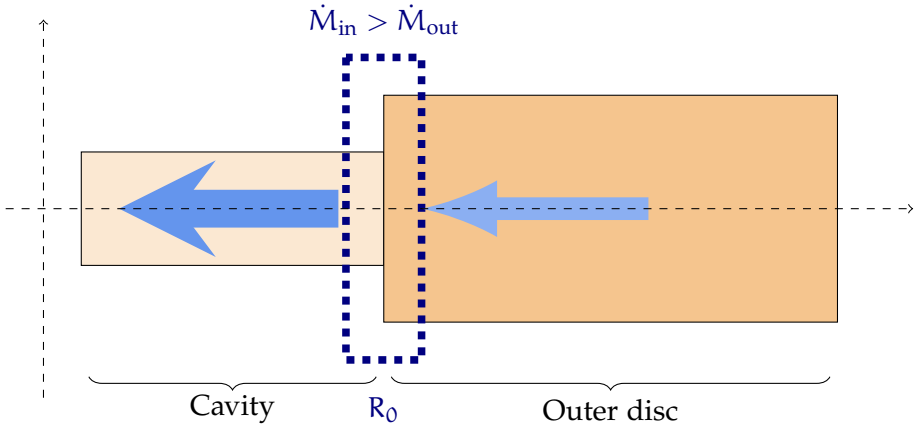

Figure 31: Schematic view of the cavity connected to the outer disc. Though of the same order of magnitude, the accretion rates are slightly mismatched.

Quantitatively, I have for the 2.5 D fiducial simulation $\kappa_{in} = 2.2 \times 10^{-2}$, $\kappa_{ext} = 2.5$, $\lambda_{in} = 23$ and $\lambda_{ext} = 3.2$. These values are coherent with the transport coefficients previously computed. One expects $\kappa \approx \beta\,\zeta/(4\,\varepsilon)$ and $\lambda \approx 1 + \varepsilon\,v_w/\zeta$ (Lesur, 2021a).
I also remark that the values of κ and λ found in the cavity match some of the historical solutions of Blandford and Payne (1982) (see their figure 2) and correspond to super-Alfvénic and collimated outflows. They are also consistent with the magnetic outflow solutions of Ferreira (1997) (see figure 3). Therefore, the cavity quantitatively matches the inner 'jet-emitting disc' (JED) proposed by Combet and Ferreira (2008).

3.1.5 *Temporal evolution of the disc*

Based on the spatio-temporal diagram of Σ (see fig. 18), I observe two kinds of time variability in the fiducial simulation. One is secular and responsible for the slow expansion of the cavity. The other occurs on much shorter timescales and accounts for the striped patterns seen in the spatio-temporal diagram of Σ. The current section aims at describing these time variability regimes, starting with the secular evolution.

3.1.5.1 *Slow cavity edge expansion*

The spatio-temporal diagram of Σ suggests that the cavity edge moves slowly outwards during the simulation. I hereafter neglect the impact of the wind regarding the mass loss rate at the cavity edge location and assume piecewise constant accretion rates and surface densities across the cavity edge (see fig. 31). Therefore, Σ and $\dot{M}$ are modelled with step functions so that $X = X_{in}$ in the cavity and $X = X_{ext}$ in the

outer disc, with X being the accretion rate or the surface density. I define $\delta X \equiv X_{\rm ext} - X_{\rm in}$ and get, based on the conservation of mass,

I recall that R_0 is the location of the cavity edge (see fig. 31).

$$\dot{R}_0 = -\frac{1}{2\pi R_0}\frac{\delta \dot{M}}{\delta \Sigma}\,, \tag{183}$$

where $\dot{R}_0$ is the cavity edge effective "expansion velocity". Around the cavity edge, I have $\dot{R}_0 = 1.8 \times 10^{-5}$ while evaluating directly the cavity edge motion $\dot{R}_0$ yields $\dot{R}_0 = 1.4 \times 10^{-5}$ (both in code units). I therefore conclude that the cavity expands because of the slight mismatch in accretion rate observed in figs. 23 and 25.

3.1.5.2 *Magnetic field transport*

The magnetic field transport is a key notion to understand the secular evolution of magnetised discs. I build a flux function ψ that embodies the magnetic field transport such that

$$\psi(r,t) = R_{\rm int}^2 \int_0^{\pi/2} B_r(R_{\rm int},\theta,t)\,\sin\theta\,{\rm d}\theta - \int_{r=R_{\rm int}}^{r} r\,B_\theta(r,\pi/2,t)\,{\rm d}r\,. \tag{184}$$

The first term accounts for the seed magnetisation and the second represents the amount of vertical magnetic field threading the disc up to a radius R.

I recall that the 'seed' refers to the inner radial boundary condition.

The isocontours of ψ depict the motion of the magnetic field footpoints in the disc plane. The corresponding spatio-temporal profile of ψ is shown in fig. 32. It appears that the magnetic flux is slowly advected towards the star in the external disc and diffused outwards in the cavity. The poloidal magnetic structure of the disc (fig. 19) shows that there is a change of sign regarding $\langle B_{z,0}\rangle$ at the transition region with $\langle B_{z,0}\rangle < 0$ between $R \approx 8$ and $R \approx 12$ and $\langle B_{z,0}\rangle > 0$ elsewhere. This transition region is recovered in fig. 32 as a region where $\partial_r \psi < 0$.

Overall, the negative field at the transition region is diffusing outwards, when the positive field of the outer disc is advected inwards. Both field reconnects around $R \approx 12$ AU, so that the large scale field progressively 'eats' the negative field of the transition region. The negative field corresponds to the poloidal magnetic loop (see fig. 19). This loop is expected to disappear on a time-scale greater than the total duration of my 2.5D simulations. Moreover, the poloidal field lines deep in the cavity also diffuse outwards.

Calculating the partial derivatives of ψ leads to

$$\begin{cases} \partial_t \psi(R,t) = -R\,\mathcal{E}_{\varphi,0}(R,t) \\ \partial_R \psi(R,t) = -R\,B_{\theta,0}(R,t) \end{cases}. \tag{185}$$

Following Guilet and Ogilvie, 2014, I postulate an advection equation for ψ that reads

$$\partial_t \psi + v_\psi\,\partial_R \psi = 0\,, \tag{186}$$

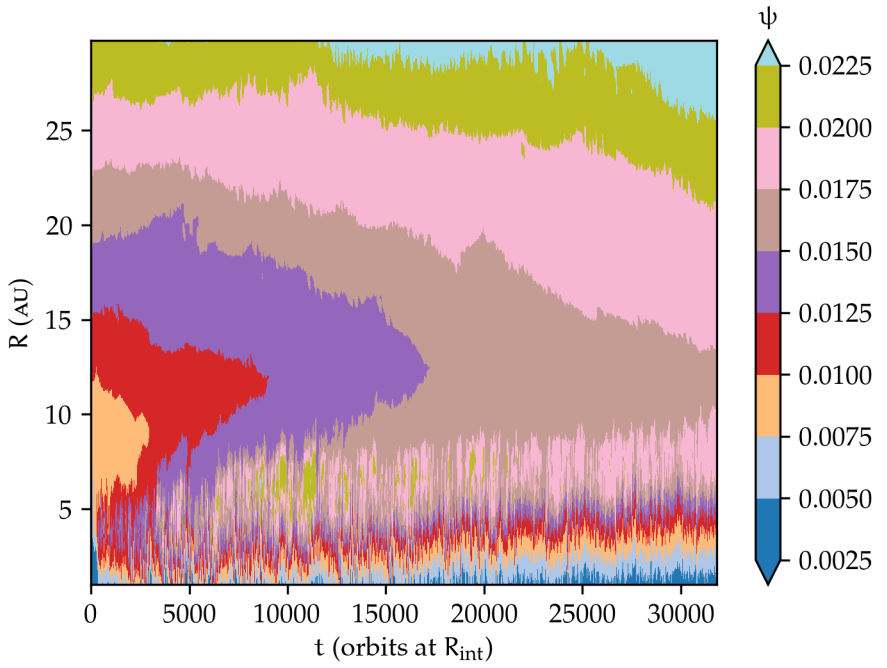

Figure 32: Flux function $\psi(R, t)$ for the 2.5 D fiducial simulation, taking into account the flux at the surface of the seed and the radial flux threading the disc.

where I define the "field advection velocity" v_ψ which satisfies

$$v_\psi = -\frac{\mathcal{E}_{\varphi,0}(R, t)}{B_{\theta,0}(R, t)}\,. \tag{187}$$

I eventually define a supplementary dimensionless parameter

$$\nu_B \equiv v_\psi / v_K\,, \tag{188}$$

which quantifies the advection speed (Bai and Stone, 2017). With the previous definitions, positive values of ν_B account for an outward motion of the magnetic field while negative values trace inward field transport. The time-averaged radial profile of ν_B is shown in fig. 33.

The external disc is characterised by an advection velocity $v_\psi = -2.6 \times 10^{-3}\, v_K$. $\langle \nu_B \rangle$ encounters changes of signs multiple times in the cavity, and finally remains negative close to the cavity edge, between $R \approx 8$ and $R \approx 12$ AU which is the transition region. The advection speed is then $v_\psi = +3.2 \times 10^{-3}\, v_K$.

Such a result is coherent with fig. 32 so that the field lines converges at the transition radius with opposite vertical polarity, which recovers my previous conclusion. In the external parts, $\langle \nu_B \rangle$ is negative, $v_\psi = -2.6 \times 10^{-3}\, v_K$ and the vertical magnetic field pointing upwards is advected. I stress that the *inward* motion of the magnetic field lines in the external disc is in sharp contrast to other work which focused on

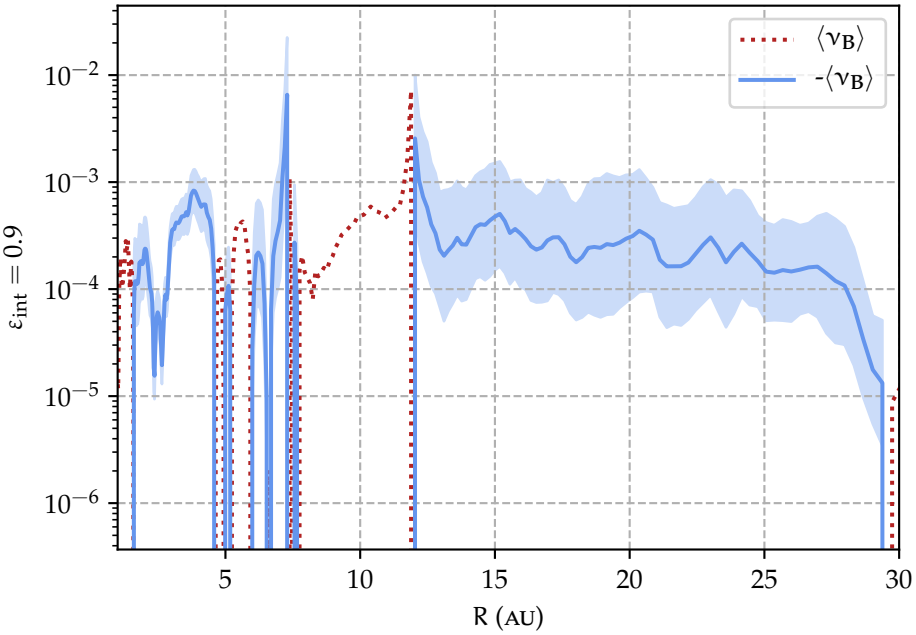

Figure 33: Time-averaged radial profile of ν_B for the 2.5 D fiducial simulation.

"full" protoplanetary discs (Bai and Stone, 2017; Gressel et al., 2020; Lesur, 2021b). This magnetic advection of flux in the outer disc of my truncated protoplanetary disc suggests a non-local influence of the cavity.

3.1.5.3 *Fast variability of the cavity*

Up until now, I focused on time-averaged quantities and yet ignored any fast variability. Despite my numerical simulations reaching quasi-steady states, they also exhibit a fast time variability, especially on a few orbits at R_{int} (see in particular the stripes in the spatio-temporal diagrams of fig. 18) and whose origin remains to be clarified.

I give the temporal evolution of a few quantities (Σ, $\dot{M}$, B_z and ζ, obtained at $R = 3$ AU) in fig. 34. All of these profiles are subject to sharp fluctuations over time that are chaotically distributed. Indeed, bursts (or 'bubbles') of matter cross the cavity from time to time and fall rapidly onto the central star. These bursts are characterized by strong sharp increases of Σ and $\dot{M}$ in fig. 34 with peaks whose typical width is ~ 5 orbits at R_{int} (I recall that the temporal resolution of my outputs is 1 orbit at R_{int}). This variability fully accounts for the stripes detected in the spatio-temporal diagrams (fig. 18).

I give a special focus to a few of these burst events in the bottom panels of fig. 34. The (b) panel also corresponds to the instantaneous pictures of the density given in fig. 35. The local maximum of B_z,

Σ and $\dot{M}$ are clearly correlated. The scenario for one stripe (i. e. one burst event) is the following. Once an inflow (a burst) of matter falls at the external edge of the cavity and is about to cross it, Σ obviously peaks as well as $\dot{M}$ so that ζ increases. B_z seems to increase a bit before Σ and $\dot{M}$, which suggest that B_z is the driver of these bursts. However, I cannot be definitive on this because of my limited temporal resolution. In the end, the rise of ζ (computed at $\varepsilon_{\text{int}} = 0.3$) is always clearly delayed compared to the other quantities. Therefore, the wind in the cavity is more efficient once a bubble has passed.

Figure 35 describes a burst event with greater details by showing the instantaneous density as well as poloidal magnetic field lines on 6 panels (1 panel every 4 orbits at R_{int}). The first panel exhibit a thin filament of matter located above the disc which extends from $(R = 10,\ Z = 5)$ to $(R = 15,\ Z = 10)$. This latter is cut in two parts on the second panel, creating two bubbles of matter. One bubble is about to fall (and will further generate the burst event) while the other is about to be ejected. The ejected bubble leaves the disc in the wind and does not interact with the cavity whatsoever.

Figure 36 shows the spatial structure of the currents in the disc. A current sheet lies under the filament location, where $|j_\varphi|$ is high and the poloidal current is parallel to the radial direction and points outwards. The sheet corresponds to the area where the filaments are detected. This location is further characterised by the fact that the *total* magnetic field cancels ($B_\varphi = 0$ at the edge of the magnetic loop and $B_p = 0$ because two antiparallel poloidal field lines meet). It is then likely that the bubbles form after the filament has encountered a magnetic reconnection event, which is studied in the context of ambipolar diffusion in Tsap et al. (2012). Magnetic reconnection is also a candidate to allow matter to enter a star magnetosphere (Bouvier et al., 2006; Zanni and Ferreira, 2013). Though there is no magnetosphere in my simulations, the characteristic elbow shape of the poloidal magnetic field lines and the current sheet still suggest magnetic reconnection and it would be interesting to do numerical simulations with a more physically accurate star/disc connection.

I now shed light on the becoming of the falling bubble which reaches the edge of the cavity on the third panel of fig. 35 before crossing it on the following one. While the gas crosses the cavity, the disc oscillates locally and is highly dynamical. After a short delay (and on the last three panels), an outflow emerges from the cavity while the wind density increases (see the values of ζ on the (b) panel of fig. 34). The ejection of gas from the cavity is not constant with time and occurs with burst events for which ζ peaks at 0.1. This may very well explain why the effective values of $\langle\zeta\rangle$ in the cavity are lower than the ones predicted by self-similar models for which the ejection is continuous and with a higher mass loss rate parameter.

These oscillations are the main reason why I adopted the modified definition of $\overline{\beta}$ which allows to catch the value of β inside the oscillating thin layer of matter in the cavity.

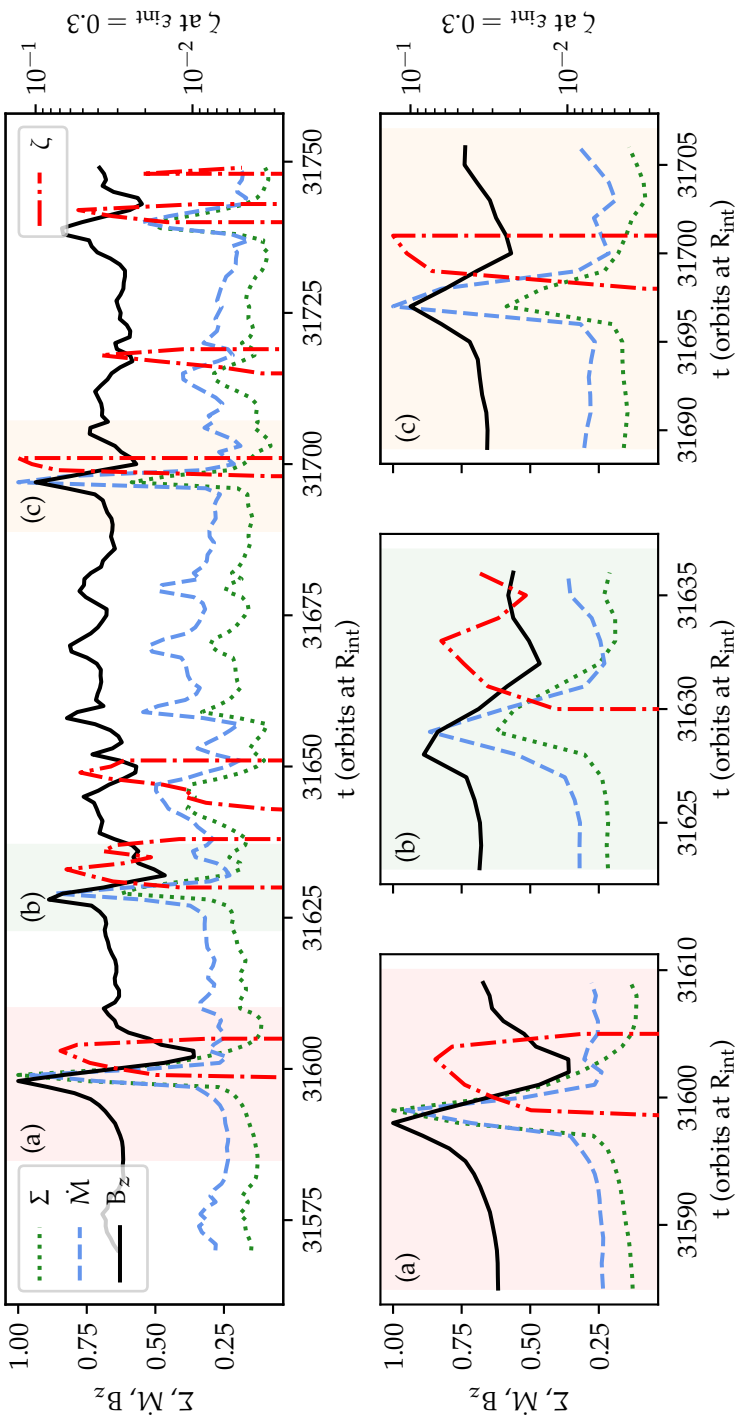

Figure 34: Temporal evolution of Σ in dotted green, $\dot{M}$ in dashed blue and B_z (vertically averaged) in black full line, all calculated at $R = 3$ AU for the 2.5 D fiducial simulation. The mass loss rate parameter ζ is calculated at $\varepsilon_{int} = 0.3$ and shown in semi-dashed red line with a logarithmic scale on the right of the panels. Apart from ζ, all the profiles are given in arbitrary units and divided by their maximum value reached during the timescale of the top panel. The bottom panels focus on 3 particular events. Note that the horizontal scales are not exactly the same for all the bottom panels.

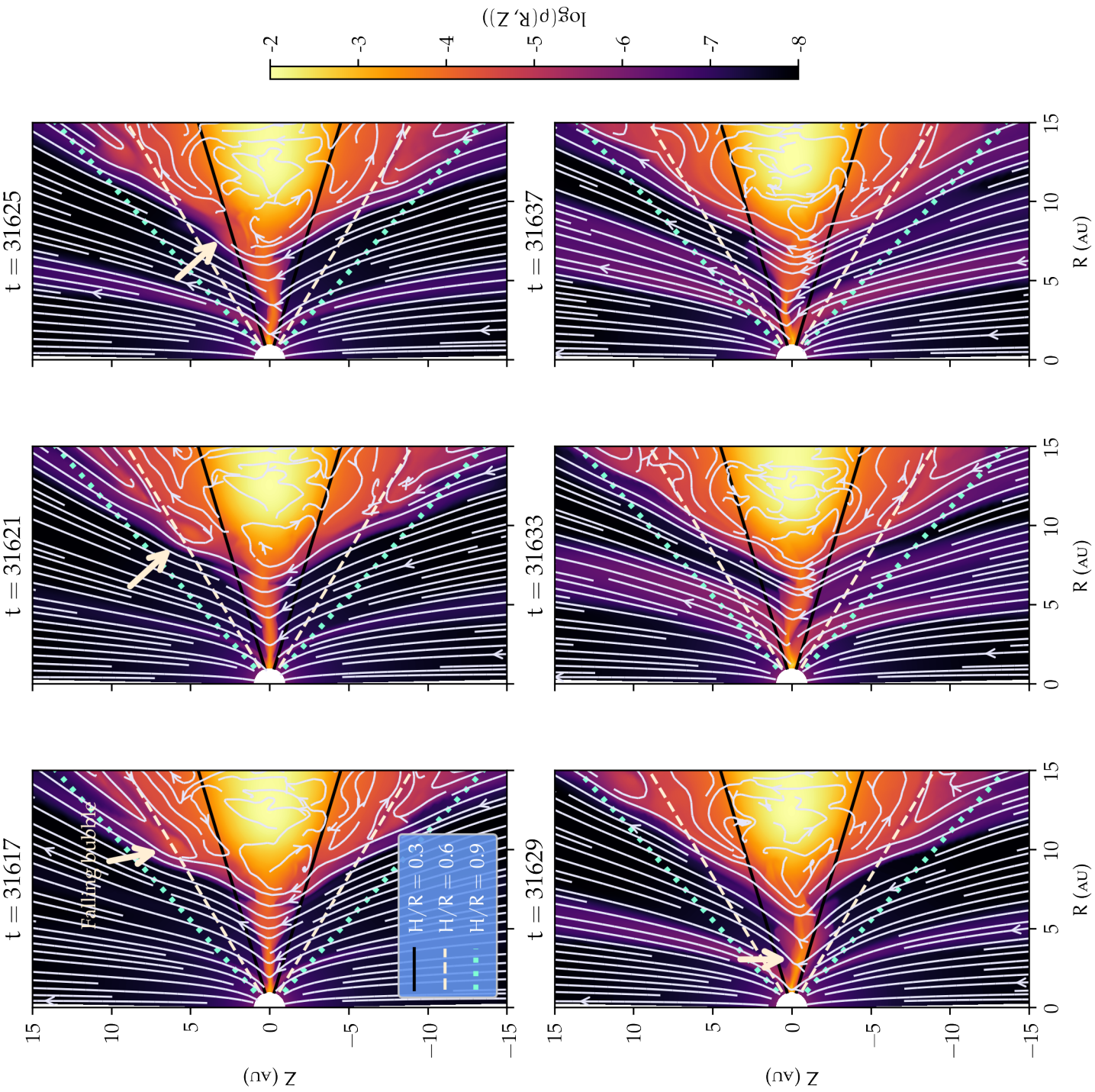

Figure 35: Instantaneous density over which poloidal magnetic field lines are plotted at different times, for the 2.5 D fiducial simulation. The arrow tracks the position of a falling bubble of matter generating a burst event (coresponding to the (b) panel of fig. 34).

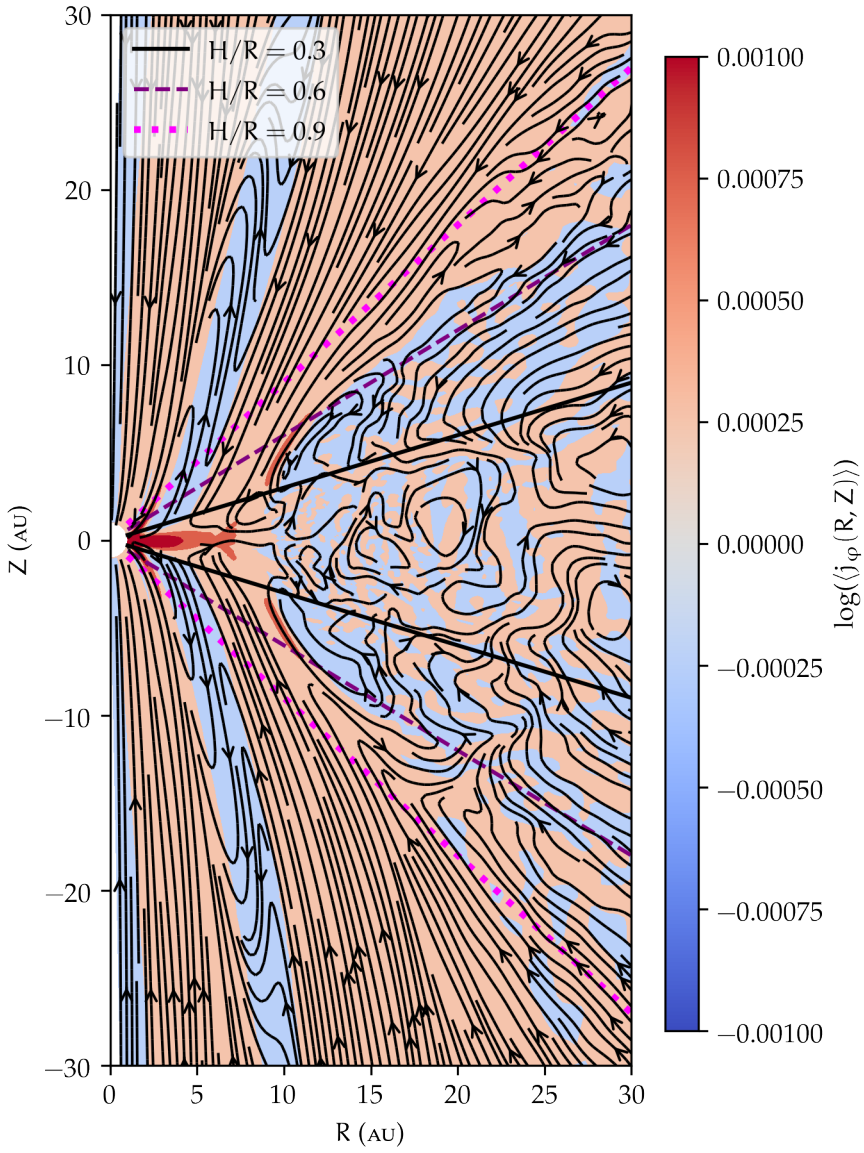

Figure 36: Time-averaged azimuthal coordinate of the current density for 2.5 D fiducial simulation.

To be more specific on the mass loss rate parameter, I give the profile of $\delta\zeta$ defined as $\delta\zeta \equiv |\zeta_+ - \zeta_-|$ in fig. 37. This quantity is designed to catch the top/down asymmetries of the ejection efficiency. Fig. 37 indeed reveals that the ejection after the bubble has crossed the cavity is not vertically symmetric, which explains why the disc oscillates so strongly. Theses observations highlight the link between wind and accretion (see fig. 25).

Combining fig. 20 and 35 eventually unveils a characteristic temporal sequence for feeding the cavity. First of all, the gas located inside the outer disc elevates from the midplane up to approximately 2 local disc height and organises itself in a filamentary way. This elevation must be linked to the complex structure of the azimuthal magnetic field (see fig. 19), whose changes of sign at the cavity edge accounts for the vertical displacement of matter up until the characteristic elbow shape structure. Once the filament has formed, a bubble of matter falls and crosses the cavity, generating the stripes in the spatio-temporal diagrams.

3.1.5.4 *Magnetic Rayleigh Taylor instability*

To account for the formation and stability of the falling bubble of matter, I study the possibility of having a magnetic Rayleigh Taylor instability (RTI, or interchange instability) triggered at the cavity edge location. This instability is in particular frequently invoked as a possible mechanism allowing matter to enter a magnetosphere (Elsner and Lamb, 1984).

RTI will exclusively refer to the magnetic Rayleigh Taylor instability throughout this manuscript.

I assume that the disc is geometrically thin inside the cavity and that the density is continuous radially. Under these conditions, I refer to the analysis of the RTI in Spruit and Taam (1990), Spruit et al. (1995), and Stehle and Spruit (2001), which assume an infinitely thin disc. I reformulate the instability criterion of Spruit et al., 1995 (see their equation 59) in terms of the plasma parameter in appendix A. The resulting criterion 223 gives a necessary condition for the occurrence of the RTI which is

$$\overline{\beta} < \beta_{\text{crit.}} \simeq 0.0355 \qquad \text{UNSTABLE}\,. \tag{189}$$

Figure 18 shows the time-averaged radial profile of $\overline{\beta}$. It appears that $\overline{\beta}$ is of the order of 0.1 in the cavity and rarely go below this value, apart from very short periods of time such as during the accretion bursts. It therefore seems unlikely that the criterion is verified in the cavity.

I finally conclude that the cavity β plasma parameter is too large to sustain the RTI on average. However I cannot exclude that it could be triggered in the rare excursions where the cavity reach $\overline{\beta} < 0.1$, as during some of the bursts.

In must be noted that Li and Narayan (2004) give another criterion

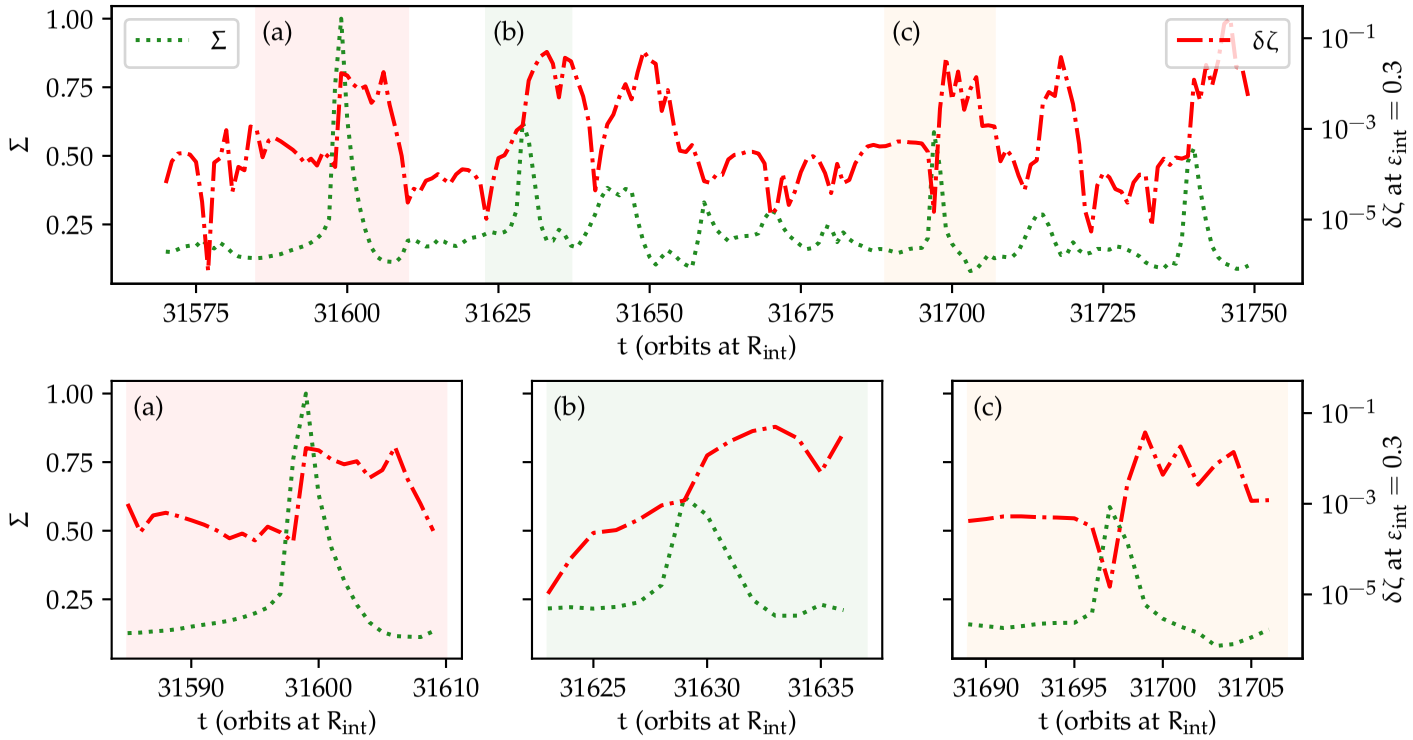

Figure 37: Temporal analysis of the 2.5 D fiducial simulation which focuses on $\delta\zeta$.

for the triggering of the RTI in the case of an infinitely thick disc (see their equation 37) with a non-axisymmetric development.
Therefore, though I cannot fully rule out the RTI, it seems likely that once the bubble has formed, it starts to rotate slower because of the braking induced by the wind so that it becomes rotationally unstable. The bubble then falls down onto the cavity, triggering the temporal sequence I discussed previously.

3.2 PARAMETERS SPACE EXPLORATION

In this section, I move to the parameter space exploration to study the impact of $\Lambda_{A,0}$, β_{in} and β_{out}, starting with $\Lambda_{A,0}$.

3.2.1 *Ambipolar Elsasser parameter*

I start by checking the influence of $\Lambda_{A,0}$ in the simulation labelled by S2DB4Bin0Am1. This one is the same as the 2.5 D fiducial one except for the initial value of Λ_A which is set to 10.

3.2.1.1 *General structure of the disc and gaps*

Just like for the fiducial simulation, I give the spatio-temporal diagrams of Σ and $\overline{\beta}$ in fig. 38 for $\Lambda_A = 10$. Contrary to the fiducial simulation, the cavity edge does not remain still. It rather shrink to less than 2 AU before widening back up to $R \gtrsim 4$ AU in a few thousands of orbits at R_{int}. The transient state is shorter than in the fiducial run and leads to reorganisation of the cavity which is eventually smaller.

Gaps are also detected both in the diagrams of Σ and $\overline{\beta}$ (see fig. 38). They are located in the outer disc and broaden with time. Such structures are characteristic of discs simulated with MHD and have been observed in numerous occasions both with ideal (Jacquemin-Ide et al., 2021) or non-ideal MHD (Béthune et al., 2017; Suriano et al., 2019; Riols et al., 2020; Cui and Bai, 2021). As in the fiducial simulation, the gaps are associated with low $\overline{\beta}$ regions. Moreover, some gaps merge with one another while some split into 2 gaps, so that only 3 of them remain after 15000 orbits at R_{int}. This result is in particular similar to what is found in Cui and Bai (2021). Focusing on the gaps is beyond the scope of this work. However, I sill wish to show that the gaps move differently in the disc, depending on their location, as shown with fig. 39. It is clear that the gap located close to $R \approx 15$ AU is moving inwards (compare the profiles at the instants 15000 and 25000 between which no merging occur) while the furthest one is moving outwards. Since the gaps are associated with a magnetic concentration, this result could indicate that some poloidal magnetic field is dragged outwards in the outermost parts of the disc and inwards

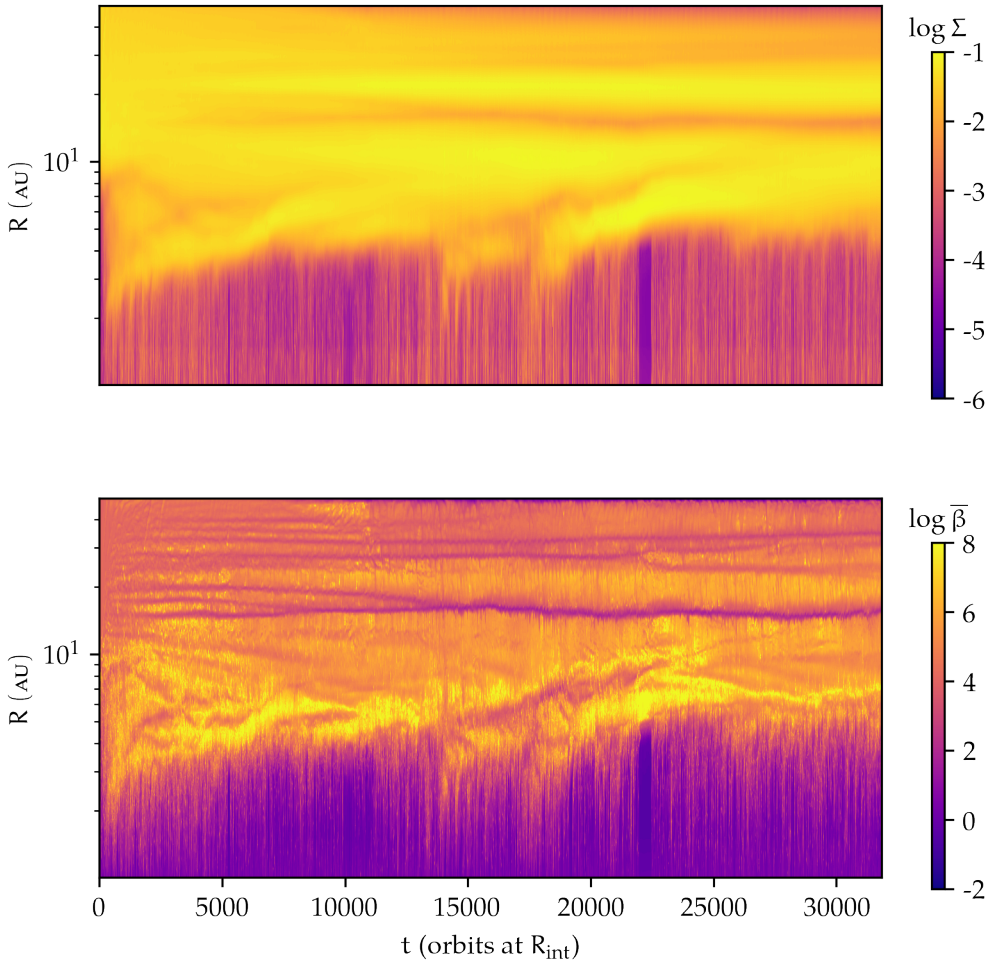

Figure 38: Spatio-temporal diagrams of Σ (top panel) and $\overline{\beta}$ (bottom panel) for the simulation S2DB4BinoAm1.

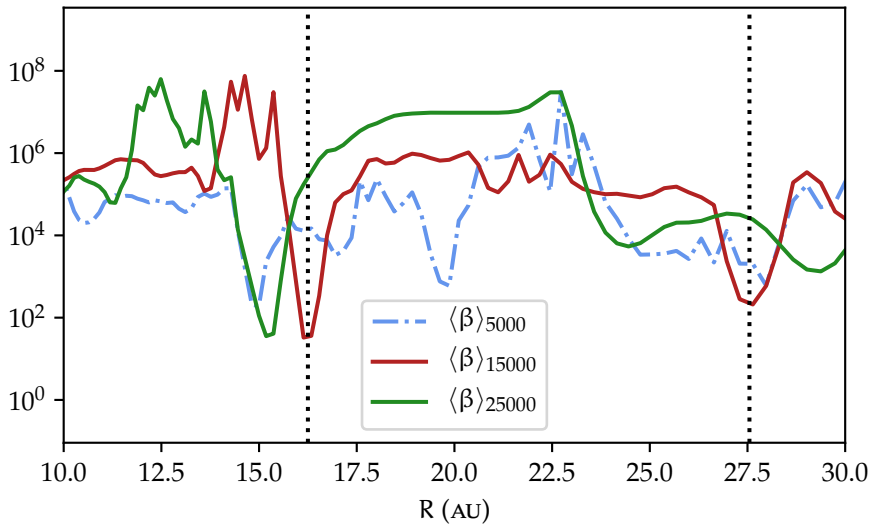

Figure 39: Profiles of β at different times, all for S2DB4BinoAm1. Each profile $\langle\beta\rangle_x$ is averaged between x and $x + 1000$ orbits at R_{int}. The profiles focus on the outer disc where $\beta \approx \overline{\beta}$.

closer to the cavity. Focusing after the merging of the inner gaps (after 15000 orbits at R_{int}), the flux function ψ shown in fig. 40 seems to strengthen this statement, as magnetic field seems to concentrate in the gaps. This highlights the complex behaviour of the magnetic field transport in the disc.

I now move on to the disc general time-averaged structure for this simulation. Figure 41 gathers the flow and magnetic field topology of the disc. The main characteristic of the 2.5 D fiducial simulation are recovered such as the elbow-shaped structure (in the poloidal magnetic structure and in the flow topology) and the associated magnetic loop. All of them lie closer to the star, since the cavity is smaller.

In contrast to the fiducial simulation, the outer disc is top/down asymmetric. This asymmetry has an impact on the shape and size of the elbow structure above and below the disc plane. In particular, the elbow is well developed above the disc but barely below it, except for a small set of stream lines close to the cavity.

At the gap location, the poloidal magnetic field lines exhibit a local slanted symmetry in the external disc. This peculiar topology is observed in ambipolar dominated discs such as Riols and Lesur (2019) and Riols et al. (2020). Small vortices in the (r, θ) plane appear at the disc surface, at the radius of each gap, suggesting a meridional circulation of matter.

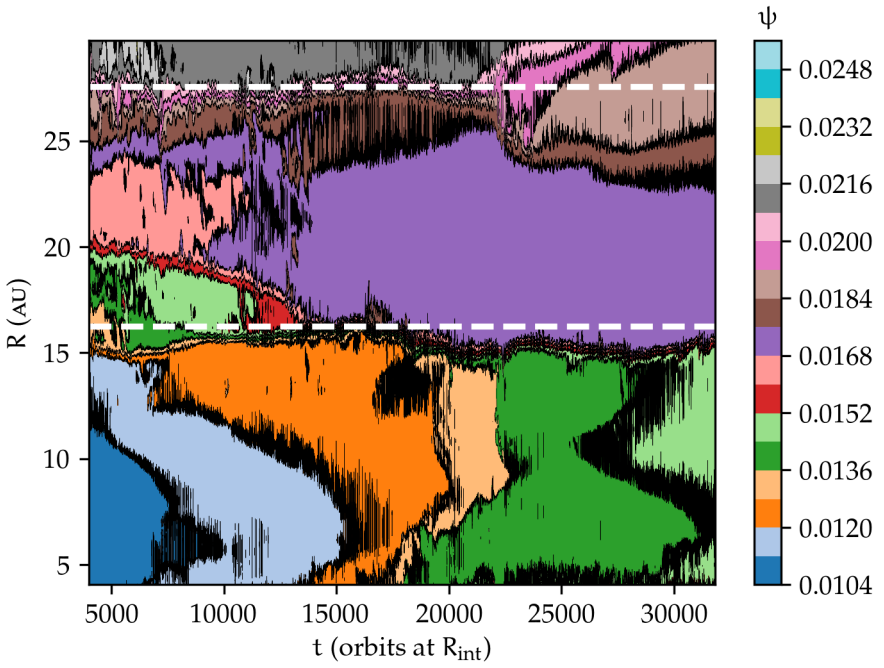

Figure 40: Magnetic field transport for the simulation S2DB4BinAm1. The white dashed lines indicate the gaps location at 20000 orbits at R_{int} after the merging of the inner gaps (see fig. 38). The black contours show highlight the contours of ψ in the outer disc only (for better readability, the inner cavity is dropped). The transient state is not shown here.

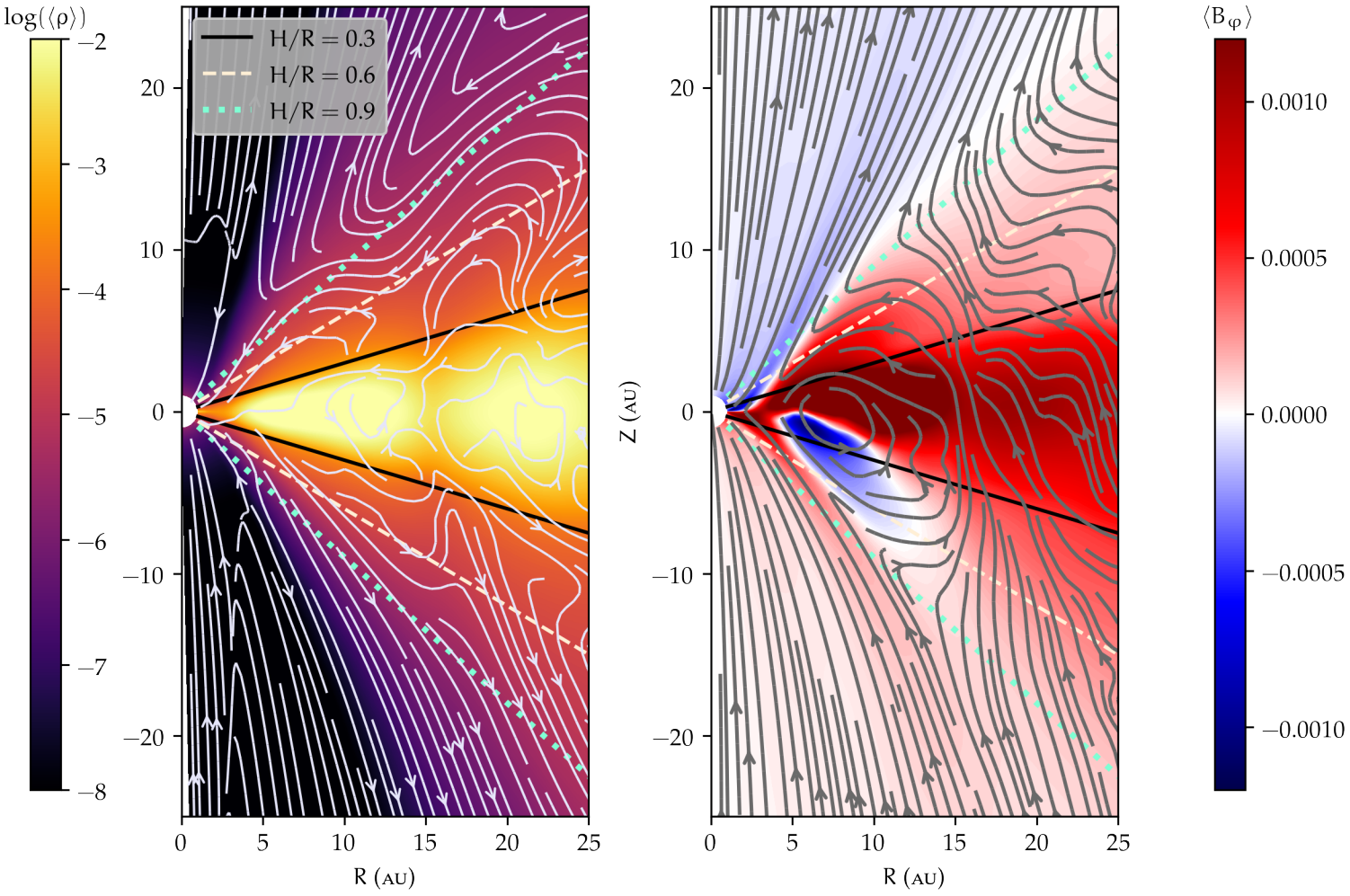

Figure 41: Time-averaged structure of the disc for S2DB4BinoAm1. Left panel: poloidal stream lines and density. Right panel: magnetic structure of the disc with magnetic poloidal field lines and $\langle B_\varphi \rangle$.

Name	$\dot{M}$	ζ_{in}	ζ_{ext}	α_{in}	α_{ext}	$\upsilon_{w,in}$	$\upsilon_{w,ext}$
Units	$M_\odot\,yr^{-1}$	10^{-2}	10^{-5}	—	10^{-3}	—	10^{-4}
S2DB4BinoAmo	1.4	2.9	6.2	13	4.9	1.0	2.3
S2DB3BinoAmo	5.1	3.8	14	19	23	1.4	31
S2DB5BinoAmo	0.27	2.1	4.5	6.6	1.0	0.18	0.19
S2DB4BinoAm1	1.2	−1.8	10	2.8	16	0.16	2.7

Table 2: Transport coefficients for a subset of simulations. The accretion rate is calculated inside the cavity.

Name	λ_{in}	λ_{ext}	κ_{in}	κ_{ext}	ω_{in}	ω_{ext}
S2DB4BinoAmo	23	3.2	2.2×10^{-2}	2.5	0.67	1.2
S2DB3BinoAmo	185	1.3	3.1×10^{-3}	9.9	0.64	0.93
S2DB5BinoAmo	4.4	1.2	1.3	18	0.69	1.1
S2DB4BinoAm1	4.9	1.5	0.24	5.0	0.23	3.6

Table 3: MHD invariants for a subset of simulations, computed with time-averaged quantities on the last 1000 orbits at R_{int}.

3.2.1.2 *Transport coefficients and wind invariants*

The accretion in the disc does not change much from the 2.5 D fiducial simulation. The accretion rate is still constant in the whole disc, close to $1.2\times10^{-7}\,M_\odot\,yr^{-1}$ while the accretion velocity remains subsonic in the outer disc and transsonic (up to $2\,c_s$) in the cavity. Eventually, the previously discussed accretion scenario holds for this simulation, with an internal transsonic regime, connecting through the cavity edge to a weakly magnetised wind.

Regarding the magnetic wind, this disc also exhibits a highly mass loaded field line in the external disc removing little angular momentum ($\lambda_{ext} = 1.5$ and $\kappa_{ext} = 5.0$), and a lighter one in the internal disc carrying a massive load of angular momentum ($\lambda_{in} = 4.9$ and $\kappa_{in} = 0.24$). Overall, the disc wind is less magnetised and more massive. Interestingly, the rotational invariant contrast is higher than in the fiducial simulation, its internal value being 3 times lower and the external 3 times higher.

3.2.2 *Influence of the initial plasma parameter*

I go on with the role of the initial plasma parameter in the disc. I start by highlighting the impact of its initial external value β_{out} be-

fore presenting the one of its initial internal value β_{in}. I change the external initial magnetisation β_{out} by adjusting the intensity of the magnetic field throughout the whole disc. I vary the internal initial magnetisation β_{in} by modifying the coefficients which control the cavity function.

3.2.2.1 *Role of the external initial plasma parameter*

I begin by studying the impact of the initial external magnetisation. In this prospect, I ran additional simulations, one with $\beta_{out} = 10^3$ (run S2DB3BinoAmo) and one with $\beta_{out} = 10^5$ (run S2DB5BinoAmo).

GENERAL OBSERVATIONS FOR S2DB5BINOAMO (LOWER MAGNETISATION CASE): As usual, I start with the spatio-temporal diagrams of Σ and $\overline{\beta}$, given in the left panels of fig. 42. At the beginning of the

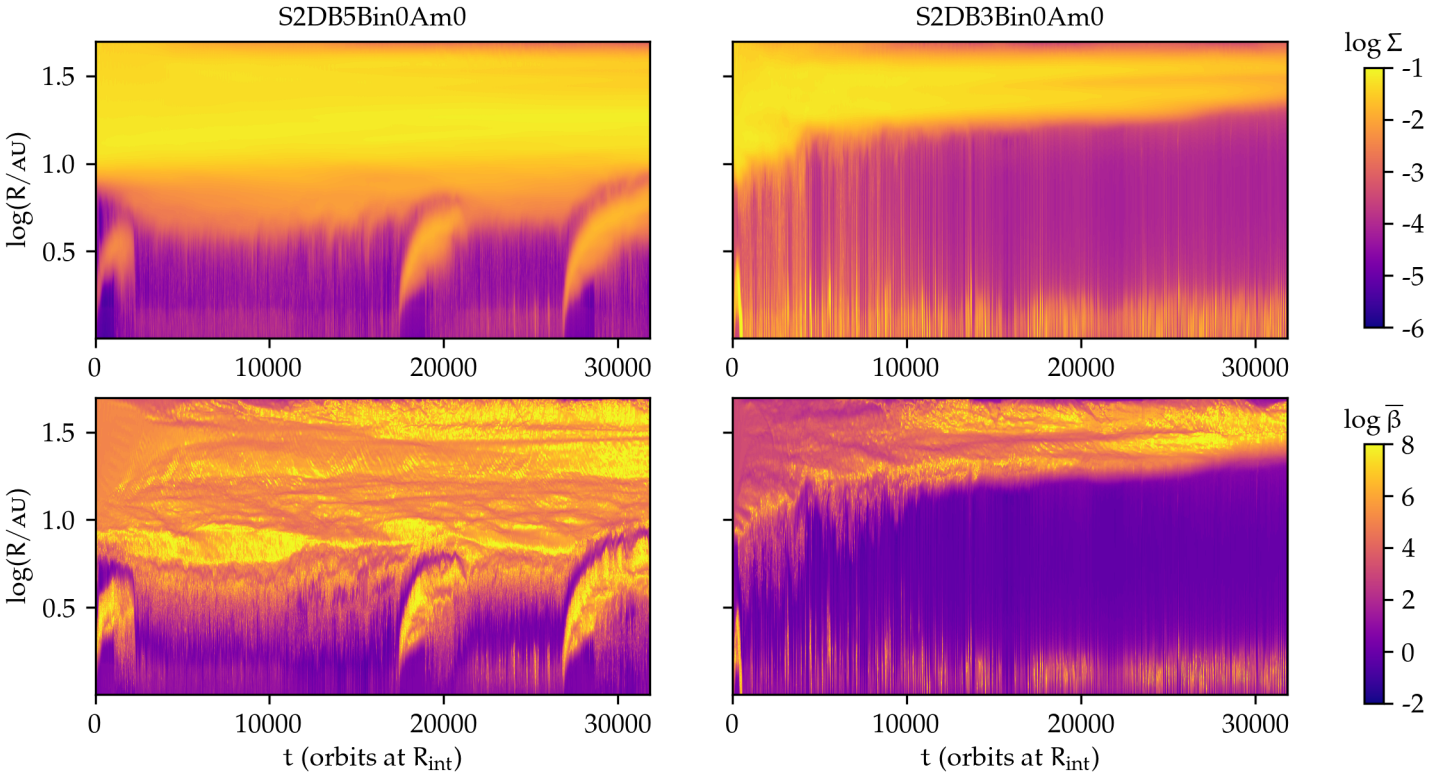

Figure 42: Spatio-temporal diagrams for Σ and $\overline{\beta}$ for S2DB5BinoAmo (left panels) and S2DB3BinoAmo (right panels).

simulation, an accumulation of matter is seen in the cavity which is subsequently refilled. This accumulation looks like a 'burst' of matter in the diagram. The radius of the cavity then remains fixed at ~ 4 AU until some other accumulations of matter occur at ~ 17400 and ~ 27000 orbits at R_{int}. These events do not affect the general properties of the disc in a significant manner.

The so-called 'bursts' of matter (at $\sim$ 17400 and $\sim$ 27000 orbits at R_{int} where I assume the first one to be due to the initial transient state) give the illusion that mass conservation is challenged. However, this is of course not the case, these accumulations are actually a consequence of gas accumulating at the boundary of an accretion 'barrier'. I investigate this point with greater details in chap. B. For now, I stress that these burst events are a limitation of my model regarding the implementation of the inner radial boundary condition. It is also worth saying that they only occur in the weakly magnetised ($\beta_{out} = 10^5$) simulations.

Finally, the expansion velocity of the cavity $\dot{R}_0$ is too difficult to obtain since the cavity edge barely move during the entire simulation (which implies that this velocity is at least slower than the one of the 2.5 D fiducial simulation).

GENERAL OBSERVATIONS FOR S2DB3BINOAMO (HIGHER MAGNETISATION CASE): The corresponding spatio-temporal diagrams are given in the right panels of fig. 42. In contrast to the less magnetised simulations, the cavity expands fast, up until its edge reaches $R \approx 15$ AU. This growth remains uninterrupted during the whole simulation so that this difference with the 2.5 D fiducial run cannot be attributed to the transient state. I estimate the corresponding expansion velocity as $\dot{R}_0 \approx 3.0 \times 10^{-5}$ c.u. This is about 3 times faster than the fiducial run. Eq. 183 gives, with $\delta\dot{M} \approx 2.3 \times 10^{-4}$ and $\delta\Sigma \approx 4.2 \times 10^{-2}$ (both in code units) that $\dot{R}_0 \approx 4.2 \times 10^{-5}$ c.u., where I choose $R_0 \approx 20$. Therefore, my simple model seems to overestimate the expansion velocity of the cavity but gives a fine order of magnitude.

To deeper the previous analysis, let me recast the eq. 183 in the following way

$$\dot{R}_0 = v_{acc.,in} \left(\frac{\Sigma_{in}}{\Sigma_{out}} - \frac{v_{acc.,out}}{v_{acc.,in}} \right) , \tag{190}$$

where I introduce the accretion velocities $v_{acc.} \equiv \dot{M}/2\pi R_0 \Sigma$, and assume that $\Sigma_{out} \gg \Sigma_{in}$. This new form highlights the fact that the expansion velocity is controlled by the term in parenthesis. The accretion velocity in the cavity is sonic for any simulations. Furthermore, it is well known that the accretion velocity in the outer 'standard' disc decreases with β. With this in mind, I can write that

I recall that I call 'standard' a protoplanetary disc that has no cavity, i. e. a full disc.

$$v_{acc.} \propto \beta^{-\sigma} , \tag{191}$$

with $\sigma > 0$. Lesur (2021b) proposes $\sigma = 0.78$ and Bai and Stone (2013b) $\sigma = 0.66$, so that previous works point towards $0 < \sigma < 1$. Assuming that there exists a value $\tilde{\beta}$ for which $\dot{R}_0 = 0$, I get the scaling

$$\dot{R}_0 = v_{acc.,in} \frac{1}{\beta_{out}} \left[1 - \left(\frac{\beta_{out}}{\tilde{\beta}} \right)^{1-\sigma} \right] , \tag{192}$$

where I use that $\Sigma_{in}/\Sigma_{out} \approx \beta_{in}/\beta_{out} = \beta_{out}^{-1}$ in my setup (see sec. 3.2.2.2 for more information on the role of β_{in}) and assumed a continuous magnetic field at the cavity edge. Equation 192 shows that when $\beta_{out} \ll \tilde{\beta}$, $\dot{R}_0 \approx v_{acc.,in}\, \beta_{out}^{-1}$, indicating that the cavity expansion velocity should increase as β_{out} gets lower, which is indeed the case for S2DB3BinoAmo.
On the contrary, for $\beta_{out} \gg \tilde{\beta}$, I get $\dot{R}_0 \approx -v_{acc.,in}\, \tilde{\beta}^{\,\sigma-1}\, \beta_{out}^{-\sigma}$, exhibiting a change of sign (and the cavity then shrinks), albeit with a reduced speed. S2DB5BinoAmo might lie within this regime, indicating that $\tilde{\beta} \simeq 10^4$.

Coming back to the global structure of the discs, the time-averaged profiles of the surface density and $\overline{\beta}$ of the fiducial run, S2DB3BinoAmo and S2DB5BinoAmo are given in fig. 43. It appears that the size of the cavity is ruled by the initial external plasma parameter. The lower β_{out} is, the wider the cavity gets once a steady state is reached. Therefore, the global aspect of the disc is fixed by the magnetisation in its outer parts but does not seem to depend on the initial one inside the cavity, as I discuss in the next subsection.

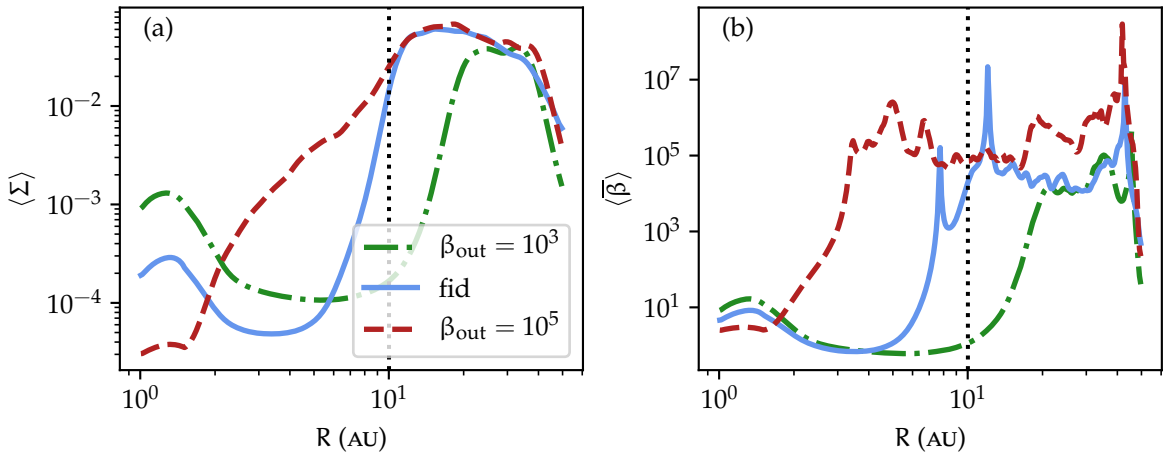

Figure 43: Time-averaged profiles of Σ (panel (a)) and $\overline{\beta}$ (panel (b)) for S2DB5BinoAmo (red dashed line), the 2.5 D fiducial run (blue full line) and S2DB3BinoAmo (semi-dashed green line). I average on the whole simulations minus the corresponding transient states. The peaks in the profiles of $\overline{\beta}$ are indicative of a sign flip of B_p.

3.2.2.2 *Role of the internal initial plasma parameter*

I study the impact of β_{in} by running a set of simulations covering all the possible initial ratios β_{in}/β_{out} where $\log \beta_{out} \in \{3, 4, 5\}$ and $\log \beta_{in} \in [\![0; \log \beta_{out}[\![$. I compare the result of each of these simulations to the one obtained with $\beta_{in} = 1$ and the corresponding value of β_{out}. The major result associated with this subsection states that the

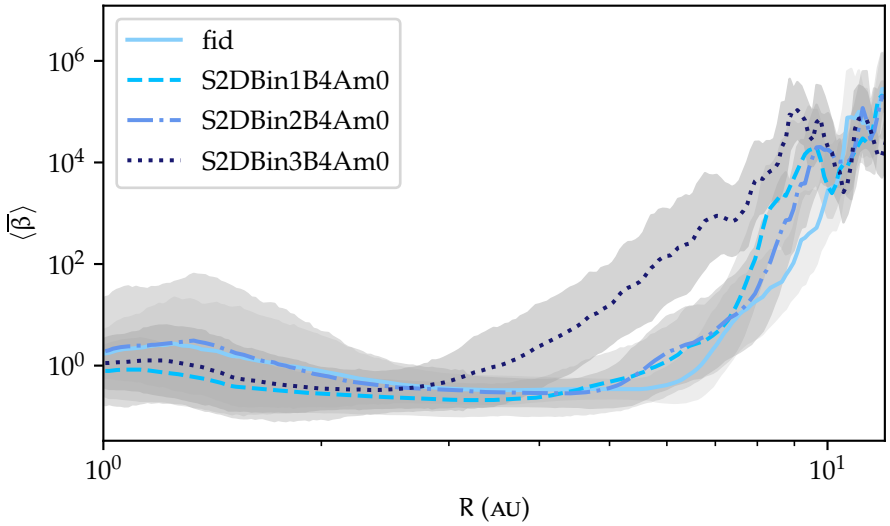

Figure 44: Impact of the internal initial value of β on the plasma parameter for $\beta_{out} = 10^4$. The figure shows the radial profiles of $\overline{\beta}$, time-averaged on the last 1000 orbits at R_{int} to cancel the effects of the transient state.

disc inner structure does not depend on β_{in}. Whichever β_{in} is initially set, a relaxation occurs during the initial transient so that the cavity reaches an imposed value of $\beta_{in} \approx 1$. Interestingly, this threshold value is the one required to have transsonic accretion, as mentioned in Wang and Goodman (2017). This statement is illustrated in fig. 44 in the case of $\beta_{out} = 10^4$, where all the simulations have converged to a same steady-state.

Of course, taking $\beta_{in} = \beta_{out}$ would create a full disc without any cavity. Therefore, a threshold value of β_{in} above which no cavity is able to form should exist. Looking at fig. 44 suggests that this threshold is at least greater than 10^3. Nevertheless, I ran an supplementary simulation with $\beta_{in} = 8000$ and $\beta_{out} = 10^4$. It appears that a cavity (that is fully similar to the cavity I have presented up until now) is also carved in this simulation, but on a much longer timescale, since the cavity radius equals 3 AU after 7000 orbits at R_{int}. Indeed, rather than a threshold value of β_{in}, the key notion at play may be a typical timescale $\tau_{cav.}(\beta_{in})$ to open a cavity. This a result indicate that transition disc could naturally arise from an almost full (if not full) inner disc.

I now give a special focus on the simulation S2DB4Bin3Am0 in order to investigate the relaxation that occurs in the cavity during the initial transient. In this prospect, I show a few handy profiles in fig. 45, that show the state of the cavity during the first 2000 orbits at R_{int}. The first panel of fig. 45 is the surface density and the relaxation

appears clearly while the cavity carves through time. This relaxation is due to matter leaving the cavity because of the fast accretion at play after a sharp increase of the magnetic field (and therefore a decrease of β). This increase of B_z is highlighted in the middle panel of fig. 45. The magnetic reorganisation of the cavity originates from the fast advection of the initial magnetic flux of the cavity down onto the seed (at $R = R_{int}$) which is initially poorly magnetised (compared to its asymptotic magnetisation), according to my initial setup.

Because the total magnetic flux is conserved, a shortage of magnetic flux occurs inside the cavity since its magnetic field is caught by the seed. At some point, the seed reaches a state where its magnetisation is almost constant (i. e. a magnetically saturated state). This saturation is shown with fig. 46. It appears that the saturation value is the same for all the simulations and therefore characteristic of the disc.

Once the seed saturates, the magnetic field accumulates at the inner boundary so that β decreases accordingly and accretion is enhanced. At this point, matter is strongly accreted. The cavity is drained of gas and finally converges towards the same state as in the 2.5 D fiducial run.

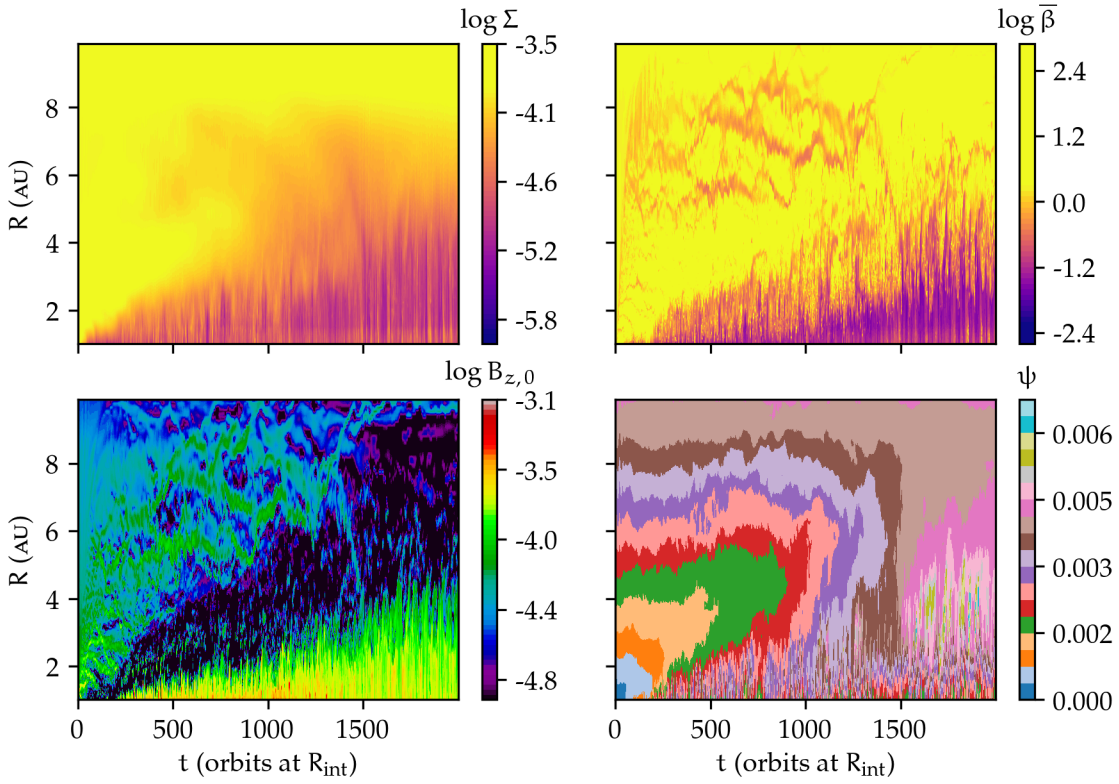

Figure 45: Spatio-temporal diagrams of Σ (top left panel), $\overline{\beta}$ (top right panel), $B_{z,0}$ (bottom left panel) the vertical magnetic field at the midplane and ψ (bottom right panel) the flux function defined in eq. 184. These profiles focus on the first orbits of the run S2DB4Bin3Amo.

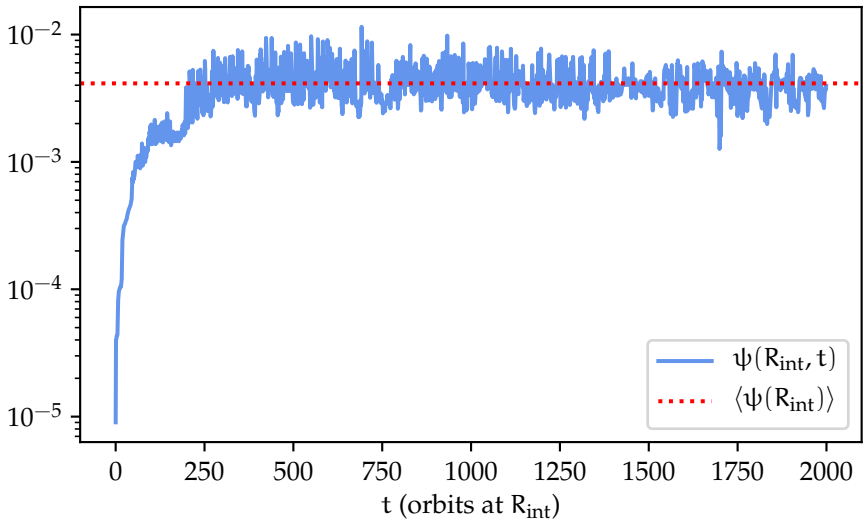

Figure 46: Magnetic saturation of the seed for S2DB4Bin3Amo. The profile shown in full blue line is the flux function ψ during the first 2000 orbits at R_{int} of the simulation, calculated at R_{in}. The red dotted line is same quantity, time-averaged on 6000 orbits at R_{int} after the saturation is reached.

From these observations, I deduce that the cavity is regulated so that the plasma parameter must reach a characteristic value of $\beta \sim 1$. The physical process underlying this transition is not entirely clear and I add a word of caution regarding the role of the inner radial boundary condition, especially with respect to the magnetic field transport at R_{int}. One could naturally invoke the RTI as responsible for the regulation of the cavity, however and referring sec. 3.1.5.4, it seems that it is hardly the case.

3.3 CONCLUSIVE REMARKS ON THE 2.5 D SIMULATIONS

I end this chapter with the current section devoted to a few conclusive remarks on my 2.5 D simulations. I will not detail any caveat of my model here and rather refer the reader to chap. 6 that contains discussions regarding the caveats of all my work (2.5 D and 3 D simulations). The description of a few 'safety' runs (e. g. studying the impact of the spatial resolution) is given app. B. For now, I start with a general scheme describing transition discs in the picture of MHD winds before moving to a brief discussion regarding these simulations.

3.3.1 *Unveiling a conclusive general scheme for transition discs*

Figure 47 pictures a model for transition discs (the cavity and the external disc are shown in light and darker orange) under the scenario

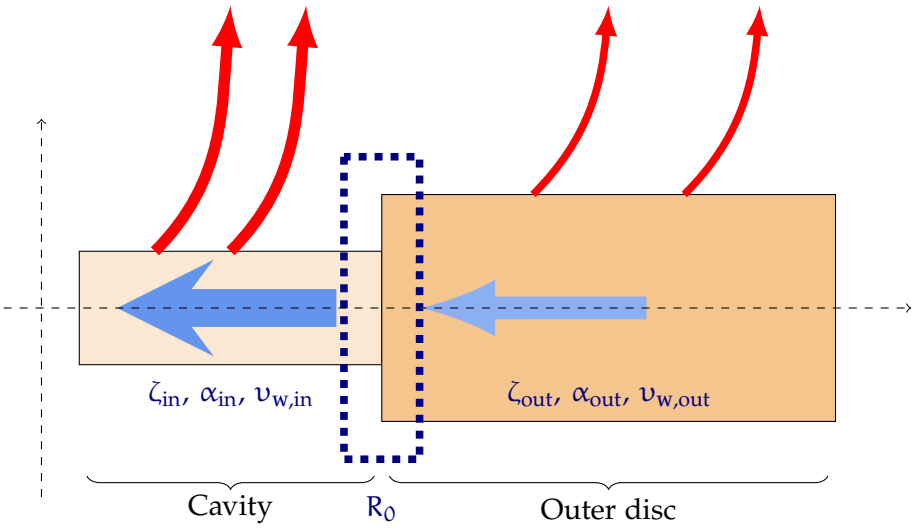

Figure 47: Schematic view of the cavity connected to the outer disc. Though of the same order of magnitude, the accretion rates are slightly mismatched.

of MHD winds (shown with red arrows). My simulations tend to show that the inner transport coefficients (labelled by "in") are regulated and do no vary on β_{in} (namely the gap in density).

On the contrary, the external transport coefficients (labelled by "out") directly depend on β_{out} and control the size of the cavity R_0, suggesting that some global magnetic flux regulation occurs in the disc as a whole. This trends seems confirmed by the non-local influence of the cavity on the magnetic field transport as discussed in sec. 3.1.5.2.

Conclusively, the cavity and the external discs see their magnetic configuration adapting to each other, in such a way that the transport of angular momentum happens smoothly through the disc. The remaining transport coefficient ν_B is affected to a regulator role through its complex behaviour in the whole disc, regarding the transport of magnetic flux.

Coming back to eq. 192, I can express the accretion rate in terms of the 2 sets of transport coefficients (the internal and external ones) and take into account the effect of the wind on the mass loss rate (by considering ζ or not) for a complete calculation. I model any transport coefficient X (among ζ, v_w and α) with a step function so that $X = X_{in}$ inside the cavity and $X = X_{out}$ in the external disc. Under this simple assumption, I find that

$$\frac{\dot{R_0}}{v_K} = \frac{1}{G-1}\left[2\,\varepsilon^2\,\alpha_{in}\left(1 - G\,\frac{\alpha_{out}}{\alpha_{in}}\right) + \varepsilon\sqrt{\frac{2}{\pi}}\,\nu_{B,in}\left(1 - G\,\frac{\nu_{B,out}}{\nu_{B,in}}\right) - \zeta_{in}\left(1 + G\,\frac{\zeta_{out}}{\zeta_{in}}\right)\right], \tag{193}$$

where $G \equiv \beta_{out}/1$ is the gap, since the cavity regulates itself until the inner β is 1. The square bracket plays the role of the one

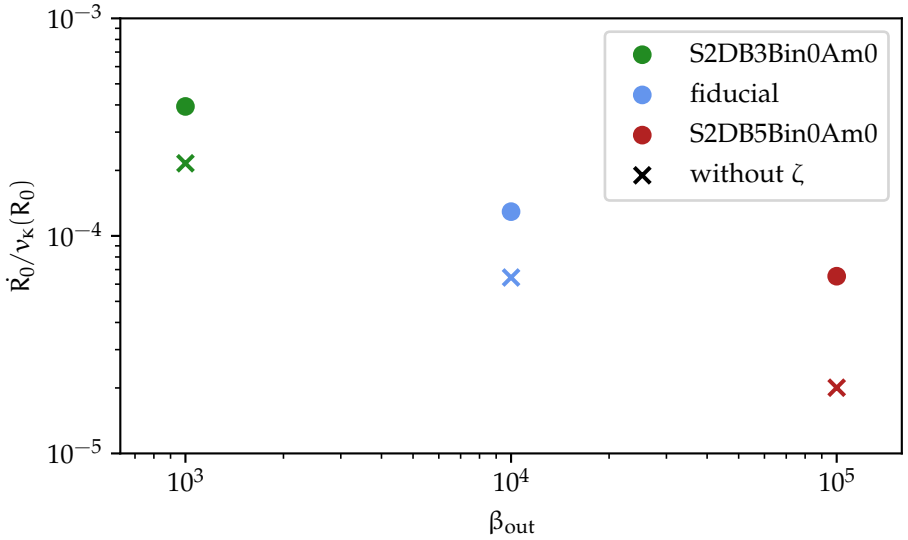

Figure 48: Widening velocity (calculated from eq. 193) of the cavity with respect to the initial external plasma parameter.

in eq. 192 and is of the order of a few, since $G\,X_{out}/X_{in} \sim 1$ and $\varepsilon^2\,\alpha_{in} \sim \varepsilon\,\nu_{B,in} \sim \zeta_{in}$. A change of sign (i. e. having an expanding or a shrinking cavity) could very well occur in the parenthesis. The corresponding estimated values for $\dot{R}_0$ are shown in fig.48 and are coherent with the measured ones. In particular, the influence of ζ seems negligible (see the crosses, that represent $\dot{R}_0/v_K$ calculated with $\zeta \to 0$).

3.3.2 *Final remarks on the 2.5 D simulations*

I modelled transition discs sustained by MHD winds by performing 2.5 D global simulations. This model is promising as the simulated cavities are persistent with time.

On long time-scales, the magnetic field strength is self-regulated with $0.1 \lesssim \beta \lesssim 1$ in the cavity, for any initial configuration. The cavity is strongly magnetised and rotates at sub-Keplerian velocities. The magnetic support is intense enough to counter gravity. The saturation of the inner seed also favours this idea. The cavity is comparable to the magnetically arrested disc (MAD) proposed by Narayan et al. (2003) in the context of black hole accretion discs, despite the use of Newtonian dynamics in my simulations (MADs are usually obtained in the context of GRMHD simulations) and despite the presence of a strong ambipolar diffusivity. This idea is developed in the next chapters.

A last point worth mentioning is the fact that the time variability

of the cavity may be related to the axisymmetric approximation used in my 2.5 D simulations. In particular, non-axisymmetric instabilities such as the Rossby Wave Instability (RWI) (Lovelace et al., 1999; Li et al., 2000) could challenge the stability of the cavity. This is why a part of my work focuses on 3 D simulations and on the stability of the cavity. I will present the results of this work in the next chapter.

CONCLUSION

My 2.5 D simulations prove that it is physically meaningful to address the question of highly-accreting TDS with magnetic winds. The resulting cavities are long-lived and characterised by strong accretion rates.
Regarding the overall structure of the discs, I find two accreting regimes. The inner one is the cavity, the second one is the full disc. Their respective transport coefficients are not continuous at the transition between the two regimes which is located at the external edge of the cavity. These discontinuities enable a smooth transition of the accretion rate.
The disc organises itself in a way that makes possible a smooth transport of angular momentum throughout the whole disc, sustained by the magnetic wind. In particular, an elbow-shaped structure together with a poloidal magnetic loop are detected at the transition between the cavity and the full disc.

However, I detect a slight mismatch between the inner and external accretion rates that is linked to the slow evolution of the disc and to the widening of the cavity.
The magnetic field transport exhibits a complex behaviour in the disc that is linked to the long-term evolution of the disc.
Regarding the fast variability of the cavity, I detect bubbles of gas that are created at the elbow structure location and probably due to magnetic reconnection events.

The parameter exploration shows that the external disc is controlled by β_{out} while the structure of the cavity does not depend on the initial value of β_{in}. Any simulated disc ends up with a well-defined seed magnetisation, that controls the innermost accretion rate.
Conclusively, the inner saturation of the magnetisation and the strong magnetic support in the cavity recall the MAD picture.

CONCLUSION

Mes simulations 2,5 D montrent qu'il est physiquement pertinent d'envisager que les disques de transition accrétant fortement soient soutenus par des vents magnétiques. Les cavités ainsi obtenues persistent dans le temps avec des forts taux d'accrétion. Ce résultat déterminant souligne tout l'intérêt de ce modèle qui permet de reproduire des disques de transition avec une cavité suffisamment large (de taille supérieure à $1-5$ UA) et une accrétion vigoureuse.

En ce qui concerne la structure générale de tels disques, je trouve que ceux-ci présentent deux régimes dynamiques différents, qui se reconnectent l'un l'autre au niveau de la frontière externe de la cavité. Cette dernière constitue le régime interne, le second étant incarné par le disque externe standard.

Les coefficients de transport de ces deux zones ne sont pas continus et présentent une différence de plusieurs ordres de grandeur au niveau de la cavité. Cependant, ces écarts majeurs permettent d'obtenir un taux d'accrétion quasiment continu dans tout le disque. En particulier, le disque adopte une structure générale qui permet un transport continu de moment cinétique dans la totalité du disque en accolant ces deux régimes dynamiques différents, tous deux soutenus par un vent magnétique.

Toutefois, je constate un léger écart entre le taux d'accrétion de la cavité et celui du disque externe. Cet écart rend possible une évolution séculaire de la cavité, se traduisant par un élargissement de cette dernière. Du fait d'une l'accrétion dans la cavité légèrement plus intense, la cavité s'errode petit à petit.

Le transport du champ magnétique présente lui aussi un comportement complexe avec une évolution sur de longues échelles de temps. Contrairement à divers travaux sur des disques magnétisés dans lesquels le champ magnétique est diffusé vers l'extérieur, j'observe un phénomène d'advection du champ magnétique dans mes disques.

La cavité est également soumise à une variabilité sur de courtes échelles de temps. Des bulles de gaz se forment au dessus de la boucle de champ magnétique poloidal lorsque des filaments de matière se scindent en deux, possiblement après un événement de reconnexion magnétique. Ces bulles de gaz tombent ensuite sur le bord externe de la cavité avant de la traverser en générant un pic d'accrétion.

L'exploration des paramètres révèle que la magnétisation externe initiale contrôle le disque externe, tandis que la cavité est indépendante de la magnétisation interne initiale. Plus précisément, la cavité se réorganise de manière à atteindre un même état, indépendamment de sa magnétisation initiale. Ce point rejoint le fait que la magnétisation de la graine centrale (la "seed") sature à une valeur donnée, contrôlant de fait l'accrétion au bord interne.

Finalement, la saturation de la magnétisation interne et le fort support magnétique dans la cavité rappelle le modèle MAD des disques d'accrétion autour des trous noirs.
Je développerai ce point notamment à l'issue du chapitre suivant qui traite de la stabilité de la cavité vis-à-vis d'instabilités hydro- et magnétohydrodynamiques.

Je poursuivrai également l'étude du modèle 2,5 D dans le chapitre 5, notamment en implémentant une troncation externe exponentielle à mon modèle et en simulant le disque sur une plage de temps dix fois plus longue.

4

3 D SIMULATIONS: STABILITY OF THE CAVITY

"The Sky is low - the Clouds are mean.
A Travelling Flake of Snow
Across a Barn or through a Rut
Debates if it will go -
A Narrow Wind complains all Day
How some one treated him
Nature, like Us is sometimes caught
Without her Diadem -"

— Emily Dickinson, *Je cherche l'obscurité* (1866)

INTRODUCTION

The previous chapter gave a general overview for transition discs sustained by magnetic winds. In particular, the secular evolution of the discs was deeply investigated (through the study of the accretion rate, the transport coefficients and the magnetic field transport in particular). The edge of the cavity appears to play a key role in the physics of transition discs sustained by MHD winds. However, 2.5 D simulations cannot characterise the stability of the frontier between the cavity and the full disc. In particular, hydro- and magnetohydro-instabilities could be triggered and affect the gas inside the cavity, which is why 3 D simulations are needed.

This chapter is devoted to a set of 3 D simulations (a fiducial one and a parameter space exploration). Its aim is to get a description of magnetic winds emitting transition discs in 3 D as well as to get an insight on physics at play in the cavity. In particular, I will study a few instabilities.

I will start with the fiducial 3 D simulation, describing its general properties before moving to salient results regarding the cavity, inside which spirals are detected. Eventually, I will describe additional 3 D simulations in a parameter space exploration.

INTRODUCTION

Le chapitre précédent m'a permis de donner une vue générale des disques de transition supportés par des vents magnétiques. Plus précisément, ces simulations m'ont donné accès à l'évolution séculaire de tels disques, notamment via l'étude du taux d'accrétion, des coefficients de transport et du transport du champ magnétique. Comme on pouvait s'y attendre, la frontière entre la cavité et le disque plein joue un rôle crucial de zone de transition dans ce modèle de disques. Malgré leurs avantages, en particulier en termes de coûts numériques, les simulations 2,5 D ne permettent pas d'étudier la stabilité de cette frontière au regard d'instabilités hydro et magnétohydro dynamiques, qui se manifesteraient de manière non axisymétriques. Une telle tâche doit donc être attribuée à des simulations à 3 dimensions, permettant de capture la physique en jeu dans la direction toroïdale.

Le présent chapitre s'attache à l'étude d'un jeu de simulations 3 D constitué d'une simulation fiduciaire et d'une rapide exploration de l'espace des paramètres, similaire à celle effectuée à 2,5 dimensions. Les objectifs premiers sont d'aboutir à une description globale de ces disques de transition à 3 dimensions et de fournir des pistes quant à la stabilité de la cavité (de sa frontière et du gaz qu'elle contient) vis-à-vis d'instabilités.

Je débuterai par une étude détaillée de la simulation de référence en me focalisant sur la structure du disque, avant d'établir les résultats les plus pertinents concernant la stabilité de la cavité. Enfin, ce chapitre s'achèvera sur une exploration de l'espace des paramètres.

Short reminder

For this chapter, I keep on using the notation $\overline{X}$ which does include a vertical integration as well as an azimuthal average. If not defined otherwise, one should assume that $\overline{X \times Y} \neq \overline{X} \times \overline{Y}$. When needed alone, the azimuthal average is denoted $\langle X \rangle_\varphi$. As an example, the surface density is defined as

$$\begin{aligned}\Sigma(R,t) &\equiv \overline{\rho}(\mathbf{r},t)\,,\\ &= \frac{1}{2\pi}\int_0^{2\pi}\int_{\theta_-}^{\theta_+} r\,\rho(\mathbf{r},t)\,\sin\theta\,d\theta\,d\varphi\,.\end{aligned}$$

In some cases (for example to check the influence of non-axisymmetries), I may use $\Sigma_{2D}(R,\varphi,t)$ defined as

$$\Sigma_{2D}(R,\varphi,t) \equiv \frac{1}{\mathcal{N}}\int_{\theta_-}^{\theta_+} r\,\rho(\mathbf{r},t)\,\sin\theta\,d\theta \equiv \langle\rho(\mathbf{r},t)\rangle_\theta\,,$$

where $\mathcal{N} \equiv 2\,\varepsilon/\sqrt{1+\varepsilon^2}$ is a normalisation factor so that $\langle\cdot\rangle_\theta$ can be thought as an average procedure.
Moreover, I recall that most of my 3 D simulations are restarted from a corresponding 2.5 D one. Shall it be done otherwise for a few simulations, I will precise it clearly.
Finally, because of the considerable computational time needed for 3 D simulations, these ones are only run for at most $\sim$ 1000 orbits at R_{int} or so. This represents 3 % of the 2.5 D fiducial simulations, so that these simulations are not designed to address the same questions as the 2.5 D simulations. They aim at investigating the stability of the cavity.
For any supplementary information, I refer to chap. 2.

4.1 RECOVERING THE PROPERTIES OF TDS WITH 3 D SIMULATIONS

Before portraying the salient and specific results of my 3 D simulations, I aim to recover some of the main properties of TDs harbouring magnetic winds that I obtained with my 2.5 D simulations. I also want to stress the differences regarding the structure of such discs when the assumption of axisymmetry is dropped. In this prospect, I will start with the general structure and evolution of the discs and focus on its properties such as the accretion rate and the wind characteristics.
The only simulation used in this section is the 3 D fiducial one that is labelled by S3DB4BinoAmo, and which was restarted from the corresponding 2.5 D fiducial simulation after 7558 orbits at R_{int}.

I recall that my 3 D simulations are all restarted from 2.5 D simulations after $\approx$ 7000 orbits at R_{int}. See the second chapter (chap. 2) for more precise explanations on this procedure.

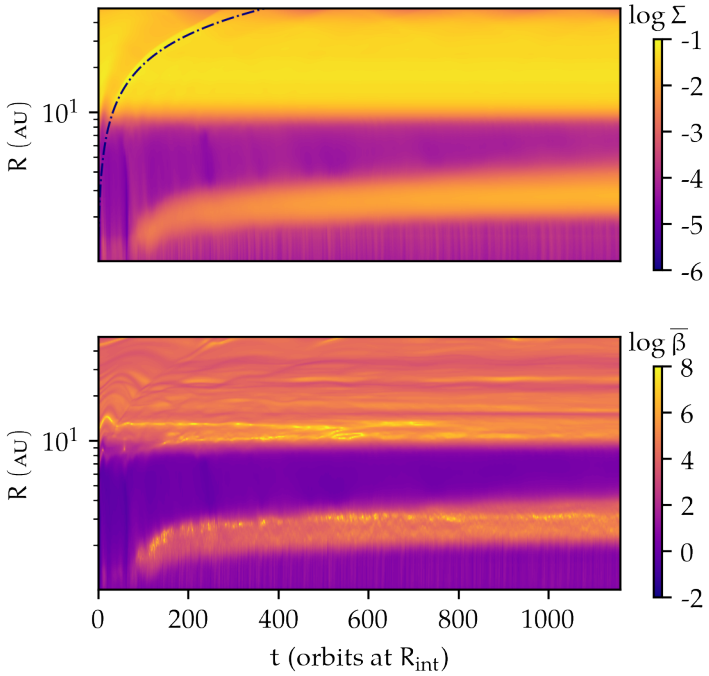

Figure 49: Spatio-temporal diagrams of Σ (upper panel) and $\overline{\beta}$ (lower panel) for the 3 D fiducial simulation. The dark blue semi-dashed line in the upper panel shows a sonic shock wave characteristic (see sec. 4.1.2).

4.1.1 *General evolution of the disc*

As for any previous simulation, I start with the spatio-temporal diagrams of the surface density and of the plasma parameter. The corresponding profiles are given in fig. 49, where I keep the very same definition of $\overline{\beta}$ that I used previously (and which includes the azimuthal average). At first glance, these profiles are fairly comparable to the 2.5 D corresponding ones (see fig. 18). The external discs exhibit similar surface density, but it is worth noting that the profile of the plasma parameter is much smoother in 3 D. The most striking difference lies within the profiles in the cavity where a clear bead forms, at $R \approx 2.6$ AU. Considering the full midplane of the disc reveals that this bead is indeed a full ring. From now on, I will refer to this structure as 'the inner ring' or just 'the ring'.
Moreover, the stripes that were seen in the 2.5 D simulations are now located between the ring and the inner boundary condition, but are hardly detected between the ring and the cavity edge. The region where most of the cavity spans is therefore smoother, suggesting a continuous flow of matter through it.

A closer inspection of the profiles is given with fig. 50, which gives

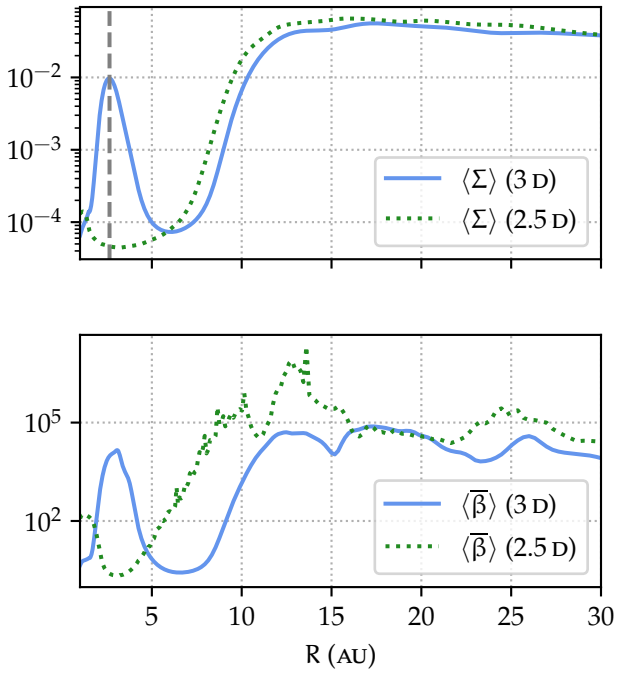

Figure 50: Time-averaged profiles of Σ (upper panel) and $\overline{\beta}$ (lower panel), with a comparison between 2.5 D and 3 D fiducial simulations. The values taken into account for the 2.5 D simulation are kept between 7558 orbits at R_{int} and up to $7558 + 1000$ orbits at R_{int}. This way, both simulation are compared meaningfully. The vertical grey dashed line at $R = 2.6$ AU in the profile of $\langle\Sigma\rangle$ indicates the location of the inner ring.

The time-averages of the 3 D profiles are performed without considering the transient state (which is inferred to span until ~ 300 orbits at R_{int} from fig. 49).

the time-averaged profiles of Σ and $\overline{\beta}$. The external parts of the discs appear to be similar between the 2.5 D and 3 D simulations, while the simulated cavities are slightly different. This graph clearly emphasizes the presence of an additional inner ring in the 3 D simulation, especially in the surface density profile (upper panel of fig. 50, see the vertical grey dashed line). The plasma parameter $\overline{\beta}$ directly time-averaged is smoother than in the corresponding 2.5 D simulation as previously suggested. Its profile also reveals a much 'cleaner' cavity in the sense that $\overline{\beta}$ is roughly constant and equal to 1 in the cavity, between the ring and its outer edge. This has to be related to the absence of bursts of matter in this region.

The radial profile of $\langle\overline{\beta}\rangle$ is also characterised by local minima (one at 15 R_{int} and the other between 20 and 25 R_{int}), which seems to correspond to two faint local minima of $\langle\Sigma\rangle$.

Finally, I want to stress a basic yet major result. The cavity remains stable with time and the disc reaches a steady state. Such key results are then confirmed by 3 D simulations and despite being obvious when looking at fig. 49, they must not be overlooked.

4.1.2 *Reorganisation of the disc*

Figure 49 exhibits a sonic shock wave propagating through the disc whose characteristic curve is plotted over the profile of Σ and defined by

$$t - t_1 = \frac{1}{3\pi\varepsilon}\left(R^{3/2} - R_1^{3/2}\right), \tag{194}$$

I assume that the sonic shock wave starts at $R_1 = 1\ R_{int}$ at $t_1 = 0$ orbits at R_{int}.

where t is the time given in orbits at R_{int} and R the radius in units of R_{int}. This shock wave is part of a reorganisation of the disc as a whole and changes its general structure (I detail this point in the upcoming sec. 4.1.3).

This reorganisation points out that the 2 D structure of my simulated TDs somehow relies on the axisymmetry assumption. Moreover, this suggests a release of the magnetic stresses due to non-axisymmetries.

4.1.3 *Structure of the disc*

4.1.3.1 *Magnetic structure of the disc*

The temporal evolution of the disc and its initial reorganisation are as many clues that there may be a shift occurring in the magnetic structure of the disc. With this idea in mind, I give the azimuthally and time-averaged toroidal magnetic in fig. 51, on which the azimuthally and time-averaged poloidal magnetic field lines are plotted.

From now one, any time-averaged calculation does not take into account the transient state of the simulation.

Inside the cavity, the magnetic structure is similar to the one in 2.5 D and the poloidal magnetic field lines are pinched at the midplane. The toroidal magnetic field above the disc midplane is negative and positive below it. Such a general structure is expected and recovered from 2.5 D simulations.

The outer disc is still separated from the cavity by a magnetic loop, however this one is much less prominent in 3 D simulations. The loop spans between $h/R = \pm 0.3$ where it used to go up and down to $h/R = \pm 0.6$ so that it is overall twice smaller in 3 D. The characteristic elbow-shape pattern has disappeared above and below the loop, along with the reorganisation of the disc. Nevertheless, the poloidal magnetic field lines still bent at the disc surface and this bending is a remnant of the elbow pattern.

The most striking magnetic structure lies inside the external disc where the magnetic poloidal field lines are roughly vertical. The vertical profile of the toroidal magnetic field undergoes at least 3 changes of sign. Starting from below the surface defined by $h/R = -0.3$ (black full line on fig. 51), $\langle\langle B_\varphi\rangle_\varphi\rangle$ is positive. A first change of sign occurs at $h/R = -0.3$, before a second one is detected between $h/R = 0.3$ and $h/R = -0.3$. The location of the second sign flip is not well located and varies radially, conferring a non-symmetric pattern to the vertical magnetic structure with respect to the disc midplane. However, the

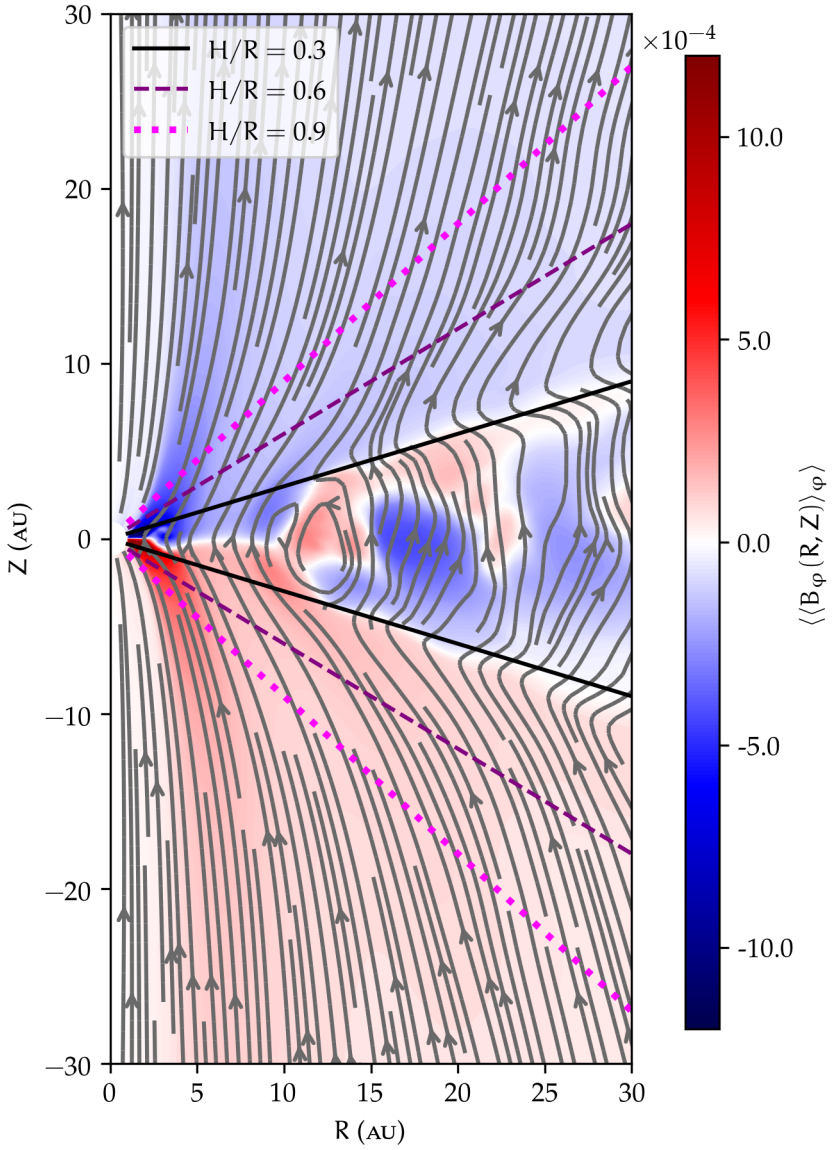

Figure 51: Azimuthally and time-averaged poloidal profile of the toroidal magnetic field, over which the poloidal magnetic field lines are plotted (and averaged under the same procedures).

last change of sign occurs at $h/R = 0.3$ in a symmetric way with the first one.

Therefore, some top/down asymmetries are to be expected regarding the disc vertical structure while the peculiar features inherent to the previous elbow-shape pattern are likely to be gone. I define $\mathcal{S}_B$ as the surface where $\langle\langle B_\varphi\rangle_\varphi\rangle = 0$ between $h/R = \pm 0.3$. This surface is highly dynamical. The toroidal magnetic field is a key quantity in particular because its sign and topology are linked to the wind, through the bending of the poloidal field lines. Another example of structures regarding the sign flips of $\langle B_\varphi\rangle$ are the patterns characteristic of MRI dynamos (Flock et al., 2011, see for example) that appear in turbulent discs with a net initial toroidal field. Such an effect is known to be shut down by non-ideal MHD effects (Bai and Stone, 2013a; Simon et al., 2013) and is not expected in my simulations.

The figure 52 shows the spatio-temporal diagram of the toroidal magnetic field, azimuthally-averaged and computed at a $R_{shell} = 15$ AU, and along a spherical shell (the diagram focuses on the region close to the midplane). Far above (resp. below) the disc plane, $\langle B_\varphi\rangle_\varphi$ is negative (resp. positive), accordingly with fig. 51. Between $z/R_{shell} = \pm 0.3$, multiple sign flips are detected (up to 5 before 700 orbits at R_{int}, which account for $\mathcal{S}_B$ being far from horizontal). This toroidal configuration is linked to the wind topology (Cui and Bai, 2021) and to the fact that the poloidal field lines are not perfectly vertical in the disc.
Eventually, $\mathcal{S}_B$ converges toward a steady configuration with 3 sign flips (the central one being located close to the midplane). This structure is reminiscent of the 2.5 D simulations, so that I expect the global magnetic configuration to recover its 2.5 D topology with a smaller loop and no more elbow pattern.

4.1.3.2 *Velocity and angular momentum flux stream lines*

I show the azimuthally and time-averaged streamlines over the profile of $\langle\langle\rho\rangle_\varphi\rangle$ in fig. 53. In the cavity, and similarly to the profile of the toroidal magnetic field component, the structure of the disc looks alike the 2.5 D corresponding simulation, with matter leaving the depleted disc in the wind above and below its midplane. The inner ring is clearly visible, close to the inner boundary condition.
As expected from the analysis of the magnetic structure, the elbow-structure faded away. The disc is now left with 2 surface flows right above and below the surfaces $z/R = \pm 0.3$ (which I recall correspond to the disc surface), pointing towards the star. The falling matter generates surface accretion, up until it reaches the cavity and crosses it in a horizontal motion. The falling material partially leaves the disc surface in the wind, a fraction of which then falls back onto the disc further out. This motion results in thin clockwise loops located at the

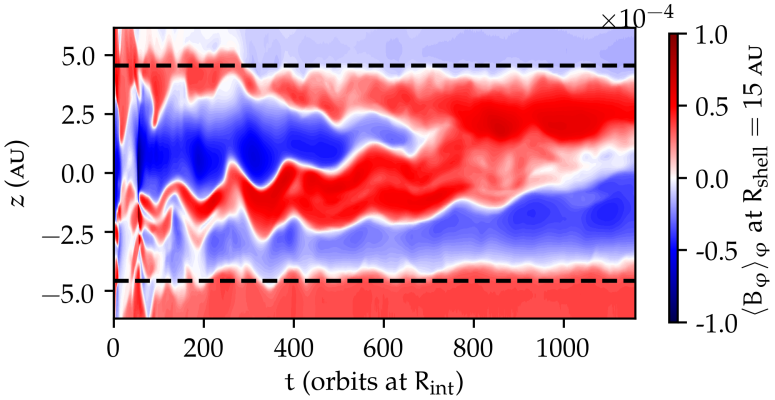

Figure 52: Spatio-temporal diagram of $\langle B_\varphi \rangle_\varphi$, computed vertically along a spherical shell of radius $R_{shell} = 15$ AU, between $z/R_{shell} = \pm 0.4$. The transient state is left and the disc reorganisation is once again clearly seen. The black dashed lines represent the surfaces defined by $z/R_{shell} = \pm 0.3$.

disc surface. This behaviour highlights the surface accretion occurring in the external disc.

I detect meridional circulation close to the midplane of the outer disc. This kind of circulation was also observed in previous simulations of turbulent PPDs (Fromang et al., 2011) and of PPDs with magnetic winds (Béthune et al., 2017). The figure 53 shows some complex vertical motions forming vortices, which are similar to the one observed by Riols et al. (2020) (see their fig. 7). Figure 54 emphasizes 2 vortices located from either side of $R = 15$ AU whose resulting shapes are asymmetric with respect to the midplane. They are separated by the surface $\mathcal{S}_B$ and turns in opposite direction (clockwise on the right and anti-clockwise on the left). The location of these vortices matches with the local minima of $\langle \overline{\beta} \rangle$ and $\langle \Sigma \rangle$ (see fig.50). The motion of matter at the frontier between 2 vortices indicates that matter can reach the disc surface from the midplane.

To end up with the disc time-averaged structure, I show the corresponding profile for the angular momentum flux field lines in fig. 55. It appears clearly that angular momentum is removed from the disc surface and from the cavity by the wind. Contrary to the 2.5 D fiducial simulation, the angular momentum loss is very well localised at the disc surface in the outer disc, once again indicating surface accretion. All the previous complex structures overlap to allow angular momentum to be lost in the wind and dragged outwards in a homogeneous fashion. At the disc midplane, the angular momentum seems to accumulate which would lead to decretion.

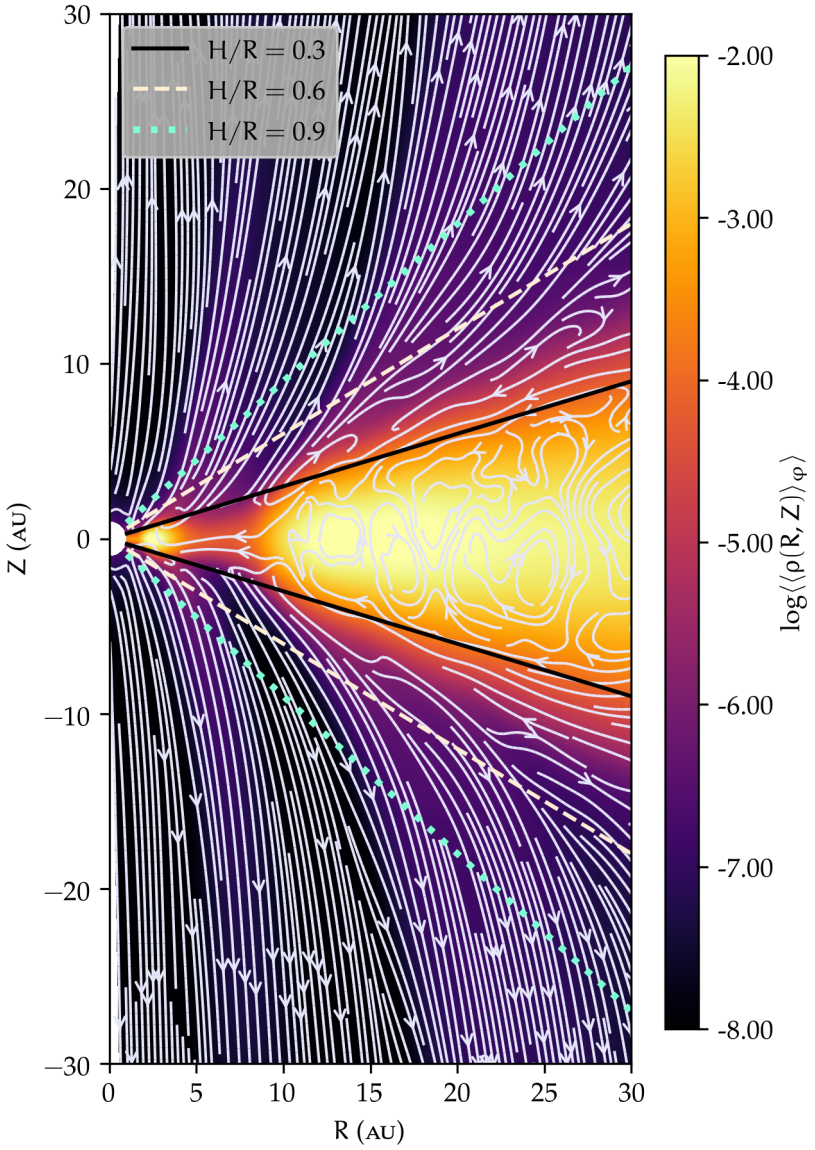

Figure 53: Azimuthally and time-averaged poloidal profile of the density, over which the stream lines are plotted (and averaged under the same procedures).

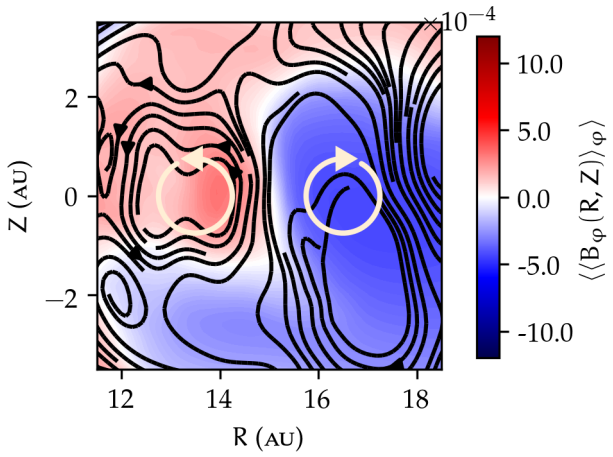

Figure 54: Zoom on 2 vortices seen in fig. 53. The background field is the toroidal magnetic field over which are plotted the stream lines. Both are azimuthally and time averaged. The arrows indicates the rotation of each vortex.

4.1.4 *Accretion theory*

My 3 D simulations were not designed to retrieve the secular evolution of TDS subject to MHD winds. This assertion is mostly due to the computational cost of a single 3 D simulation compared to its corresponding axisymmetric one. Nevertheless, I can still very well study the accretion rate as well as the transport coefficients in order to check their orders of magnitude and compared their corresponding profiles to the 2.5 D structure. Let me start with the accretion rate first.

The radial time-averaged profiles of $\dot{M}$ are given in fig. 56. I computed the accretion rates for $\varepsilon_{\text{int}} = 0.9$ and compare the fiducial 3 D simulation with the 2.5 D one.
The accretion rate between the inner boundary condition and the inner ring is $\langle \dot{M}_1 \rangle = 3.5 \times 10^{-8}\ M_\odot\ yr^{-1}$. This value is very close to 4 times lower than the accretion rate in the cavity in the fiducial 2.5 D simulation. Between the ring and the cavity edge, the accretion rate is $\langle \dot{M}_2 \rangle = 8.2 \times 10^{-8}\ M_\odot\ yr^{-1}$. In this area, the accretion rate profile is constant with the radius. Finally, the $\langle \dot{M}_3 \rangle = 1.4 \times 10^{-7}\ M_\odot\ yr^{-1}$ between $R = 12$ and 15 AU. At greater radius ($R > 15$ AU), the accretion exhibits a radial oscillation that could account for the vortices detected in the structure of the flow (see fig. 53).
These different areas unveil the following radial structure. The inner ring arises from a drop in the accretion rate, since $\langle \dot{M}_1 \rangle \approx 2-3\ \langle \dot{M}_2 \rangle$ and recalls the accumulations of matter seen in the cavity for weakly magnetised 2.5 D simulations. I therefore expect this ring to be a transitory structure that could dissipate on long enough time-scales. In-

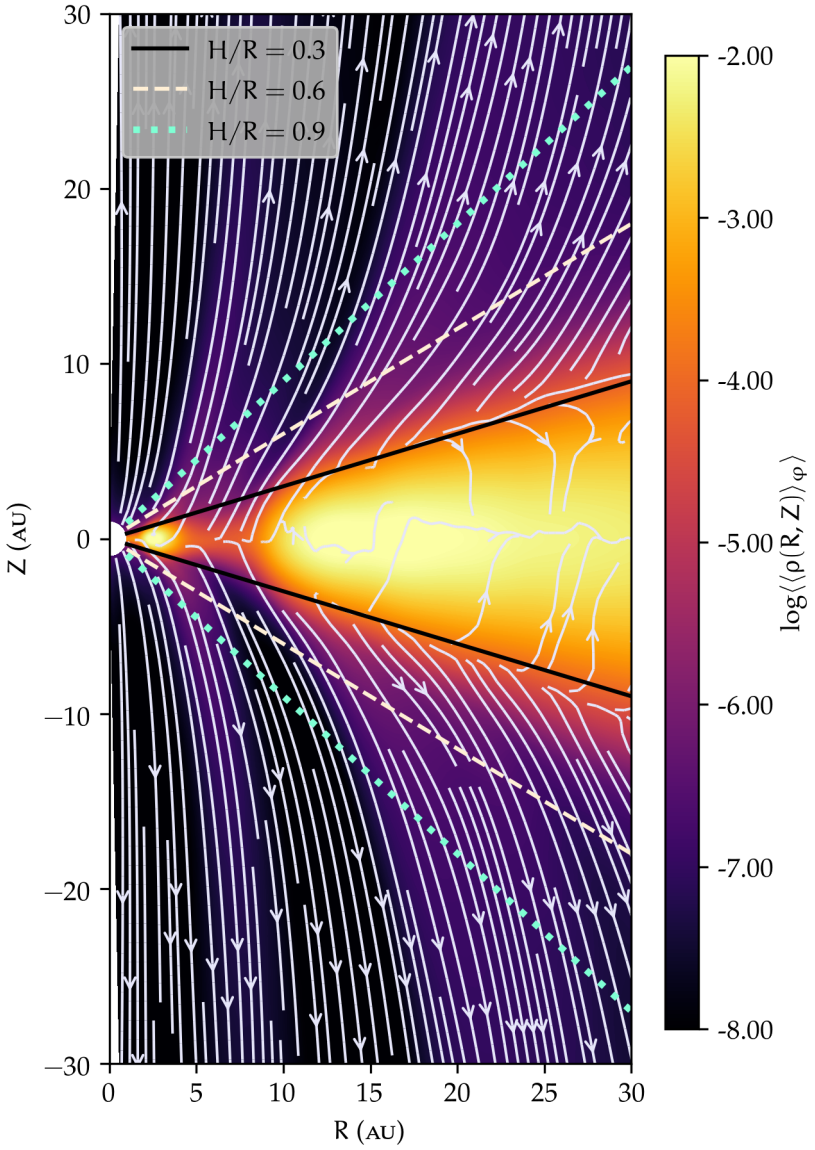

Figure 55: Azimuthally and time-averaged poloidal profile of the density, over which the angular momentum flux stream lines are plotted (and averaged under the same procedures).

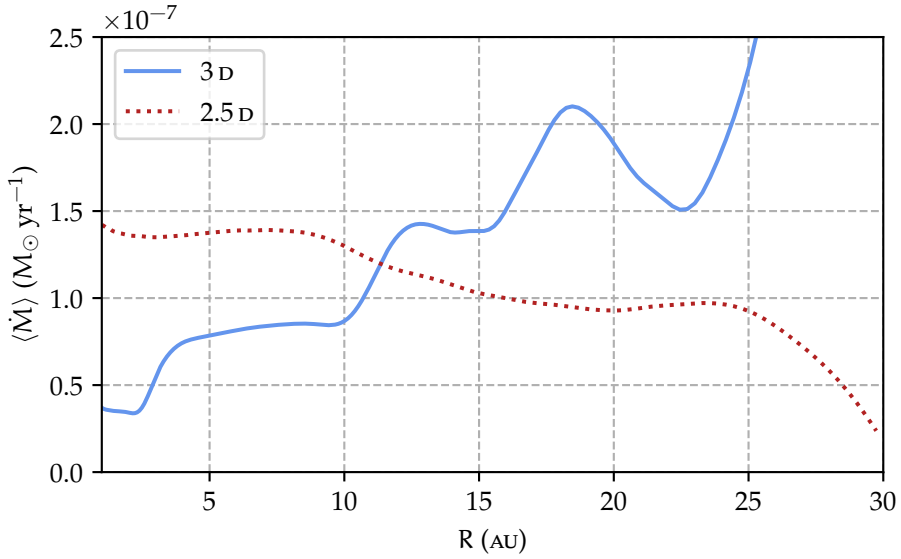

Figure 56: Azimuthally and time-averaged accretion rates for $\varepsilon_{\rm int} = 0.9$. The blue full line corresponds to the 3 D fiducial simulation and the red dashed one to the 2.5 D one for comparison.

side the cavity, the flatness of the accretion rate suggests a continuous and steady accretion flow, close to $\sim 10^{-7}\ M_\odot\ yr^{-1}$. The third value of $\dot{M}$ that I highlighted suggests a stronger accretion rate in the external disc than in the cavity. This result contrasts with the 2.5 D simulations and especially affects the temporal evolution of the cavity edge. However, the 3 D simulation does not last long enough to draw definitive conclusions on the secular evolution of the cavity. Because of lower magnetic torques, it takes much more time to dissipate the ring and reach a configuration with a stronger inner accretion rate (like in 2.5 D simulations).

For the sake of completeness, I give the profiles of the transport coefficients in fig. 57. I find the same ordering than the one found in 2.5 D simulations, which reads

$$\langle \alpha \rangle \gg \langle v_w \rangle \gg \langle \zeta \rangle \,. \tag{195}$$

Regardless of the inner ring influence, the profile of $\langle \alpha \rangle$ is fairly identical to its 2.5 D counterpart. The effect of the ring translates into a drop of $\langle \alpha \rangle$ at the ring location. The mass-loading parameter is now positive in the whole disc. This confirms that the negative parts of ζ in 2.5 D are due to the elbow-shaped pattern. The most striking difference is the maximum value of $\langle v_w \rangle$ reached in the cavity, which is ~ 10 times lower than in 2.5 D. It is worth noting that the peak value of $\langle \alpha \rangle$ is also ~ 3 times lower in 3 D. As a conclusion, the decrease of the magnetic torques inside the cavity leads to lower transport coefficients, especially regarding the vertical transport of angular momentum.

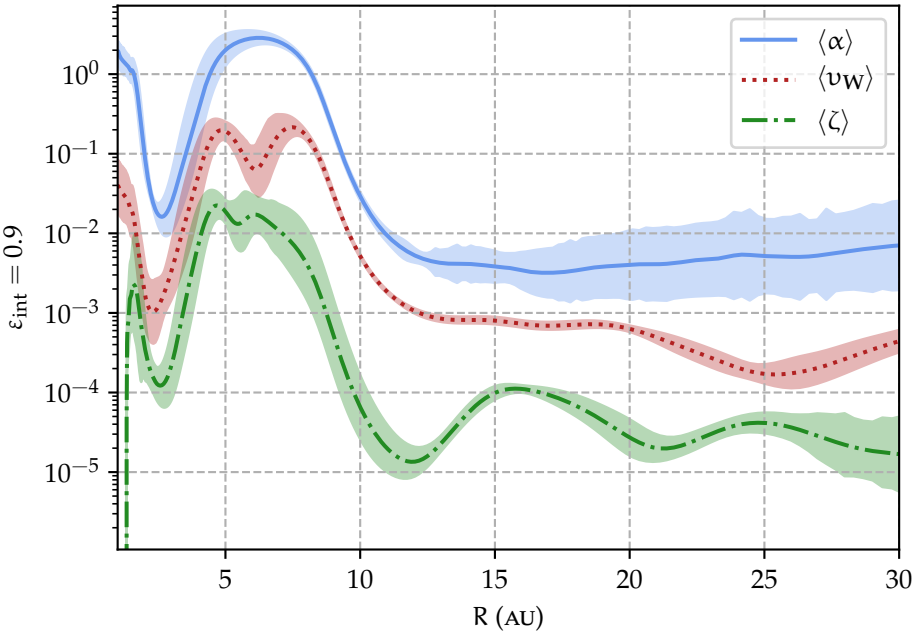

Figure 57: Azimuthally and time-averaged transport coefficients for $\varepsilon_{int} = 0.9$.

4.1.5 MHD *wind*

Let me now describe the structure of the magnetic winds through the analysis of the MHD invariants. Because of the inner ring, I do not select the same field lines as I did for the 2.5 D simulation. The inner poloidal magnetic field line is taken at $R_{in} = 6$ AU the external one at $R_{out} = 15$ AU. One can see the selected field lines in fig. 58.

The corresponding MHD invariants computed along the selected field lines are shown in fig. 59. Two main results are definite eye-catchers. Firstly, the magnetic lever arm in the cavity reaches $8 - 9$. This value is still far greater than the critical value of $3/2$ but remains smaller by a few than its 2.5 D counterpart. This result comes as a natural reformulation of the decrease of the transport coefficient.
Moreover, lowering the magnetic torque should partly release the magnetic braking of the disc in the cavity. This effect is observed in the panel (c) of fig. 59, that shows the rotational invariant being equal to $0.8 - 0.9$ in the cavity, where it was close to 0.6 in 2.5 D.

Because of the duration of the 3 D simulation, I average the wind invariants on the whole simulation (minus the transient state), which is similar to averaging on the last 1000 orbits at R_{int}.

The study of the magnetic wind in 3 D confirms the decrease of the magnetic effects in the cavity. Nevertheless, the cavity remains sub-Keplerian and characterised by a strong lever arm.

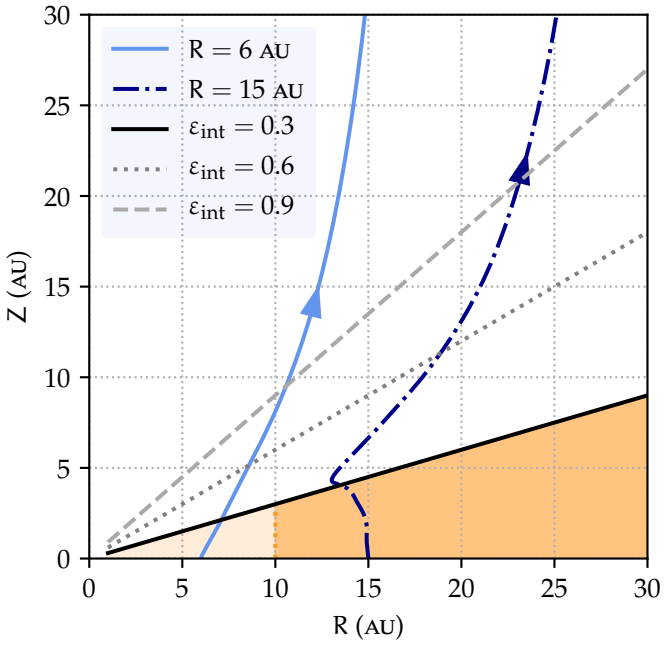

Figure 58: Azimuthally and time-averaged selected field lines along which I will compute the MHD invariants.

4.1.6 *Temporal evolution and magnetic field transport*

The secular evolution of the cavity edge is out of reach with 3 D simulations. However, it is still valuable to check the magnetic field transport in the disc. In this prospect, I show the magnetic flux function ψ spatio-temporal profile in fig. 60. The definition of ψ is the same as in 2 D with azimuthally-averaged quantities. From fig. 60, it seems that the same general trend holds. In the outer part of the disc, the magnetic field is advected towards the cavity edge while it is diffused out in the cavity. For a better insight on the magnetic field transport, I give the time-averaged profile of ν_B in fig. 61. The magnetic transport coefficient confirms that the magnetic field is diffused out between $R \approx 4$ and $R \approx 10$ AU and advected between $R \approx 10$ and $R \approx 15$ AU. Further in the disc ($R \gtrsim 15$ AU), ν_B exhibits multiple sign flips suggesting magnetic field accumulations that would coincide with the vortices seen in fig.53. Conclusively, it seems that I recovered the accumulation process of magnetic flux (that is associated to gaps and vortices) that was proposed by Riols et al. (2020). This conclusion is to be considered with caution, since the fiducial 3 D simulation is way less converged than the 2.5 D corresponding one.

Nevertheless, there is still an interesting result regarding the flux function ψ and its inner saturation value in 3 D $\langle\psi\rangle_{3D}$, whose temporal profile is shown in fig.62. The initial value of ψ associated to the

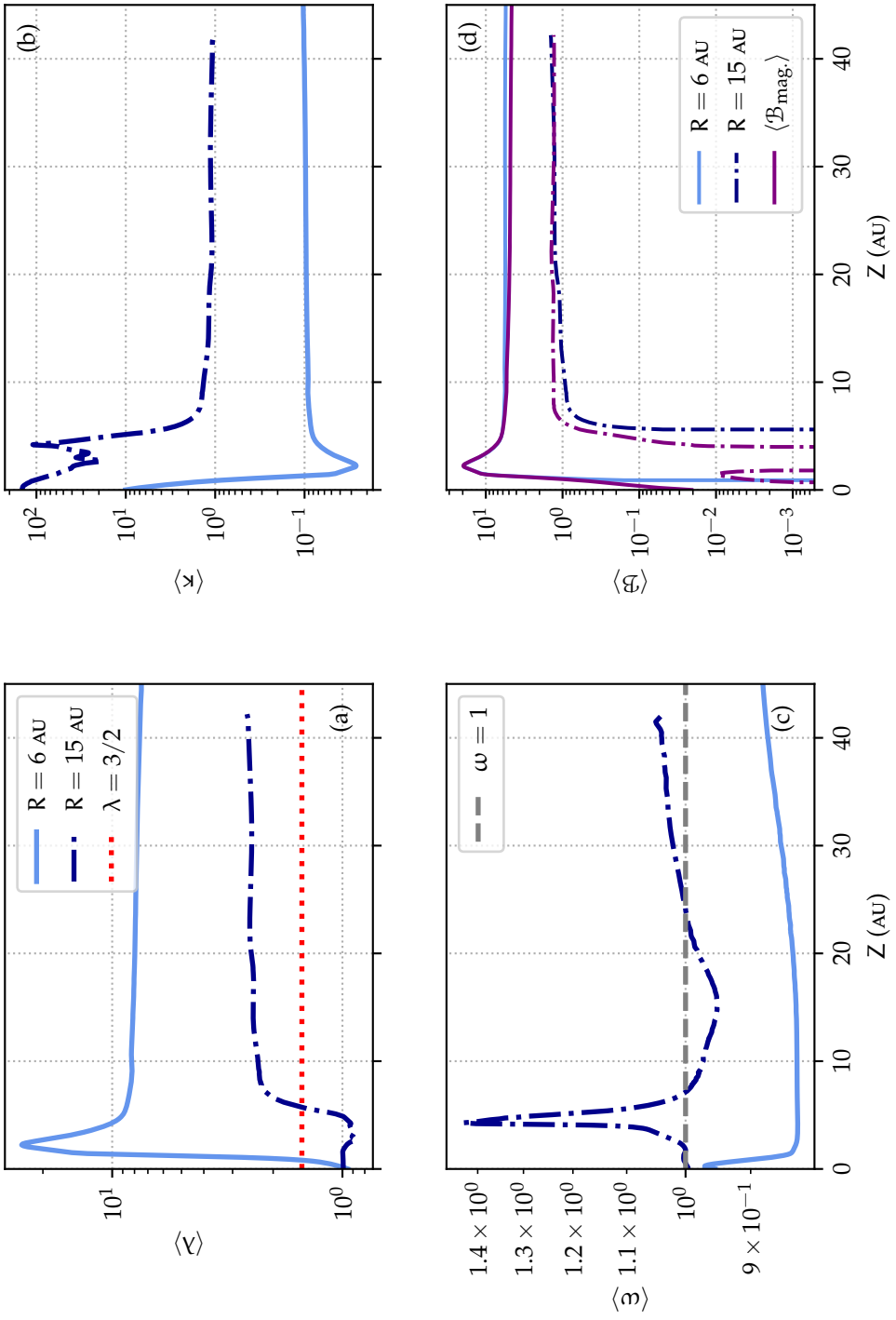

Figure 59: Azimuthally and time-averaged selected field lines along which I will compute the MHD invariants.

seed in 3 D is logically close to the averaged value of ψ from the corresponding 2.5 D simulation. The seed magnetisation exhibits a sharp decrease during the initial transient, accordingly with the previous diagnosis done before (drop of v_w, higher ω in the cavity). Eventually, $\psi(R_{int}, t)$ reaches a saturation value $\langle\psi\rangle_{3\,D} = 2 \times 10^{-3}$ which is to be compared to its 2.5 D counterpart $\langle\psi\rangle_{2.5\,D}$ that reads $\langle\psi\rangle_{2.5\,D} = 2\langle\psi\rangle_{3\,D}$. Together with the decrease of the accretion rate at the inner boundary condition, one gets

$$\frac{\langle\psi\rangle_{2.5\,D}}{\sqrt{\dot{M}_{2.5\,D}}} = \frac{\langle\psi\rangle_{3\,D}}{\sqrt{\dot{M}_{3\,D}}}. \tag{196}$$

Interestingly, the quantity $\Phi = \psi/\sqrt{\dot{M}}$ in the innermost region of discs is tracked in simulations of magnetically arrested discs (MADs) in the context of accretion discs around black holes (Tchekhovskoy et al., 2011; Begelman et al., 2022).

Note that the work of Begelman et al. (2022) is based on GRMHD so that the metric they use affects the values of Φ.

As an illustration, Begelman et al. (2022) report values of Φ contained between 20 and 150. In such works, the hereby defined Φ is supposed to be constant with time and indicative of a magnetically supported disc whose inner accretion is ruled by its inner magnetic flux. Figure 63 reveals the temporal evolution of Φ, confirming that $\Phi \approx \langle\Phi\rangle$ is constant with time, with the exception of accretion burst events. In particular, the value of Φ at the beginning of the simulation also remains constant, so that the decrease of $\psi(R_{int}, t)$ completely compensates for the drop in the accretion rate and vice versa.

4.2 INSTABILITY OF THE CAVITY

Before moving to the parameter space exploration, I want to analyse a major aspect of the 3 D simulations that is the stability of the cavity, especially under hydro- and MHD instabilities. This investigation relies on the azimuthal analysis of the 3 D fiducial simulation and focuses on the cavity. I start by showing a map of the surface density inside the cavity at a given time $t = 445$ orbits at R_{int} in fig. 64. I enhance the contrast inside the cavity, and some spirals appear.
In the current section, I want to describe these spirals in detail, based on this first qualitative observation.

4.2.1 *Spirals*

Once the transient state is over, spirals appear in the cavity. More specifically, two sets of spirals are seen. One is located between the inner boundary and the ring and the other between the ring and the cavity frontier with the full disc. The innermost spirals rotate faster than the other. I will refer to the first set as the inner spirals and to the second one as the cavity spirals for convenience.

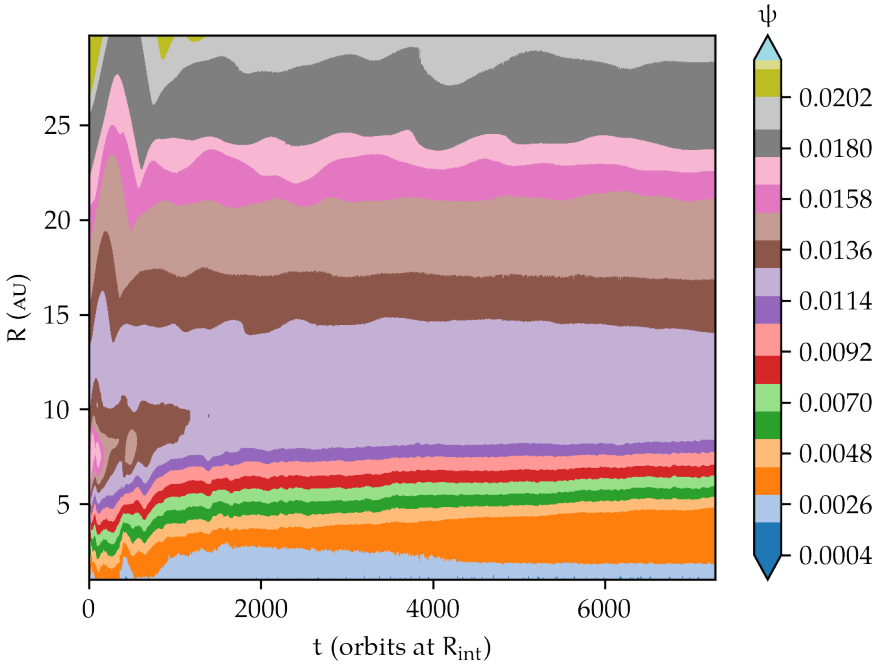

Figure 60: Magnetic field transport illustrated with the flux function ψ for the 3D fiducial simulation.

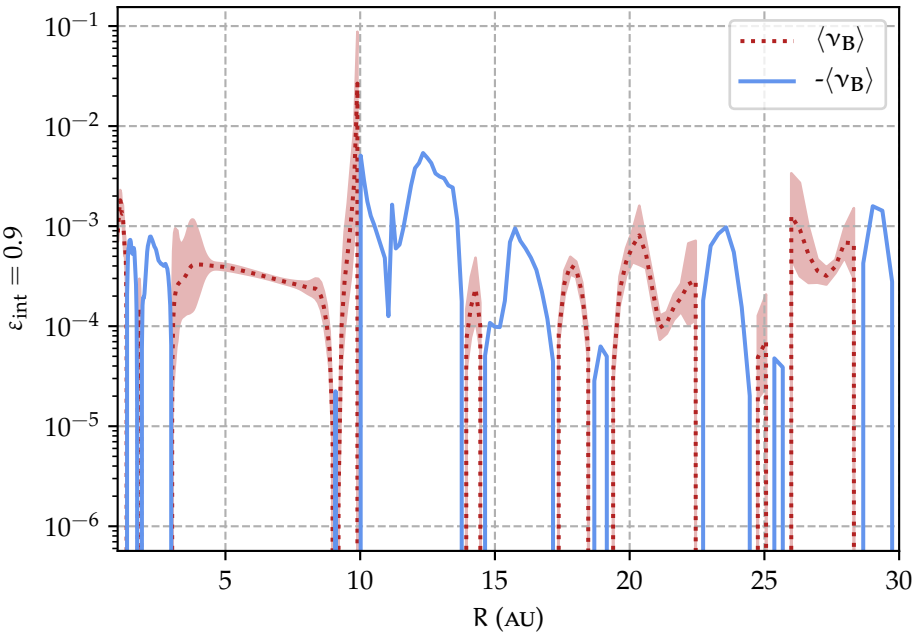

Figure 61: Time-averaged profile of ν_B for the 3D fiducial simulation.

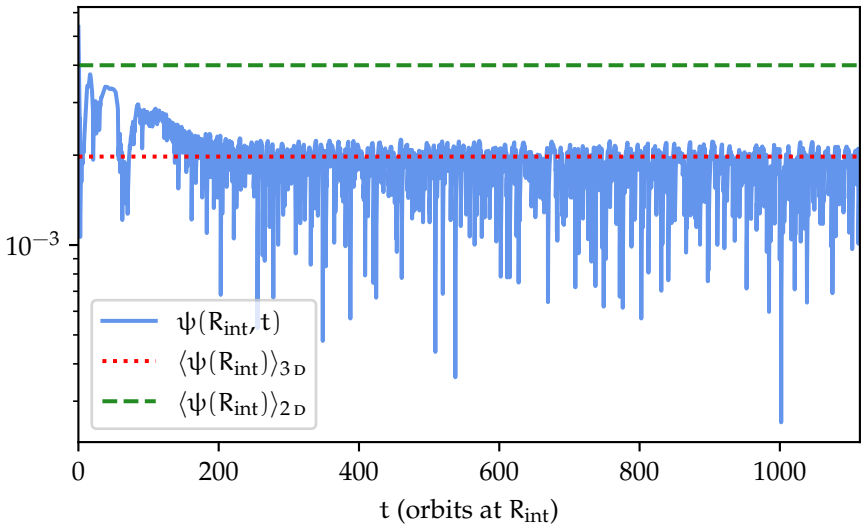

Figure 62: Inner saturation of the flux function $\psi(R_{int}, t)$ for the 3 D fiducial simulation. The red-dotted line is the time-averaged saturated value for the 3 D fiducial simulation while the green-dashed line represents the same quantity for the 2.5 D fiducial simulation.

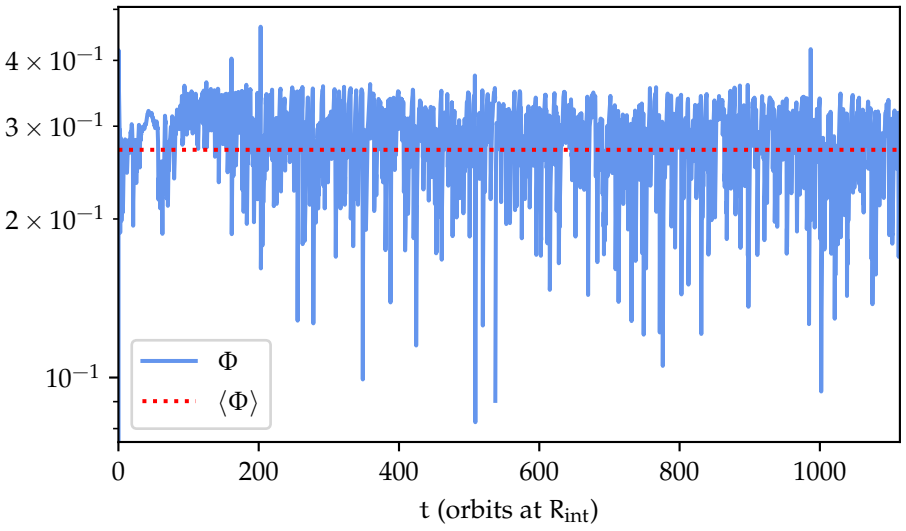

Figure 63: Temporal evolution of $\Phi = \psi(R_{int}, t)/\sqrt{\dot{M}(R_{int}, t)}$ for the fiducial 3 D simulation. The red dotted line shows the time-averaged value of Φ on the last 100 orbits at R_{int}.

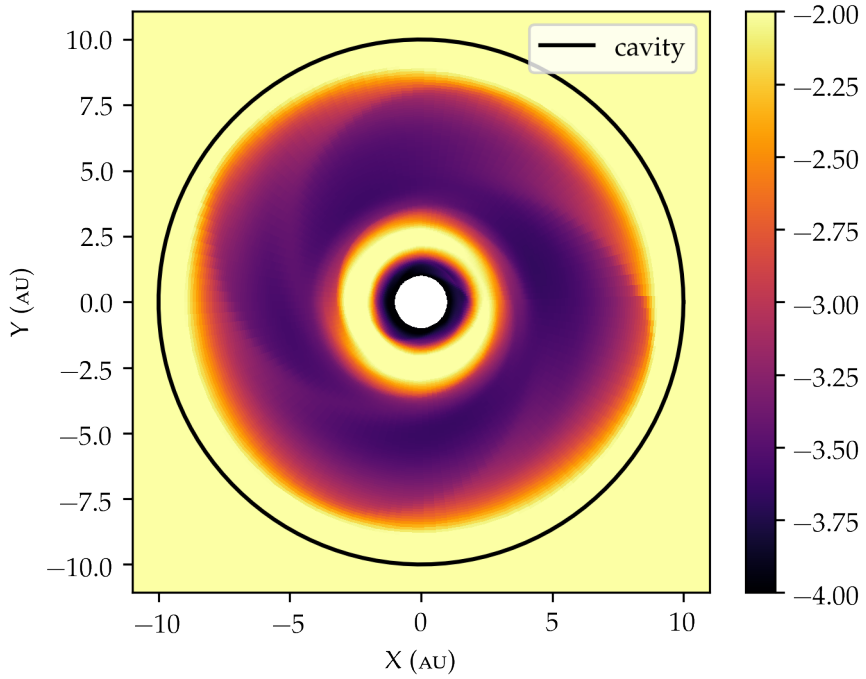

Figure 64: Surface density inside the cavity at $t = 445$ orbits at R_{int}. The black ring marks the cavity edge. The colorbar is chosen so that the outer disc is saturated and one can focus on the cavity.

4.2.1.1 *Azimuthal analysis*

Let me start by investigating the azimuthal organisation of the disc around the midplane from a temporal point of view. To do so, I study the disc at a given time $t = 445$ orbits at R_{int} past the transient state and in particular, the ring is formed. I introduce the surface density deviation $\delta\Sigma$ defined as

Check the box at the beginning for the definition of Σ_{2D}.

$$\delta\Sigma \equiv \frac{\Sigma_{2D} - \langle\Sigma_{2D}\rangle_\varphi}{\langle\Sigma_{2D}\rangle_\varphi}\,. \tag{197}$$

This definition of δ can be applied to other quantities and enables to catch non axisymetries in the disc.

I show $\delta\Sigma$ in fig. 65. I complete the description of the disc midplane with fig. 66 for $\delta\dot{M}$ and fig. 67 for $\delta\beta$ (which is vertically averaged with $\langle\cdot\rangle_\theta$). The profile of Σ exhibits strong asymetries. The top panel of fig. 65 shows the disc as a whole and sheds the light on some outer spirals localised at radii greater than the cavity edge which is shown in black full line. However, a closest inspection of the figure reveals that the density fluctuations are of the order of a few % and overlap one with each other so that the overall pattern may very well be noise. This conclusion is supported by the top panels of figs. 66 and 67. I will come back to this point at the end of this subsection.
A clear asymetry is seen by the cavity edge. On the first panel, the

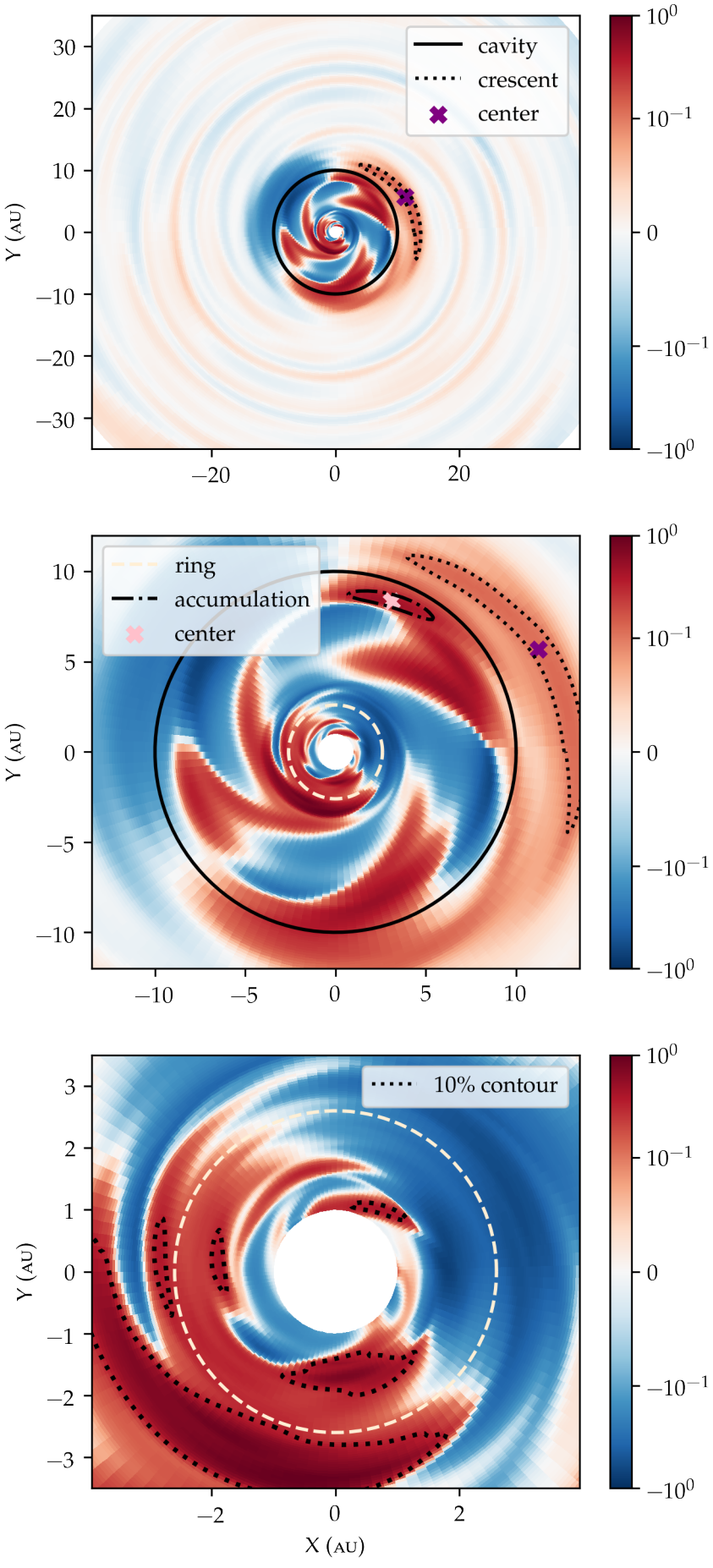

Figure 65: Deviation of the surface density in the disc midplane (X, Y) at $t = 445$ orbits at R_{int} for the fiducial 3 D simulation. The top panel covers most of the disc, the middle one the cavity and the bottom one the innermost part of the disc.

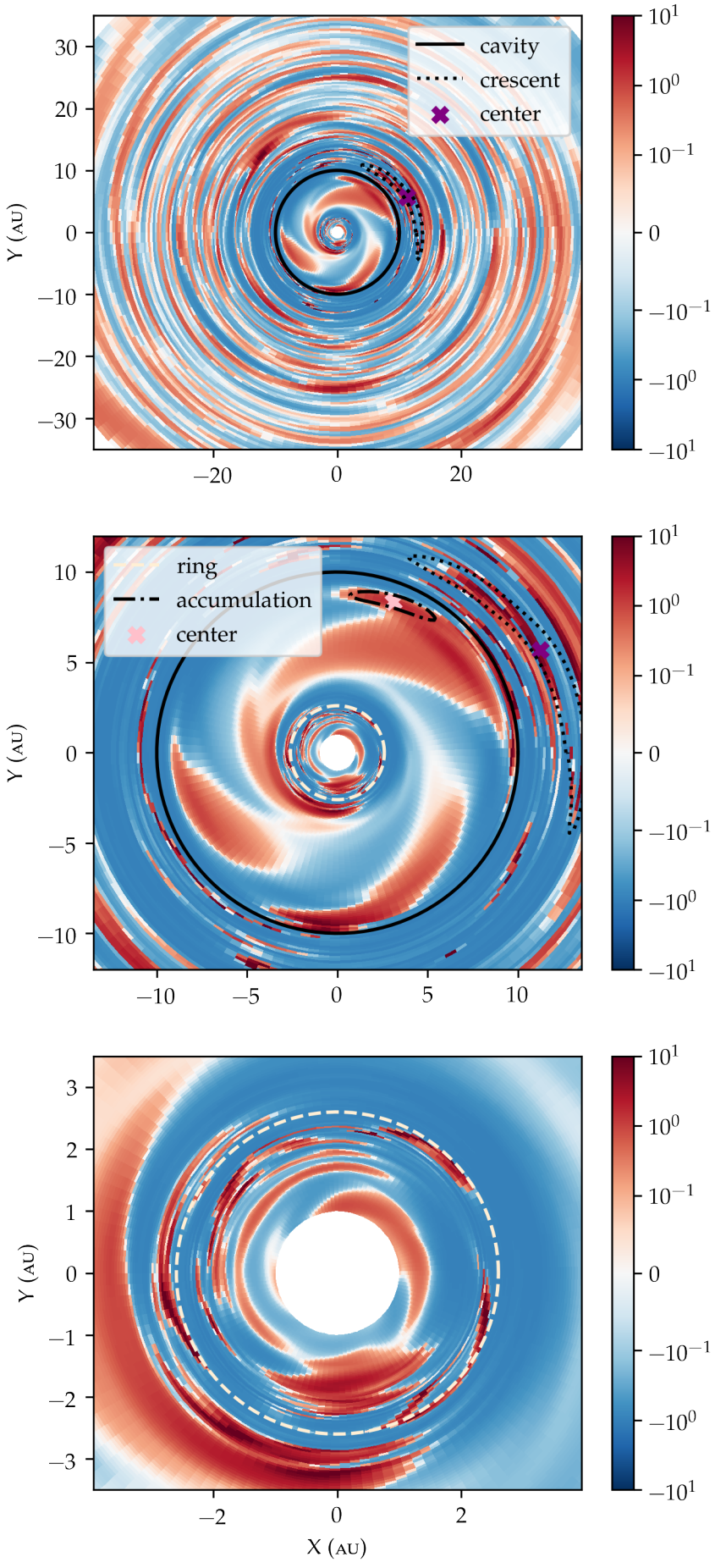

Figure 66: Deviation of the accretion rate in the disc midplane (X, Y) at t = 445 orbits at R_{int}. The general organisation of the figure is the same as for fig. 65.

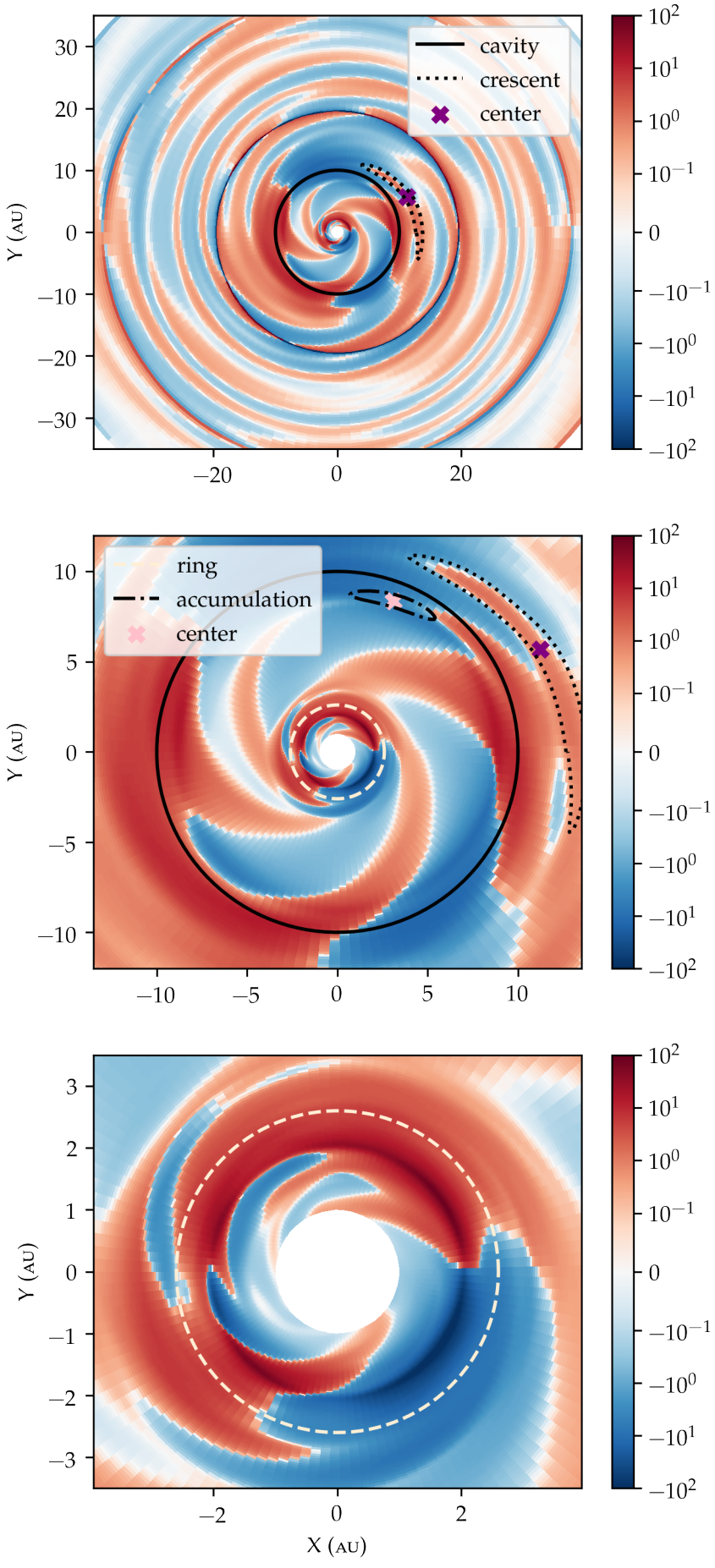

Figure 67: Deviation of the plasma parameter in the disc midplane (X, Y) at t = 445 orbits at R_{int}. The general organisation of the figure is the same as for fig. 65.

right part of the cavity edge is covered by an overdensity while an underdensity spans on its left part. I mark the location of a crescent structure at the overdensity location with a dotted black contour (indicating a +10% variation) and a purple cross. This peculiar shape is also plotted over figs. 66 and 67.

The crescent pattern is also shown in the second panel which shows several features. First, four spiral arms (that I will call spirals) connect the cavity edge and the inner ring (localised with a yellow dashed line). These spirals seem to be associated with localised overdensities at the cavity edge. I highlight one of these accumulations with a semi-dashed black contour and a pink cross that marks its center on all the figures studied here. The corresponding spiral arm is anti-clockwise like all the others. The spirals are seen in the profiles of $\delta\Sigma$, $\delta\dot{M}$ and $\delta\beta$. Two spirals overlap in the profile of $\delta\dot{M}$ but fig. 67 finds 4 spirals across the cavity. The crescent is well defined for $\delta\beta$ but undetectable in the profile of $\delta\dot{M}$.

The bottom panels of all the figures zoom in the area close to the inner boundary, including the inner ring. For fig. 65, I show the 0.1 (10%) contour of $\delta\Sigma$ with black dotted lines. The ring is characterised by a strong non axisymetry, the left half of it being denser than its right part. A clear crescent shape is found aside the bottom left part of the disc and a second set of spirals is detected between the ring and the inner boundary. This echoes the organisation of the disc by the cavity edge, as previously described.

4.2.1.2 *Spirals properties*

Now that I have shown the spirals, I will give some of their properties, such as their phase velocity and their corotation radius.
I get the phase of the spirals by computing the modes m of the Fourrier transform of the surface density in the azimuthal direction, denoted by $\hat{\Sigma}_{2D,m}$. Then, I unwrap the array that I obtain and get the phase $\Delta\varphi$ by taking its argument, so that

$$\Delta\varphi = \arg\left(\hat{\Sigma}_{2D,m}\right) . \tag{198}$$

I give the temporal evolution of the phase I calculated with this method at $r_1 = 2$, $r_2 = 5$ and $r_3 = 10$ AU in fig. 68. Further than the ring location (r_2 and r_3), nothing changes when the ring appears and the phase follows $\Delta\varphi = a\,t + b$ with a and b 2 constants. The constant a carries the information on $\dot{\Delta\varphi}$ and I can estimate the phase velocity as

$$\omega_m = \frac{d}{dt}(\Delta\varphi) \times \frac{m}{R} , \tag{199}$$

at a given radius R. It is worth saying that the appearance of the ring does affect the inner radii (r_1 for example). Their time variation gets

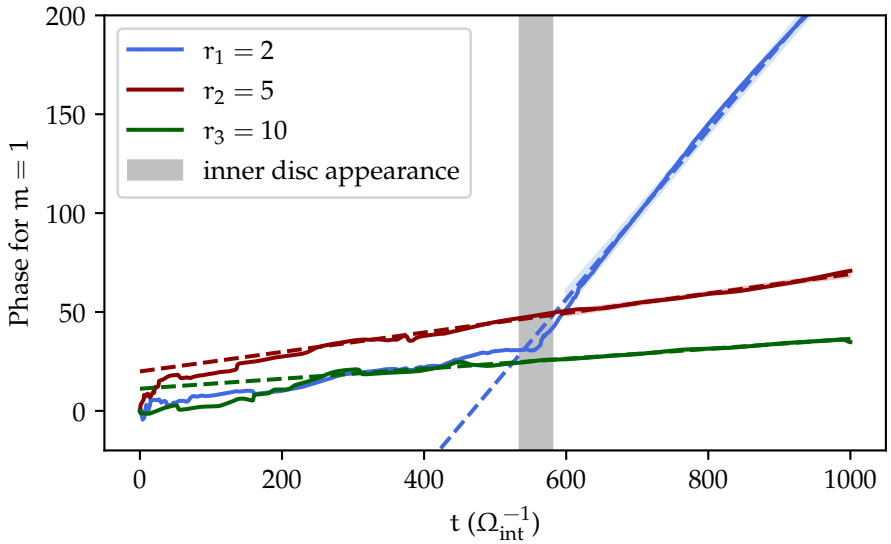

Figure 68: Phase of the spirals for $m = 1$. The grey bar indicates the moment when the ring appears.

steeper, so that the phase velocity increases sharply. This indicates that the innermost spirals are due to the ring. Now that I can trace the phase velocity with respect to time, I can plot it at any radius in the disc and time-average it to get the phase velocity profile. I show this profile in fig. 69.

A striking result lies with the two flat and well defined plateau of ω_1. This shows that the two sets of spirals are indeed patterns rotating at fixed angular velocities. The innermost set rotates faster than the other one. The phase velocity of any set does not depend on the radius, so that for the inner set of spirals, $\omega_{in} = 0.38$ and for the other one $\omega_{ext} = 0.060$ (both in code units). The corresponding corotation radii are $r_{int} = 1.89$ and $r_{ext} = 6.50$ AU. The spirals between the ring and the cavity edge rotates with a fairly sub-Keplerian speed. On the contrary, the innermost spirals are super-Keplerian close to the ring, so that the gas could go outwards, hence enhancing the ring formation. This claim is supported by fig. 66. Lastly, nothing but noise is detected further in the disc, which echoes my initial claim regarding the possibility to detect spirals further than the cavity edge.

4.2.2 *Instabilities*

To explain the formation of these spiral patterns, several instabilities can be proposed.

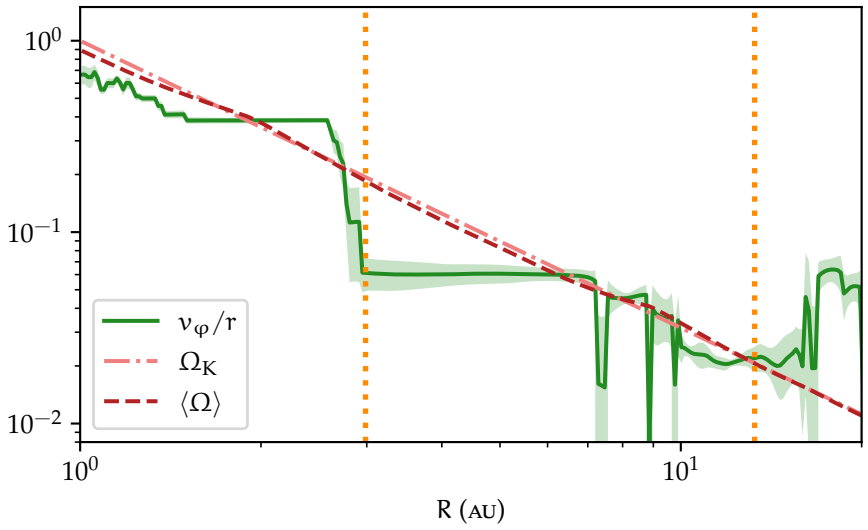

Figure 69: Phase velocity of the spirals, time-averaged and with respect to the radius, for $m = 1$ and for the 3D fiducial simulation. The red dashed line is the angular velocity of the disc and the semi-dashed pink one is the keplerian angular velocity. The yellow dotted lines represent the maximum of the characteristic function $\mathcal{L}$ for the analysis of the RWI.

4.2.2.1 *Rotational instability*

The rotational instability is a hydrostatic instability that can occur in PPDs with a steep surface density profile and a large radial pressure gradient force, such as in Ono et al. (2014). The Rayleigh's criterion for the instability to occur (Chandrasekhar, 1961) states that the specific angular momentum ℓ must decrease with the radius R, so that

$$\partial_R \ell < 0\,, \qquad \text{UNSTABLE} \tag{200}$$

Figure 70 shows the radial profile of $\partial_R \ell$, time-averaged and computed at the disc midplane. $\partial_R \ell$ is not even close to being negative, which rules out the rotational instability as a plausible mechanism to generate the spirals. For completeness, I add that I also computed $\partial_R \ell$ with an average along θ, which was still positive.

4.2.2.2 *Rossby Wave Instability (RWI)*

The Rossby Wave Instability (RWI, Lovelace et al., 1999; Li et al., 2000; Li et al., 2001) is a promising hydrodynamical instability that could account for the observed spirals. Because of the contrast in density at the edge of the cavity, the RWI is likely to occur, as a peculiar realisation of the Kelvin-Helmholtz instability. This instability in also known to be still enabled and slightly enhanced in the presence of large-scale poloidal magnetic fields, as shown by Yu and Lai (2013).

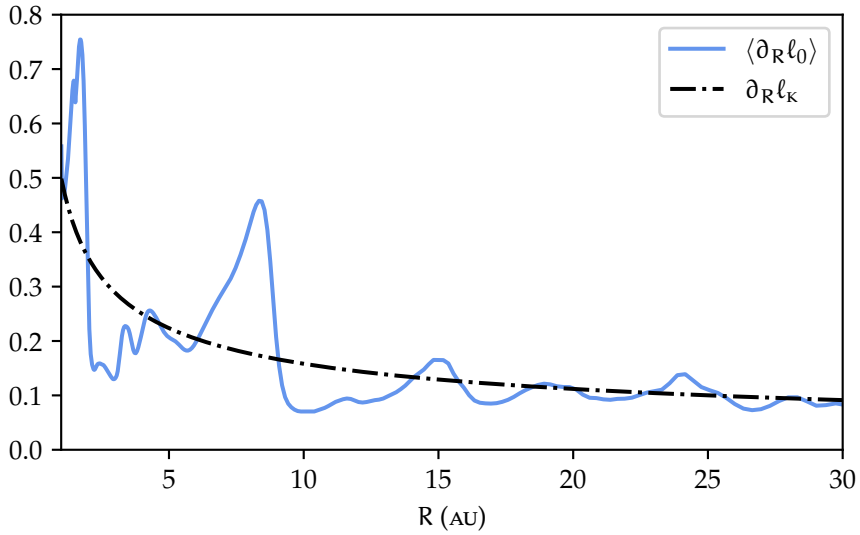

Figure 70: Analysis of the rotational instability in my simulated disc for the 3 D fiducial simulation.

Many previous works focus on the occurrence of RWI in 2 D simulations such as Robert et al. (2020). However, global 3 D simulations studying RWI were carried by Meheut et al. (2010) and Meheut et al. (2012). 3 D resistive MHD simulations were also performed by Lyra and Low (2012), regarding this very same instability.

Following Lovelace et al. (1999), I introduce the characteristic function $\mathcal{L}$ (which is the inverse of the potential vorticity) in spherical coordinates that reads

$$\mathcal{L} = -\frac{1}{2}\frac{\Sigma}{\langle(\boldsymbol{\nabla}\times\mathbf{v})\cdot\mathbf{e}_\theta\rangle_\varphi}\,, \tag{201}$$

which can be recast using ℓ as

$$\mathcal{L} = \frac{1}{2}\frac{r\Sigma}{\langle\partial_r\ell\rangle_\varphi}\,. \tag{202}$$

A necessary criterion for RWI stability states that $\mathcal{L}$ needs to have a maximum so that the instability can occur (Lovelace et al., 1999). Though it is still possible to have a maximum for $\mathcal{L}$ without RWI to happen.

The characteristic function $\mathcal{L}$ is shown in fig. 71. Two maxima of $\mathcal{L}$ are detected, at $r_1 = 2.99$ AU and $r_2 = 13.2$ AU. One is located at the inner ring position and the other is right after the cavity edge. Although these maxima are observed, this is not sufficient to conclude that RWI is indeed occurring.

Figure 69 shows the phase velocity for the mode $m = 1$ with respect to R. I analysed the case $m = 2, 3$ and 4 with the same pro-

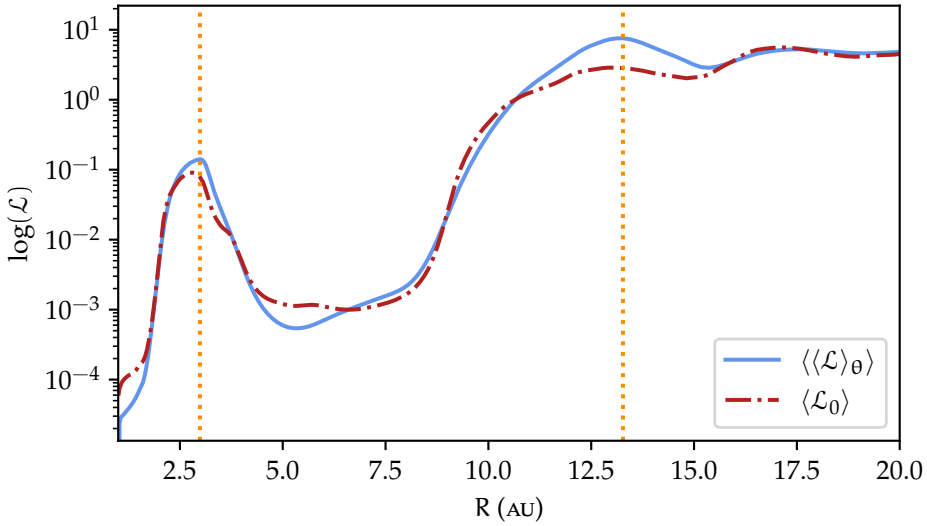

Figure 71: Characteristic function $\mathcal{L}$, theta and time-averaged in full blue line and taken at midplane and time-averaged in semi-dashed red line. The yellow dotted vertical lines mark the maxima of $\mathcal{L}$, at $r_1 = 2.99$ AU and $r_2 = 13.2$ AU.

cedure. I found the same phase velocity by taking $m = 2$, but for higher modes, the curves are noisier and the plateau are harder to detect. This results in an impossibility to have access to the phase velocity with a great precision. Since the ordering of the phase velocities and their corresponding order of magnitude ($\omega_{m,int} \sim 0.05 - 0.1$ and $\omega_{m,ext} \sim 0.3 - 0.4$) are preserved for any m, I will assume that fig. 69 is a good indication of the phase velocity of any spiral, regardless of its mode.

According to Li et al., 2000, and defining $\Delta\omega_m = \omega_m - m\,\Omega$, where Ω is the angular velocity calculated at the radius that corresponds to the maximum of $\mathcal{L}$, one gets

$$\Delta\omega_m = -\frac{k_{\varphi,m}\, c_s^2/\Omega}{1 + k^2\, h^2}\left[(\ln\mathcal{L})' \pm \sqrt{(\ln\mathcal{L})^2 - \frac{1 + k^2\, h^2}{L_s\, L_p}}\right] \tag{203}$$

where k is the norm of the wave vector, $h = c_s/\Omega$, the prime denotes the derivative with respect to R and L_s and L_p are defined as

$$L_s = 1 \Big/ \left[\frac{d}{dt}\ln\left(\frac{P}{\Sigma}\right)\right], \tag{204}$$

$$L_p = 1 \Big/ \left[\frac{d}{dt}\ln(P)\right]. \tag{205}$$

Considering that $k^2\, h^2 \ll 1$, one can consider that RWI modes are in corotation with a maximum of $\mathcal{L}$. In the following, I test whether the

phase velocity of the spirals corresponds to the azimuthal velocity at a radius corresponding to a maximum of $\mathcal{L}$.

None of the corotation radii previously calculated corresponds to a local maximum of $\mathcal{L}$. I conclude that the criterion for RWI is not satisfied so that RWI is unlikely to be triggered.
However, the phase velocity is not well defined around the external maximum of $\mathcal{L}$ in fig. 69 which is itself not very sharp. This is why I try to push the analysis a step further regarding this maximum.
If the RWI were to be triggered, one would see a vortex in the disc midplane. Since I detected a faint crescent in fig. 65, I tried to check if it could be associated to a vortex triggering the RWI at the second maximum of $\mathcal{L}$ location. Figure 72 shows the disc midplane at the same moment as for fig. 65. Over the surface density fluctuations are plotted the streamlines that are theta-averaged and defined by $\langle \rho \boldsymbol{v}_\mathcal{V} \rangle_\theta$, with $\boldsymbol{v}_\mathcal{V}$ being the velocity in the frame corotating with the centre of the crescent shape. Figure 72 shows that the crescent is located close to a vortex, but this latter does not overlap completely with the crescent and their centres do not match.
These statements lower drastically the likelihood to have the RWI triggered in the disc, because the current physical mechanisms that enable the RWI remain unobserved. Indeed, because the RWI is promising and often detected in simulations, I pushed this hypothesis the furthest I could do. Nevertheless, the conclusion reached is the fact that it seems unlikely that the RWI is occurring.

I am now left with no clear hint regarding the definitive nature of the instability at play in the cavity. One could think of instabilities invoking reflected waves between the cavity edge and the inner ring such as Tagger and Pellat (1999) with the accretion-ejection instability (AEI). However, such a work would still rely on an initial instability and the possibilities displayed in Tagger and Pellat (1999) that could be applied to my simulation still imply the RWI.

4.2.2.3 RTI *or interchange instability*

I previously referred to the RTI (Kruskal and Schwarzschild, 1954) in chapter 3, which had already been discarded at that time, with the use of a criterion from Spruit and Taam (1990), Spruit et al. (1995), and Stehle and Spruit (2001). The plasma parameter $\beta \lesssim 1$ in the cavity was not low enough to trigger the instability criteria that I recall here

$$\beta \leqslant 0.0355\,. \qquad \text{UNSTABLE} \tag{206}$$

Figure 73 shows the plasma parameter, azimuthally and time-averaged in the cavity. The conclusion is straightforward, since $\langle \beta \rangle$ is equal to 1 and far from β_{crit}, so that the RTI is not occurring in the cavity.

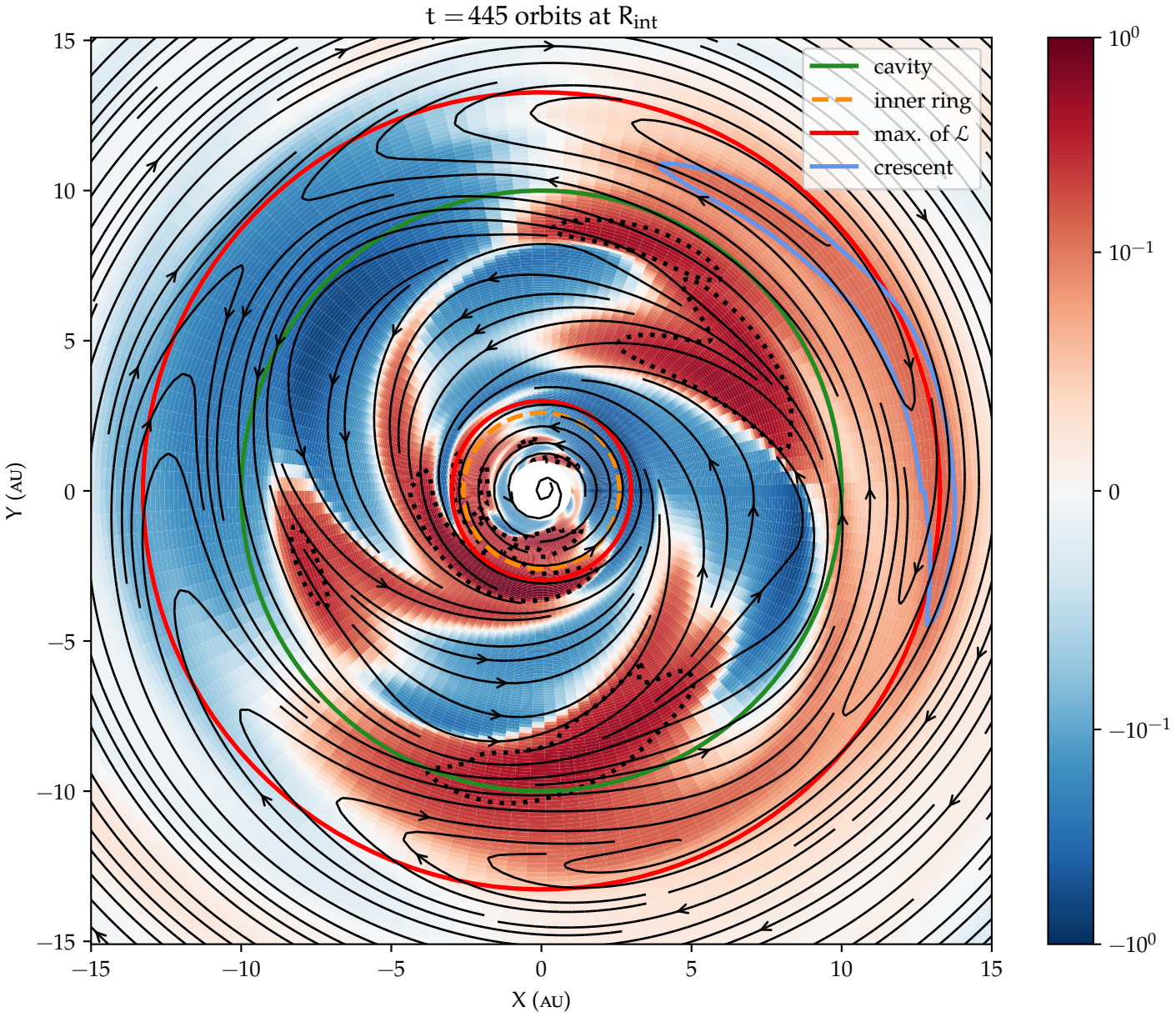

Figure 72: Deviation of the surface density at the midplane for the 3D fiducial simulation. The red full lines mark the maxima of $\mathcal{L}$, the black full line is the cavity edge, the orange dashed one is the location of the inner ring and the blue contour is the crescent shape seen in fig. 65. Over the image are plotted the streamline on a cartesian grid, in the frame corotating with the centre of the crescent shape.

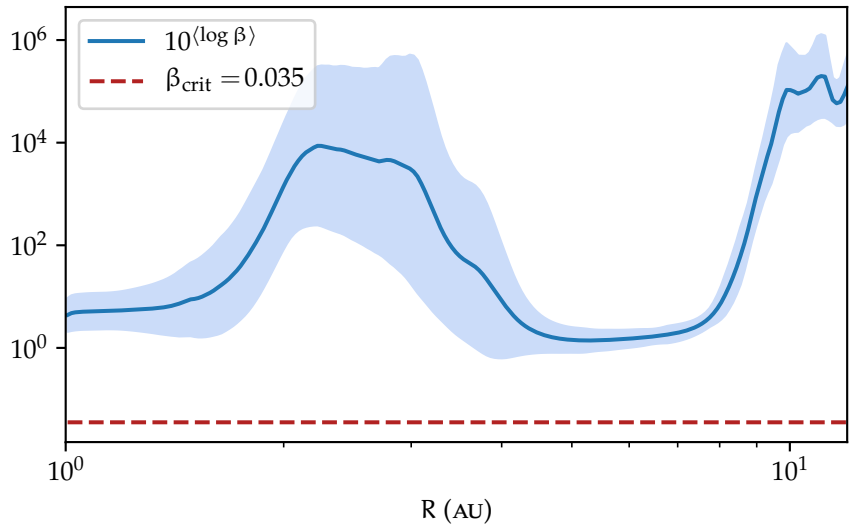

Figure 73: Azimuthally and time-averaged plasma parameter for the 3 D fiducial simulation, compared to the critical value $\beta_{crit} = 0.0355$.

4.2.3 RTI *again*

Leaving the discussion on the spirals behind, I want to focus on the innermost radii of the simulation. I observe that the seed expels magnetic flux randomly and in a non-axisymmetric manner, as illustrated on fig. 74. This figure shows the plasma parameter $\overline{\beta}$ at $t = 461$ orbits at R_{int}. The light contour highlights the value $\overline{\beta} = \beta_{crit}$, so that it is clear that the RTI is triggered occasionally at the innermost radius of the simulation, as the criterion is fulfilled by far. The occurrence of this instability at that location as well as its qualitative shape recalls MADs simulations in GRMHD, such as in McKinney et al. (2012) and Ripperda et al. (2022) and of simulations of discs around magnetised stars (Romanova et al., 2008).

4.3 PARAMETER SPACE EXPLORATION

Now that I have given the most relevant results regarding the 3 D simulations, I will move on a brief parameter space exploration. This exploration is similar to the 2.5 D one.

4.3.1 *Influence of the initial Elsasser number*

I start with the simulation labelled S3DAm1B4Bino, based on its 2.5 D corresponding simulation and launched after 7557 orbits at R_{int}. In particular, the gaps had already formed. I recall that the difference with the fiducial simulation is that $\Lambda_A = 10$.

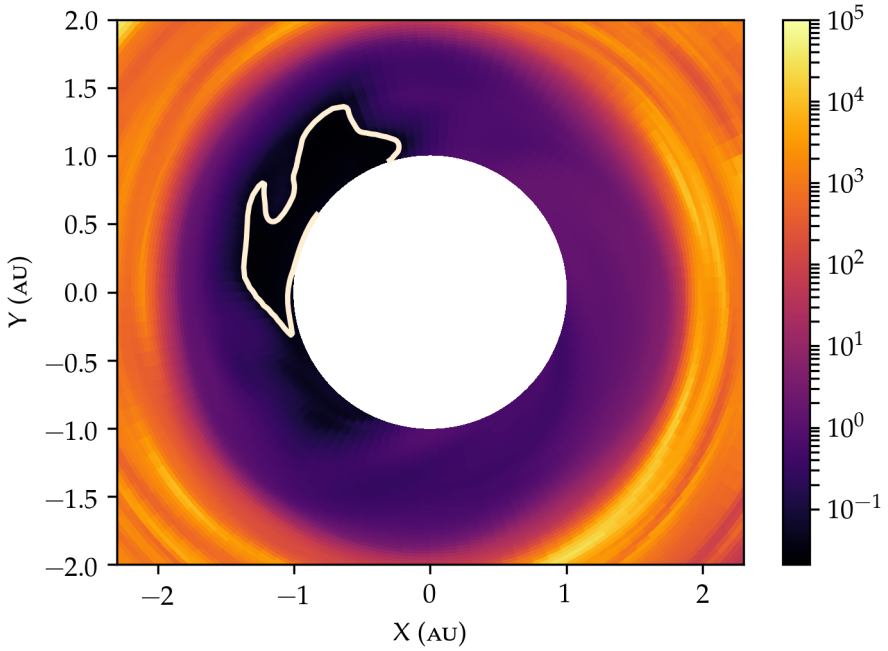

Figure 74: $\overline{\beta}$ at the midplane for the fiducial 3 D simulation, at t = 461 orbits at R_{int}.

4.3.1.1 *Structure of the disc*

The figure 75 shows the spatio-temporal evolution of Σ and $\overline{\beta}$. The beginning of the simulation is characterized by the same disc reorganisation as in the fiducial 3 D run. The cavity and the gaps stand until the end of the simulation. Though, the cavity is refilled and its radius moves towards the internal radius until it reaches a steady state after $\sim$ 700 orbits at R_{int}. The gaps widths are less sharp than in the 2.5 D analogous run. One is clearly identified around $R \sim 16$ AU and is spotted by white dotted line in both the Σ and $\overline{\beta}$ profiles of fig. 75. It clearly correspond to one of the gaps described in the corresponding 2.5 D run. The other gap previously discussed is not seen but was not fully formed when the 3 D simulations was launched. The Σ profile exhibits a stripe shaped structure inside the cavity, suggesting that accretion is still occurring. Despite this accretion, no inner ring of matter forms close to the inner boundary. This may favour the hypothesis that the inner ring observed in the fiducial run is not due to the inner boundary condition.

The global structure of the disc remains similar to the 2.5 D run and is pictured in fig. 76. No elbow shaped structures are seen, neither above nor below the disc, therefore, no matter is falling down onto the disc surface which suggest a ζ transport coefficient positive at any radius, contrary to what is observed in the 2.5 D analogous sim-

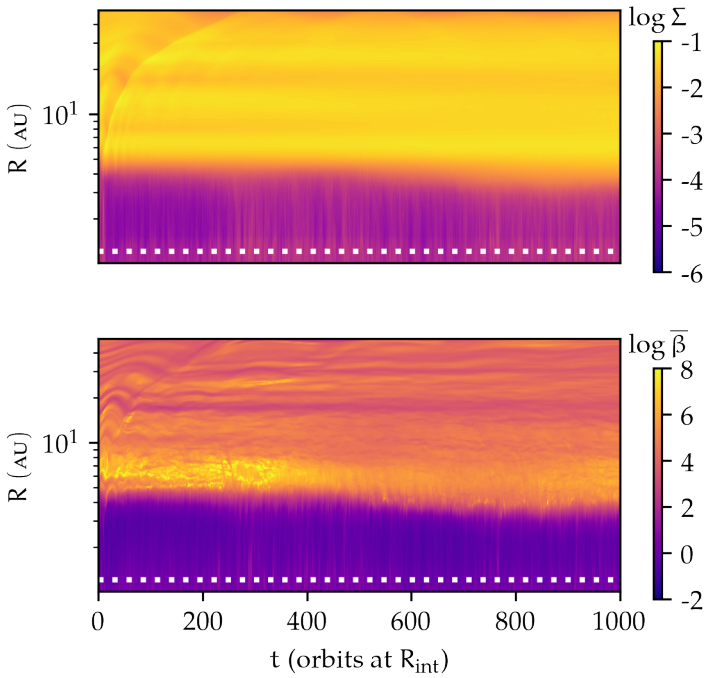

Figure 75: Spatio-temporal diagram of Σ (top panel) and $\overline{\beta}$ (bottom panel) for the simulation S3DB4BinoAm1.

ulation. The vertical structure of the disc is still not symmetric. Such an asymmetry is also observed in the wind shape, this latter being wider above the disc.

The structure of the angular momentum stream lines is similar to the one observed in the 3 D fiducial simulation and shown in fig. 78. They exhibit a vertical structure inside the disc with angular momentum removed downwards and towards the external part of the disc. The asymmetry that is observed in the stream lines structure is recovered among the angular momentum stream lines one. There is a surface above the midplane between $h/R = 0.9$ and $h/R = 0.3$ where the vertical motion of the angular momentum flow changes. Above this surface, it is removed upwards while it moves downwards below.

The main difference with the 2.5 D corresponding simulation occurs in the magnetic structure of the disc shown in figure 77. Contrary to the 2.5 D run, the loop structure that is observed at the cavity radius is considerably reduced in size. The B_φ polarity change is located in a small zone at $R \approx 6$ AU. The poloidal field lines in the cavity are similar to the ones in the 2.5 D simulation. Right after the gap location, the poloidal magnetic flux is concentrated.

4.3.1.2 *Cavity stability*

A similar instability is observed inside the cavity with 3 spirals clearly identified. Their phase velocity is constant from $R \sim 1$ AU to $R \sim 3$ AU

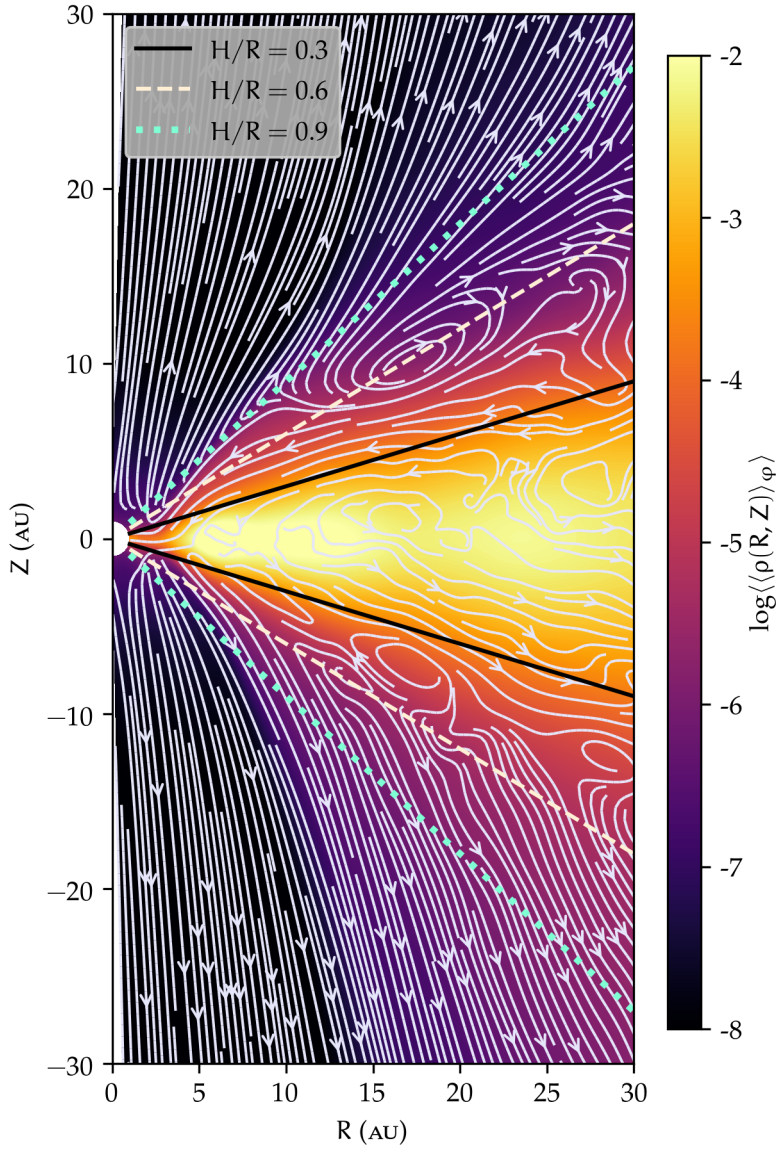

Figure 76: Azimuthally and time-averaged poloidal profile of the density, over which the stream lines are plotted (and averaged under the same procedures), for S3DB4Bin0Am1.

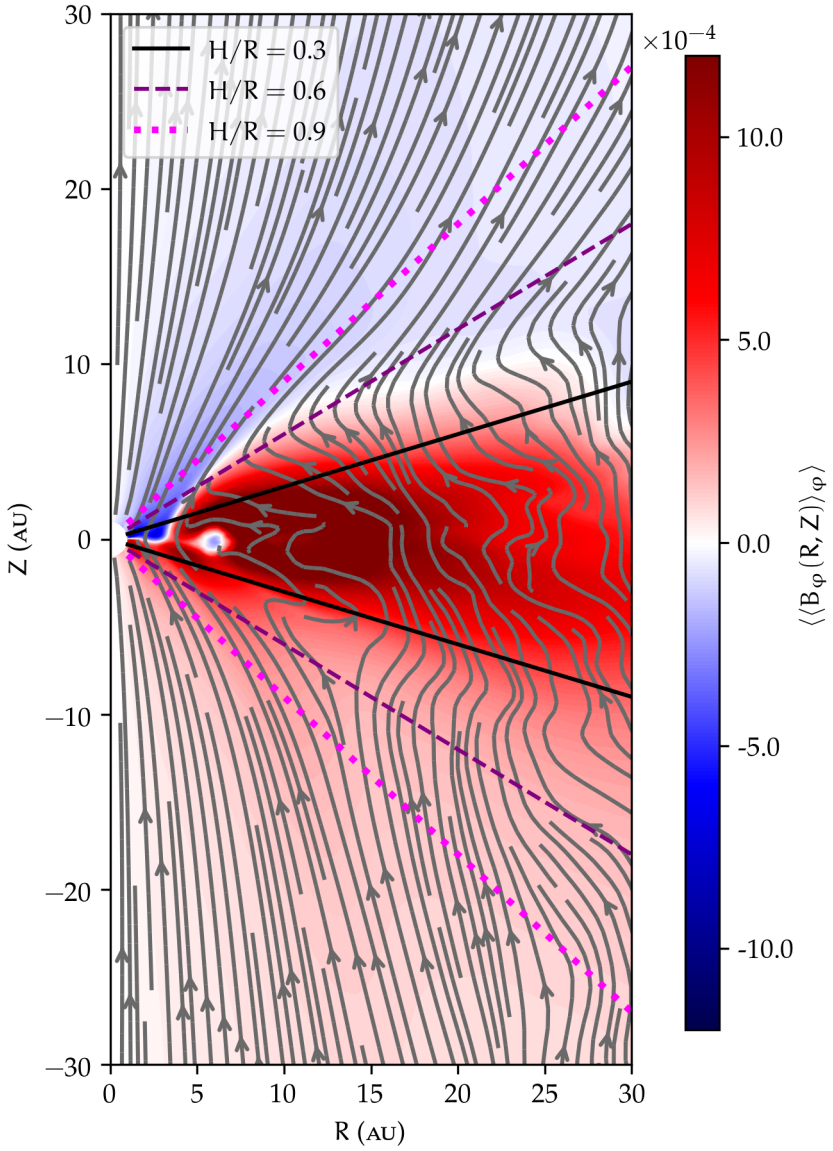

Figure 77: Time-averaged magnetic structure for S3DB4BinoAm1.

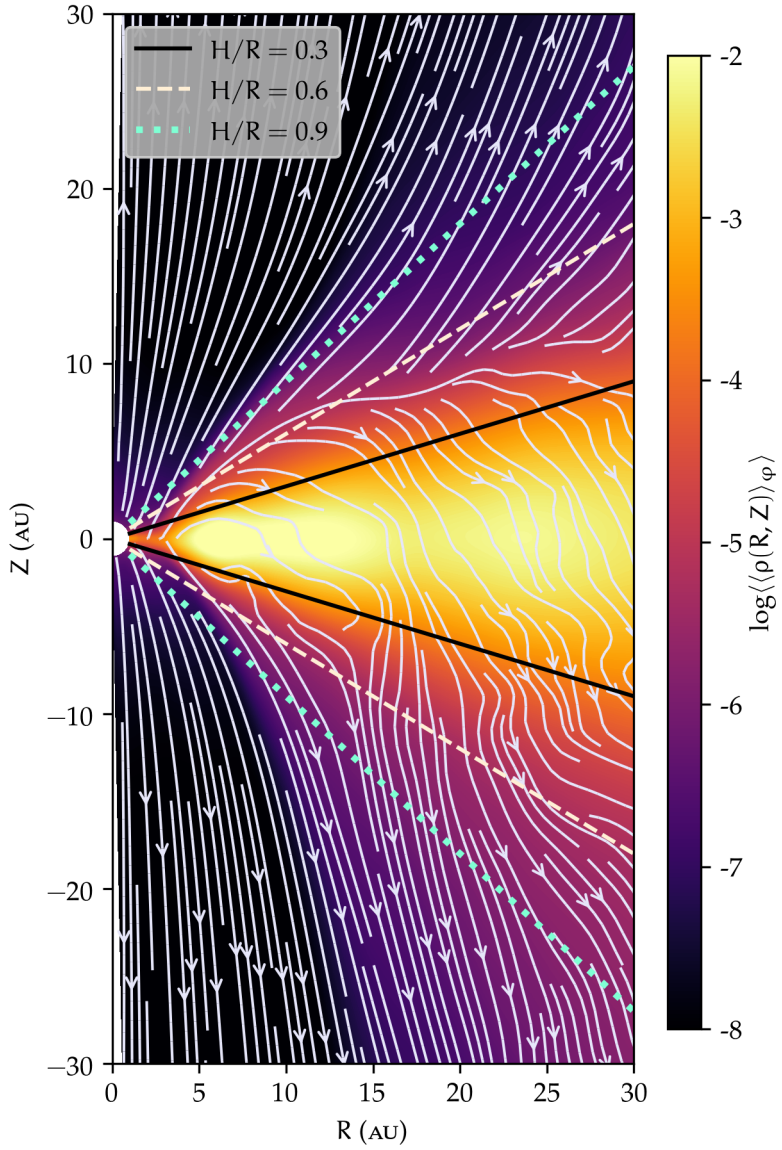

Figure 78: Azimuthally and time-averaged poloidal profile of the density, over which the angular momentum flux stream lines are plotted (and averaged under the same procedures), for S3DB4BinoAm1.

and equals 0.27 code units. This coincide with a sub-keplerian profile for Ω inside the cavity. I get a single set of spirals but no ring is observed in this run. $\partial_r \ell$ is positive everywhere in the disc, discarding the rotational instability. The characteristic function $\mathcal{L}$ reaches a maximum at $R \sim 6.5$ AU so that no new conclusion can be drawn regarding RWI. Lastly, the cavity is also stable with respect to the interchange instability criteria.

4.3.2 *Influence of the external magnetisation*

4.3.2.1 *Lower plasma parameter*

The spatio-temporal evolution of Σ and $\overline{\beta}$ for the 3 D simulation restarted from the one with $\beta = 10^3$ is given in fig 79. The disc reorganisation is observed and comes along with the formation of a ring of matter wider than the one in the 3 D fiducial run. This ring is fuelled by two bursts of accretion from the external disc that occur at $t \sim 150$ and $t \sim 500$ orbits at R_{int}. The edge of the cavity stands still at $R_{cav} \sim 15$ AU after the sonic shock wave crossed the disc and a steady state is reached. Both the profile of Σ and $\overline{\beta}$ exhibit a gap located at $R = 27$ AU and spotted by a white line in fig. 79. The global structure of the disc exhibit minor differences with the corresponding 2.5 D simulations and no peculiar properties have not been yet discussed with the 3 D fiducial simulation.

Regarding the cavity stability, two sets of spirals are observed. One is seen from $R = 1.65$ to 3.45 AU and the other from $R = 4.15$ to 9.1 AU. The angular velocity of the spirals closest to the star is $\omega_{\varphi,1} = 0.30$ while the other set is characterized by $\omega_{\varphi,2} = 0.03$. In particular, $\omega_{\varphi,1} \approx 10\,\omega_{\varphi,2}$. After the transient state, the cavity is fully stable with respect to the RTI. Once again, the rotational and Rossby wave instabilities are dismissed and cannot account for the observed spirals.

4.3.2.2 *Higher plasma parameter*

The simulation restarted from the one with $\beta = 10^5$ follows the same pattern as the others restarted runs. An inner ring of matter develops close to the star while the global structure of the disc remains pretty much the same up to the same differences that are seen from S2DB3BinoAmo to S3DB3BinoAmo. The general conclusions regarding accretion, the MHD wind and the stability of the cavity remain the same.

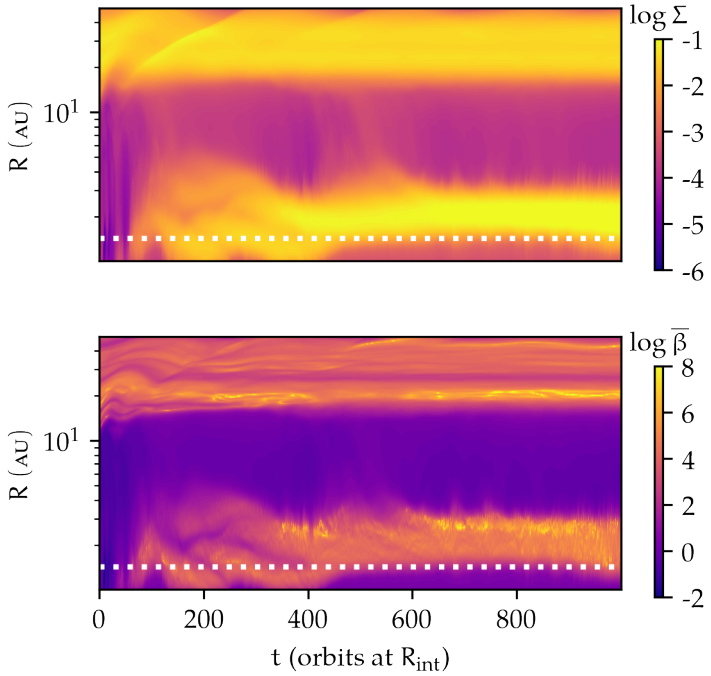

Figure 79: Spatio-temporal diagram of Σ (top panel) and $\overline{\beta}$ (bottom panel) for the simulation S3DB3BinoAmo.

4.3.3 *Influence of the internal magnetisation*

Two simulations were conducted in 3D with different internal magnetisation, $\beta_{in} = 10^1$ and 10^2. Since the 2.5D simulations showed that the impact of this parameter is negligible, I just checked if it was still the case for 3D simulations. The restart procedure force the simulations to be launched with an initial state very close to the 3D fiducial run, so that no big changes were expected. Very same results were obtained also in 3D simulations. The only interesting fact to notice is that the internal ring is not located at the same radius for the two simulations. $R_{ring} \approx 1.5$ AU for the run with $\beta_{in} = 10^2$ and $R_{ring} \approx 2$ AU for the one with $\beta_{in} = 10^1$.

4.4 CONCLUSION

The 3 D fiducial simulation was rich and I got detailed results from it. The most striking result is the detection of spirals inside the cavity, which I characterised.
I also studied the simulated discs and give some of their properties.

A first interesting point is the initial reorganisation of the disc that happens together with the disappearance of the elbow-shaped structures. Once the disc reaches a stationary state, an inner ring is observed. Most of the properties of the disc (transport coefficients values, accretion rate, rotation of the cavity) are coherent with the decrease of the inner magnetisation, leading to lower magnetic torques.
I still try to investigate the temporal evolution of the disc and showed that the accretion rate was of the same order of magnitude as in the 2.5 D corresponding simulation.

Regarding the stability of the cavity, spirals were detected inside it, while its frontier remains at the same location throughout the simulation. These spirals were characterised with their rotation speeds and their corotation radii. Despite having studied several instabilities such as the RWI, I could not fully confirm which one was triggered and generating the spirals.

Finally, I went through a parameter space exploration that gave results that were either similar to the corresponding 2.5 D simulations or changes that were the same as the differences between the 2.5 D and 3 D fiducial simulations. Nevertheless, the case with a higher ambipolar Elsasser number (S3DB4BinoAm1) suggests that the inner ring detected in the 3 D fiducial simulation may have a physical origin.

The accretion rate and the magnetic flux at the innermost radius of the disc, as well as the occurrence of the RTI at the very same location are analogous of GRMHD simulations of MADS. This description is mostly and commonly used to describe accretion disc around black holes. Nevertheless, it seems perfectly relevant to interpret the innermost part of the cavity that is highly magnetised. This result is not straightforward and ties an interesting bound between accretion disc of completely different origins. This calls for deepest investigations, in particular regarding the secular evolution of cavity-hosting magnetised discs.

CONCLUSION

Les simulations 3D réalisées sont riches d'enseignements et de résultats.
Le résultat principal et majeur est la détection de spirales à l'intérieur de la cavité ainsi que leur caractérisation. En plus de ce résultat, j'ai également décrit la structure 3D des disques simulés et mis à jour plusieurs propriétés intéressantes.

Un premier point à souligner concerne la réorganisation initiale du disque qui se déroule concomitamment à la disparition des structures caractéristiques des simulations 2,5D en forme de coude.
Une fois un état stationnaire atteint, l'apparition d'un anneau interne est constatée. Par ailleurs, la plupart des propriétés du disque, comme son taux d'accrétion, ses coefficients de transport ou encore la vitesse de rotation du gaz dans la cavité, sont cohérentes avec une diminution du flux magnétique dans la cavité, donnant lieu notamment à des couples magnétiques moins intenses.

Par la suite, j'ai essayé de donner quelques résultats concernant l'évolution du disque et ses propriétés en termes d'accrétion. En particulier, les disques en 3D accrètent toujours à des taux forts, similaires aux taux des simulations 2,5D quoique légèrement inférieurs.

L'étude de la stabilité de la cavité a produit des résultats particulièrement pertinents, notamment grâce à la détection de spirales en son sein, tout en maintenant une frontière stable entre la cavité et le disque plein.

J'ai caractérisé les spirales en étudiant leurs vitesses de phase ainsi que leurs rayons de corotation. Cependant et malgré plusieurs tentatives, je n'ai pas pu déterminer de manière définitive l'instabilité à l'œvre dans la cavité et formatn les spirales. La Rossby Wave Instability (RWI) semble être un candidat envisageable, mais les analyses de la simulation fiduciaire n'ont pas pu confirmer cela.

En dernière partie de ce chapitre, j'ai étudié quelques simulations me permettant d'accéder à une partie de l'espace des paramètres. La plupart des résultats associés montraient soit des similarités avec la simulation 2,5D correspondante, soit des différences similaires à celles observées entre les simulations de référence à 2,5 et 3 dimensions.
Cependant, l'analyse de la simulation moins résistive ne présentant pas de formation d'anneau interne suggère une origine physique à ce dernier dans la simulation de référence à 3 dimensions.

Le taux d'accrétion, le flux magnétique de la graine et le déclenchement de la RTI au niveau du bord interne sont autant d'éléments rappelant la physique des disques de type MAD dans le cadre de la magnétohydrodynamique en relativité générale.

Ce paradigme est couramment et essentiellement utilisé dans la physique des disques d'accrétion autour des trous noirs, mais apparaît tout à fait pertinent pour produire une description des parties les plus internes de la cavité, caractérisées par une forte magnétisation.

Ce résultat non trivial crée un pont entre des disques d'accrétion d'origines absolument différentes. Par ailleurs, ce point demande de plus amples travaux, notamment concernant l'évolution séculaire du flux magnétique dans la cavité.

Part III

PERSPECTIVES AND CONCLUSION

I end up with this last part focused on some perspectives for future works. Its first chapter is devoted to some observational links with my simulations and to a future numerical setup. I eventually conclude on my work in the last chapter.

5

OBSERVATIONS AND OUTER TRUNCATION OF TDS

"Dès l'enfance, je percevais l'écoulement des heures,
indépendantes de toute référence, de tout acte et de tout
événement, la disjonction du temps de ce qui n'était pas lui,
son existence autonome, son statut particulier, son empire, sa tyrannie.
Je me rappelle on ne peut plus clairement cet après-midi où,
pour la première fois, en face de l'univers vacant, je n'étais plus que fuite
d'instants rebelles à remplir encore leur fonction propre.
Le temps se décollait de l'être à mes dépens."

— Emil Cioran, *De l'inconvénient d'être né* (1973)

INTRODUCTION

This chapter aims at including the model of TDs sustained by magnetic winds in a broader picture. In particular, I want to link my simulations to observations. I will also present an upgraded implementation of my simulated discs that takes into account the outer truncation of the disc.

I focus on four kinds of results that are promising to test my model in the first section. The first one relies on the detection and characterisation of magnetic winds, involving in particular the magnetic lever arm.
Kinematic predictions then lead to useful prediction regarding the dynamics of the cavity of TDs. The transsonic accretion speed and the sub-keplerian rotation of the gas in the cavity are specifically promising.
I also check the possibility to use the detection of various structures (gaps, spirals, inner rings) as efficient probes to discriminate my model from others.
Finally, synthetic images will be a determinant tool to further link the simulations to the observations. I show a few images built from the 2.5 D simulations as a first step towards detailed comparison with observations.
The results are as many direct ways to test this model of wind emitting TDs. Still, it is possible to disentangle this model with other diagnostics involving statistical data on TDs and outer edge of discs observations. It is therefore needed to push further the model I used by implementing a realistic description of the outer truncation of TDs.
I ran such a simulation with my 2.5 D framework that I modified accordingly. I describe this work in the second section. Moreover, I let this simulation run for a very long time to study the dispersal processes of TDs and the role of the magnetic field transport. In particular, the magnetic field plays a prominent role in driving wind, so that it is essential to address the question of its transport throughout the disc.

INTRODUCTION

Ce chapitre a pour but d'inclure le modèle de disques de transition que j'ai utilisé dans le cadre plus général de la formation stellaire et planétaire. Le lien avec les observations est particulièrement essentiel afin de tester les hypothèses que j'ai utilisées ainsi que la pertinence du modèle. Ce travail est détaillé dans la première section du présent chapitre.
Par ailleurs, je présente également dans ce chapitre les résultats d'un travail préliminaire se focalisant sur la troncation externe de disques de transition. Un tel travail permet d'étendre mon modèle à des disques de transition dans leur globalité. Les résultats associés à cette étude sont compilés dans la seconde section du chapitre.

Le lien avec les observations est présenté sous 4 approches, basées sur les résultats de mes simulations numériques 2,5D et 3D. Je commence par évoquer la détection de vents magnétiques et les caractéristiques générales des vents magnétiques, en particulier via le bras de levier magnétique λ. Le vent magnétique est en effet l'ingrédient clé pour mettre au point le modèle de disques de transition que j'ai étudié.
Un aspect prometteur issu de mes simulations vient des diagnostiques cinématiques dans la cavité. L'accrétion transsonique et la cavité sous-keplerienne sont deux points particulièrement pertinents. Ces résultats peuvent être liés aux observations, notamment à partir d'images synthétiques construites sur la base de mes simulations. Je présente certains de ces résultats, comme un premier pas vers un lien plus concret avec les observations de disques de transition.
Enfin, les différentes sous-structures que je détecte dans mes simulations (sillons, anneau interne, spirales) sont autant de prédictions observationnelles qui permettront de discriminer mon modèle parmi les autres modèles de disques de transition.
Toutes ses approches forment un ensemble de pistes rendant pertinent le modèle que j'ai utilisé dans le cadre d'observations de disques. Cependant, il serait également envisageable de proposer d'autres diagnostiques pertinents, notamment avec une approche statistique des disques de transition (âge, taille de la cavité) ou encore via un travail sur la troncation externe de ces disques. Par conséquent, il est nécessaire d'améliorer le modèle numérique, ce que j'ai fait en implémentant une description simple et réaliste de la bordure extérieure du disque. Les résultats de ce travail sont présentés dans la seconde section du chapitre.

Dans le cadre de mes simulations 2,5 D, j'ai étudié l'influence d'une troncation exponentielle à partir d'un rayon caractéristique. Par ailleurs, j'ai laissé tourné la simulation en question 10 fois plus longtemps que celle de référence en 2,5 D. Ce choix est nécessaire pour assurer une convergence dans les parties les plus externes du disques et m'a permis d'étudier plus en détail la dispersion du disque ainsi que le transport du champ magnétique à l'intérieur de ce dernier. Cette dernière thématique est par ailleurs tout à fait critique dans le cadre des disques émettant des vents magnétiques, puisque le champ magnétique joue alors un rôle prépondérant, en contrôlant de nombreuses propriétés du disques (couple magnétique et accrétion notamment).
Poursuivre et approfondir un tel travail permettra une meilleure compréhension des disques magnétisés et en particulier des processus en lien avec la dispersion des disques protoplanétaires.

5.1 OBSERVATIONAL EVIDENCES

Important note

This section contains some radiative transfer computations. This work was performed based on my 2.5 D simulations and deeper investigations will be done in a near future for my 3 D simulations. This upcoming work shall be included in the article related to my 3 D simulations. Still, I want to show some of these results here, since they build a bridge with observations. They also nicely tie up all my results together and draw a satisfying conclusion from the epistemological point of view.

A compelling way to rule out or favour the model I studied during my thesis would be a direct comparison with observations. In particular, radiative transfer is a perfect tool to get synthetic images from my simulations and a first step towards linking them to observations. However, this work is beyond the scope of my thesis and should be my next preoccupation as a researcher. Still, I want to give some insights on the relevant properties of my simulations regarding comparison to observations. This is the aim of the first section.

5.1.1 MHD *winds: the first building block*

When considering a model of transition discs sustained by MHD winds, the very first question anyone would ask is: 'Do we detect such winds?'. MHD disc winds have been detected in PPDs, and I refer to the introduction chapter (chap. 1) as well as to Whelan et al. (2021). Recent observations of outflows from planet-forming systems succeeded in disentangling the star and discs components, with the detection of a nested outflow in DG Tau B in de Valon et al. (2020) or the detection of a wind in HH 120 in Lee et al. (2021). When assuming a magnetic wind model for DG Tau B, de Valon et al. (2020) finds in particular a magnetic lever arm of $\lambda = 1.6$. Diverse estimations of λ for HH 212 lead to $\lambda = 5.5$ (Tabone et al., 2020) or $\lambda = 3.5$ (Lee et al., 2021). Of course, λ is not directly measured in discs observations but estimated based on models, such as Ferreira et al. (2006) or Anderson et al. (2003) for DG Tau B.

However and when it comes to the detection of MHD winds in TDs, the literature remains sparse. TW Hydrae is a well-known transition discs (see for example Menu et al., 2014) and previous work devoted to photoevaporation were performed (Pascucci and Sterzik, 2009). This disc was studied in Ricci et al. (2021) in which the authors tested photoevaporation and MHD disc winds, based on observations and simulations. They used previous simulations of magnetic winds (Milliner

et al., 2019; Weber et al., 2020) to estimate the free-free emission from an MHD wind as it was done for a photoevaporation wind (Pascucci et al., 2012). The possibility to have an MHD wind remains open and it is worth noting that it could be launched from the innermost regions of the disc, contrary to the photoevaporation wind.

A state of the art compilation of disc winds in PPDs and TDs can be found in Pascucci et al. (2022). Despite the detection of gas in the cavity of TDs with the help of numerous tracers such as H_2 fluorescent (Hoadley et al., 2015), [OIλ6300] (Fang et al., 2018) or CO fundamental emission (Pontoppidan et al., 2011), the presence of inner MHD winds is hard to confirm.
The [OIλ6300] profile is used as a good indicator of the presence of inner winds in full accreting discs. However, Fang et al. (2018) report that a small proportion of TDs exhibit a high velocity component and their observations of [OIλ6300] in TDs are consistent with bound gas in the dust cavity (see for example Simon et al., 2016; Pascucci et al., 2020).
Nevertheless, observations are encouraging and gain significant precision with time, so that MHD winds detections in TDs are anything but a vain dream and a worthwhile endeavour.

Considering this observational picture, my simulations give useful predictions, especially regarding the magnetic lever arm. This parameter is directly linked to the wind emission and the accretion rate at the magnetic field line footpoint radius R_0 following Pelletier and Pudritz (1992)

$$\lambda^{-1} \approx \frac{\dot{M}_{\rm wind}(R_0)}{\dot{M}(R_0)}\,, \tag{207}$$

where $\dot{M}_{\rm wind}$ is the wind mass loss rate. Defining the ejection efficiency $\xi \equiv \mathrm{d}\log\dot{M}/\mathrm{d}\log R$, the magnetic lever arm parameter reads (Ferreira, 1997)

$$\xi \approx \frac{1}{2\,(\lambda-1)}\,. \tag{208}$$

This short formulae are indicative of the key role of λ in the MHD winds models, which is why observational works try to evaluate this number. My simulations suggest strong values of λ for the magnetic wind emitted from the cavity, with $\lambda_{2\,\mathrm{D}} \sim 10$ and a slightly lower value in 3D $\lambda_{3\,\mathrm{D}} \sim 7-8$. I give in fig.80 the solutions of my simulations in the (κ,λ) plane (which should be compared to Blandford and Payne, 1982 fig. 2 and Lesur, 2021b fig. 9). It appears that in the full external disc, my solutions are similar to what is found in the literature. In particular, I compare my values to the ones found by Lesur (2021b) who used self-similar model of wind-emitting disc dominated by ambipolar diffusion. My simulations renders values that are comparable to the self-similar ones obtained for high-magnetisation such as

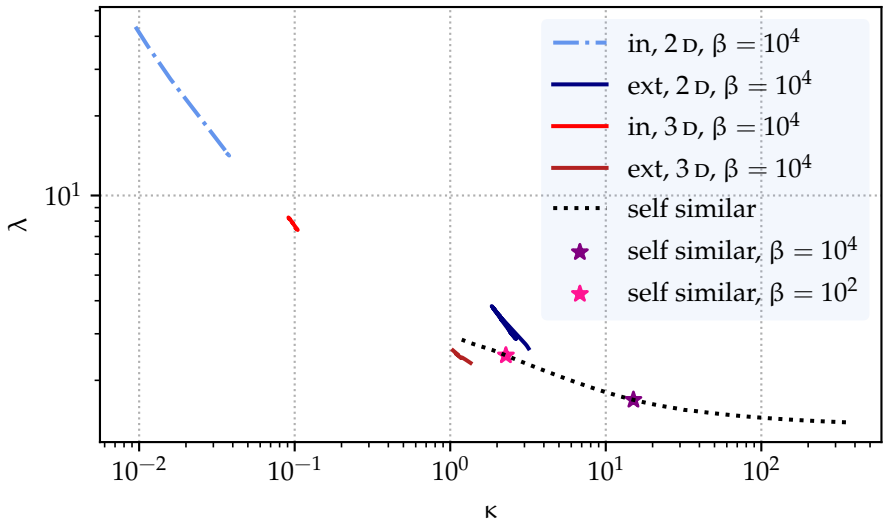

Figure 80: (κ, λ) plane for my 2 D and 3 D simulations. The values labelled by 'in' refer to an inner poloidal magnetic field line (at 3.5 AU for the 2 D simulation and at 6 AU for the 3 D one) while 'ext' indicates field lines in the external disc (at 15 AU for both simulations). To account for the variability of κ and λ close to the midplane, I only kept the values calculated along the field lines high enough in the disc ($Z > 10$ AU). The black-dotted line are values in the plane (κ, λ) taken from Lesur (2021b), for various values of β (or β_{out} using my notation), the purple cross indicates the self similar values for $\beta = 10^4$.

$\beta_{out} \sim 10^2$. On the contrary, the cavity is characterised by high values of λ (and therefore small ones for κ).

Considering the physical units I chose, I show in fig. 81 the norm of the time-averaged poloidal velocity computed from the fiducial 2.5 D simulation. This gives an order of magnitude of the velocity associated to the wind emitted from the cavity. I find that $\langle \|\boldsymbol{v}_p\| \rangle \sim 1 - 10 \text{ km s}^{-1}$.

5.1.2 *Kinematics prediction*

Rather than testing directly the presence of a magnetic wind, one could look for its consequences on the disc. In this subsection, I will show preliminary results of radiative transfer calculations based on my 2.5 D fiducial simulation.

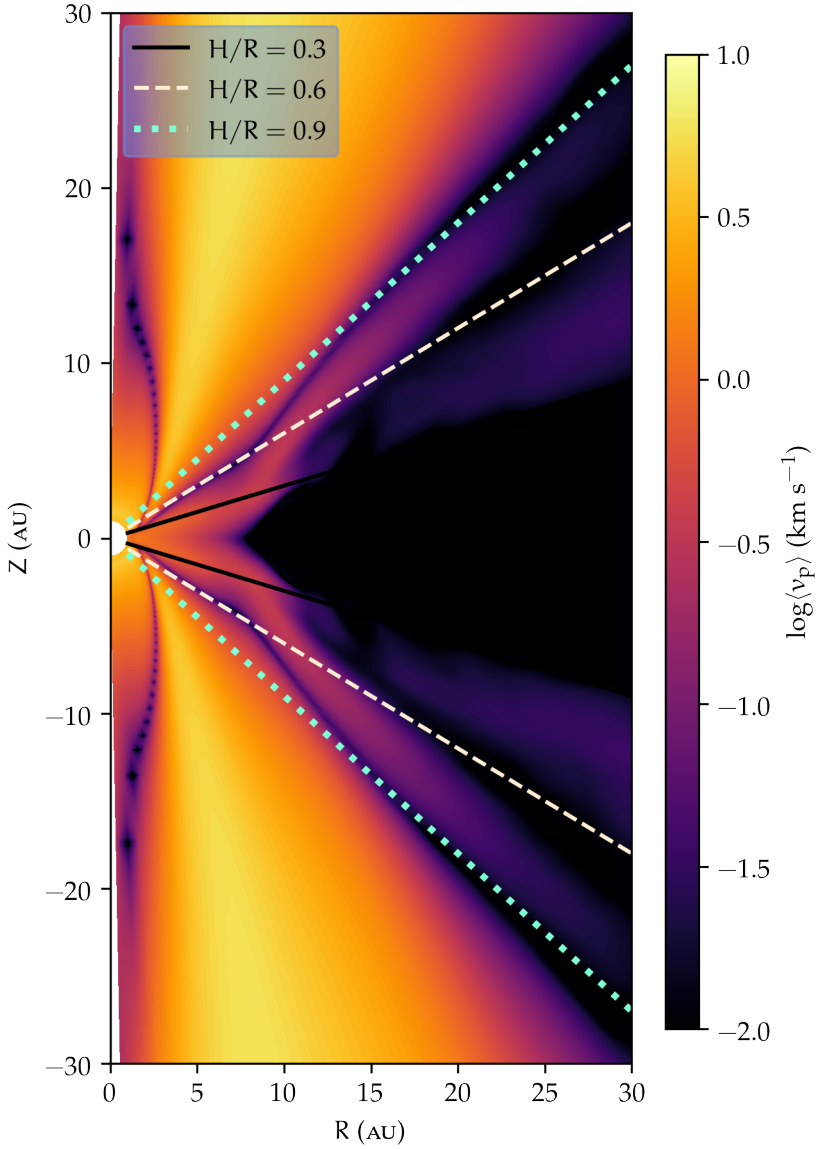

Figure 81: Time-averaged norm of the poloidal velocity $\langle v_p \rangle$ for the 2.5 D fiducial simulation, given in physical units.

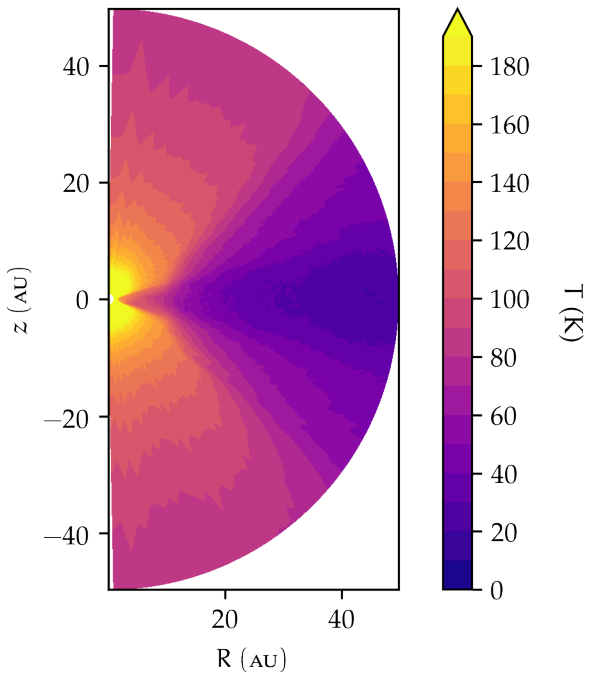

Figure 82: Temperature in a simulated disc from my 2.5 D fiducial simulation.

5.1.2.1 *Modelisation*

In this subsection, I present the code that I used to generate the synthetic images that I will show in the next subsections. I used the RADMC-3D Monte Carlo radiative transfer code (Dullemond et al., 2012). I consider a solar mass star, with a luminosity of 1 $L_\odot$ and a temperature of 4000 K. My simulated PPD is supposed to be at 140 pc with a 20 degrees inclination. I keep the same physical units (mass, time, length) as I have in my simulations.
My simulations being dust free, I start by computing the H_2 column density based on the density profile of my simulation. The gas repartition is converted into a dust repartition with a reference file that mimics a constant dust to gas ratio. The temperature of the gas is then taken to be the temperature of the dust which is shown in fig. 82.
I show the brightness temperature of the disc in fig. 83 in which the cavity is clearly seen in the middle.

5.1.2.2 *Accretion speed in the cavity*

The model of TDs I studied implies a transsonic accretion speed. This property is suggested in particular in Wang and Goodman (2017). I highlight this result in particular with my 2.5 D simulations.
Interestingly, a fast radial inflow could be detected with the combination of rotated isovelocity contours (with respect to the disc axis)

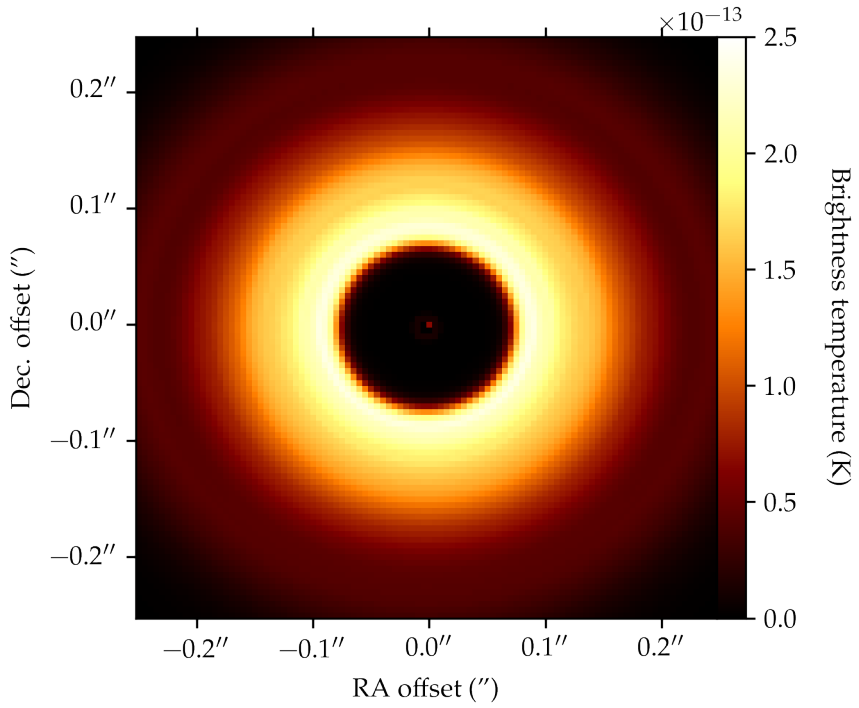

Figure 83: Brightness temperature synthetic image of a simulated disc from my 2.5 D fiducial simulation.

in channel maps of optically thick lines and twisted isophotes. This method is detailed in Rosenfeld et al. (2014), and I give some explanations in the next lines. To explain this potential observation, one can start by giving the projected velocity (v_x, v_y) for a Keplerian flow to which an accretion flow is added whose radial velocity in units of the local Keplerian speed is χ. One can write

$$\begin{aligned} v_x &= -v_K \sin\theta && -\chi\, v_K \cos\theta\,, \\ v_y &= \underbrace{v_K \cos\theta}_{\text{Keplerian rotation}} && \underbrace{-\chi\, v_K \sin\theta}_{\text{accretion}}\,. \end{aligned}$$

The velocity along the line of sight is then given by

$$v_{los} \equiv -v_y \sin i = -v_K \sin i \cos\theta + \chi\, v_K \sin i \sin\theta\,, \tag{209}$$

with i the inclination angle. In the end, the region of the projected plane where v_{los} cancels is a straight line inclined with respect to the horizontal axis, by the angle θ_{sys} defined by

$$\theta_{sys} = \arctan(1/\chi)\,. \tag{210}$$

If the accretion speed is given in units of c_s as $v_{acc.} = a\, c_s$, then $\chi = \varepsilon\, a$, with $\varepsilon = 0.1$ in my simulations. Considering a purely Keplerian flow (without accretion), this angle should be 90 degrees. For an imaginary purely radial flow (no Keplerian rotation), this angle should be

0 degrees if the disc is inclined with a rotation around the horizontal axis. The combination of the two leads to the angle defined by eq. 210 (see the fig. 2 in Rosenfeld et al., 2014).
Despite how promising this may sound, it has been suggested that these very observational properties could be the result of a warped inner disc (e. g. Casassus et al., 2015, for HD 142527). Still, this method is definitively something to try with observations of TDs, as recalled by Pascucci et al. (2022).

I show in fig. 84 the computed zeroth and first orders with RADMC-3D. The images are calculated from the final file of my 2.5 D fiducial simulation. The zeroth order is partially masked by a dark spot due to an outflow leaving the cavity. The first order moment could present the influence of a radial transsonic accretion flow.
Looking at the last file of my simulation, I have an accretion speed $v_{acc} = 1 - 5\, c_s$ which depends on the radius. The corresponding θ_{sys} is between 63 and 84 degrees with respect to the horizontal axis, which means between 6 and 27 degrees with respect to the vertical axis.
Back to the bottom panel of fig. 84, one can see that the outflow makes it difficult to measure precise angles. However, it still seems that the cavity is 'rotated' by some angle which corresponds to the previous values. This observation is preliminary and I leave it as an illustration. More work is to be done, but applying this method to my simulated discs surely is promising.

5.1.2.3 *Azimuthal velocity in the cavity*

Keeping up with velocity profiles in the disc, the rotation speed in the cavity is an interesting property to investigate. I found that the cavity was strongly sub-Keplerian. The effective rotation profile is $\sim 60\%$ of the Keplerian velocity in the 2.5 D simulations and $\sim 80 - 90\%$ of Ω_K in the 3 D ones.
This implies that the inner regions of my simulated discs are slowly rotating (in the sense that they rotate slower than they do for a full disc), while the remaining disc is Keplerian. In channel maps, this property should be detected by the presence of a 'kink' corresponding to the shift of velocity profile (e. g. from $\sim 0.8\, v_K$ to v_K). Some kinks are observed in channel maps of PPDs and indicative of a planet such as in Harsono et al. (2018), Pinte et al. (2019), and Calcino et al. (2022). TDs surveys render channel maps of these discs (e. g. van der Marel et al., 2016b). However such observations can be challenging and unworkable for TDs with small cavities as can be seen with van der Marel et al. (2022). Since the kink should operate at the cavity location, the observations would be even harder to achieve. To cope with this difficulty, a possibility could be to work with TDs harbouring very wide cavities, one TD of the system ISO-Oph 2 (González-Ruilova et al., 2020) being a good candidate.

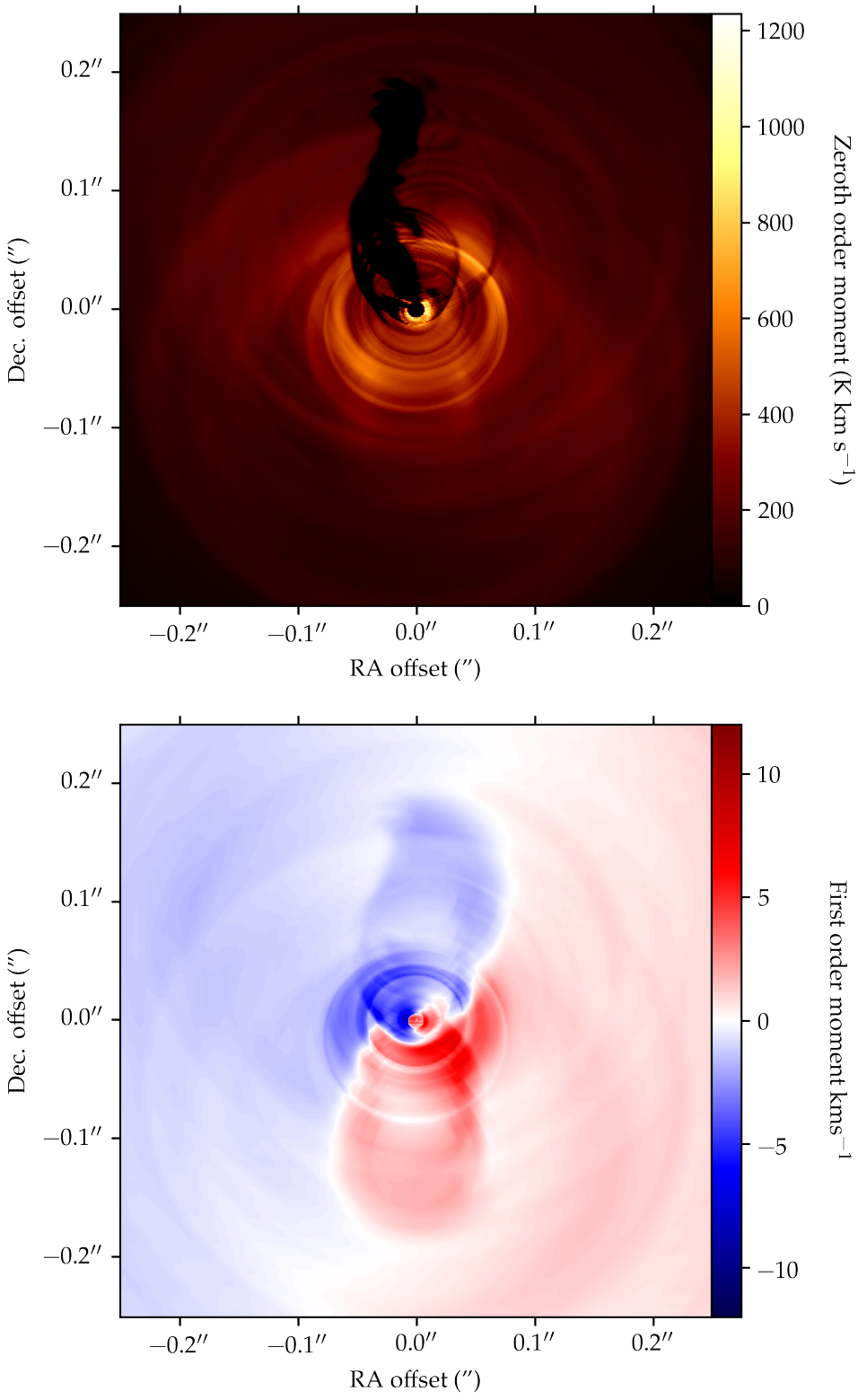

Figure 84: The top panel is the zeroth order moment and the bottom one the first order moment. Both were computed for my 2.5 D fiducial simulation, based on the final file of the simulation.

Back to my simulations, I computed channel maps for my 2.5 D fiducial simulations. However, the results are now far from being conclusive.

5.1.3 *Substructures in the disc*

Substructures in PPDs are now thought to be common features of discs (Andrews et al., 2018; Long et al., 2018). It is then of prime interest for me to check the plausible links with observations based on the substructures I detected in my simulations.

5.1.3.1 *Spirals*

As exposed in the introduction (chap. 1), spirals are routinely detected in observations of PPDs (Pérez et al., 2016). TDs also exhibit spirals, some in their outer parts (i. e. not in the cavity) such as van der Marel et al. (2016a), while some others see their cavity filled with whirlpool-like structures (see e. g. Cuello et al., 2019).

Though the instability at play has not yet been clearly characterised, my 3 D simulations consistently render spirals inside the cavity of simulated TDs. The phase velocity of the spirals between the inner ring and the cavity is somewhat close to the keplerian speed at the cavity edge location. This result may be a good indirect way to test the this model of TDs. However, the short duration of my 3 D calls for deeper studies of these spirals.

5.1.3.2 *Inner ring*

Despite being initially not wanted, an inner ring forms in some of my 3 D simulations. This ring may have numerical origins such as the restart procedure or the inner boundary condition (see chap. 2). In the end, the fiducial 3 D simulation of the cavity still share the stage with this ring. Inner rings in TDs have been observed in several discs (see e. g. Francis and van der Marel, 2020; Uyama et al., 2022).
I get simulations with or without inner ring, so that detecting or not a ring in any TDs cannot help to discriminate or favour the model I work with. However, if the presence of a ring could be linked to the one of two sets of spirals, maybe this could be of interest. Nevertheless, the somehow 'accidental' appearance of the inner ring calls for more converged 3 D simulations (which is computational-time demanding) or for a numerical setup devoted to the study of inner rings (by restarting a 2.5 D simulations harbouring such a disc for example).

5.1.3.3 *Outer gaps*

I discussed the presence of gaps already (see chap. 3 and 4). Still, I want to recall that these common structures naturally arise in the non-ideal MHD framework. Simulations conducted on much longer time-scales could enable the study of rings, how they merge, separate and more specifically, how they interact with the cavity edge.
Lastly, adding planets in the outer disc or inside the cavity would be of prime interest, to include MHD wind launching TDs in the bigger picture of planetary formation. The interaction between planets and gaps can be complex (Wafflard-Fernandez and Baruteau, 2020) while their interplay with TDs cavities is a broad topic. Previous works studied the effects of having planets in a cavity of TD (Baruteau et al., 2021; Debras et al., 2021; Chen et al., 2021), so that doing so with this new model of TDs sounds promising.

5.1.4 *Cavity expansion*

The long term evolution of PPDs is key to get access to their age and put constraints on planetary formation. The effects of MHD winds on the secular evolution of PPDs were studied for full PPDs with the help of 1 D simulations with the work of Tabone et al. (2022b), Tabone et al. (2022a), Trapman et al. (2022a), and Zagaria et al. (2022). These simulations give access to the disc sizes as well as to their ages.
A similar work could be done for TDs. I dwell on the peculiar behaviour of the cavity edge in my simulations (especially the 2.5 D ones). In particular, the sizes of the cavities could be used to estimate the age of TDs based on the model I used. This idea is developed in sec. 5.2.

5.2 MDW LAUNCHING DISCS WITH INNER AND OUTER TRUNCATIONS: TOWARDS A GLOBAL DESCRIPTION OF THE DISPERSION OF PPDS

Important note

The work that I present in this section is preliminary and based on a single 2.5 D supplementary simulation. This is not directly related to disc observations, but rather a refinement of my 2.5 D simulations, as an attempt to get a broader view of TDs. This work should be understood as a side project on its own, that aims to show the possibility of the model I used regarding the dispersal processes of PPDs.

5.2.1 *Introduction and presentation of the model*

5.2.1.1 *Motivation*

The peculiar behaviour of the magnetic field transport in my 2.5 D simulations is hard to understand, mainly because of its non-local nature. In MHD models of PPDs, the magnetic plays a major role as it controls a considerable part of (if not most of) the magnetic torques that brake the disc, the accretion and any transport coefficients. Therefore, it is of prime interest to unveil the dynamics of the magnetic field on long time-scales. Nonetheless, three results of my 2.5 D simulations make it very challenging to get access to this dynamic.

First, the non local influence of the cavity calls for a global approach of such TDs. Global simulations must be used (as I did in 2 D and 3 D) and the disc should be entirely simulated. At least the outer must span on greater radii, in order to lower the influence of the cavity and possibly recover usual behaviours of magnetic field transport.

Second, localised structures were detected in my 2.5 D simulations (the elbow structure, the magnetic loop), which rule out the use of self similar solutions. This structures also make the use of 1 D models such as in Suzuki et al. (2016) and Tabone et al. (2022b) complicated at first. The profiles of ζ, α and v_w that I obtained in my 2.5 D simulations could be implemented in similar 1 D models. A precise parametrisation could then capture the effects of these structures. However, 2.5 D simulations would still be needed to give such a parametrisation. This last point calls for a long-lasted 2.5 D simulations to catch the evolution of a TD on a very long time scale (longer than just a few 10^4 orbits at R_{int}.)

Third and finally, the characteristic transport velocity of the magnetic field is about $\sim 10^{-4}\, v_K$. This small velocity (compared to the local keplerian speed) imposes to run simulations that can catch the *very* long-term evolution of the discs. 10^4 orbits at R_{int} are not enough to handle these slow processes with good accuracy and a factor at least $\times 10$ is needed.

Remark on computational time

I only consider doing 2.5 D simulations, assuming that targeting any 'secular' or 'long term' evolution rules out any possibility to do 3 D simulations, because of their computational, financial and ecological costs. As an example, since 1000 orbits at R_{int} cost $\sim 3 \times 10^6$ h CPU, 10^5 orbits would require $\sim 300 \times 10^6$ h CPU^{-1} which means $\sim$ 17 yrs on 2000 CPUs. I do not think I need to further out comment on why this is out of reach!

To address the second and third points, I run a new 2.5 D global simulation of a TD with MDW on 3×10^5 orbits at R_{int} (which is 10 times longer than my fiducial 2.5 D simulation). I solve the first point by adding an outer truncation to my newly simulated TD, which now exhibits inner and outer truncations. Previous 2.5 D simulations of PPDs (without cavity), with an outer truncation, ambipolar diffusion and magnetised winds were performed by Yang and Bai (2021). The authors showed that the magnetic field was transported outwards in their work. Therefore, I expect that the magnetic field in my new simulation will be dragged inwards because of the cavity up to some radius where the global influence of the outer truncation will take over the cavity influence. Such a model of TD is an opportunity to study a somehow realistic model of global TD and to explore the mechanism responsible for the dispersion of discs.

The outer edges of PPDs are interesting to study because they provide a way to disentangle viscous and magnetically-driven evolutionary models of discs. In particular, the viscous spreading of the outermost parts of PPDs is expected with the viscous approach of discs, based on the pioneer works of Shakura and Sunyaev (1973) and Lynden-Bell and Pringle (1974). Moreover, several observational have already gathered data on the outer truncation of PPDs, such as Barenfeld et al. (2017), Tazzari et al. (2017), Ansdell et al. (2018), and Sanchis et al. (2021), some specifically focusing on the gas spreading of discs (Najita and Bergin, 2018). These works studied both the gas and dust sizes of PPDs. Some 1 D simulations aim to get the gas (Tabone et al., 2022a) and dust (Zagaria et al., 2022) sizes of discs to use it with a statistical approach. Such works also are sustained by simulations with higher dimensions, such as Yang and Bai (2021). Eventually, my project to compute the first simulations of outer-truncated TDs sustained by MHD winds in the context of ambipolar-dominated discs is a good starting point to get access to the dispersal mechanisms of TDs.

5.2.1.2 *Presentation of the model*

The description of the numerical model I used is simple. I start with the a numerical setup identical to the one that I used for my 2.5 D simulations. In particular, I keep the same values $\beta_{out} = 10^4$, $\beta_{in} = 1$, $\Lambda_A = 1$ and $R_{cav} = 10\ R_{int}$ as in my 2.5 D fiducial simulation. Only the gas component of the discs is simulated. Hence any dust-related phenomena such as grain growth or migration of solids (Birnstiel and Andrews, 2013) is neglected.
I ensure that no mass can come from the outer boundary condition and choose an outer truncation radius $R_{trunc.} \equiv R_c = 50\ R_{int} = 5\, R_{cav}$. I implement the outer truncation following Yang and Bai (2021), with an exponential cutoff so that the initial density profile is given by

I recall here that the function f carves the cavity and ρ_{HD} accounts for the initial hydrostatic equilibrium.

$$\rho(R, Z) = f(R) \times \rho_{HD}(R, Z) \times \exp\left[-(R/R_c)^2\right]. \tag{211}$$

I keep the same resolution for θ (240 points on a stretched grid covering the full domain including the poles) and I increase the radial one so that I have 448 points logarithmically spaced between $R_{int} = 1$ and $R_{out} = 150\, R_{int} = 3\, R_c$. I let the simulation run for 300000 orbits at R_{int}, which means 9487 orbits at the initial cavity edge location or 849 orbits at the initial outer truncation radius. In particular, more than 150 orbits are done at any radius in the disc. As a comparison, this is approximately 10 the length of the fiducial simulation of Yang and Bai (2021).
I want to shed light on the radial profile of Λ_A which does not take into account the outer truncation. However, this is not a problem because this far from the star (for $R \geqslant 50$ AU), one can expect the disc and its upper layers to be poorly ionised with ambipolar diffusion dominating even a bit higher from the disc surface. Finally, I add that I lowered by a factor 10 the maximum value of η_A because of some issues I had regarding the resistive time-step. Apart from these differences, everything else is kept the same.

Eventually, this simulation was run on 128 cores of the machine Dahu from the mesocentre Gricad for more or less ~ 8 months, which corresponds to ~ 737280 h CPU. I label this simulation with S2Dext.

5.2.2 *General overview of the disc*

I start by giving the spatio-temporal diagram of Σ in fig. 85. Contrary to the previous simulations, I give up the logarithmic scale for the radius, to get a picture more reading-friendly. In particular, this enable to catch a global picture of the disc and to better evaluate its size. On the contrary, the figure 86 shows the spatio-temporal diagram of Σ with a logarithmic scale for the radius, supplemented by the spatio-temporal diagram of $\overline{\beta}$. This representation focuses on the inner cav-

Note that the lower range of the colorbar of the figure 85 differs from the similar spatio-temporal diagrams shown in the previous chapter.

ity of the disc. I also give the temporal evolution of the θ−averaged vertical magnetic field squared in the left panel of fig. 87. This panel is complemented by the profile of the magnetic flux function ψ (right panel of fig. 87)

Figure 85 shows that the disc encounters various dynamical regimes with time. I indicate the 3 regimes with the numbers (1), (2) and (3) on fig. 85. I describe each of them in the following paragraphs.

The beginning and the end of the regimes are arbitrary, since the evolution of the disc is continuous and occurring on long time-scales (longer than 10^3 orbits at R_{int}). It is difficult to select a definite instant where to end and start these dynamical regimes. I rather indicate period of time and focus on their physical characteristics, which is what matters the most in the end.

FIRST REGIME (1): The first regime spans between the start of the simulation and $t \sim 50000$ orbits at R_{int}. The configuration of the disc corresponds to the common one found with other 2.5 D simulations. This is confirmed by fig. 86 with the striped-cavity that distinguishes this regime. I will not describe in depth the structure of the disc between 1 and 50 AU as all the results from the 2.5 D simulations stand (the magnetic loop and the elbow-shaped structures are present in particular).

The outer truncation encounters a transient state, bringing the whole disc to a state characterised by a dynamically active cavity, the development of gaps in the whole outer part of the disc, a widening cavity and a slowly shrinking outer truncation. This last result is in contrast with the viscous-disc picture and confirms the observation of Yang and Bai (2021). Looking at the profile of $\overline{\beta}$, I note that a magnetic reorganisation of the disc occurs in the outer part of the disc, with $\overline{\beta}$ varying from 10^4 up to 10^{8-10} after 5000 orbits at R_{int}. This is to be linked with the advection of magnetic field that was detected in the 2.5 D simulations. Fig. 87 recovers this result. The vertical magnetic field decreases in the outer part of the disc (left panel) and the advection of magnetic field is easily tracked by the contours of ψ in the right panel. At the end of this first regime, the outer parts of the disc are less magnetised. On the contrary, the cavity is larger and threaded by a considerable amount of magnetic field.

SECOND REGIME (2): Between ~ 50000 and 150000 orbits at R_{int}, the disc is characterised by a moderate activity on short time-scales in the cavity ($t \sim 1-10$ orbits at R_{int}) and a stable configuration on longer time-scales ($t \sim 100-1000$ orbits at R_{int}).

An important property is the fact that the magnetic loop is not present anymore in the disc. The supplementary $\langle B_\varphi \rangle$ sign flip also disappeared. The disappearance of the loop removed the elbow-shaped structure, disabling the formation of the filaments of matter that were previously seen with 2.5 D simulations. The magnetic structure of the disc is shown time-averaged between 50001 and 60000 orbits at R_{int} in the right panel of fig. 88. I do not detect any bursts of accretion in the cavity. Consequently, the cavity looses its temporal stripes and takes

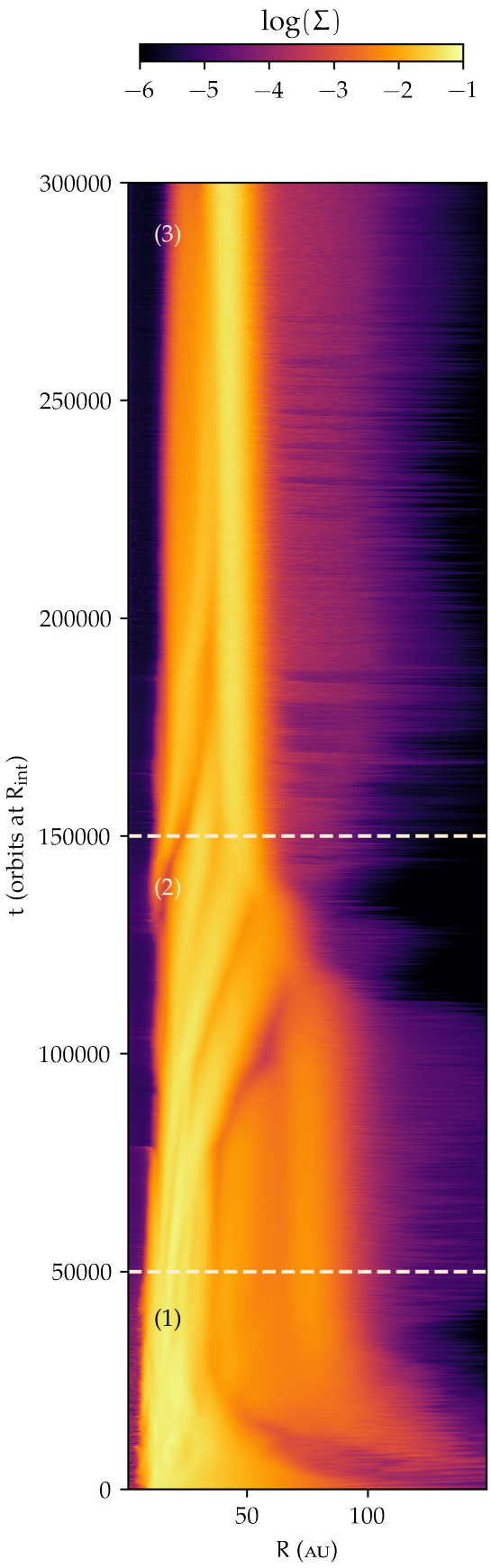

Figure 85: Spatio-temporal diagram of Σ alone (computed with $\varepsilon_{int} = 0.3$), for the simulation S2Dext. The radius is not shown with a logarithmic scale in this figure. The numbers indicate the 3 dynamical regimes that are separated with yellow dashed lines.

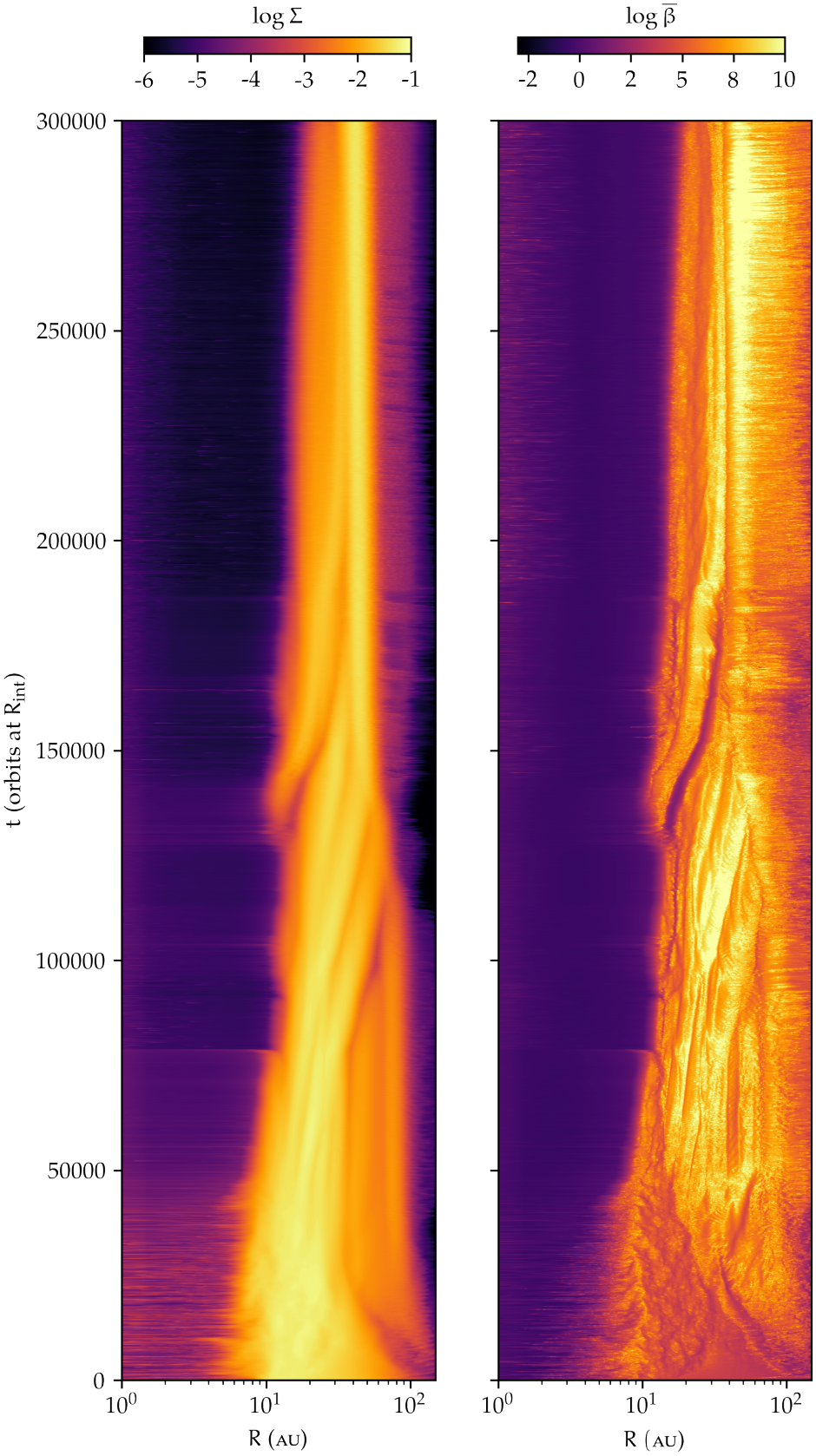

Figure 86: Spatio-temporal diagrams of Σ and $\overline{\beta}$ (computed with $\varepsilon_{\text{int}} = 0.3$), for the simulation S2Dext. The radius is shown with a logarithmic scale in this figure.

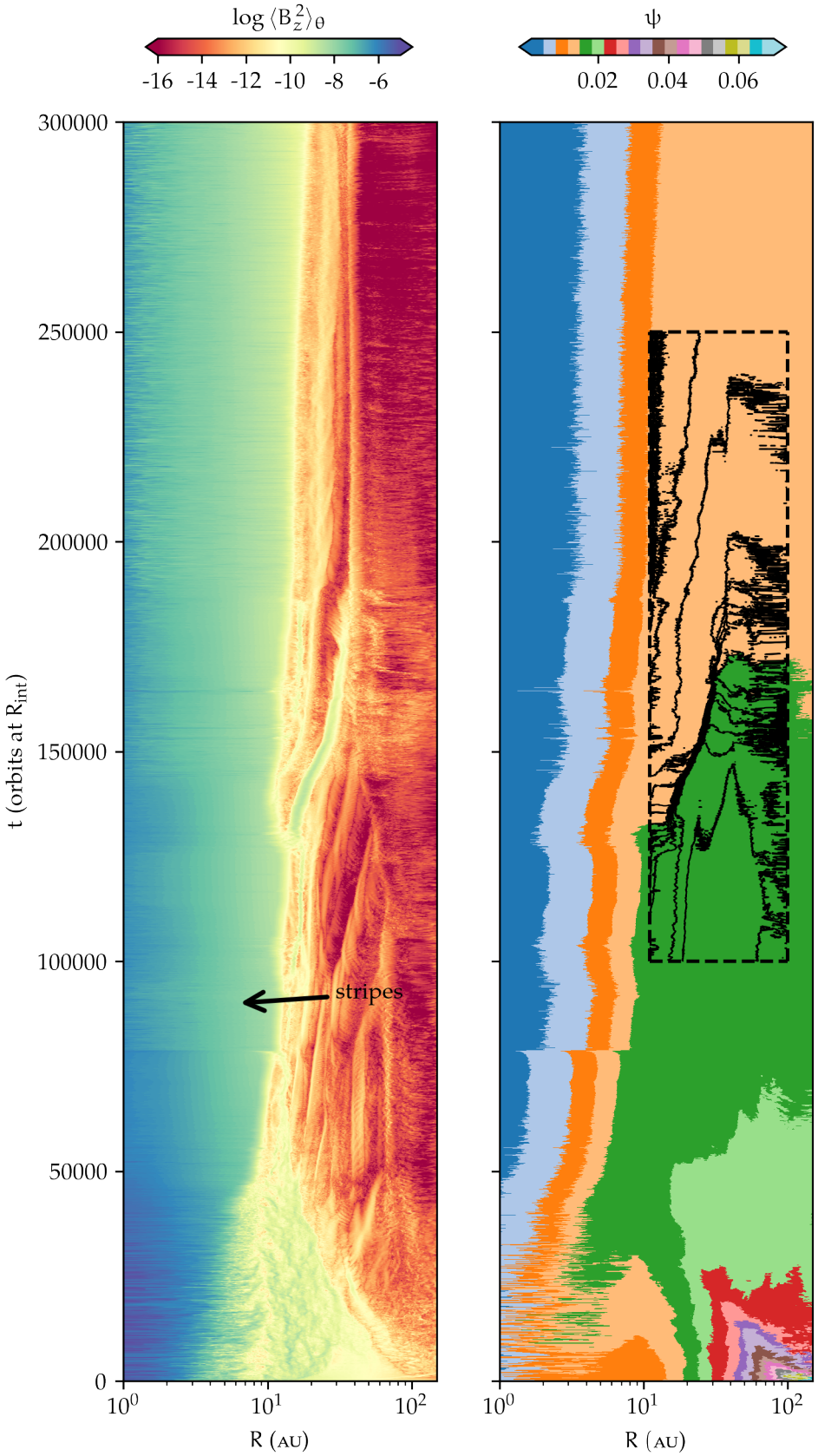

Figure 87: Spatio-temporal diagrams of $\langle B_z^2 \rangle_\theta$ (left panel) and ψ (right panel), for the simulation S2Dext. On the right panel, I highlight a few contours in black full lines to clarify the magnetic field transport in the outer disc. The radius is shown with a logarithmic scale in this figure. The arrow indicates the location of peculiar stripes in the cavity (see sec. 5.2.3).

the shape of a continuous and thin accretion flow located at the disc midplane. This is shown in the left panel of fig. 88, inside the cavity. The plasma parameter also reaches $\overline{\beta} = 1$ in the cavity with little to no temporal variation.

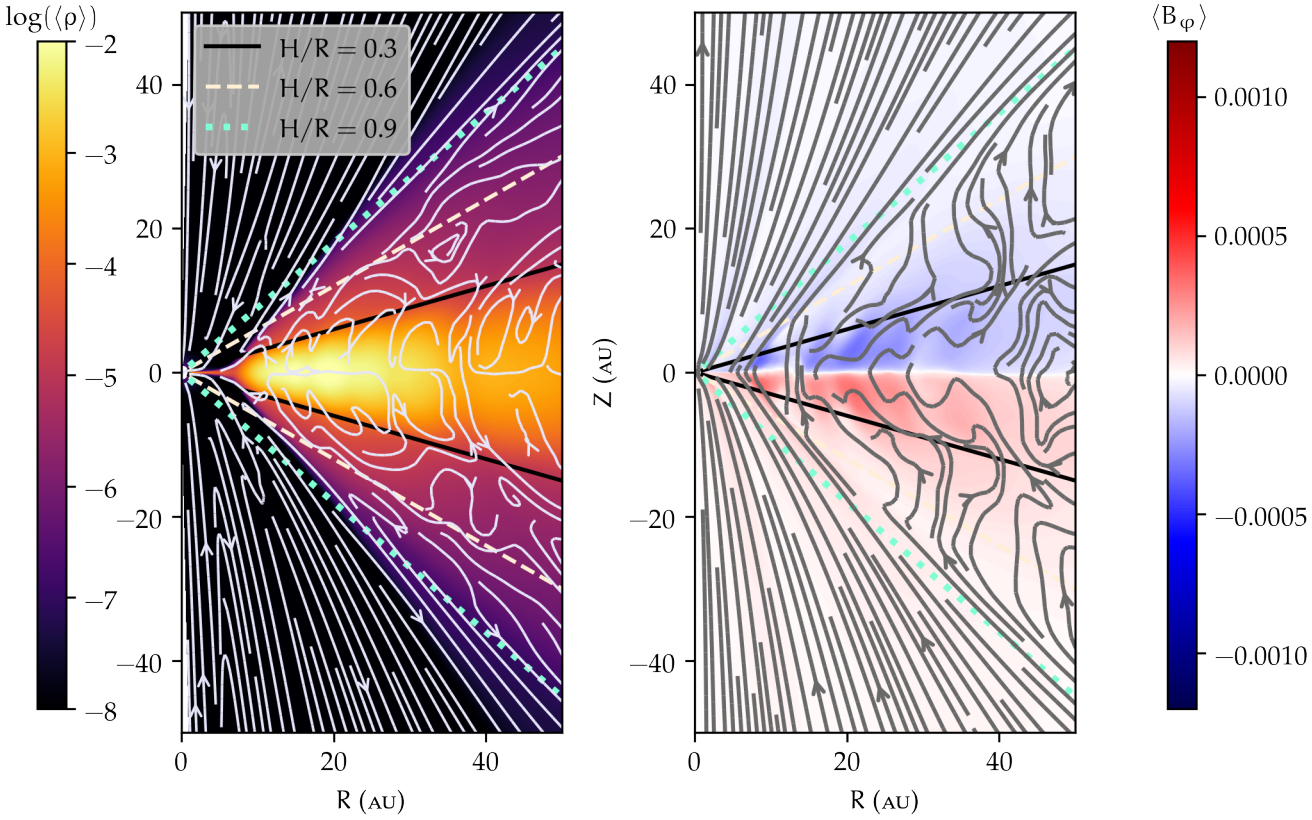

Figure 88: Density (left panel) and toroidal magnetic field (right panel) for the simulation S2Dext. The quantities are averaged on 10000 orbits at R_{int} between 50001 and 60000 orbits at R_{int}. I plot the stream lines in the right panel and the poloidal magnetic field lines on the left one. This figure highlights disc between $R = 1$ and 50 AU.

The cavity (resp. the outer truncation) keeps widening (resp. shrinking) (see fig. 85). Multiple gaps appear with time in the outer disc. All of them migrate outwards and eventually disappear, making them transitory structures that are very dynamical on long time-scales ($\sim 10^3 - 10^4$ orbits ar R_{int}). The displacement of the gaps comes along with the transport of the magnetic field. The contours of ψ indicate that the magnetic field is transported outwards in the cavity and in the outer part of the disc up to $R \approx 40$ AU. For better visibility, I highlight some contours of ψ in fig. 87 with black full lines over the image. In particular, the contours for radii greater than $R \approx 40$ AU show that some magnetic field is advected inwards from the outermost parts of the disc.

In this regime, the outermost part of the disc gets less and less mag-

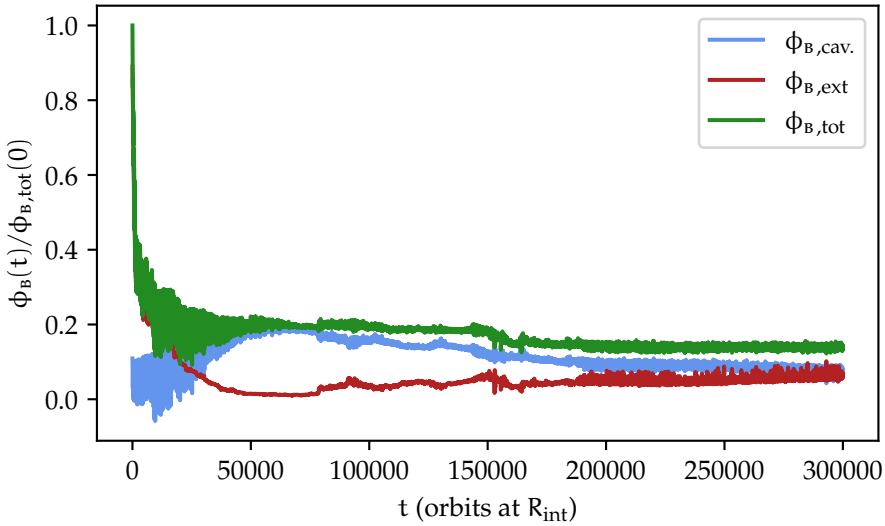

Figure 89: Vertical magnetic flux in the cavity ($\phi_{B,\,cav.}$, full blue line), in the external part of the disc ($\phi_{B,\,ext}$, full red line) and in the whole disc ($\phi_{B,\,tot}$, full green line) for the simulation S2Dext.

netised. Therefore, the magnetic field accumulates at the cavity edge location which keeps moving outwards. The total magnetic flux of the cavity remains constant and hence gets 'diluted' as the cavity expands. I define the radially integrated magnetic field ϕ_B as

$$\phi_B(t, R_1, R_2) \equiv \int_{R=R_1}^{R=R_2} -\overline{B_\theta}(R, t)\, R\, dR\,. \tag{212}$$

I also introduce the magnetic flux in the cavity $\phi_{B,\,cav.} = \phi_B(t, 1, 10)$, in the external part of the disc $\phi_{B,\,ext} = \phi_B(t, 10, 150)$ and in the whole disc $\phi_{B,\,tot} = \phi_B(t, 1, 150)$. The corresponding profiles are given in fig. 89. Figure 89 shows that the total magnetic flux is roughly constant once the seed has reached its saturation value. The flux in the cavity then represents most of the total magnetic flux threading the disc during the whole simulation. The fact that the flux in the cavity decreases after $t \approx 200000$ orbits at R_{int} illustrates that the magnetic field in the cavity is diluted because I only compute ϕ_B until $R = 10$ AU which is not the cavity edge anymore (since the cavity expands).

LAST REGIME (3): After 150000 orbits at R_{int} (and up to the end of the simulation), the disc finally converges to a last regime. The disc ends up with a wide gap in its outer part (see fid. 85) which is slightly migrating inwards past 250000 orbits at R_{int}, towards the cavity edge location. The cavity has a sharp density contrast with the full disc

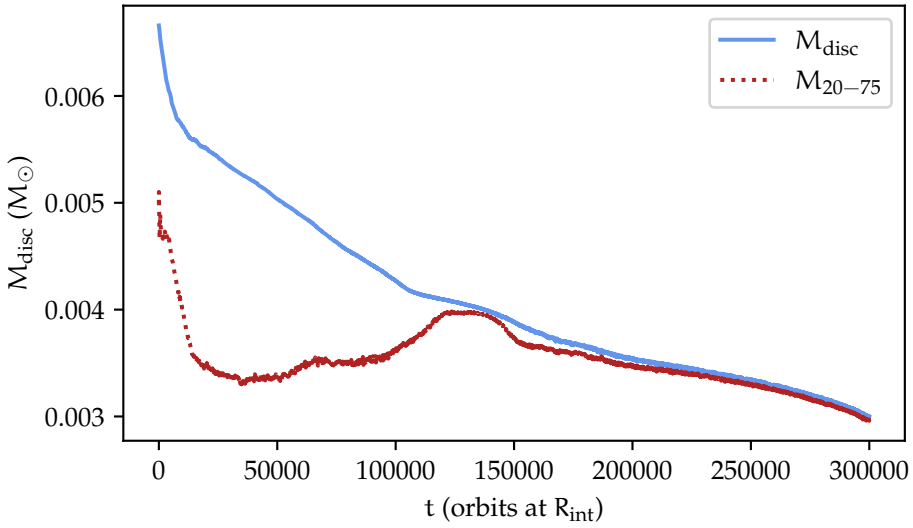

Figure 90: Total mass of the disc (M_{disc}, full blue line) and mass of the disc between $R = 20$ and 75 AU (M_{20-75}, dotted red line).

and is once again characterised by temporal stripes. These stripes are however not of the same nature as the previous ones and will be described in sec. 5.2.3.
The cavity is still widening and the outer truncation is shrinking. After a few hundreds of thousands orbits at R_{int}, the disc size is divided by a factor ~ 2. I define the disc total mass by

$$M_{disc}(t) \equiv \int_{R=R_{int}}^{R=R_{out}} \Sigma(R,t)\, R\, dR\,, \tag{213}$$

and the mass of the disc calculated between $R = 20$ and 75 AU by

$$M_{20-75}(t) \equiv \int_{R=20\,R_{int}}^{R=75\,R_{int}} \Sigma(R,t)\, R\, dR\,. \tag{214}$$

I show the corresponding evolution of M_{disc} and M_{20-75} in fig. 90. After 150000 orbits at R_{int} (which marks the beginning of the third regime), M_{20-75} represents 95 % of the disc total mass. 98.1% of the disc total mass at $t = 200000$ orbits at R_{int} concentrates between $R = 20$ AU and $R = 75$ AU. In the end, half of the initial mass is lost (mostly due to the accretion on the central star).
As a conclusion, the magnetic wind enables a fast evolution of the disc size together with a strong accretion.

The outer truncation is characterised by a temporal evolution which once again looks like temporal stripes. This evolution is also seen in the profile of $\overline{\beta}$ (fig. 86) and corresponds to the advection of magnetic flux from the outermost part of the disc (see fig. 87). To understand this temporal evolution, I show the global structure of the disc

in fig. 91. A first observation is the huge clockwise loop seen with the time-averaged poloidal field lines. This result echoes a conclusion of Yang and Bai (2021) and is now demonstrated to be a long-lived structure. This loop comes together with a peculiar flow structure. Between the surfaces defined by $\varepsilon_{\rm int} = \pm 0.6$, the matter that leaves the disc surface falls back on the disc. This is seen with a symmetric loop in the stream-lines profile (left panel of fig. 91). Once this falling matter has reached the midplane, it is transported inwards and fuels the wind and the accretion in the inner part of the disc.

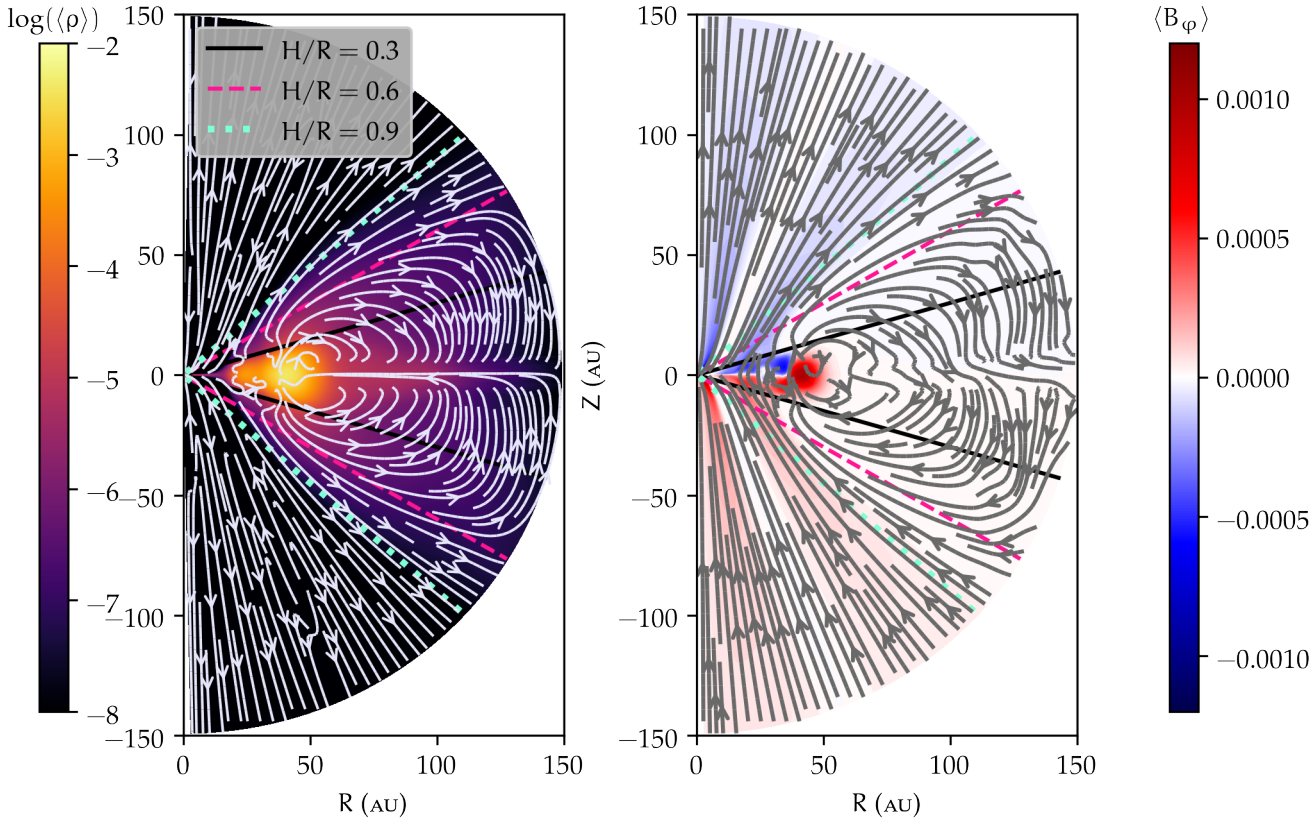

Figure 91: Density (left panel) and toroidal magnetic field (right panel) for the simulation S2Dext. The quantities are averaged on 10006 orbits at $R_{\rm int}$ between 290001 and 300006 orbits at $R_{\rm int}$. I plot the stream lines in the right panel and the poloidal magnetic field lines on the left one. This figure shows the whole disc, from $R = 1$ to 150 AU.

However, the figure 91 is time-averaged so that the temporal variability inherent to the outer stripes is not caught. To explain the stripes, I show a snapshot of the S2Dext at $t = 199600$ orbits at $R_{\rm int}$ in fig. 92 showing the density profile in the whole disc. Focusing on the outermost part of the disc, one can see volutes of gas falling from above and below the disc midplane. When the 2 volutes collide, they form a stream of matter whose location oscillates with time since the volutes are not perfectly symmetric with respect to the disc midplane.

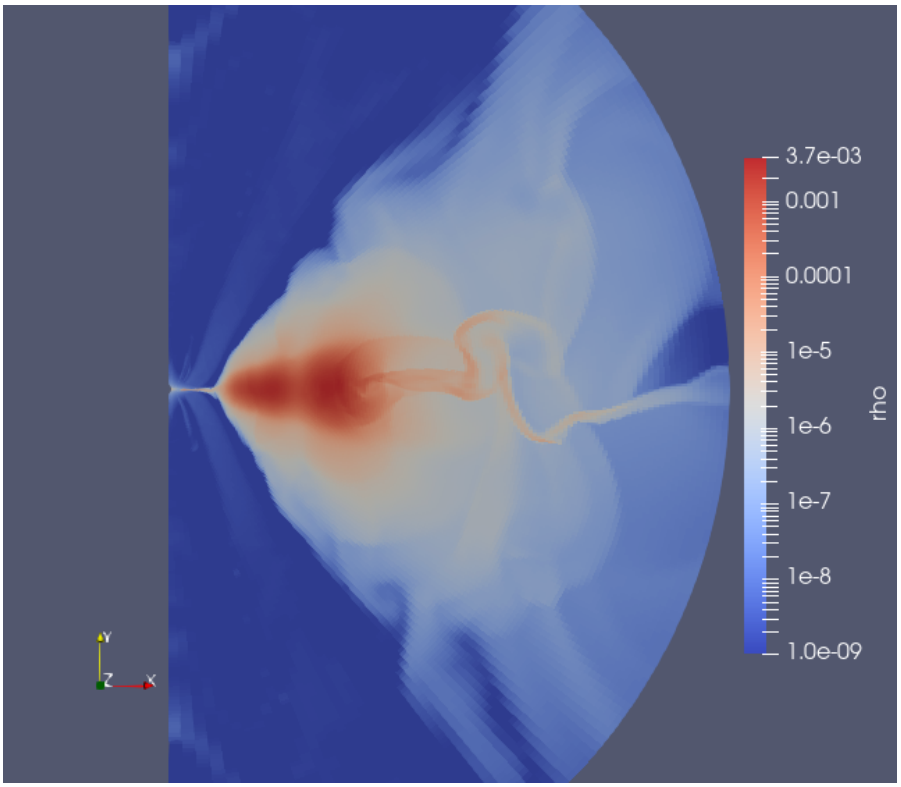

Figure 92: Snapshot of the simulation S2Dext at t = 199600 orbits at R_{int}. The background field is the density.

The temporal variation of the disc outer truncation (the temporal stripes) are explained by these volutes. Interestingly, this configuration implies that angular momentum is transported inwards from the outermost part of the disc (R = 150 AU) down to R ~ 130 AU. I show the structure of the angular momentum flux stream lines in fig. 93. The convergence point of the angular moment flux at R ≈ 130 AU suggests that these volutes are characterised by decretion flows.

5.2.3 *Cavity-hosting discs as transition discs: secular evolution*

Now that I have described the three regimes occurring throughout the evolution of the disc, I want to describe a few additional results regarding the second regime.
In particular, I want to start with the temporal stripes that can be seen inside the cavity in the left panel of fig. 87 for example. If one looks cautiously around t ~ 75000 orbits at R_{int}, one can see some of these stripes (indicated by a black arrow). Looking at the right panel of the figure, the stripes appear right after a rapid advection of magnetic flux and a locally fast expansion of the cavity (with a chunk of disc being accreted). Once the third regime is established, these stripes are continuously occurring in the cavity, whereas they are only detected

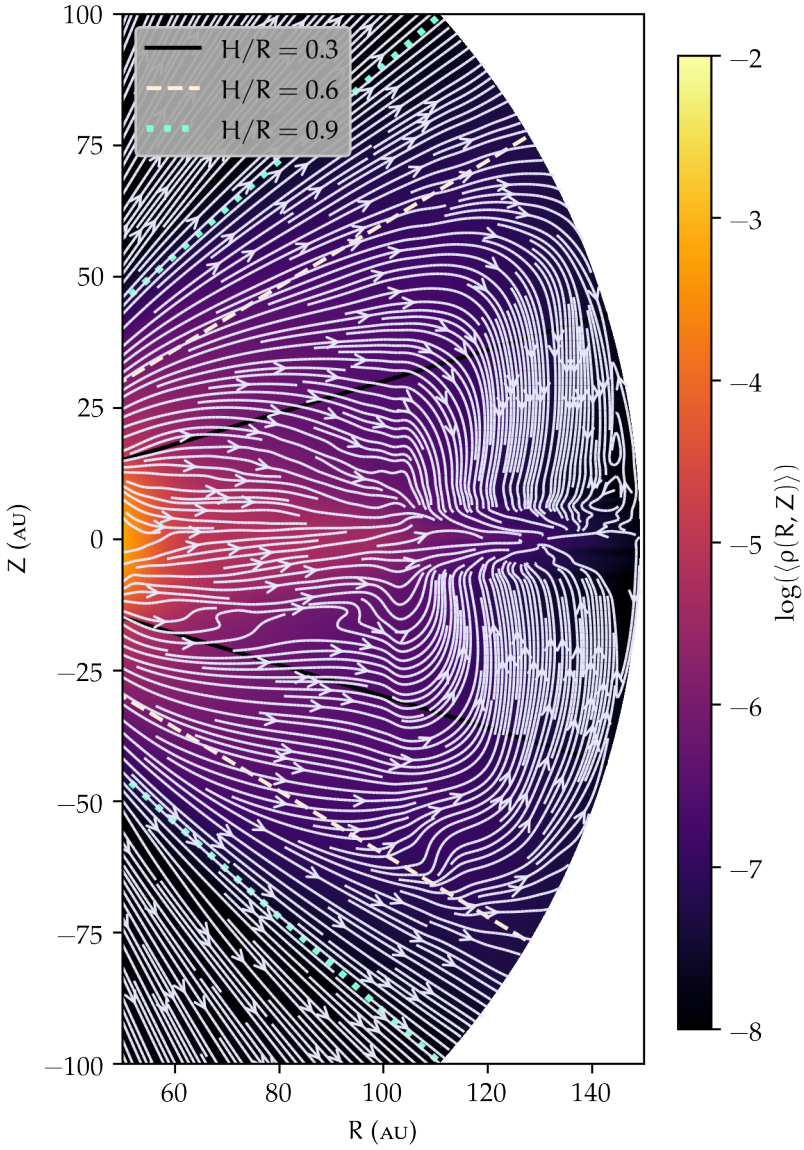

Figure 93: Time-averaged density over which the momentum flux stream lines are plotted for S2Dext, between 290001 and 300006 orbits at R_{int}. This image focuses on the outermost part of the disc.

from time to time during the second regime. Therefore, the second regime can be understood as a transitory configuration regarding the secular evolution of the disc.

During the second regime, the cavity is characterised by 2 states. The first one is the steady and thin accretion flow located at the mid-plane that I already described. The second one is characterised by the stripes. The corresponding flow of accretion is torn around the mid-plane, thinner (the flow is sometimes 1 cell thick) and even arrested from time to time. Moreover, the associated wind escaping the cavity becomes highly turbulent once the stripes has appeared. As an illustration of this statement, I give two snapshots of the density in figs. 94 and 95 around the appearance of the stripes. The stability of magnetic winds was discussed by Lubow et al. (1994), Königl and Wardle (1996), Cao and Spruit (2002), Königl (2004), and Lesur et al. (2013). In particular, Moll (2012) performed 2D shearing box simulations with high magnetisations (to suppress the MRI) that exhibit unstable outflows. It is then likely that the magnetic wind launched from the cavity is subject to an instability.

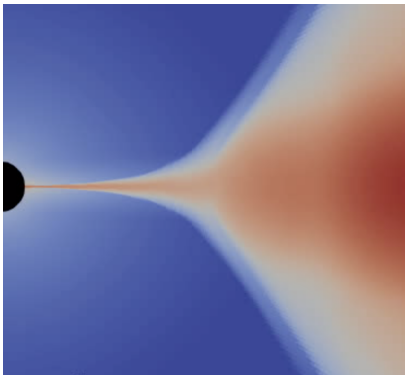

Figure 94: Snapshot of the density right before the appearance of stripes, focusing on the cavity.

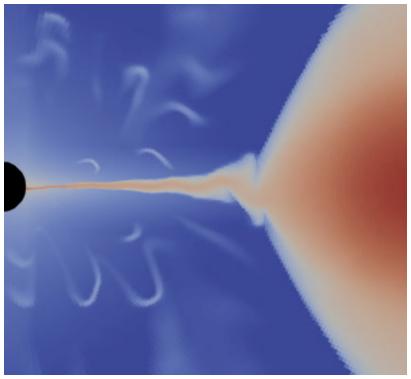

Figure 95: Same profile but after the stripes have appeared.

In the end, the cavity converges toward a configuration where it has accumulated most of the magnetic flux of the total disc. Its accretion gets more and more regularly arrested while the cavity grows with time due to the accumulation of magnetic field at the cavity edge location.
With the MAD picture in mind (discussed in the previous chapters), it seems that this model is a relevant analogy to address the physics of cavity.

CONCLUSION

I started this chapter by gathering a few observational predictions. In particular, the kinematics prediction in the cavity are the most promising ones. Together with the observations of specific substructures, the study of the accretion and rotation speeds in the cavity are encouraging and based on specific predictions.
These predictions could prove being compelling and call for a deeper work on synthetic observations that will be done with my 3D simulations in a near future.

My work devoted to the outer truncation of TDs appears to be fruitful. The results are different from the viscous framework as no viscous spreading is detected but rather a shrinking truncation.
Regarding the secular evolution of the discs, I isolated three dynamical regimes. The magnetic field transport also behaves in a complex manner. In the end, TDs encounter various transitory states and structures and much will be learn by improving the model I used regarding the outer truncation of discs. Specifically, an exploration of the parameter space should be considered.

CONCLUSION

Ce chapitre s'ouvre avec une discussion concernant le lien entre mes simulations et de possibles observations. J'ai produit un panorama de quelques observations envisageables qui permettraient de favoriser ou au contraire écarter le modèle que j'ai utilisé. Les observations concernant la cinématique dans la cavité paraissent tout particulièrement pertinentes. Couplées à la détection de sous-structures spécifiques (sillons, spirales, anneau interne), de telles observations seront possiblement à même de renseigner sur la structure des disques de transition abritant des vents magnétiques.
Ces prédictions incitent à élargir leur usage à mes simulations 3 D, ce qui sera réalisé dans un futur proche.

En sus de la discussion sur le lien aux observations, j'ai présenté un travail supplémentaire focalisé sur l'étude de la troncation externe de disques de transition et permettant également de mettre à jour certains résultats concernant l'évolution séculaire du disque. Ce travail s'est avéré riche en enseignements en dévoilant une évolution séculaire complexe caractérisée par plusieurs régimes rencontrés par le disque. Je confirme des résultats déjà remarqués (comme l'absence d'étalement visqueux) que j'ai pu approfondir, notamment en ce qui concerne la structure du vent au niveau de la troncation externe.
En ce qui concerne le transport de champ magnétique, celui-ci est naturellement fortement couplé à l'évolution du disque (dynamique des sillons, déplacement de la frontière entre la cavité et le disque plein).

Les disques de transition soutenus par des vents magnétiques sont caractérisés par plusieurs structures et configurations transitoires et il ne fait nul doute qu'améliorer ce modèle de troncation externe pourra renseigner sur la dispersion des disques protoplanétaires. En particulier, explorer l'espace des paramètres est une étape à envisager avec ce modèle.

6

CONCLUSIONS AND PERSPECTIVES

"So that it seemed in the end as though all the sciences
I studied at the university existed only to prove and
make evident to me as I went more deeply into them that
I was ridiculous."

— Fedor Dostoïevsky, *The Dream of a Ridiculous Man* (1877)

INTRODUCTION

In the previous chapters, I have detailed the work I did during my thesis. I studied a model of TDs harbouring magnetic winds with 2.5 D and 3 D numerical simulations. In this last short chapter, I want to discuss some aspects of this work, give perspectives and share some thoughts about it. Eventually, I will draw a conclusion.

INTRODUCTION

Dans les chapitres précédents, j'ai détaillé le travail que j'ai effectué pendant ma thèse. J'ai mis au point un modèle numérique de disques de transition munis de vents magnétiques, en travaillant avec des simulations 2,5 D et 3 D. Ce dernier chapitre me permet de conclure et de développer quelques limites de ce travail.

6.1 DISCUSSION ON THE RESULTS OF MY SIMULATIONS

6.1.1 2.5 D *simulations*

I modelled transition discs sustained by MHD winds by performing a first set of 2.5 D global simulations. This model acts as a proof of concept, showing that steady-state discs with both a cavity and a magnetic wind can be obtained. The resulting simulated discs are characterised by two different zones with contrasted dynamics.

Firstly, the outer disc behaves like standard simulations of weakly-magnetised and ambipolar-dominated PPDs (Lesur, 2021b; Cui and Bai, 2021). In particular I find mass and angular momentum transport coefficients, wind properties and accretion rates comparable to those found in the literature for 'full' discs. I also find weak gaps which are characteristic of non-ideal MHD discs (Riols and Lesur, 2019; Riols et al., 2020). However, the magnetic field transport in the outer disc differs from previous studies: I find that the magnetic field lines are advected inwards in the outer disc, in contrast to measurements in full discs which always show opposite transport (Bai and Stone, 2017; Gressel et al., 2020; Lesur, 2021b). This discrepancy is likely due to the fact that the field lines in the cavity are more collimated (i. e. less opened), which results in a lower pressure on the magnetic surfaces in the outer disc, but possibly also connected to the peculiar elbow shaped magnetic surfaces at the transition radius. In any case, it points to the fact that magnetic field transport is a non-local phenomenon: it depends on the global disc structure. The model of TDs with an outer truncation (which is integrated on a much longer time scale) tends to confirm this hypothesis. The magnetic loop disappears at some point which directly affects the magnetic field transport. However, additional simulations are required to reach a definitive conclusion on this topic.

In contrast to the outer disc, the cavity (or inner disc) is strongly magnetised ($\beta \approx 1$) because of its low surface density. I emphasise here that the absolute magnetic field strength in the cavity is not stronger than standard protoplanetary disc models. In practice, and given my set of units, I have $B_0 \approx 0.13$ G (with $\beta_{\rm out} = 10^4$) so that initially, $B_z \approx 1.25$ mG at $R = 42$ AU in my simulations, which is of the same order of magnitude as the upper limit of $B_z(R = 42\ \text{AU}) = 0.8$ mG found in Vlemmings et al. (2019) for example. Hence, while the cavity is strongly magnetised, its field strength is compatible with observational constraints.

Compared to the outer disc, the mass and angular momentum transport coefficients in the cavity are all of the order of unity, resulting in

transsonic accretion velocities and faster wind with large lever arms ($\lambda \gtrsim 10$). Overall, this picture matches quantitatively the inner jet emitting disc proposed by Combet and Ferreira, 2008. Interestingly, in all of my models, the cavity manages to reach an accretion rate close to the outer disc one by self-regulating the magnetic stresses. I find that most of the angular momentum transport is due to the laminar stress indicating that turbulent transport (possibly MRI-driven) is unimportant in the cavity. This is not surprising since my discs are dominated by ambipolar diffusion which mostly suppresses MRI turbulence (Bai and Stone, 2011).

I get a significant deviation of the rotation profile in the cavity as a result of the strong magnetic stress due to the wind and typical rotation velocities of the order of $70-80\%$ of the Keplerian velocity. This fact, combined with the transsonic accretion, implies that the kinematics of these cavities have singular observational signatures. Fast accretion kinematics have been observed in some transition discs (Rosenfeld et al., 2014) though I am aware that these signatures might also be due to a warped circumbinary disc as reported by Casassus et al. (2015).

As a result of the stress balance mentioned above, I obtain accreting cavities that survive thousands of orbits and which are slowly expanding or contracting, depending on the outer disc magnetisation. This result suggests that a cavity could be carved spontaneously if the magnetisation of the outer disc is high enough. There are already hints of such a process in global simulations: for instance Cui and Bai (2021) show a gas-depleted cavity forming in the inner profile of Σ (see their figure 5, first row and first column panel). While this is by no mean a proof since the boundary conditions are probably unrealistic, it shows that the secular evolution of wind-driven discs should be investigated systematically to check whether or not cavities could spontaneously form in these models.

The temporal analysis of the disc reveals the appearance of dynamical structures. In particular, I highlight the formation of gas filaments above the disc surface that end up forming 2 bubbles of gas each, one being ejected while the other one falls down onto the cavity before crossing it. At some point, the falling matter has to cross the poloidal magnetic field lines at the magnetic field loop location, recalling to some extent the magnetospheric accretion observed in young stars (Bouvier et al., 2006; Pouilly et al., 2020; Bouvier et al., 2020a; Bouvier et al., 2020b) and magnetospheric ejection events (Zanni and Ferreira, 2013; Čemeljić et al., 2013). However, there is no magnetosphere in my simulations so the magnetic topology is different from that of magnetospheric interaction.

By analogy with magnetospheric accretion, I have checked whether the time variability seen in our simulations could be due to a magnetic RTI. I have studied a criterion for the RTI, in the form of a radial interchange of poloidal field lines. I found however that the RTI requires magnetisations stronger than the ones found in my simulations, ruling out the RTI in the form I have assumed. It is however still possible that another branch of this instability is present.

On longer time scales, averaging out the fast variability, the magnetic field strength appears to be self-regulated with $0.1 \lesssim \beta \lesssim 1$ in the cavity, independently on the initial field strength. As a result, the cavity is strongly magnetised and rotates at sub-Keplerian velocities, indicating a substantial magnetic support against gravity in this region. In essence, the regime of my cavity is similar to the magnetically arrested disc (MAD) proposed by Narayan et al. (2003) in the context of black hole accretion discs. McKinney et al. (2012) shown that MADs could be regulated by magnetic RTI leading to magnetically chocked accretion flows (MCAF). The MAD model is also associated to the formation of plasmoids by reconnection events (Ripperda et al., 2022). These features are recovered in my models of transition discs, despite the fact that I have used Newtonian dynamics (MADs being usually found in GRMHD simulations) and the presence of a strong ambipolar diffusivity in my models. Hence, my models could be interpreted as non-ideal non-relativistic models of MADs.

The time variability of the cavity is likely to be related to the axisymmetric approximation used in my work since it suppresses non-axisymmetric instabilities which seem to play a key role in MADs simulations (e. g. McKinney et al., 2012; Liska et al., 2022). Additionally, I note that the question of non-axisymmetric hydrodynamical instabilities such as the RWI (Lovelace et al., 1999; Li et al., 2000) at the cavity edge is still open to debate in a magnetised environment (Bajer and Mizerski, 2013). I addressed these points using full 3 D simulations.

6.1.2 3 D *simulations*

My 3 D simulations recovered most of the results of the 2.5 D ones. In particular, the simulated TD remains stable. Nevertheless, a reorganisation of the disc occurs when a 2.5 D is restarted in 3 D. As a matter of fact, the magnetic stress is lowered inside the cavity in the 3 D simulations. Consequently, the transport coefficient that accounts for the wind efficiency is also reduced and so is the inner magnetisation. However, the accretion rate remains of the same order of magnitude (it is a bit lowered) and the cavity still rotates at a sub-Keplerian speed (80 to 90 % of the Keplerian speed). Indeed, the structure of the innermost part of the cavity is once again similar to the MAD picture.

The most striking observation in my 3D simulations is the development of spirals inside the cavity. Though I was unable to conclude on the instability at play (the RWI seems discarded and so does the magnetic RTI), I could describe their structure. I detected 2 sets of spirals, each characterised by rotation speeds that are constant with respect to the radius.

These spirals appear together with an inner ring whose origin remains unclear in some (but not all) of my 3D simulations. Inner rings are observed in TDs (Pinilla et al., 2021), so that studying the inner ring itself is still interesting. It is likely that this inner ring would disappear if the simulation lasted long enough. Moreover, the restart procedure may play a significant role on the appearance of the ring. Therefore, just like for the 2.5D simulations, a work on the implementation of a realistic inner boundary condition is necessary.

6.2 CAVEATS AND PERSPECTIVES

Regarding the caveats of my simulations, I remark that the inner radial boundary is probably the most stringent caveat of my numerical model. In particular, I found that this inner boundary condition is sometime expelling some poloidal magnetic flux. However, the weakly magnetised simulations are the only ones exhibiting these events, and once the transient state is over, all the simulations reach comparable steady states. So the inner boundary condition is likely not affecting the long term evolution of my models. Future models should nevertheless try to either include an inner turbulent disc, or possibly the magnetospheric interaction with the central star. Connecting a cavity of TD sustained by magnetic winds to a magnetosphere would enable to describe the accretion process with greater accuracy.

Another possible limitation of my model one could raise concerns the role of the MRI. My simulated discs are dominated by ambipolar diffusion, and as such, subject to MRI quenching by the non-linearity embedded in the ambipolar diffusivity ($\eta \propto B^2$). This saturation is different from the saturation by 3D turbulence observed in the ideal MHD regime. It is suggested that the MRI saturates in very similar ways in 2D and 3D under strong ambipolar diffusion (see e. g. Béthune et al., 2017; Cui and Bai, 2021). This is also confirmed by my own 3D simulations. Hence, the fact that my first set of simulations is 2.5D has a very limited impact on the turbulent transport one may observe.

Note that my simulations used a simplified treatment of thermody-

namics and ionisation chemistry. More numerically involved models, such as Wang and Goodman (2017), use a refined computation of the ionisation fraction and Λ_A inside the cavity of a TD, including several chemical species. This work highlights in particular the influence of the x-ray luminosity of the star L_X (see their fig. 2, panels 2 and 3) as well as the role of the temperature T_0 at 16 AU (fig. 2, panels 6 and 7). Regarding my profile of $\Lambda_A \approx 1-10$, my work is similar to their models 2 (with $L_X = 10^{29}$ erg s^{-1}) and 6 (where $T_0 = 30$ K). Therefore, I anticipate that an increase of 2 orders of magnitude for L_X would lead to $\Lambda_A > 10^2$ in most of the cavity. Such a change would greatly alter the dynamical regime of the cavity since MRI would then play a significant role (Blaes and Balbus, 1994; Bai and Stone, 2011). However, the role of the temperature is less straightforward and seems to have a little impact on Λ_A.

Additionally, dust plays a significant role in Wang and Goodman (2017) regarding the ionisation of the disc. As a matter of fact, only their models with dust reach low values of Λ_A. The effect of dust in transition discs is a major subject that is not addressed in my work. Dust can modify the ionisation fraction but also create peculiar structures at the interface between the disc and cavity. In particular, I mention the interplay between dust and the radiation pressure, that is known to create non-axisymmetric structures at the cavity edge (Bi and Fung, 2022) or an inner rim with an accumulation of matter due to photophoresis (Cuello et al., 2016).

In the end, studying TDs as well as PPDs in general serves the greater goal of understanding how planets formation works. The interplay between cavities and planets is investigated (Rometsch et al., 2020; Baruteau et al., 2021). It would then be of prime interest to check the influence of my solutions of cavities with magnetic winds on planetary migration.

6.3 FINAL REMARKS AND CONCLUSION

I performed 2.5 D and 3 D global numerical simulations of transition discs in the context of non-ideal MHD with magnetic wind launching. My simulation design is initialised with a cavity in the gas surface density profile, and a power law distribution for the vertical magnetic field strength, resulting in a strongly magnetised cavity surrounded by a standard weakly magnetised disc. The main results are summarised in the following points.

1. I have modelled strongly accreting transition discs that reach a quasi steady state that last for at least tens of kyrs. The accretion rate inside the cavity connects smoothly to the accretion rate in the external part of the disc.

2. The cavity itself is characterised by a strong sub-Keplerian rotation and a transsonic accretion velocity. These kinematic signatures could potentially be verified observationally.

3. The magnetic field is advected inwards in the outer disc, in contrast to full disc simulations. This points to the possible non-locality of large-scale field transport.

4. A much longer simulation confirms the complex spatio-temporal organisation of the magnetic field transport. In particular, its global structure is closely linked to the local magnetic structure (the magnetic loop).

5. The cavity structure (density and field strength) is self-regulated and insensitive to a change in the initial internal magnetisation. Its characteristic internal magnetisation is $0.1 \lesssim \beta_{\rm int} \lesssim 1$.

6. The temporal analysis of the cavity dynamics highlights the formation and accretion of bubbles of gas (in 2.5 D above the disc which cross the cavity at sonic speeds. These structures are not seen in the 3 D simulations.

7. The 3 D simulations show the formation of spirals inside the cavity, with rotation speeds that are constant with respect to the radius.

8. The overall stability of the simulated discs is also ensured in 3 D simulations, despite an initial reorganisation of the disc.

9. The physics of the cavity (accretion speed, wind lever arm and mass loading) match previously published jet emitting disc solutions (Ferreira, 1997; Combet and Ferreira, 2008), both in the 2.5 D and 3 D simulations. The presence of a strong radial magnetic support is also reminiscent of MADs in black hole physics (Narayan et al., 2003; McKinney et al., 2012). These resemblances suggest that transition discs could be an instance of MADs applied to protoplanetary discs.

In the end, my work prove that numerical simulations of TDs with magnetic winds are physically meaningful and provide a new model. These solutions are a new tool that can possibly help to interpret the observations of strongly-accreting TDs.

Part IV

APPENDIX

This supplementary part has 3 chapters. The first one is about some theoretical calculations needed to establish the criterion for the RTI. The other two chapters show some additional minor results regarding respectively the 2.5D and the 3D simulations.

"It is myself I have never met,
whose face is pasted on the underside of my mind."

— Sarah Kane, *4.48 Psychosis* (2000)

A

CRITERION FOR THE RTI

I express the instability criterion for the interchange instability (or RTI) calculated in Spruit et al., 1995 (equation 59) in terms of the plasma parameter. This criterion reads

$$g_m \, \partial_R \ln \frac{\Sigma}{B_z} > 2 \left(r \frac{d\Omega}{dr} \right)^2 \equiv 2 \, S^2 \, , \tag{215}$$

where S is the shear that I approximate with $S^2 = 9/4 \, \Omega^2$ and g_m is

$$g_m \equiv \frac{B_R^+ \, B_z}{2\pi \, \Sigma} \, . \tag{216}$$

B_R^+ is the radial component of the magnetic field at the disc surface. Let me rewrite the previous expression in terms of β, q (defined with $B_R^+ = q \, B_z$) and δ (defined as $\delta = -d \ln \Sigma / d \ln R$):

$$\frac{B_R^+ \, B_z}{2\pi \, \Sigma} \partial_R \ln \frac{\Sigma}{B_z} = \frac{B_R^+ \, B_z}{2\pi \, \Sigma} \frac{\Sigma'}{\Sigma} - \frac{B_R^+ \, B_z}{2\pi \, \Sigma} \frac{B_z'}{B_z} \, , \tag{217}$$

$$= \frac{q \, B_z^2}{2\pi \, \Sigma} \frac{-\delta}{R} - \frac{q}{4\pi \, \Sigma} \left(B_z^2 \right)' \, , \tag{218}$$

where X' denotes the derivative of X with respect to R. With $P = c_s^2 \, \rho = (h \, \Omega_K)^2 \, \Sigma / (\sqrt{2\pi} \, h)$, I get

$$\beta = \frac{4\sqrt{2\pi} \, R \, \varepsilon \, {\Omega_K}^2 \, \Sigma}{{B_z}^2} \, . \tag{219}$$

Therefore, the instability criterion becomes

$$S^2 < -\frac{4 \, \varepsilon \, {\Omega_K}^2 \, q \, \delta}{\sqrt{2\pi} \, \beta} - \frac{q}{4\pi \, \Sigma} \partial_R \left(\frac{4\sqrt{2\pi} \, R \, \varepsilon \, {\Omega_K}^2 \, \Sigma}{\beta} \right) \, , \tag{220}$$

ε being constant in the disc as well as β inside the cavity. Ω_K varies as $R^{-3/2}$ and Σ as $R^{-\delta}$ so that

$$S^2 < \frac{4 \, \varepsilon \, {\Omega_K}^2}{\sqrt{2\pi} \, \beta} \, q \, (-\delta + 1 + \delta/2) \, . \tag{221}$$

By taking $S^2 / \Omega_K^2 = 9/4$, the RTI can be triggered when

$$\beta < \frac{16 \, \varepsilon}{9\sqrt{2\pi}} \, q \, \left(1 - \frac{\delta}{2} \right) \, . \tag{222}$$

If I now assume that $\delta = q = 1$ for simplicity, I finally get

$$\beta < \frac{8 \, \varepsilon}{9\sqrt{2\pi}} \approx 0.355 \, \varepsilon = 0.0355 \equiv \beta_{\text{crit.}} \, , \tag{223}$$

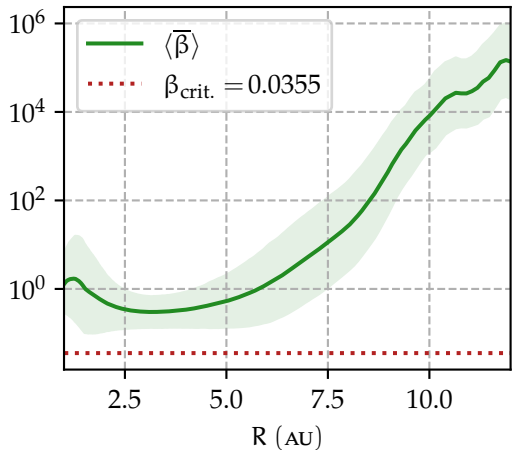

Figure 96: Interchange instability criteria for the fiducial 2.5 D simulation. In red dotted line is shown the critical value of $\beta_{\text{crit.}}$ while the solid green line is obtained with eq. 222.

where $\varepsilon = 0.1$.

Figure 96 compares the time-averaged values of $\overline{\beta}$ with the criterion given in eq. 223. The value of $\beta_{\text{crit.}}$ is anyhow below the time-averaged values of $\overline{\beta}$. Though this simple analysis makes it difficult to be definitive on this subject, it seems that the interchange instability is not triggered inside the cavity.

B

2.5 D ADDITIONAL SIMULATIONS

I ran a set of additional 2.5 D 'control' simulations to address a few interesting topic. One will find in the following order a discussion on numerical aspects of my work such as the impact of the resolution of the 2.5 D simulations and the role of the inner boundary condition.
This discussion is followed by numerical simulations devoted to physical specific points. I will describe a purely HD run, an MHD run with no cavity, check the influence of the initial size of the cavity and have a look at the impact of the thermodynamics (in the disc and in the corona).
Eventually, I will then discuss about some more physical aspects of my simulations with a short discussion on the role of the MRI.

B.1 NUMERICAL ASPECTS

B.1.1 *Spatial resolution*

I start by a short discussion on the impact of the spatial resolution of my 2.5 D simulations on my results. Figure 97 shows the surface density for 3 different resolutions. FID refers to the 2.5 D fiducial simulation, LOW to a 2.5 D simulation with a resolution divided by 2 in every directions (160×120), and HIGH to a 2.5 D simulation with a resolution multiplied by 2 in every direction (640×480).
The upper panel shows the mean value of Σ inside the cavity ($\Sigma_{\text{cav.}}$ is the surface density averaged between $R = 1$ and 10 AU). The bubbles of matter that cross the cavity proved to be chaotically distributed with time and their occurrence strongly vary from one resolution to another. Therefore, the occurrence of a bubble is somehow related to the numerical spatial resolution. This result may favour the magnetic reconnection to be the formation mechanism of these temporal structures, through the numerical resistivity (e. g.: Rembiasz et al., 2017).
The lower panel shows the surface density at $R = 25$ AU.

The first panel shows that the transient states are similar between the fiducial simulation and the one with a higher resolution. After 500 orbits at R_{int}, the 3 resolutions render similar values of Σ. However, the simulation with the lowest resolution encounters bursts of matter in the cavity.
Regarding the value of Σ at $R = 25$ AU, the fiducial simulation and the one with the highest spatial resolution are similar while the simulation with the lowest resolution diverges rapidly (with respect to the

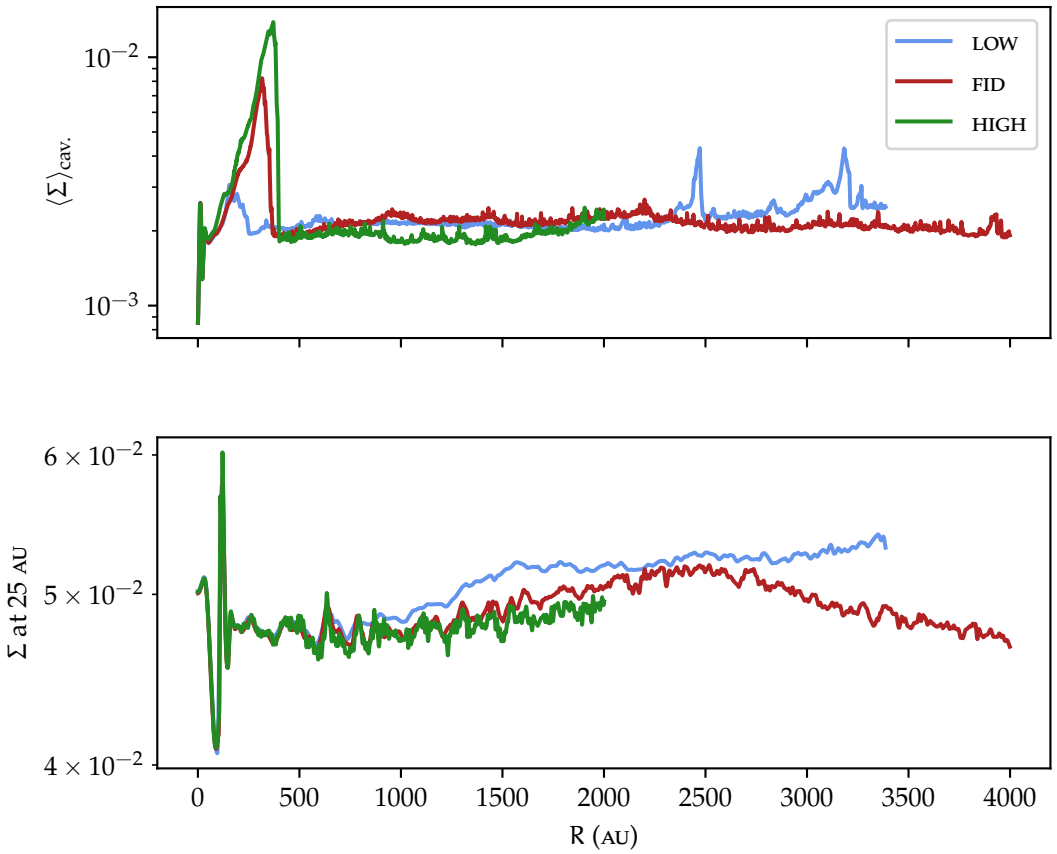

Figure 97: Influence of the spatial resolution on the 2.5 D simulations. The upper panel is the average value of the surface density (between $R = 1$ and 10 AU) and the lower panel is the surface density at $R = 25$ AU. The blue line is the simulation with the poorest spatial resolution, the green line is the one with the highest, and the red line is the fiducial run.

simulation with the highest spatial resolution).

Conclusively, the spatial resolution of the fiducial simulation is well chosen, as the external structure of the disc is properly recovered while the cavity does not experience bursts of matter. Eventually, I add that the surface density differs by less than 8 % in the cavity and by less than 1 % when considering the entire domain, between the fiducial run and the high resolution one.

B.2 POLOIDAL VELOCITY RELAXATION AND INNER BOUNDARY CONDITION

B.2.1 *Poloidal velocity relaxation*

I want to address the influence of the poloidal velocity relaxation on my results to test my control on the inner boundary condition. Two additional simulations were conducted respectively with the same setup as S2DB4BinoAmo (fiducial run) and S2DB5BinoAmo (weakly magnetised run), but without the relaxation procedure. The results are given in fig. 98, where I show the surface density $\langle\Sigma\rangle_{4000}$ time-averaged on the first 4000 orbits at the internal radius (when the differences are enhanced), with a focus on the innermost radii. I highlight that these differences do not rise up for $t > 4000$ orbits at R_{int}. For S2DB5BinoAmo, the right panel of fig. 98 suggests that the relaxation procedure influences how the initial burst is evacuated since we detect differences between the surface density profiles at $R > 1.5$. However, releasing this inner constrain reduces the inner peak of the profile of Σ, but does not prevent the initial accumulation of matter from appearing. In particular, the bursts of matter seen with the less magnetised simulation are not due to this condition. For the fiducial simulation, I estimate differences of 15% until $R = 2$, 7% until $R = 10$ and less than 2% until $R = 50$. I conclude that the slight accumulation of matter inside the cavity is due to this procedure contrary to the occurrence of bursts in the simulation with a weakly magnetisation.

B.2.2 *Inner boundary condition*

I implemented several inner radial boundary conditions, trying to check its influence on the magnetic field transport at R_{int}. I compare the spatio-temporal profiles of ψ on the first 700 orbits at R_{int} on fig. 99.
The first panel labelled by 'fid' is the 2.5 D fiducial simulations, shown for comparison. The second panel, 'old fid', refers to a first set of simulations in which the magnetic field was prevented from crossing the inner radial boundary condition. The third one is the same simulation as the fiducial one, to which I added an initial supplementary vertical magnetic field in the inner region $R \leqslant 1.5$ AU. The idea was to check if it was possible to lower the effects of the initial transient state by imposing a higher magnetisation around the seed. The last panel, is the same simulation as the one in the third panel, but the added magnetic field is more intense and I used a vertical exponential cutoff to generate a magnetic poloidal loop (anti clockwise, like the magnetic poloidal field, which is why negative values are detected at the beginning of the simulation).

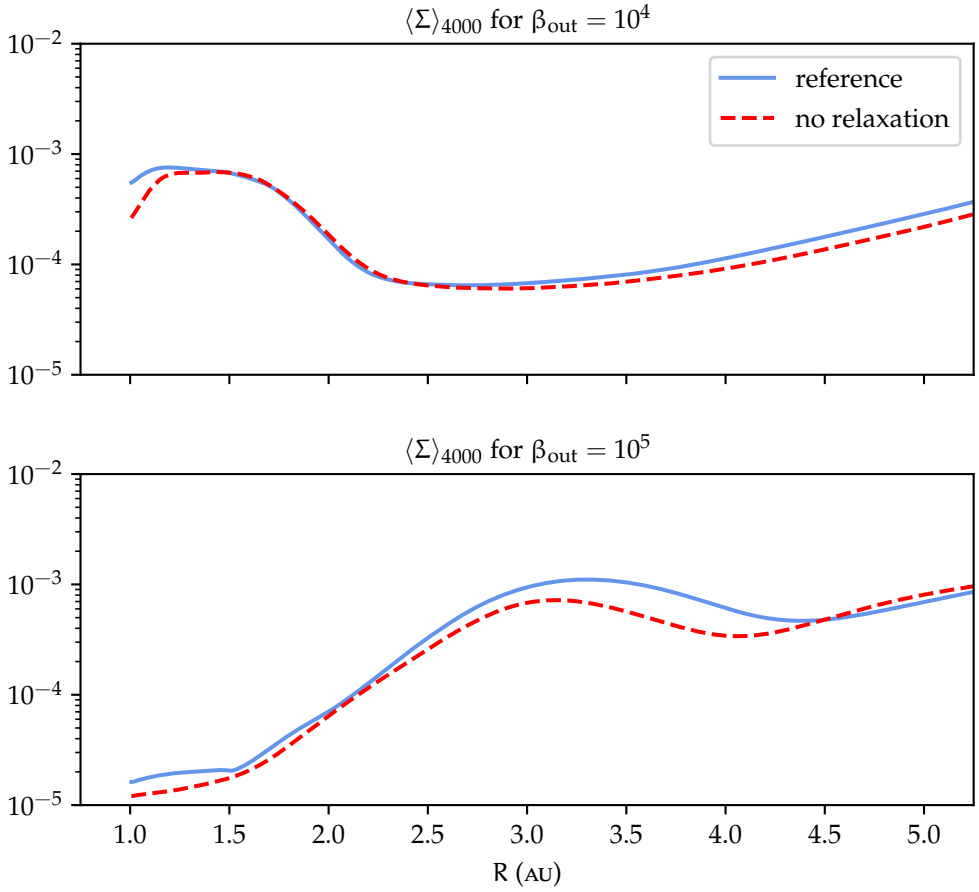

Figure 98: Surface density time-averaged on the first 4000 orbits at R_{int}. The blue lines are the reference runs (left panel: fiducial run, right panel: S2DB5BinoAm0) and the red-dashed mines are the corresponding runs without the relaxation.

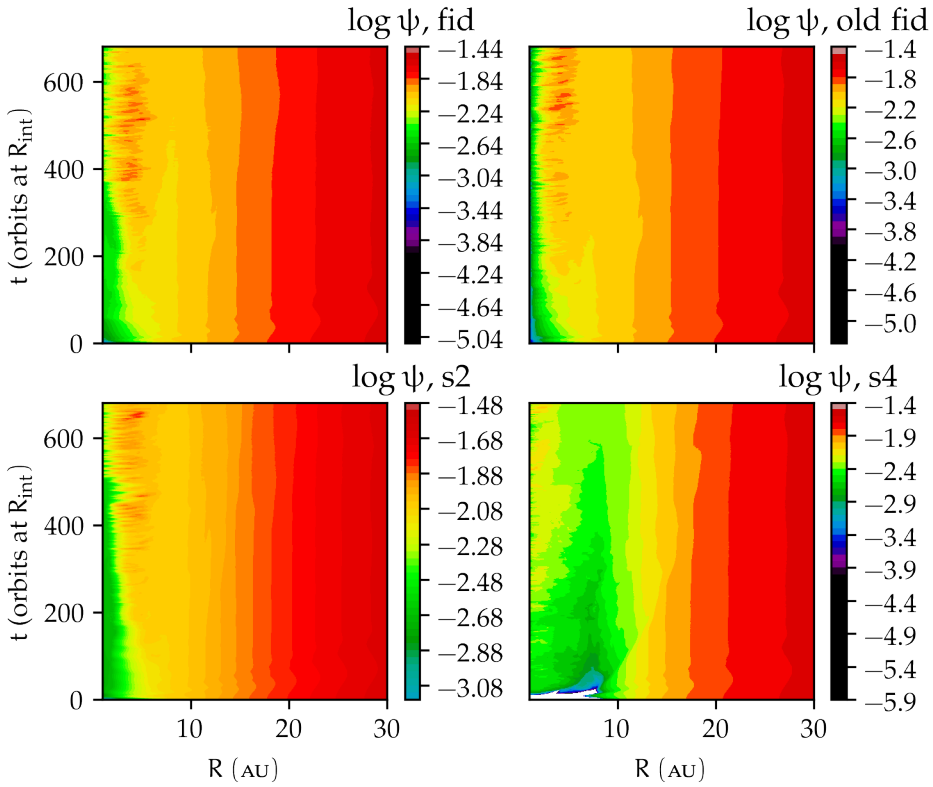

Figure 99: Spatio-temporal diagrams for ψ for 4 simulations.

Looking at fig. 99, I conclude that no change of boundary conditions ended up with a significant impact on the inner magnetisation or on the magnetic structure of the cavity. The only thing that changes is the duration of the initial transient state.
Therefore, I expect the inner magnetic structures of my cavities to be rather robust.

B.3 PHYSICAL ASPECTS

B.3.1 *Hydrodynamical simulation*

I ran one hydrodynamical simulation (without magnetic field) of a cavity-hosting disc. I show the corresponding spatio-temporal diagram of Σ in fig. 100 where the cavity is clearly visible. I detect no bubble of gas crossing the cavity. The elbow-shaped structure, the wind from the cavity and of course any magnetic structure are not seen in this simulation. The accretion rate in the cavity is $\sim 10^{-8}\ M_\odot\ yr^{-1}$ at the inner boundary condition and decreases with radius until 5 AU where it reaches zero and flips its sign.
As expected, the relevant physical processes in my 2.5D MHD sim-

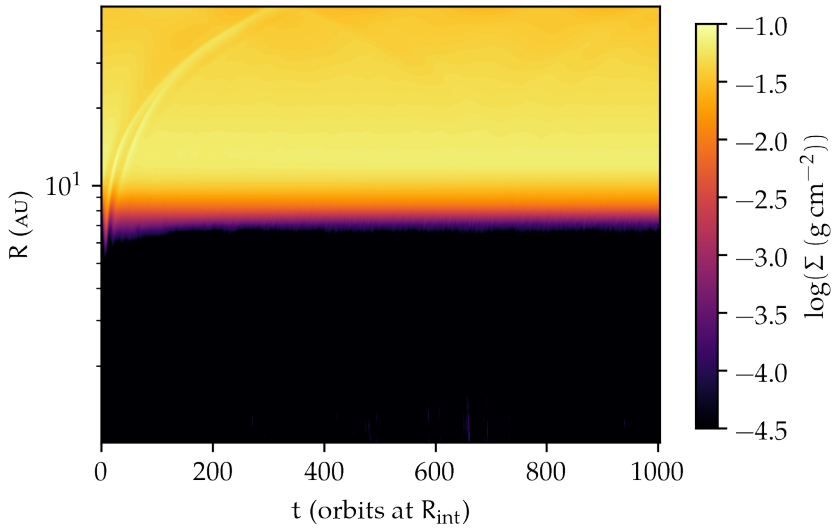

Figure 100: Spatio-temporal diagram of the surface density for the hydrodynamical 2.5 D simulation.

ulations are driven by the magnetic field. In particular, the strong accretion is due to the magnetic stresses.

B.3.2 *Run without a cavity*

For comparison, I performed a 2.5 D simulation with no initial cavity (the cavity function f is 1 everywhere). I show the associated spatio-temporal diagram of Σ in fig. 101. A major result is the spontaneous carving of a cavity. This result suggests that magnetic TDs may appear naturally with time. Another possibility is that my setup favours the appearance of cavities.

B.3.3 *Size of the cavity*

I performed a simulation with a double-sized cavity ($R_0 = 20$ AU) in order to check the impact of the cavity size. The simulation was integrated for 1000 orbits at $R = 10$ AU so that it reaches 355 orbits at $R = 20$ AU. The general observations are confirmed such as the elbow-shaped structure, the magnetic loop, the magnetic field advection in the outer disc as well as the conclusions regarding the accretion. While the cavity size is identical to S2DB3BinoAmo (the one with a higher magnetisation), the behaviour of the disc is exactly the same as the fiducial one (see fig. 102), indicating that β_{out} is the main parameter regulating the cavity expansion. This means that the global picture where two types of discs are connected is robust and

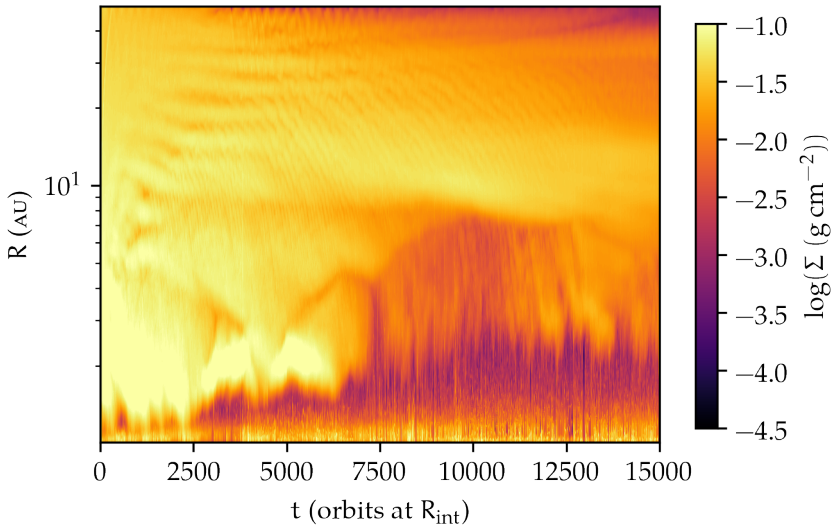

Figure 101: Spatio-temporal diagram of the surface density for the 2.5 D simulation without cavity.

not linked to limitations in the cavity size or artefacts due to the inner boundary condition.

B.3.4 *Thermodynamics*

B.3.4.1 *Disc*

I show the profile of the density time-averaged over the 8000 first orbits at R_{int} in fig. 104. The disc is twice thinner as expected. An interesting difference with the fiducial simulation is the size of cavity, which is twice smaller. This is likely due to the elbow-shaped structure that is smaller than in the fiducial simulation, so that it is easier for the matter to end up falling inside the cavity.

B.3.4.2 *Corona*

I ran a 2.5 D simulation with a twice hotter corona. The most relevant difference with the fiducial simulation is the fact that the elbow-shaped structure and the magnetic loop are significantly bigger (approximately twice higher). I show the density profile time-averaged over the 15000 first orbits at R_{int} in fig. 104.

B.4 LAMINAR TRANSPORT COEFFICIENTS

In order to discuss the role of the MRI,, I must highlight the impact of the laminar stress and its contribution to the transport coefficients. To compare the turbulent effects, I decompose the stresses with a tur-

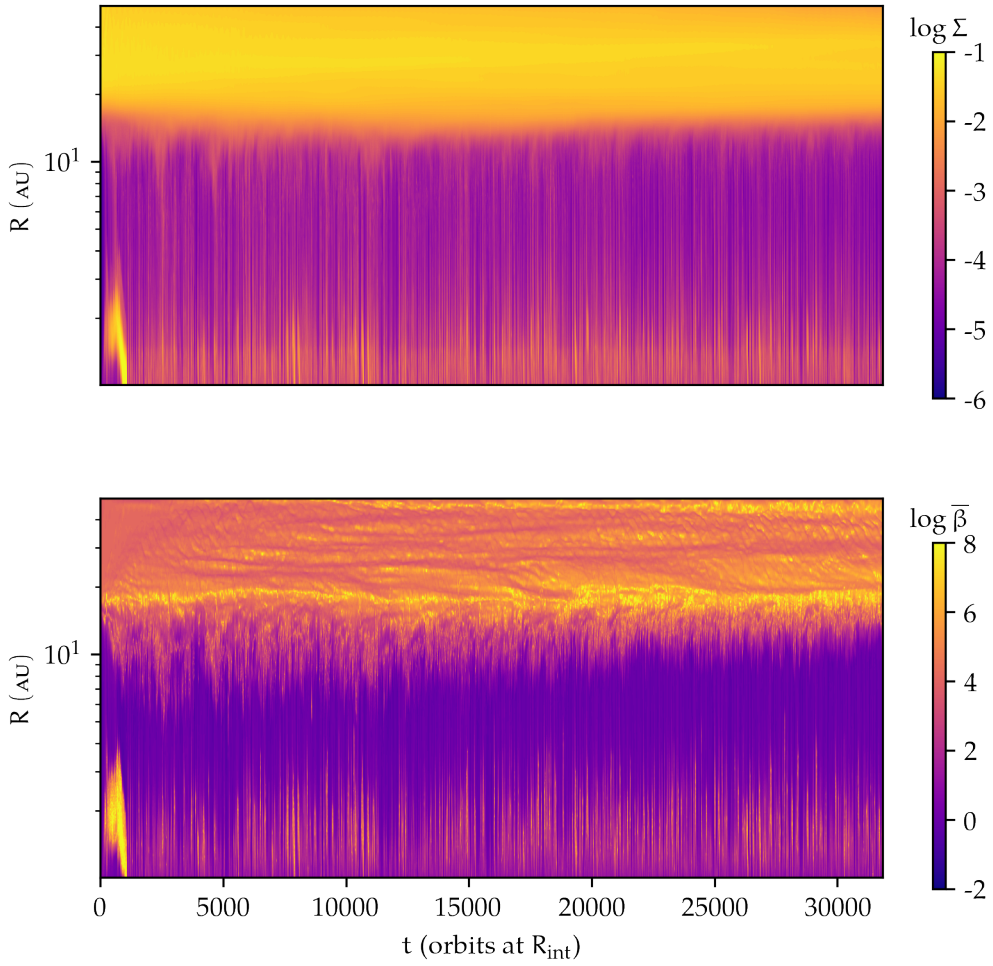

Figure 102: Spatio-temporal diagrams for $\langle\Sigma\rangle$ and $\langle\beta\rangle$ for the simulation with a twice larger cavity.

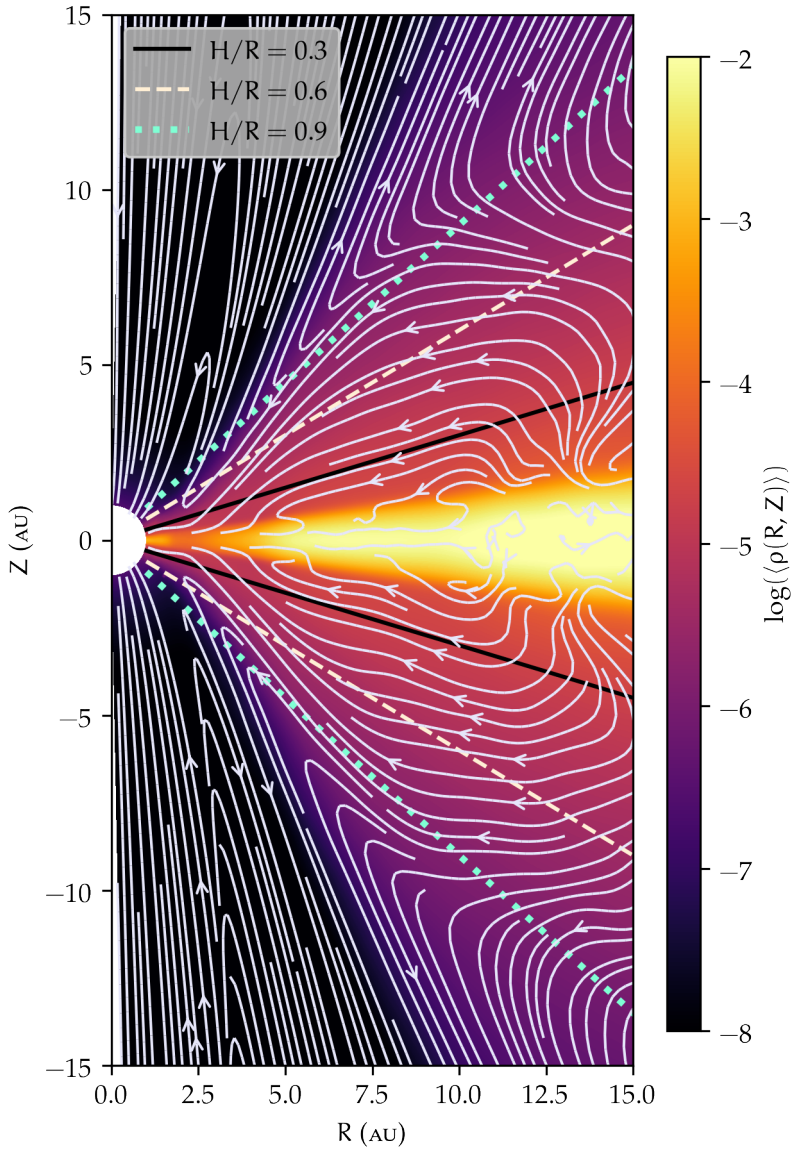

Figure 103: Time-averaged profile of the density over which are plotted the stream lines (for the simulation with a colder disc).

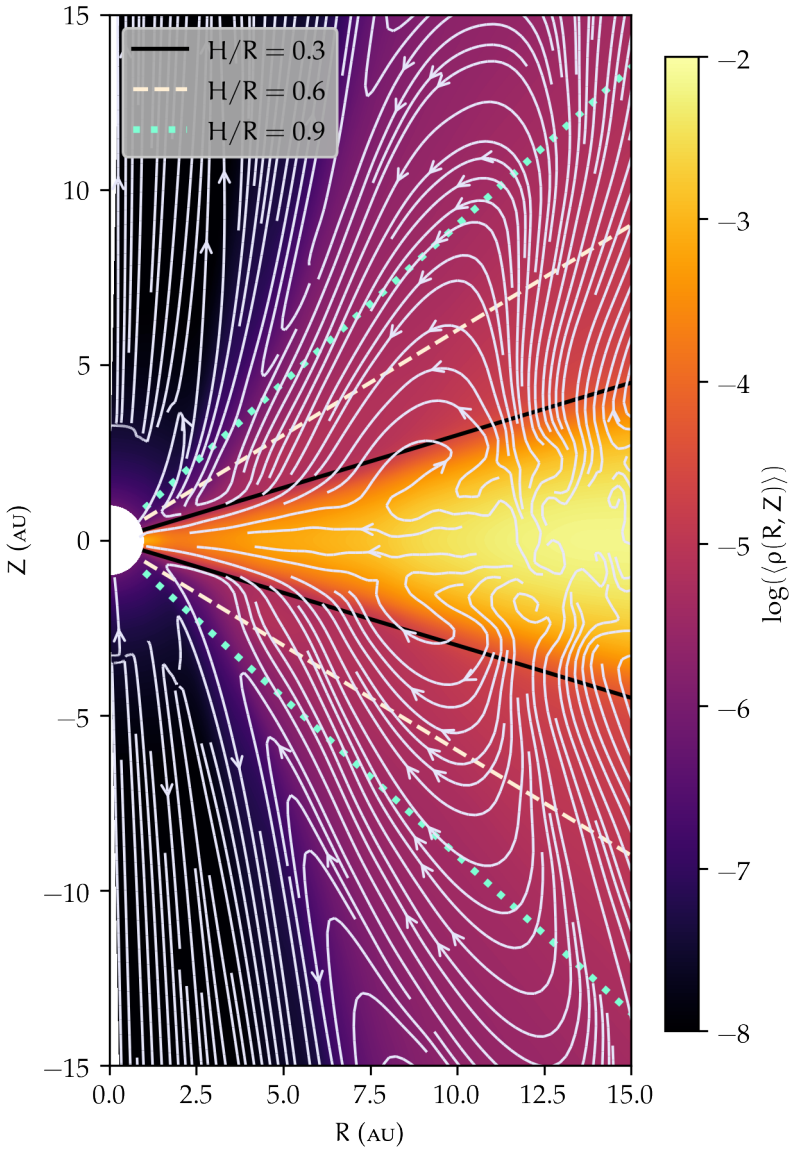

Figure 104: Time-averaged profile of the density over which are plotted the stream lines (for the simulation with a hotter corona).

bulent and a laminar part. In this prospect, I introduce the deviation to the temporal mean such that

$$\delta X \equiv X - \langle X \rangle \,. \tag{224}$$

Focusing on $W_{r\varphi}$, I expand the magnetic term as

$$\overline{\langle B_r \, B_\varphi \rangle} = \underbrace{\overline{\langle B_r \rangle \, \langle B_\varphi \rangle}}_{\text{laminar}} + \underbrace{\overline{\langle \delta B_r \, \delta B_\varphi \rangle}}_{\text{turbulent}} \,. \tag{225}$$

Concerning the turbulent stresses, I refer to Jacquemin-Ide et al. (2021) (see their appendix A) as I only compute the laminar ones and compare the laminar transport coefficients calculated in chap. 3. Therefore, I adopt the following definition for the laminar radial stress

$$\langle W_{r\varphi}^{\text{lam.}} \rangle \equiv -\frac{1}{4\pi} \overline{\sin\theta \, \langle B_r \rangle \, \langle B_\varphi \rangle} \,, \tag{226}$$

and for the laminar surface stress

$$\langle W_{\theta\varphi}^{\text{lam.}} \rangle \equiv -r \left[\sin^2\theta \, \frac{\langle B_\theta \rangle \, \langle B_\varphi \rangle}{4\pi} \right]_{\theta_+}^{\theta_-} \,. \tag{227}$$

These definitions are coherent with previous works (Béthune et al., 2017; Mishra et al., 2020; Jacquemin-Ide et al., 2021). Hence, the laminar transport coefficients are given by

$$\begin{cases} \langle \alpha^{\text{lam.}} \rangle \equiv \dfrac{\langle W_{r\varphi}^{\text{lam.}} \rangle}{\langle \overline{P} \rangle} \\ \langle \upsilon_w^{\text{lam.}} \rangle \equiv \dfrac{\langle W_{\theta\varphi}^{\text{lam.}} \rangle}{r \, \langle P_0 \rangle} \end{cases} , \tag{228}$$

while we define their turbulent counterparts as

$$\begin{cases} \langle \alpha^{\text{turb.}} \rangle \equiv \langle \alpha \rangle - \langle \alpha^{\text{lam.}} \rangle \\ \langle \upsilon_w^{\text{turb.}} \rangle \equiv \langle \upsilon_w \rangle - \langle \upsilon_w^{\text{lam.}} \rangle \end{cases} . \tag{229}$$

The results are shown in fig. 105. The laminar contribution is the major one for $\langle \upsilon_w \rangle$ in the whole disc so that I only show its laminar contribution with respect to the full coefficient, as they take essentially the same values. Nevertheless, despite the laminar term being high for $\langle \alpha \rangle$, a strong turbulent term is at play, especially in the external part of the disc where it is dominant. Inside the cavity, $\langle \alpha \rangle$ is fairly distributed between the laminar and turbulent contributions. However, I recall that the wind may act on the turbulent component of $\langle \alpha \rangle$ too since the magnetic field also appears in eq. 225.

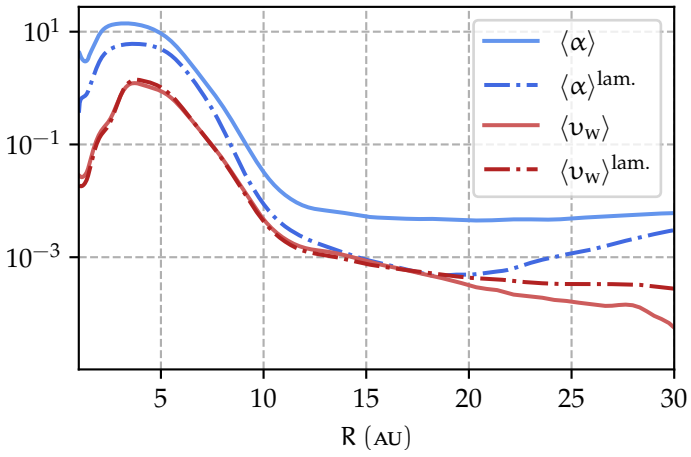

Figure 105: Time-averaged transport coefficients and their laminar and turbulent contributions. I give the laminar and turbulent contributions for $\langle\alpha\rangle$ and the total profile with its laminar contribution for $\langle v_W\rangle$.

C

3 D ADDITIONAL SIMULATIONS

Alike for my 2.5 D simulations, I ran some control simulations for my 3 D simulations. Of course and because of the computational time needed, I did not test as many parameters as with my 2.5 D simulations. I start by checking the impact of my restart procedure before showing some results for a cavity twice bigger.

C.1 NUMERICAL ASPECT: RESTART PROCEDURE

I start by checking the impact of my restart procedure. To do so, started a 3 D simulation restarted from the initial state of the fiducial 2.5 D one. I show an extract of the spatio-temporal diagram of Σ in fig. 106. The relevant observation is the appearance of a bead whose location is not the same as in the 3 D fiducial simulation. However, this inner ring corresponds the accumulation of matter that is observed in any of my 2.5 D simulation. This ring should disappear with time long enough, which is out of reach considering the fact that the magnetic torques are lower in 3 D.
It is difficult to conclude whether the inner ring observed in my 3 D fiducial simulation is due to the restart procedure or not. Still, it is a possibility that the appearance of such ring is due to the choice of a peculiar 2.5 D restart file.

C.2 PHYSICAL ASPECT: SIZE OF THE CAVITY

Lastly, I ran a 3 D simulation restarted from the 2.5 D simulation with a twice bigger cavity. I show the spatio-temporal diagrams of Σ and $\overline{\beta}$ in fig. 107. An inner ring also appears in the cavity. However, its location is note even close to being twice further than the ring in the 3 D fiducial simulation. Therefore, it suggests that these rings are either linked to the inner radial boundary condition or to the choice of a specific 2.5 D restart file.

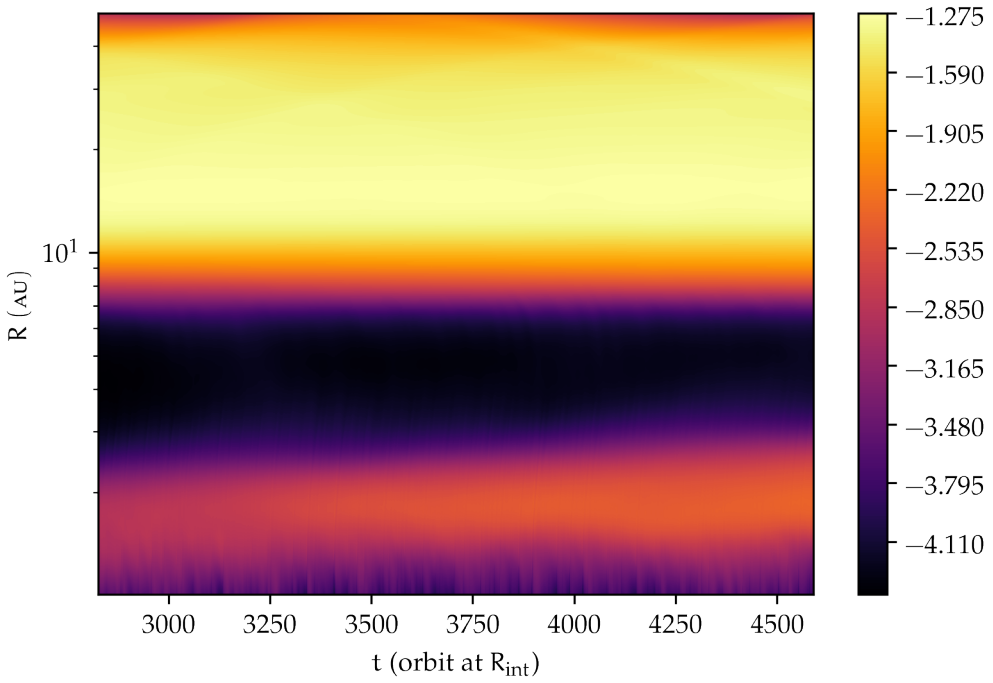

Figure 106: Spatio-temporal diagram of Σ for my 3 D simulation without the use of my restart procedure.

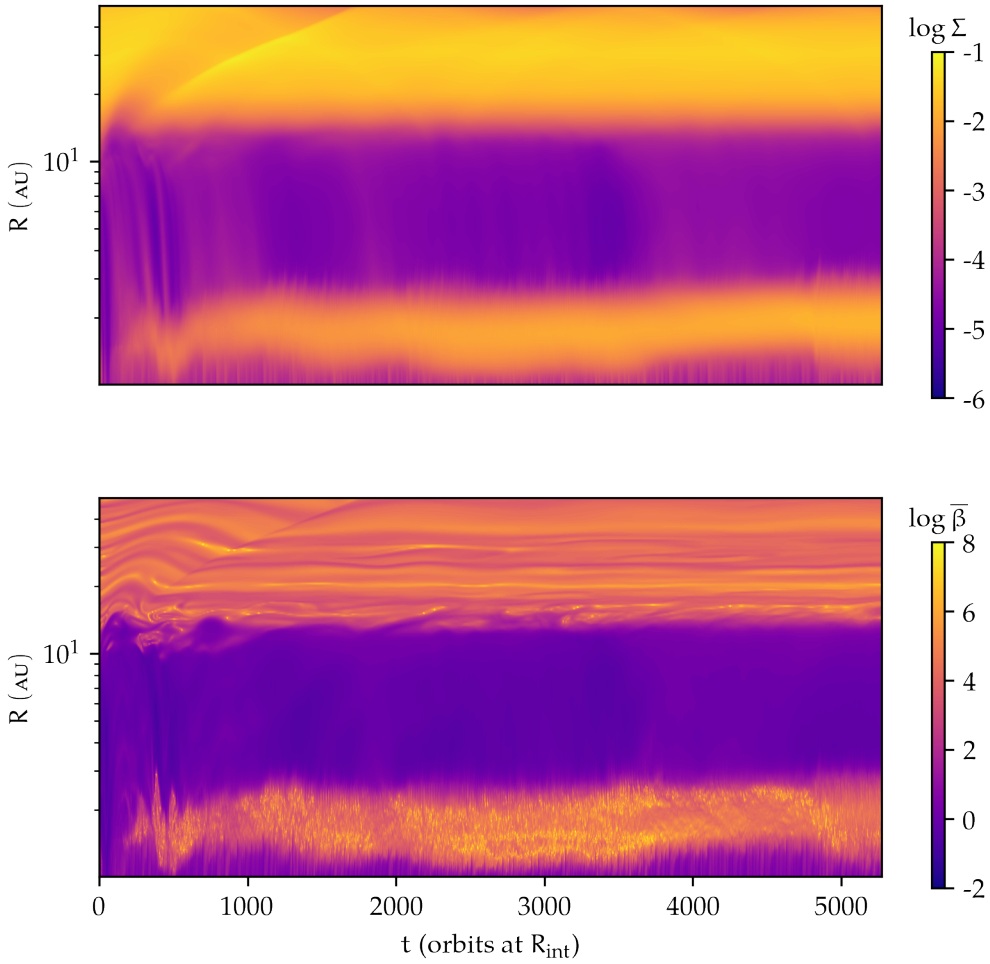

Figure 107: Spatio-temporal diagram of Σ and $\overline{\beta}$ for my 3D simulation restarted from the 2.5D simulation with a twice bigger cavity.

D

ARTICLE PUBLISHED IN A&A

This appendix is made of the article that I wrote on the results of my 2.5 D simulations and which is published in A&A (Martel and Lesur, 2022).

A&A 667, A17 (2022)
https://doi.org/10.1051/0004-6361/202142946

Astronomy & Astrophysics

Magnetised winds in transition discs

I. 2.5D global simulations★

Étienne Martel and Geoffroy Lesur

Univ. Grenoble Alpes, CNRS, IPAG, 38000 Grenoble, France
e-mail: etienne.martel@univ-grenoble-alpes.fr

Received 17 December 2021 / Accepted 3 May 2022

ABSTRACT

Context. Protoplanetary discs are cold, dense, and weakly ionised environments that witness planetary formation. Among these discs, transition discs (TDs) are characterised by a wide cavity (up to tens of au) in the dust and gas distribution. Despite this lack of material, a considerable fraction of TDs are still strongly accreting onto their central star, possibly indicating that a mechanism is driving fast accretion in TD cavities.
Aims. The presence of radially extended 'dead zones' in protoplanetary discs has recently revived interest in magnetised disc winds (MDWs), where accretion is driven by a large magnetic field extracting angular momentum from the disc. We propose that TDs could be subject to similar disc winds, and that these could naturally explain the fast-accreting and long-lived cavities inferred in TDs.
Methods. We present the results of the first 2.5D global numerical simulations of TDs harbouring MDWs using the PLUTO code. We imposed a cavity in the gas distribution with various density contrasts, and considered a power-law distribution for the large-scale magnetic field strength. We assume the disc is weakly ionised and is therefore subject to ambipolar diffusion, as expected in this range of densities and temperatures.
Results. We find that our simulated TDs always reach a steady state with an inner cavity and an outer 'standard' disc. These models also maintain an approximately constant accretion rate through the entire structure, reaching $10^{-7}\ M_\odot\ \mathrm{yr}^{-1}$ for typical surface density values. The MDW launched from the cavity is more magnetised and has a significantly larger lever arm (up to 10) than the MDW launched from the outer disc. The material in the cavity is accreted at sonic velocities, and the cavity itself is rotating at 70% of the Keplerian velocity due to the efficient magnetic braking imposed by the MDW. Overall, our cavity matches the dynamical properties of an inner jet emitting disc (JED) and of magnetically arrested discs (MADs) in black-hole physics. Finally, we observe that the cavity is subject to recurring accretion bursts that may be driven by a magnetic Rayleigh-Taylor instability of the cavity edge.
Conclusions. Some strongly accreting TDs could be the result of magnetised wind sculpting protoplanetary discs. Kinematic diagnostics of the disc or the wind (orbital velocity, wind speeds, accretion velocities) could disentangle classic photo-evaporation from MDW models.

Key words. accretion, accretion disks – protoplanetary disks – magnetohydrodynamics (MHD) – methods: numerical

1. Introduction

Transition discs (TDs) are protoplanetary discs exhibiting a deficit of near-infrared emission, indicating a significant drop in the abundance of small dust grains in the regions inside a few tens of au (Espaillat et al. 2014). These objects are believed to be the intermediate stage between 'full' primordial T Tauri discs and disc-less young stellar objects, hence their name. In this framework, TDs are the result of an inside-out dispersal process, which is usually believed to be a combination of viscous accretion, dust growth (Dullemond & Dominik 2005), giant planets (Marsh & Mahoney 1992), and photo-evaporation (Clarke et al. 2001; Alexander et al. 2014).

Despite their cavities, a large fraction of TDs are accreting onto their protostars. While Najita et al. (2007) quoted a median accretion rate reduced by one order of magnitude in Taurus compared to 'primordial' discs, more recent studies find even stronger accretion rates. Fang et al. (2013) showed that accreting TDs have a median accretion rate similar to normal optically thick discs. Manara et al. (2014) finds that TDs accrete similarly to classic T Tauri stars and that there is no correlation between the accretion rate and the cavity size. The fact that TDs are accreting systems should not give the impression that their cavity is depleted only in dust grains: TDs also exhibit cavities in the gas distribution (Zhang et al. 2014), with gas surface density increasing with radius (Carmona et al. 2014). Probing rotational emission of CO, van der Marel et al. (2015, 2016) find a drop in gas surface density by two to four orders of magnitude, while the drop in dust surface density goes up to six orders of magnitude. Similar results hold in ro-vibrational CO lines, probing the cavity further in, leading to a gas drop of two to four orders of magnitude in the inner (<3 au) regions (Carmona et al. 2017).

The picture that emerges is that of discs with a drop in gas surface density by several orders of magnitude, which are accreting similarly to (or slightly less than) primordial discs. There can be only two explanations for this phenomenon: either accretion is due to a 'hidden' mass reservoir localised close to the star, and what we observe is the transient accretion of this reservoir, or gas somehow manages to penetrate the cavity with a much larger velocity than the usual viscous accretion velocity. In that case, one typically needs an accretion velocity of the order of

★ The data underlying this article will be shared on reasonable request to the corresponding author.

the sound speed to reconcile the accretion rate with the drop in surface density (Wang & Goodman 2017).

In the first category of models, we find scenarios involving photoevaporation combined with an inner dead zone (Morishima 2012; Gárate et al. 2021). This inner dead zone, typically extending between 1 and 10 au, sets the radius of the mass reservoir and therefore the cavity inner edge. While it predicts a fraction of TDs with accretion rates of $\dot{M} \sim 10^{-9}\ M_\odot\,\mathrm{yr}^{-1}$, it also predicts a large fraction of non-accreting TDs, which is not observed (Gárate et al. 2021). In addition, these models rely on the Ohmic dead zone model of Gammie (1996), while it is now understood that dead zones are much more extended radially because of ambipolar diffusion (Simon et al. 2013), casting doubts on the applicability of inner dead zone models. The second type of model requires a mechanism to boost angular-momentum transport in the cavity. The most studied candidate for this is planet-disc interaction with planets (typically more than 3) embedded in the inner cavity. This scenario, however, finds gaps that are not necessarily sufficiently 'clean' (Zhu et al. 2011) and predicts that multiple giant planet systems in resonance are much more common than observed (Dong & Dawson 2016).

It should be noted that all of these scenarios make the explicit assumption of viscous accretion, the viscosity being due to some kind of small-scale turbulence, which could be of hydrodynamic (vertical shear instability or VSI, Nelson et al. 2013) or magnetic (magneto-rotational instability or MRI, Balbus & Hawley 1991) origin. It is, however, becoming clear that accretion in the regions outside of 1 au is probably partially driven by magnetic winds (Bai & Stone 2013; Lesur et al. 2014; Béthune et al. 2017). While the accretion rate of viscous models is proportional to the gas surface density, the accretion rate of magnetohydrodynamic (MHD) wind-driven models is mostly controlled by the strength of the large-scale magnetic field, and much less by the surface density (for instance, Lesur 2021b proposes $\dot{M} \propto \Sigma^{0.2}\, B^{1.6}$). Hence, if one carves a cavity in a disc without significantly modifying its magnetic field distribution, one could in principle create a population of accreting TDs not so different from classical T Tauri discs in terms of accretion rates. This kind of scenario is found in secular evolution models that include a realistic dependence of the wind stress on the surface density (e.g. Suzuki et al. 2016, see their Σ-dependent wind torque models). Hence, MHD winds could, in principle, generate and sustain a fast-accreting TD cavity.

The idea of having a magnetic wind-driven cavity was first proposed by Combet & Ferreira (2008). In this work, the cavity (named the jet emitting disc, or JED) is diluted, accreting at sonic velocities, and it sustains an accretion rate similar to that of the outer disc. The same angle of attack was more recently tackled by Wang & Goodman (2017), who showed that the magnetic diffusion properties of TD cavities were reminiscent of the magnetic wind solutions of Wardle & Koenigl (1993), indicating that all of the conditions required for efficient magnetic wind launching were met in TD cavities. While this picture is promising to explain accreting TDs, no dynamical model exists connecting an outer 'standard' disc to an inner cavity accreting thanks to magnetised winds.

In this work, we present the first self-consistent (under the standard MHD assumptions) numerical models of accreting TDs based on the MHD wind scenario. The model we propose does not enforce accretion (e.g., with an α parameter that would be added by hand). Accretion and the disc equilibrium are natural consequences of the first principles of MHD, in the sense that their origins lie within the magnetic stresses arising from the initial vertical magnetic field. Our aim is to demonstrate that a fast accreting cavity can connect to a standard wind-emitting outer disc, subject to realistic magnetic diffusion, and that the resulting configuration can be long-lived. Given the richness of the dynamics, we first concentrated on 2.5D models in this work, and we will discuss 3D models in a follow-up paper. The paper is divided as follows. We first introduce the model equations, physical quantities, and numerical setup. We then discuss an in-depth investigation of a fiducial model, which possesses a cavity with a drop of four orders of magnitude in gas surface density. We finally explore alternative models, varying the cavity depth and size, and the diffusion coefficients before concluding. We stress that we focus here on a proof of concept that such a TD configuration is sufficiently stable to be observable, but we do not discuss 'how' a primordial disc could have ended in such a configuration. This will be the subject of future work.

2. Physical and numerical setups

2.1. Physical model

2.1.1. Governing non-ideal MHD equations

In the following, we place ourselves in the non-relativistic, non-ideal MHD regime and consider a thin, locally isothermal disc to follow the evolution of the gas. The mass and momentum conservation equations and the induction equation respectively read

$$\partial_t \rho + \boldsymbol{\nabla} \cdot (\rho\, \boldsymbol{u}) = 0, \tag{1}$$

$$\partial_t (\rho\, \boldsymbol{u}) + \boldsymbol{\nabla} \cdot (\rho\, \boldsymbol{u} \otimes \boldsymbol{u}) = -\boldsymbol{\nabla} P - \rho\, \boldsymbol{\nabla} \Phi_* + \frac{\boldsymbol{J} \times \boldsymbol{B}}{c}, \tag{2}$$

$$\partial_t \boldsymbol{B} = -\nabla \times \boldsymbol{\mathcal{E}}, \tag{3}$$

where ρ, P, $\boldsymbol{u}$, and $\boldsymbol{B}$ are, respectively, the density, the thermal pressure, the plasma velocity, and magnetic field. $\Phi_* = -GM_*/r$ is the gravitational potential due to the central star of mass M_*, G being the gravitational constant. To close this system of equations, we assume the plasma follows a non-ideal Ohm's law including ambipolar diffusion:

$$\mathcal{E} = -\boldsymbol{u} \times \boldsymbol{B} - \frac{4\pi}{c}\, \eta_\mathrm{A}\, \boldsymbol{J} \times \hat{\boldsymbol{b}} \times \hat{\boldsymbol{b}}, \tag{4}$$

where $\hat{\boldsymbol{b}}$ is a unit vector parallel to $\boldsymbol{B}$, $\boldsymbol{J}$ is the electric current, c is the speed of light, and η_A is the ambipolar diffusivity. No turbulence was added in this model whatsoever. In addition to these equations, the plasma follows the Maxwell equations:

$$\boldsymbol{\nabla} \cdot \boldsymbol{B} = 0 \tag{5}$$

and

$$\boldsymbol{J} = \frac{c}{4\pi}\, \boldsymbol{\nabla} \times \boldsymbol{B}. \tag{6}$$

We place ourselves in a spherical coordinate system (r, θ, ϕ) centred on the star. For convenience, we also introduce the cylindrical coordinates $R = r\,\sin\theta$, $\vartheta = \varphi$ and $z = r\,\cos\theta$.

Since we work in a thin disc, the azimuthal angular velocity Ω is expected to be close to the Keplerian angular velocity $\Omega_\mathrm{K}(r) = (G\,M_\star/r^3)^{1/2}$. It is therefore useful to introduce a deviation from the Keplerian velocity $\boldsymbol{v}$, defined as

$$\boldsymbol{v} = \boldsymbol{u} - r\,\sin\theta\,\tilde{\Omega}(r)\,\boldsymbol{e}_\varphi, \tag{7}$$

with $\tilde{\Omega}(r) \equiv \Omega_{\rm K}(r)/\sin^2\theta$. We note that the latitudinal dependence of $\tilde{\Omega}$ is somewhat arbitrary and need not be a particular equilibrium state. Here, our choice of $\tilde{\Omega}(r)$ ensures that our reference Keplerian velocity has constant specific angular momentum on spherical shells and eliminates surface terms that are otherwise present in angular-momentum conservation equations (e.g. the last term of Eq. (16) in Zhu & Stone 2018). This will simplify the interpretation of angular-momentum budgets later.

2.1.2. Equation of state and cooling function

As a simplification, we assume the flow follows an ideal equation of state and is approximately locally isothermal, that is $T \approx T_{\rm eff.}(R)$ where $T_{\rm eff.}$ is a prescribed radial temperature profile. This is achieved by solving the energy equation

$$\partial_t P + \boldsymbol{u}\cdot\boldsymbol{\nabla}P + \Gamma P\,\boldsymbol{\nabla}\cdot\boldsymbol{u} = \Lambda, \tag{8}$$

where we defined a heating and cooling function

$$\Lambda = \frac{P}{T}\frac{T - T_{\rm eff.}}{\tau}, \tag{9}$$

where τ is the cooling time that is set to 0.1 time code unit (see below) and $\Gamma = 1.0001$ is the polytropic index of the gas. The target temperature profile is

$$T_{\rm eff.}(R) = T_0\left(\frac{R}{R_{\rm int}}\right)^{-1}, \tag{10}$$

where T_0 is the midplane temperature at the inner radius $R_{\rm int}$. This choice of cooling function allows us to enforce a chosen temperature profile that mimics the real radiative equilibrium and avoid the development of the vertical shear instability (VSI, Nelson et al. 2013), which would appear in a strictly locally isothermal approximation.

Since the gas is ideal, we can define an isothermal sound speed $c_{\rm s}^2 \equiv P/\rho$. It can be shown that as a result of the vertical hydrostatic equilibrium, $c_{\rm s}$ and $\Omega_{\rm K}$ are related to the vertical disc thickness $h(R)$ through

$$h(R) = c_{\rm s}(R)/\Omega_{\rm K}(R). \tag{11}$$

Assuming the disc is at thermal equilibrium ($T = T_{\rm eff.}(R)$), we have $c_{\rm s} \propto R^{-1/2}$, and hence the disc aspect ratio $\varepsilon \equiv h/R$ is constant. For the following, we chose T_0 in (10) so that $\varepsilon = 0.1$.

2.2. Numerical method and parameters

2.2.1. Integration scheme

The simulations were performed using the PLUTO code (Mignone et al. 2007) that solves the MHD equations with a conservative Godunov-type scheme and a second-order Runge–Kutta time stepping. We used a HLLD type Riemann solver to compute the intercell fluxes. In order to ensure the solenoidal constraint (6), we used the constrained transport approach (Kane 1966; Evans & Hawley 1988). The implementation of ambipolar diffusion in the PLUTO code follows that of Lesur et al. (2014) and Béthune et al. (2017).

2.2.2. Code units and notations

The internal radius is $R_{\rm int} = 1$, which sets the length code unit and is chosen to be 1 au while $R_{\rm ext} = 50$. The time code unit is $\Omega_0^{-1} \equiv \Omega_{\rm K}(R_{\rm int})^{-1} = 1$, which is set to $1/2\pi$ years so that $G\,M_* = 1$, with $M_* = 1\ M_\odot$, $M_\odot$ being 1 solar mass. Therefore, $\Omega_{\rm K}(R) = \Omega_0\ (R/R_{\rm int})^{-3/2} = R^{-3/2}$. We chose $300\,{\rm g\,cm^{-2}}$ as a unit for the surface density and express the accretion rate in $M_\odot\,{\rm yr}^{-1}$. We denote code units as c.u. hereafter. We use the subscript X_0 to indicate that the quantity X is considered on the midplane ($\theta = \pi/2$) and the subscript $X_{\rm p}$ when X is a poloidal quantity.

2.2.3. Dimensionless numbers and definitions

We used the plasma parameter β to quantify the disc magnetisation, which is defined from the midplane properties of the disc as

$$\beta = \frac{8\pi P_0}{\boldsymbol{B}_{\rm p,0}^2}. \tag{12}$$

When considering the initial state of a given simulation, we refer to the initial magnetisation inside the cavity as $\beta_{\rm in}$ and to the initial magnetisation in the external part of the disc as $\beta_{\rm out}$. The second key parameter of this study is the strength of ambipolar diffusion, quantified with the Elsasser number

$$\Lambda_{\rm A} \equiv \frac{v_{\rm A}^2}{\Omega_{\rm K}\,\eta_{\rm A}}, \tag{13}$$

where $v_{\rm A} = B/(4\pi\rho)^{1/2}$ is the Alfvén speed. We refer the reader to Appendix A for detailed information on the justifications of the model we adopted for $\Lambda_{\rm A}$ and how we modelled its spatial dependencies in our simulations. These two dimensionless numbers are the main control parameters of our study.

The disc refers to the whole part of the simulation that covers $r \in [1; 50]$ and $z/R \in [-0.3; 0.3]$. The cavity is the region where the surface density is reduced by a given factor in the innermost part of the disc (i.e. from $r = 1$ to $r = 10$ in most of the models). The external part of the disc or so-called outer disc refers to the region where the disc is full and described by a standard protoplanetary disc (without a drop in the density profile) and which extends from $r \approx 10$ to $r = 50$. Finally, we refer to the region defined by $r \leq 1$ of our disc as 'seed', which is at play in our simulations through the inner radial boundary condition.

2.2.4. Computational domain

The radial direction is divided into 320 cells that expand from the inner radius $r \equiv R_{\rm int}$ to the external one $r \equiv R_{\rm ext}$ and are uniformly meshed on a logarithmically shaped grid. The colatitude domain is mapped on a stretched grid near the poles (from $\theta = 0$ to $\theta = 1.279$ and from $\theta = 1.862$ to $\theta = \pi$, with 72 cells in each zone), while the grid is chosen to be uniform around the midplane (from $\theta = 1.279$ to $\theta = 1.862$ with 96 cells) for a total of 240, which increases the precision in the region of interest. The disc scale height h is then covered by 16 points in the case where ε is fixed as constant and equal to 0.1.

2.2.5. Boundary conditions

Outflow boundary conditions are used in the radial direction so that no matter can come from the inner radius. In addition, we added a wave-absorbing zone for radii $r < 1.5$, which dampens

poloidal motions on an orbital timescale. We detail the impact of this procedure in Appendix B.

In these 2.5D simulations, axisymmetric conditions with respect to the polar axis are enough to handle the boundaries for the colatitude direction. With the aim of reducing the impact of the outer boundary conditions, we focused on radii lower than 30.

2.2.6. Initial condition, wind, and cavity

The initial temperature profile is the effective temperature profile given in (10). The initial states for the density and the azimuthal velocity $v_\varphi = R\,\Omega_\mathrm{K}$ mimic those of Nelson et al. (2013) to account for the hydrostatic equilibrium, while $v_\mathrm{r} = v_\theta = 0$ initially. These profiles read, without taking into account the cavity,

$$\rho(R,z) = \rho_0 \left(\frac{R}{R_\mathrm{int}}\right)^p \exp\left[\left(\frac{\Omega_\mathrm{K}(R)\,R^3}{c_\mathrm{s}(R)}\right)^2 \left(\frac{1}{\sqrt{R^2+z^2}} - \frac{1}{R}\right)\right], \tag{14}$$

$$v(R,z) = v_\mathrm{K}(R)\left[(p+q)\left(\frac{c_\mathrm{s}(R)}{\Omega_\mathrm{K}(R)\,R^2}\right)^2 + (1+q) - \frac{q\,R}{\sqrt{R^2+z^2}}\right]^{1/2}, \tag{15}$$

with ρ_0 being the density at the internal radius. We chose $q = -1$ and $p = -3/2$ for the Eqs. (14) and (15), which is consistent with self-similar stationary disc solutions (Jacquemin-Ide et al. 2021).

The initial vertical magnetic field follows a power law $B_z \propto R^{(p+q)/2}$ so that the plasma β parameter in the unperturbed disc is constant. To ensure that $\boldsymbol{\nabla}\cdot\boldsymbol{B} = 0$, we initialised the magnetic field using its vector potential $\boldsymbol{A}$, defined so that $\boldsymbol{B} = \boldsymbol{\nabla}\times\boldsymbol{A}$. Following Zhu & Stone (2018), we chose

$$A_\varphi = \begin{cases} \dfrac{1}{2}\,B_0\,R & \text{if } R \le R_\mathrm{int} \\ B_0\dfrac{R_\mathrm{int}^2}{R}\left(\dfrac{1}{2} - \dfrac{1}{m+2}\right) + R\left(\dfrac{R}{R_\mathrm{int}}\right)^m \dfrac{1}{(m+2)} & \text{if } R > R_\mathrm{int} \end{cases}, \tag{16}$$

where $m = (p+q)/2 = -5/4$. This results in a poloidal magnetic field that depends on the radius only:

$$\boldsymbol{B} = B_0\left(\frac{R}{R_\mathrm{int}}\right)^m \boldsymbol{e}_z. \tag{17}$$

The initial strength of the magnetic field is controlled by β_out, so that $B_0 \propto \beta_\mathrm{out}^{-1/2}$.

To add a cavity and mimic a TD, we multiplied the density profile by a function f that depends on the radius only, so that

$$\Sigma(R) = f(R)\times\Sigma_0(R), \tag{18}$$

with

$$f(R) = a\left(1 - c\,\tanh\left[b\left(1 - \frac{R}{R_0}\right)\right]\right), \tag{19}$$

where $\Sigma_0(R) \propto R^{p+1}$ is a standard surface density profile for a protoplanetary disc. The a, b, and c coefficients are defined as

$$\begin{cases} b = \dfrac{2}{n}\left(\dfrac{\delta R}{R_0}\right)^{-1} \\ a = \dfrac{\beta_\mathrm{in}/\beta_\mathrm{out} + \tanh(b)}{1+\tanh(b)} \\ c = \dfrac{1-\beta_\mathrm{in}/\beta_\mathrm{out}}{\beta_\mathrm{in}/\beta_\mathrm{out} + \tanh(b)} \end{cases},$$

where R_0 is the radius of the cavity (in code units), n the number of cells on which the transition spans, and $n\,\delta R$ the corresponding length in code units. We note that while the density profile exhibits an inner 'hole', the magnetic field distribution is kept as a power law (17). As a consequence, the initial magnetisation $\beta(R)$ also exhibits a jump in the cavity since $P \propto \Sigma(R)$.

Therefore, $\beta_\mathrm{out}/\beta_\mathrm{in}$ is equal to the contrast in the gas surface density. In short, the function f creates a cavity in Σ but does not affect B_p. As a result, we simulate a TD with a strongly magnetised cavity ($\beta_\mathrm{in} = 1$). A typical radial profile of the quantities discussed above is shown in Fig. 1.

2.3. Integration and averages

Several integrations and averages are used throughout the text. In this manuscript, we use the following proxy for the vertical integration along θ:

$$\overline{X}(r,t) = r\int_{\theta_+}^{\theta_-} X(\boldsymbol{r},t)\sin\theta\,\mathrm{d}\theta. \tag{20}$$

$\theta_\pm$ quantify the integration height as shown in Fig. 2 so that

$$\frac{\theta_- - \theta_+}{2} = \arctan\left(\frac{h_\mathrm{int}}{R}\right) = \arctan\varepsilon_\mathrm{int}, \tag{21}$$

with h_int being the integration height at radius R given by an integration effective aspect ratio $\varepsilon_\mathrm{int} \equiv h_\mathrm{int}/R$. We note that this integration 'height' is not necessarily the disc thickness h. We introduce $\overline{\beta}$ as

$$\overline{\beta} \equiv \frac{8\pi\,\Sigma\,\overline{c}_{\mathrm{s},0}^2}{\sqrt{2\pi}\,R\,\varepsilon\left(\overline{B_r}^2 + \overline{B_\theta}^2\right)}, \tag{22}$$

which corresponds to a theta-averaged 'effective' midplane β plasma parameter. It is defined so that it matches the midplane β parameter in a hydrostatic isothermal disc. This more general definition is needed when the disc midplane is displaced vertically such as inside the cavity (see Sect. 3.5.3). Finally, we added the time average defined by

$$\langle X(\boldsymbol{r})\rangle = \frac{1}{T}\int_{t_0}^{t_0+T} X(\boldsymbol{r},t)\,\mathrm{d}t. \tag{23}$$

We ran the 2.5D simulations so that we reach 1000 orbits at $R = 10$, which means ≈31 000 orbits at R_int. If not specified, time averages were calculated taking into account the whole simulation without the first 4000 orbits at R_int to suppress the transient state. Otherwise, we indicate our choice of notation when needed, $\langle X\rangle_{1000}$ being the time-averaged value of X during the last 1000 orbits at $R_\mathrm{int,}$ for example.

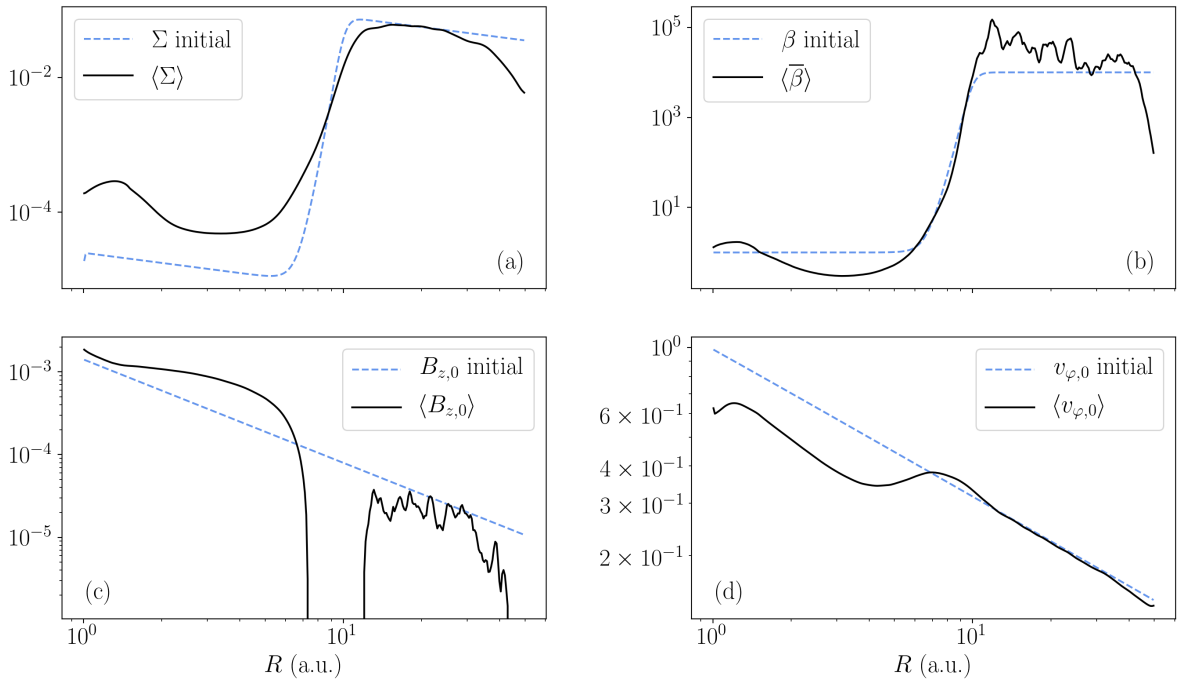

Fig. 1. Initial and time-averaged profile of Σ (*top left panel*), $\overline{\beta}$ (*top right*), $B_{z,0}$ (*bottom left*), and $v_{\varphi,0}$ (*bottom right*), with respect to R.

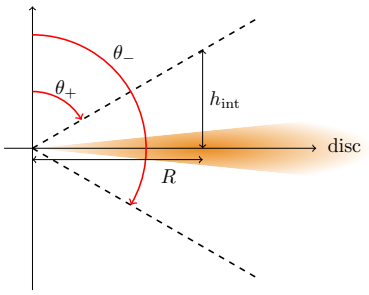

Fig. 2. Schematic view of the disc represented in orange. $\theta_{\pm}$ define the vertical integration surface and $h_{\rm int}$ is the integration scale height at a given radius R.

2.4. Simulation table

All the simulations performed are listed in Table 1. The characteristic parameters are the external initial plasma parameter $\beta_{\rm out}$, the internal initial plasma parameter $\beta_{\rm in,}$ and the initial ambipolar Elsasser number $\Lambda_{\rm A,0}$. Additionally, we performed a convergence test by running a high-resolution (640×480) simulation similar to the fiducial one that exhibits profiles that differ by less than 8% in the cavity and by less than 1 % when considering the entire domain.

3. Fiducial simulation

We start this section by describing our fiducial simulation in detail ($\beta_{\rm out} = 10^4$, $\beta_{\rm in} = 1$, $\Lambda_{\rm A} = 1$ and $R_0 = 10$), before turning to an exploration of the parameter space.

3.1. Evolution of surface density and plasma magnetisation

We first look at the temporal evolution of the surface density (Fig. 3). We find that the cavity stands during the whole simulation as its radius remains close to its initial value. As we show in Sect. 3.5.1, the cavity tends to expand slightly. The cavity location, defined as the radius where the surface density equals half of its maximum value, is subject to a small variation of $\Delta R/R = 10.3\%$ over the duration of the simulation. While the external disc is relatively smooth with respect to time, the cavity is striped by temporal variations of Σ, which may suggest that matter is moving inside the cavity at relatively fast speeds. We study these stripes in depth in Sect. 3.5.3. A small accumulation of material is seen close to the inner radius at $R \leq 1.5$. We refer the reader to Appendix B for a quantitative discussion on this accumulation.

Table 1. Simulation information. B4Bin0Am0 is the fiducial simulation.

Name	$\beta_{\rm out}$	$\beta_{\rm in}$	$\Lambda_{\rm A,0}$	R_0 (au)
B4Bin0Am0	10^4	1	1	10
B3Bin0Am0	10^3	1	1	10
B5Bin0Am0	10^5	1	1	10
B4Bin0Am1	10^4	1	10	10
B4Bin1Am0	10^4	10	1	10
B4Bin2Am0	10^4	10^2	1	10
B4Bin3Am0	10^4	10^3	1	10
B5Bin1Am0	10^5	10	1	10
B5Bin2Am0	10^5	10^2	1	10
B5Bin3Am0	10^5	10^3	1	10
B5Bin4Am0	10^5	10^4	1	10
B3Bin1Am0	10^3	10^1	1	10
B3Bin2Am0	10^3	10^2	1	10
R20FID	10^4	1	1	20

Notes. B4Bin0Am1 quantifies the influence of $\Lambda_{\rm A,0,}$ while B5Bin0Am0 and B3Bin0Am0 are the reference runs for $\beta_{\rm out} = 10^5$ and $\beta_{\rm out} = 10^3$. All the runs with Bin $\neq 0$ in their label explore the role of the initial value of β at $R_{\rm int}$. R20FID is the same simulation as the fiducial one, with a cavity that is twice as big. The bold font indicates the fiducial simulation values.

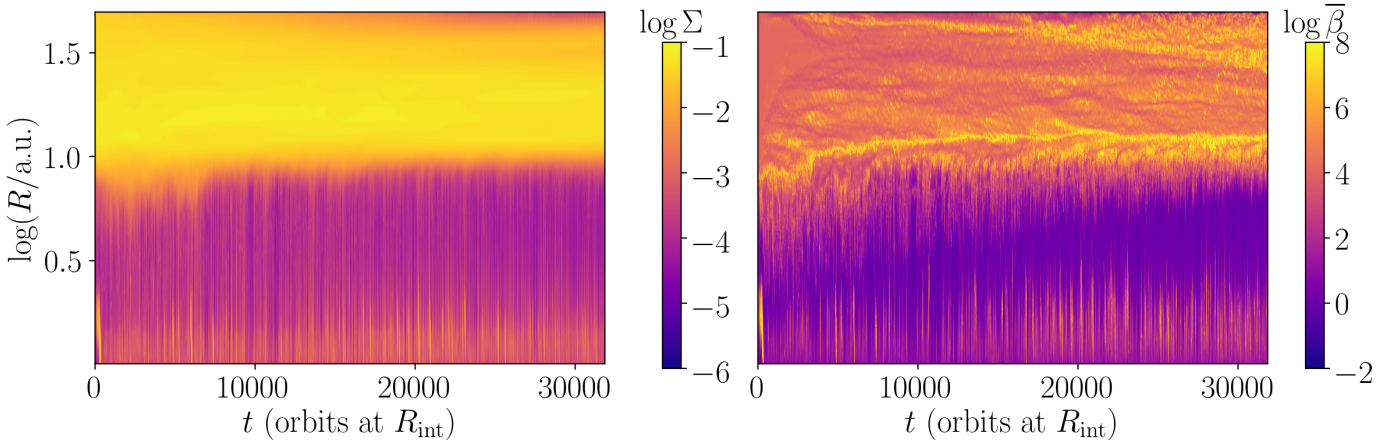

Fig. 3. Surface density (*left panel*) and plasma beta parameter $\overline{\beta}$ (*right panel*) as a function of R at midplane and time for the fiducial simulation. The cavity remains during the entire simulation and keeps a relatively strong magnetisation with $\overline{\beta} \sim 1$.

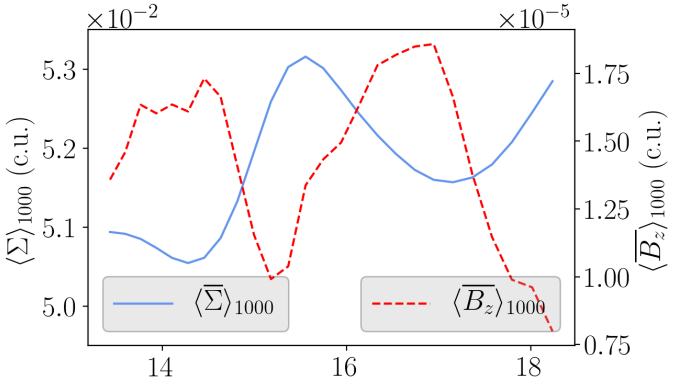

Fig. 4. Radial profiles of the surface density and of the vertical magnetic field in the midplane, time-averaged on the last 1000 orbits at $R_{\rm int}$. The vertical magnetic field is vertically averaged, and both profiles are given in arbitrary units.

Figure 3 also pictures the evolution of $\overline{\beta}$, whose results are similar to the ones for Σ. Inside the cavity, $\overline{\beta}$ exhibits a striped-like pattern with an accumulation close to the internal radius. The edge of the cavity is not smooth at all but varies around its initial value of 10. Though $\overline{\beta}$ stays on average around 1 in the cavity, some low values around 10^{-2} are reached from time to time. After approximately 4000 orbits at the internal radius, both Σ and $\overline{\beta}$ reach a quasi-stationary state.

Gaps and rings are detected in the outer part of the disc, in the spatio-temporal diagram of both Σ and β (Fig. 3). We also emphasise that these structures are observed in all of our simulations (see Figs. 19, 21, and 25). Regarding the fiducial simulation, we detect two main gaps after the cavity edge and before $R = 30$. For better visibility, we show the surface density and the vertical magnetic field, time averaged on the last 1000 inner orbits and a focus in the region $R = 12$–18 au (where the gaps are detected) in Fig. 4. Gaps are characterised by a drop of ∼5% of the local surface density and their location is correlated with a sharp increase of the vertical magnetic field, which matches the secular wind instability described by Riols et al. (2020). These structures are enhanced in the simulation with a higher ambipolar Elsasser number, as can be seen in Fig. 20. In addition, we observe the merging of gaps on longer timescales (Fig. 19) similarly to Cui & Bai (2021). While of interest for the dynamics of the outer disc, we did not address the evolution of these rings and gaps any further and instead focused on the dynamics of the cavity.

3.2. Disc structure

3.2.1. Magnetic structure

We show the time-averaged magnetic field in Fig. 5. In the cavity, the poloidal magnetic field lines are pinched at the midplane, but they remain vertical in the outer disc. These two regions are separated by a transition zone located at the cavity edge that exhibits a magnetic loop. Inside this loop, the polarity of the azimuthal component is reversed, with $B_\varphi > 0$ in the upper hemisphere close to the disc. The poloidal field lines present an elbow-shaped structure above and below the transition with significant changes of direction at $h_{\rm int}/R \approx \pm 0.3$, ± 0.6, and $\pm 0,9$.

3.2.2. Velocity streamlines

We show the time-averaged density and streamlines in Fig. 6. The disc clearly appears around the midplane for $R \gtrsim 10$, while the depleted profile in ρ indicates the cavity for $R < 10$. We find that a wind is emitted from the cavity, with poloidal streamlines approximately parallel to magnetic field lines, as expected from ideal MHD. A closer inspection of the streamlines, however, shows that in the regions close to the transition radius $R \gtrsim 8$, matter is falling into the cavity. Figure 6 shows that this material is actually coming from the outer disc. It is originally ejected from this disc, before being deflected and accreted into the cavity, generating an elbow-like shape similar to the one found for magnetic field lines (Fig. 5). This accretion stream then stays localised close to the cavity midplane down to the inner radius of the simulation. In the outer disc, the motion of the gas is not as well organised, though it is approximately symmetric with respect to the midplane.

3.2.3. Angular-momentum-flux streamlines

In order to deepen the analysis of the role of the magnetic structure, we concentrated on the time-averaged angular-momentum flux, defined by

$$\mathcal{L}_{\rm p} = r \sin\theta \langle \rho \boldsymbol{u}_{\rm p} u_\varphi \rangle - r \sin\theta \langle \boldsymbol{B}_{\rm p} B_\varphi \rangle. \quad (24)$$

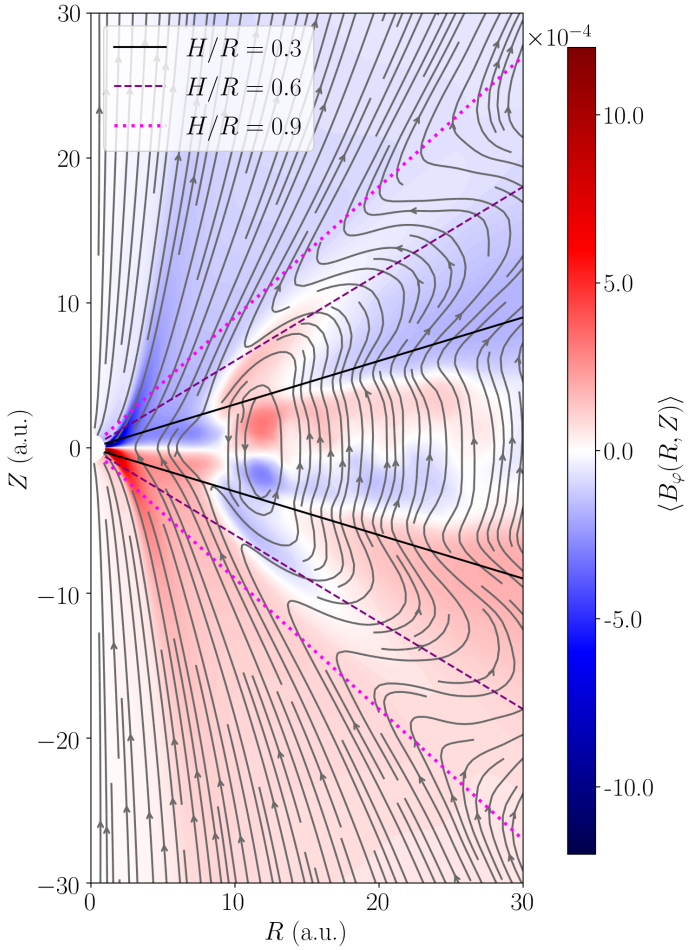

Fig. 5. Time-averaged poloidal magnetic field lines and toroidal field component $\langle B_\varphi \rangle$ for the fiducial simulation. We note the peculiar field topology close to the truncation radius.

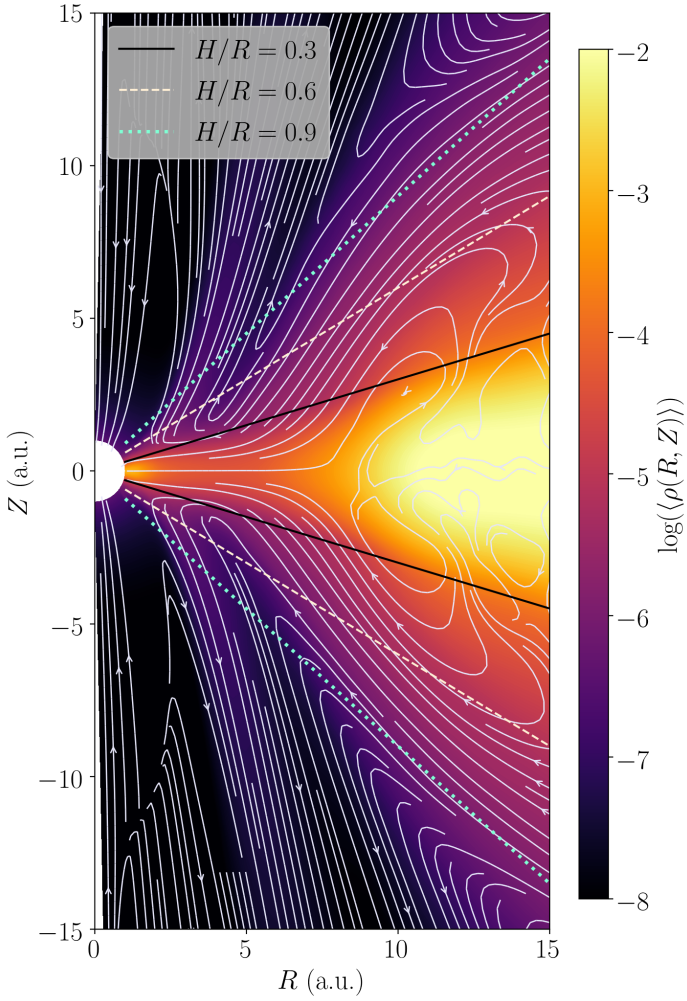

Fig. 6. Time-averaged streamlines and density for the fiducial simulation. We note the peculiar shape of the streamlines around the transition radius.

The poloidal flux lines associated with this angular-momentum flux are shown in Fig. 7. It appears that angular momentum is extracted from the disc midplane and carried both radially and vertically in a relatively homogeneous manner. In particular, we note that there is no elbow-like shape for the angular-momentum flux, in contrast to the magnetic and velocity streamlines, indicating that the cavity + outer disc system has adapted its magnetic topology to transport angular momentum homogeneously.

3.3. Accretion theory

3.3.1. Accretion rate

The first step to study the accretion in the disc is to investigate the accretion rate $\dot{M}$ defined as

$$\dot{M}(R,t) = -2\pi R \overline{\rho v_r}. \tag{25}$$

The height over which ρv_r is integrated has a direct influence on $\dot{M}$, mostly because of the elbow-shaped streamlines. It is then useful to change the thickness of the integration domain, which is controlled by the parameter $\varepsilon_\mathrm{int} \equiv \tan\left[(\theta_+ - \theta_-)/2\right]$. Results are presented in Fig. 8 for three values of ε_int. For $\varepsilon_\mathrm{int} = 0.3$ and around $R = 10$, the accretion rate is close to zero, indicating that the gas does not plunge directly in the cavity from the disc midplane. This radius corresponds to the location of the basis of the elbow-shaped loop along which the gas is moving. Averaging higher above the disc allows us to cancel out this effect. Moving to $\varepsilon_\mathrm{int} = 0.6$ and 0.9, the accretion rates in the disc and in the cavity eventually match by less than 50%, despite a jump of more than two orders of magnitude in Σ. This clearly indicates that the accreted material effectively 'jumps' above the transition radius, and that a steady state is reached with the whole system (cavity + outer disc) accreting at a constant rate.

The fact that the accretion rate is approximately constant while the surface density decreases by two orders of magnitude implies that the accretion speed should increase dramatically. This is clearly visible in Fig. 9, which shows the radial profile of the accretion speed $v_\mathrm{acc.}$ for $\varepsilon_\mathrm{int} = 0.9$, defined by

$$\langle v_\mathrm{acc.}\rangle \equiv \frac{\langle \dot{M}\rangle}{2\pi R \langle\Sigma\rangle}. \tag{26}$$

This velocity profile exhibits a well-defined transition between subsonic accretion outside the cavity with $\langle v_\mathrm{acc.}\rangle \sim 10^{-3}\langle c_\mathrm{s}\rangle$ and transsonic accretion inside with $\langle v_\mathrm{acc.}\rangle \sim \langle c_\mathrm{s}\rangle$.

3.3.2. Governing equations for accretion

Accretion theory can be understood as the secular evolution of $\dot{M}$ and Σ. In systems driven by MHD processes, these two quantities are usually supplemented by the magnetic field B_z threading the

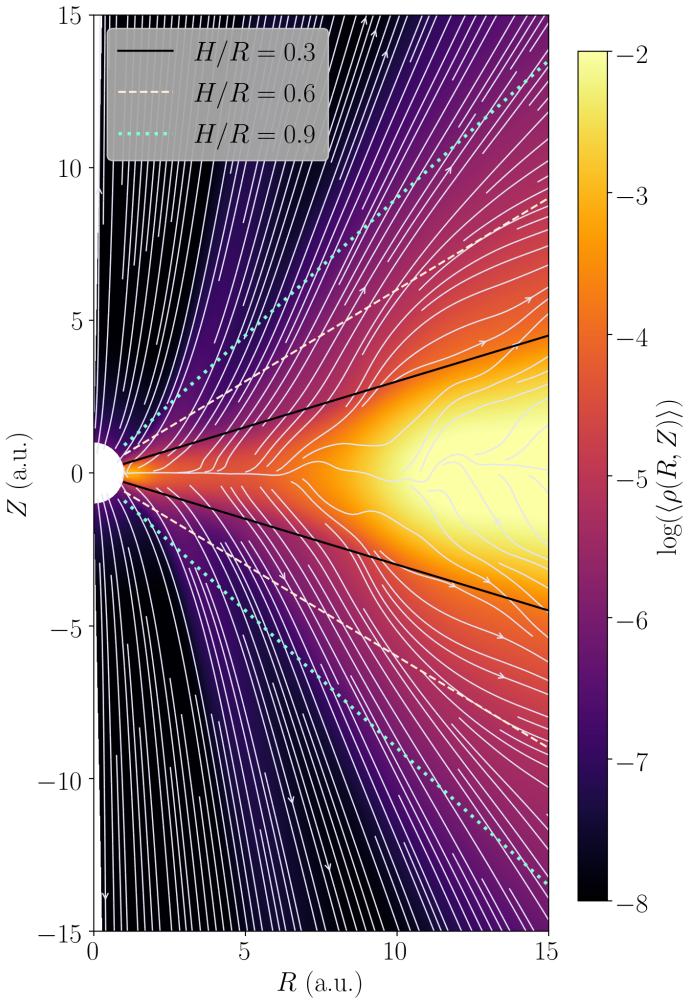

Fig. 7. Time-averaged angular-momentum-flux streamlines over time-averaged density for the fiducial simulation. Angular momentum leaves the disc midplane because of the wind.

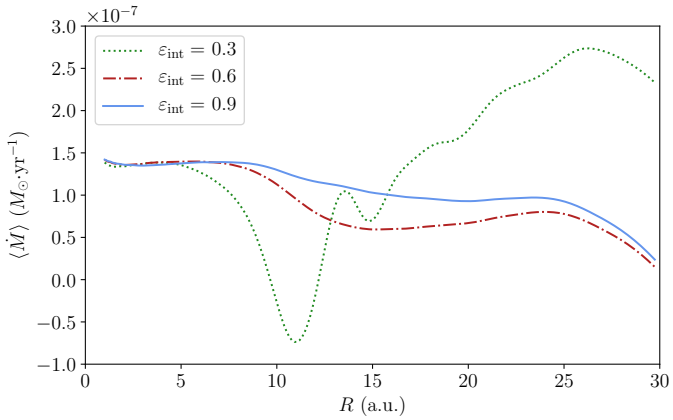

Fig. 8. Accretion rates for different integration height scales with respect to the radius inside the disc. The higher ρv_r is integrated the closer to a constant value $\dot{M}$ is in the cavity. The average value inside the cavity (from $R = 1$ to $R = 10$) is $\dot{M} = 1.4 \pm 0.2 \times 10^{-7}\ M_\odot\ \mathrm{yr}^{-1}$.

disc. We apply the vertical integration procedure to the mass and angular-momentum conservation equations, which become

$$\partial_t \Sigma - \frac{1}{2\pi r}\partial_r \dot{M} = -\left[\sin\theta \rho v_\theta\right]_{\theta_+}^{\theta_-} \tag{27}$$

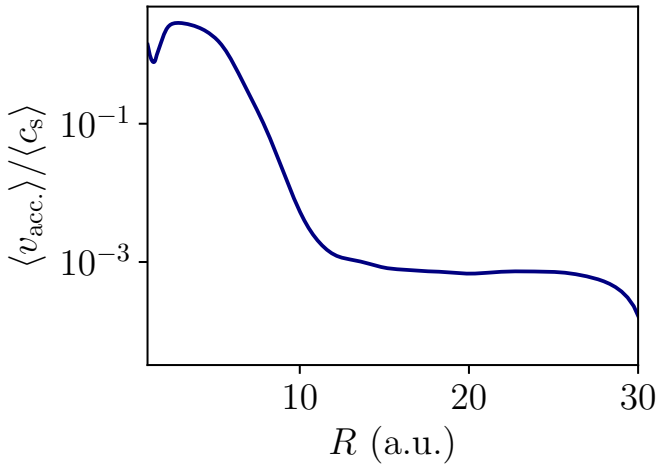

Fig. 9. Accretion speed for $\varepsilon_{\rm int} = 0.9$ in units of local sound speed c_s. The profile exhibits a clear transition between subsonic and transsonic accretion that occurs where the edge of the cavity is located.

$$\partial_t\left(\overline{r\,\sin\theta\rho v_\varphi}\right) - \frac{1}{2\pi r}\dot{M}\,\partial_r\left(r^2\,\sin^2\theta\tilde{\Omega}(r)\right) = -\frac{1}{r}\partial_r\left(r^2\,W_{r\varphi}\right) - W_{\theta\varphi,} \tag{28}$$

We defined $W_{r\varphi}$ and $W_{\theta\varphi,}$ respectively, as the radial and surface stresses by

$$\begin{cases} W_{r\varphi} \equiv \overline{\rho\,\sin\theta\,v_r\,v_\varphi} - \overline{\sin\theta\,\dfrac{B_r\,B_\varphi}{4\pi}} \\ W_{\theta\varphi} \equiv \left[r\,\sin^2\theta\left(\rho\,v_\theta\,v_\varphi - \dfrac{B_\theta\,B_\varphi}{4\pi}\right)\right]_{\theta_+}^{\theta_-}. \end{cases} \tag{29}$$

We remind the reader that we use a peculiar definition of the velocity deviation $\boldsymbol{v}$ so that no additional surface terms appear in Eq. (28). In order to take into consideration the role of the magnetic wind, we complete this set of equations by the vertical magnetic flux conservation

$$\partial_t B_{\theta,0} = \frac{1}{r}\,\partial_r\left(r\,\mathcal{E}_{\varphi,0}\right). \tag{30}$$

3.3.3. Mass conservation and mass-loss-rate parameter

The mass conservation equation is given by Eq. (27). Figure 10 shows the mass conservation for $\varepsilon_{\rm int} = 0.9$ with time-averaged quantities. The first information is that inside the cavity, the time derivative of Σ is close to zero, meaning the simulation reaches a steady state up to $R \approx 8$. Closer to the cavity edge, we note that this same term is negative, which is linked to the slow expansion of the cavity; this is discussed later in Sect. 3.5.1.

The main contribution of the wind mass loss is located in the cavity at $R < 5$ and is completely compensated by the radial derivative of the accretion rate. Additionally, the 'wind' mass flux turns negative around the cavity edge, which is due to matter being accreted from the outer disc atmosphere (see the 'elbow-shaped structure' in the poloidal streamlines).

In order to quantitatively account for the role of the wind, we constructed the mass-loss-rate parameter $\zeta = \zeta_+ + \zeta_-$ (Lesur 2021b), where ζ_+ and ζ_- are defined by

$$\langle\zeta_\pm\rangle \equiv \pm\frac{\langle\rho v_z\rangle(\theta_\pm)}{\langle\Sigma\rangle\,\Omega_{\rm K}} = \pm\frac{\langle\rho v_r\,\cos\theta\rangle - \langle\rho v_\theta\,\sin\theta\rangle}{\langle\Sigma\rangle\,\Omega_{\rm K}} \tag{31}$$

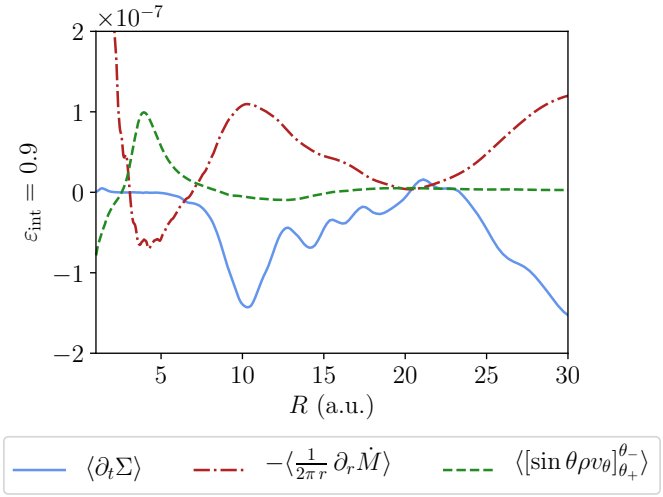

Fig. 10. Mass conservation for $\varepsilon_{\rm int} = 0.9$. The time derivative of Σ remains perfectly constant and equal to zero inside the cavity and only becomes moderately negative at the cavity edge $R = 10$. This suggests that the simulation indeed reaches a steady state for radii up to ≈8. The mass conservation is also correctly recovered. The three lines do not add up to zero because we used a moving average for better visibility, and the quantities are time-averaged on a sample selection of output files that do not contain all the time steps computed by the code.

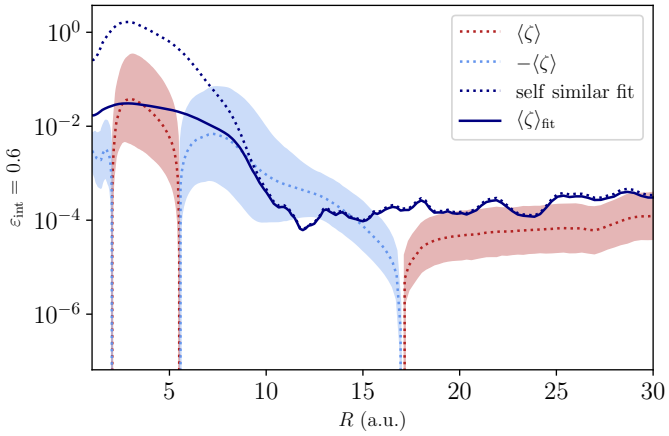

Fig. 11. $\langle \zeta \rangle$ parameter for $\varepsilon_{\rm int} = 0.6$. The self-similar fit shown here is for comparison only and was also obtained for $\varepsilon_{\rm int} = 0.6$. It appears that it is coherent for the external disc, while it predicts a wind way too intense in the internal part, therefore, another model is used to describe $\langle \zeta \rangle$ in the whole disc.

and the corresponding quantities are time averaged. The signs of $\zeta_\pm$ are chosen accordingly so that a positive value of $\zeta_\pm$ corresponds to matter leaving the surface at $\theta_\pm$. Since ζ_+ and ζ_- are pretty much symmetric with respect to the midplane, we focus on ζ only. The results are illustrated in Fig. 11 where both $\langle \zeta \rangle$ and $-\langle \zeta \rangle$ are shown. In order to compare with self-similar models (Lesur 2021b), we studied the values of $\langle \zeta \rangle$ at $z_0 = 6\,h$, which corresponds to $\varepsilon_{\rm int} = 0.6$. The mass-loss-rate parameter is approximately constant in the external part of the disc around 6.2×10^{-5}, while it peaks at 2.9×10^{-2} in the inner part. We find two zones where $\langle \zeta \rangle < 0$. One is close to the inner boundary and probably a boundary condition artefact, while the other extends from $R \approx 5$ to $R \approx 17$ au and is related to the material falling down on the disc around the transition zone, such a contribution being notably stronger for $\varepsilon_{\rm int} = 0.6$.

To compare to self-similar solutions, we show the self-similar scaling of the mass-loss-rate parameter with respect to $\langle \beta \rangle$ derived by Lesur (2021b), which reads $\langle \zeta_{\rm self} \rangle = 0.24\,\langle \beta \rangle^{-0.69}$. It comes as no surprise that this fit does not account for negative values of $\langle \zeta \rangle$ since these are due to the transition radius, which is not self-similar.

The wind mass-loss-rate parameter is smaller than the self-similar scaling in the outer disc by a factor of a few. This discrepancy is probably due to the influence of the cavity magnetosphere that compresses the disc magnetosphere, resulting in a deviation of ζ from the self-similar result. Moreover, it seems that the further we move outward, the closer we are to the self-similar values, indicating that we recover self-similar scalings far 'enough' from the cavity, as expected.

In the cavity, ζ is significantly weaker than expected from a naive extrapolation of self-similar scaling laws. This indicates that the mass-loss rate saturates at $\beta \sim 1$, a regime which was not explored by Lesur (2021b).

An alternative model to the self-similar one is used to describe $\langle \zeta \rangle$ with greater accuracy. The self-similar fit is kept for the external parts of the disc $\zeta_{\rm ext} = \zeta_{0,\,\rm ext}\,\langle \beta \rangle^{a_{\rm ext}}$, with $a_{\rm ext} = -0.69$ and $\zeta_{0,\,\rm ext} = 0.24$. Another one is then calculated for the inner part only, $\zeta_{\rm int} = \zeta_{0,\,\rm int}\,\langle \beta \rangle^{a_{\rm int}}$, with $a_{\rm int} < 0$, so that the final profile is given by

$$\langle \zeta \rangle_{\rm fit} = \frac{\zeta_{0,\,\rm ext}\,\langle \beta \rangle^{a_{\rm ext}}}{1 + \frac{\zeta_{0,\,\rm ext}}{\zeta_{0,\,\rm int}}\,\langle \beta \rangle^{a_{\rm ext} - a_{\rm int}}}. \tag{32}$$

We obtain $a_{\rm int} = -0.20$ and $\zeta_{0\,\rm int} = 0.018$. Such a model, with $a_{\rm ext} - a_{\rm int} < 0$, allows us to recover both of the previous regimes with a reasonably accurate depiction of the disc. The final profile exhibits a transition occurring at $\beta_{\rm t} \approx 5$, which is close to the lowest value of the ones used to build the self-similar fit in Lesur (2021b). The final curves are rendered in Fig. 11. The fit does not account for the negative values, but it properly catches both the inner and external parts of the disc.

3.3.4. Angular-momentum conservation

In Fig. 12, we show the terms involved in the angular-momentum conservation Eq. (28). These are time averaged and multiplied by $r^{-3/2}$ for better readability.

The integration height is $\varepsilon_{\rm int} = 0.9$ and chosen so that the influence of the cavity edge is diminished. In contrast to the mass-conservation equation, the time derivative is negligible. The surface stress ('wind') removes angular momentum from the whole disc with a major contribution right after the cavity at $R \approx 13$. We also observe that the radial stress is always positive, except at the cavity edge.

Such a cancellation suggests that two accretion regimes are observed in the disc, which echoes the radial profile of both the accretion rate and speed. To characterise the radial stress term, we introduced the α parameter of Shakura & Sunyaev (1973). It must be noted that the origin of this stress is in no way solely linked to turbulence and is considerably driven by the laminar structure of the magnetic wind. Appendix D details the origin of the stress and sheds light on the turbulent versus laminar origin of α. Nevertheless, the α parameter can still be used in this wind model, whose definition when time averaged is

$$\langle \alpha \rangle \equiv \frac{\langle W_{r\varphi} \rangle}{\langle \overline{P} \rangle}. \tag{33}$$

Table 2. Transport coefficients for a subset of simulations.

Name	$\dot{M}$ ($10^{-7}\,M_\odot\,\mathrm{yr}^{-1}$)	$\zeta_{\rm in}$ (10^{-2})	$\zeta_{\rm ext}$ (10^{-5})	$\alpha_{\rm in}$	$\alpha_{\rm ext}$ (10^{-3})	$\upsilon_{\rm W,\,in}$	$\upsilon_{\rm W,\,ext}$ (10^{-4})
B4Bin0Am0	1.4	2.9	6.2	13	4.9	1.0	2.3
B3Bin0Am0	5.1	3.8	14	19	23	1.4	31
B5Bin0Am0	0.27	2.1	4.5	6.6	1.0	0.18	0.19
B4Bin0Am1	1.2	–1.8	10	2.8	16	0.16	2.7
R20FID	1.1	4.5	5.8	15	2.4	1.2	10

Notes. The accretion rate is calculated inside the cavity. The bold font indicates the fiducial simulation values.

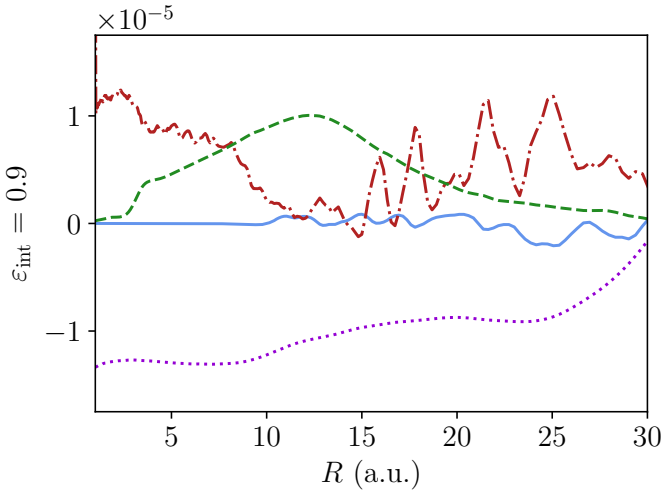

Fig. 12. Angular momentum conservation multiplied by $r^{-3/2}$ and time averaged. Full blue line is $\langle \partial_t(\overline{r\,\sin\theta\,\rho v_\varphi})\rangle\, r^{-3/2}$, red dot-dashed line is $\langle \partial_r(r^2\,W_{r\varphi})\rangle\, r^{-3/2}$, green dashed line is $\langle W_{\theta\varphi}\rangle\, r^{-3/2}$, and purple dotted line is $-\langle \frac{1}{2\pi r}\dot{M}\,\partial_r(r^2\,\tilde{\Omega})\rangle\, r^{-3/2}$.

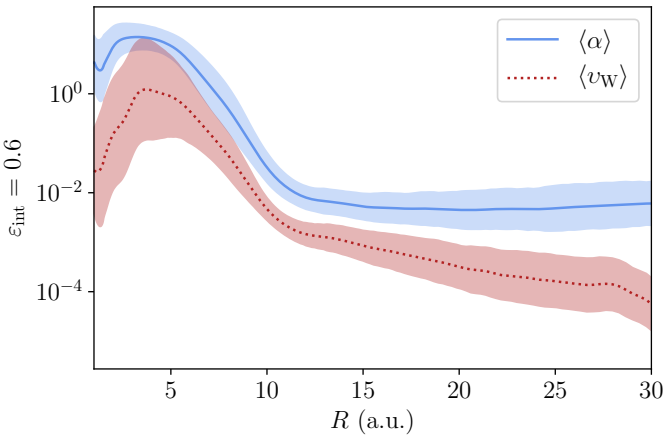

Fig. 13. Time-averaged transport coefficients $\langle\alpha\rangle$ and $\langle\upsilon_{\rm W}\rangle$ for $\varepsilon_{\rm int} = 0.9$.

The corresponding profile is given in Fig. 13, where $\varepsilon_{\rm int} = 0.9$. In the external part of the disc, $\langle\alpha\rangle = 49 \pm 5 \times 10^{-4}$, while it reaches a maximum value inside the cavity $\langle\alpha\rangle = 13 \pm 5$.

Following a similar procedure as the one for α, we define a dimensionless number associated with the surface stress component, $\upsilon_{\rm W}$. As for ζ, we define $\upsilon_{\rm W,\pm}$, which were chosen to be positive for angular momentum leaving the disc on both sides:

$$\langle\upsilon_{\rm W}\rangle = \langle\upsilon_{\rm W,+}\rangle + \langle\upsilon_{\rm W,-}\rangle = \frac{\langle W_{\theta\varphi}\rangle}{r\,\langle P_0\rangle}. \tag{34}$$

We show the dependence of $\upsilon_{\rm W}$ on R in Fig. 13. In the external disc, $\langle\upsilon_{\rm W}\rangle = 2.3 \pm 1.1 \times 10^{-4}$, while it rises up to $\langle\upsilon_{\rm W}\rangle = 1.0 \pm 0.1$ inside the cavity. The same observations are drawn for both $\langle\alpha\rangle$ and $\langle\upsilon_{\rm W}\rangle$ as for $\langle\zeta\rangle$. Therefore, two separate regimes are at stake in the disc. The outer disc regime is typical of wind-emitting protoplanetary discs, with transport coefficients close to the ones found in self-similar wind models for $\beta \sim 10^4$, indicating that the dynamical properties of the outer disc are not perturbed by the presence of the cavity. On the contrary, the second regime describes the inner part of the disc with fast accretion and high values for α and $\upsilon_{\rm W}$, which are both of the order of unity. Table 2 displays the transport coefficient values for all the simulations.

3.4. MHD wind

It is well known that steady-state MHD winds in ideal MHD can be characterised by a set of MHD invariants (Blandford & Payne 1982), which are conserved quantities along each poloidal field line (Fig. 5). In our axisymmetric simulations, a steady state is approximately achieved above the disc, in the ideal MHD region. Hence, we can measure these invariants on field lines attached in the cavity and in the outer disc.

Table 3. MHD invariants for a subset of simulations, computed with time-averaged quantities on the last 1000 orbits at $R_{\rm int}$.

Name	$\lambda_{\rm in}$	$\lambda_{\rm ext}$	$\kappa_{\rm in}$	$\kappa_{\rm ext}$	$\omega_{\rm in}$	$\omega_{\rm ext}$
B4Bin0Am0	23	3.2	2.2×10^{-2}	2.5	0.67	1.2
B3Bin0Am0	185	1.3	3.1×10^{-3}	9.9	0.64	0.93
B5Bin0Am0	4.4	1.2	1.3	18	0.69	1.1
B4Bin0Am1	4.9	1.5	0.24	5.0	0.23	3.6
R20FID	26	2.1	1.8×10^{-2}	2.8	0.52	1.4

Notes. The bold font indicates the fiducial simulation values.

In the following, we select a field line anchored in the disc midplane at $R \equiv R_{\rm w}$. The corresponding Keplerian angular velocity is $\Omega_{\rm w}$, while $B_{\rm w}$ is the poloidal magnetic field at the midplane. We then consider the following invariants, built on time-averaged quantities and listed in Table 3.

The mass-loading parameter accounts for the quantity of matter that escapes the disc with the wind and is defined as

$$\kappa \equiv 4\pi\,\frac{\rho\,\upsilon_{\rm p}\,\Omega_{\rm w}\,R_{\rm w}}{B_{\rm p}\,B_{\rm w}}. \tag{35}$$

The rotation parameter is given by

$$\omega \equiv \frac{\Omega}{\Omega_{\rm w}} - \frac{\kappa\,B_{\rm w}\,B_{\rm p}}{4\pi\,\rho\,R\,R_{\rm w}\,{\Omega_{\rm w}}^2}. \tag{36}$$

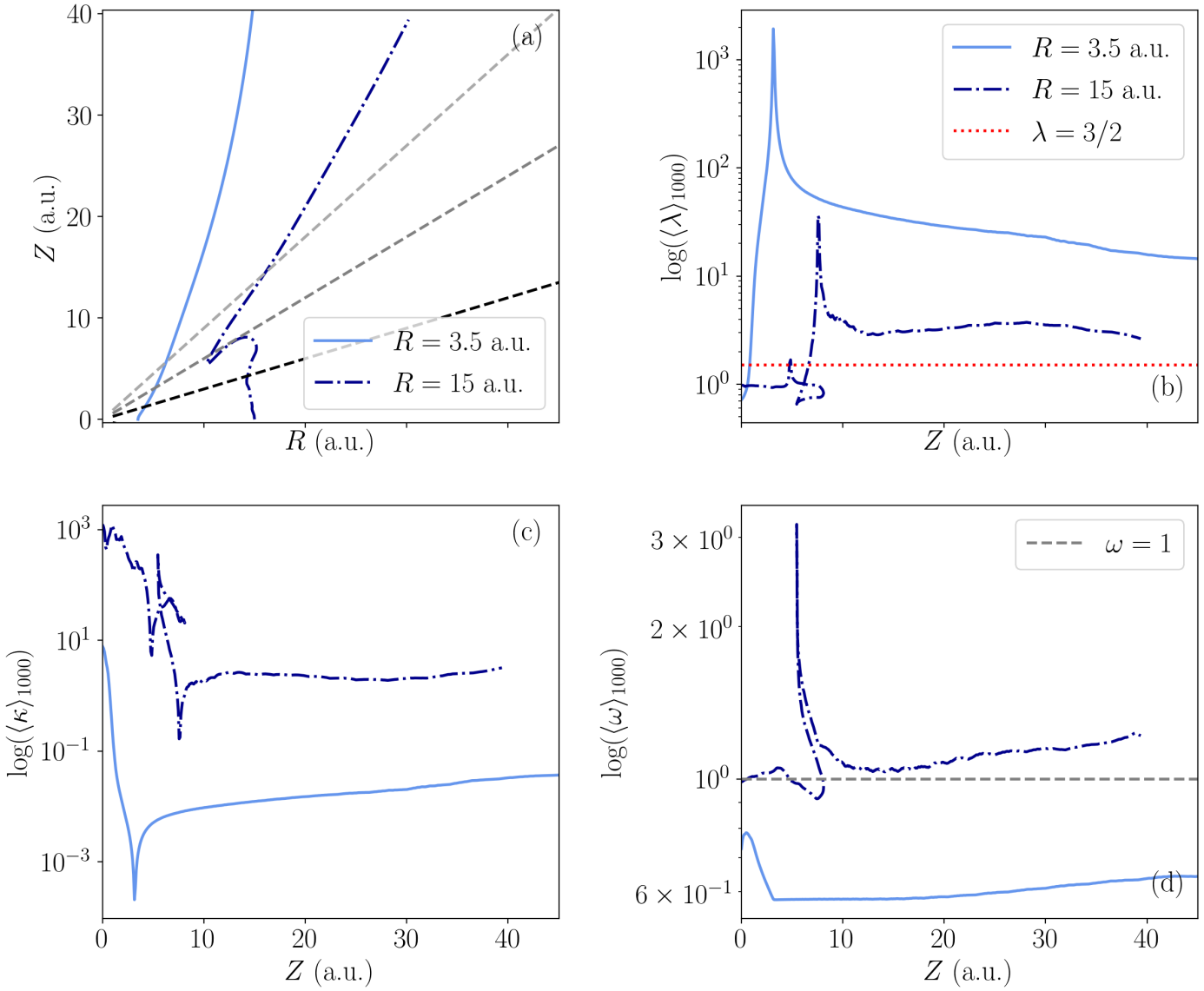

Fig. 14. General structure of the wind and MHD invariants. First panel shows the field lines in the internal and external disc. The grey dashed lines represent the surfaces at $h/R = 0.3$; 0.6 and 0.9. The three other plots display the MHD invariants for the internal field line (full, light blue) and the external one (semi-dashed, dark blue). The invariants are time averaged on the last 1000 orbits.

The magnetic lever arm accounts for the angular momentum that is removed from the disc by the wind is defined as

$$\lambda \equiv \frac{\Omega R^2}{\Omega_w {R_w}^2} - \frac{R B_\varphi}{R_w B_w \kappa}. \tag{37}$$

Of course, these invariants echo the transport coefficient definitions previously used to describe the disc, and one expects $\kappa \approx \beta\zeta/4\varepsilon$ and $\lambda \approx 1 + \varepsilon v_w/\zeta$ (Lesur 2021a).

To compute these invariants, we arbitrarily chose one field line in the cavity (referred to as 'in') leaving the midplane at $R_{in} = 3.5$ au and one in the external disc (referred to as 'ext') leaving the midplane at $R_{ext} = 15$ au (see the first panel of Fig. 14). We note that the disc thickness affects the MHD invariants since the physical foot points of the field lines are not located at the midplane but slightly above. Such a limitation especially concerns the field lines in the external disc, which are subject to a large-scale oscillation close to the transition radius. Therefore, the calculated MHD invariants are subject to caution and we only draw general conclusions regarding the nature of the wind.

We show the invariants along the chosen field lines in Fig. 14. We find that all of the invariants remain reasonably constant once high enough above the disc, as expected from a steady-state ideal MHD flow. The wind launched from the cavity is different from the disc one. The cavity wind has a much weaker mass loading parameter and a much larger lever arm (by almost a factor 10). We also find that its rotation parameter differs significantly from 1, indicating that field lines are rotating at 80% of Ω_K in the cavity. This point is probably related to the fact that the disc itself is sub-Keplerian in this region (Fig. 1). Quantitatively, we find $\kappa_{in} = 2.2 \times 10^{-2}$, $\kappa_{ext} = 2.5$, $\lambda_{in} = 23$ and $\lambda_{ext} = 3.2$. These values are coherent with the transport coefficients computed in previous sections. We also note that the values of κ and λ in the cavity match some of the historical solutions of Blandford & Payne (1982) (see their Fig. 2), which correspond to super-Alfvénic and collimated outflows. These values are also consistent with the magnetic outflow solutions of Ferreira (1997) (see Fig. 3). Hence, the cavity we find quantitatively matches the inner JED proposed by Combet & Ferreira (2008).

3.5. Temporal evolution

We observe two kinds of time variability in the fiducial simulation: a secular variability responsible for the slow expansion of the cavity, and a short timescale variability responsible for the striped patterns observed in space-time diagrams (Fig. 3). At this point, we started our exploration of time variability by focusing on the secular evolution, beginning with a discussion of the cavity expansion.

3.5.1. Slow cavity-edge expansion

As previously mentioned, the cavity edge moves slowly outwards during the simulation. Neglecting the impact of the wind in terms of mass-loss rate at the cavity edge location, which is coherent with Fig. 10, and assuming piecewise constant accretion rates and surface densities across the cavity edge, one obtains

$$\dot{R}_0 = -\frac{1}{2\pi R_0}\frac{\delta\dot{M}}{\delta\Sigma}, \tag{38}$$

where $\dot{R}_0$ is the cavity edge 'velocity' and $\delta\dot{M}$ and $\delta\Sigma$ are the jump in accretion rate and surface density at the cavity edge. By calculating $\dot{M}$ and Σ around R_0, we find $\dot{R}_0 = 1.8\times10^{-5}$ while directly evaluating the cavity edge motion $\dot{R}_0$ yields $\dot{R}_0 = 1.4\times10^{-5}$ (both in c.u.). Therefore, the cavity is expanding because of the slight mismatch in accretion rate observed in Fig. 8.

3.5.2. Magnetic field transport

To interpret the time evolution of the magnetic field, we studied the transport of magnetic flux inside the disc and defined a flux function ψ such that

$$\psi(r,t) = R_{\rm int}^2\int_0^{\pi/2} B_r(R_{\rm int},\theta,t)\,\sin\theta\,{\rm d}\theta - \int_{r=R_{\rm int}}^{r} r\,B_\theta(r,\pi/2,t)\,{\rm d}r. \tag{39}$$

Assuming the total flux is constant with respect to time, the iso-contours of ψ describe the motion of the magnetic field lines in the disc plane. The spatio-temporal diagram for ψ is shown in Fig. 15. The magnetic flux is advected slowly towards the star in the external disc, while it tends to diffuse outwards from the inner part of the disc to the cavity edge. The poloidal magnetic field lines in Fig. 5 show that $\langle B_{z,0}\rangle < 0$ in the transition region ($8 \lesssim R \lesssim 12$) and $\langle B_{z,0}\rangle > 0$ otherwise. This transition region is recovered in Fig. 15 as a region where $\partial_r\psi < 0$.

Overall, we observe that the negative field of the transition region is diffusing outwards, while the positive field of the outer disc is advected inwards. We therefore observe a reconnection of the large-scale field around $R \approx 12$, which progressively 'eats' the negative field of the transition region. In addition to this, we observe that field lines deep in the cavity also diffuse outwards.

To achieve a quantitative estimate of the field line advection speed, we first note that the evolution equations for ψ read

$$\begin{cases}\partial_t\psi(R,t) = -R\,\mathcal{E}_{\varphi,0}(R,t)\\ \partial_R\psi(R,t) = -R\,B_{\theta,0}(R,t)\end{cases}. \tag{40}$$

Following Guilet & Ogilvie (2014), we rewrote these evolution equations as an advection equation for ψ :

$$\partial_t\psi + v_\psi\,\partial_R\psi = 0, \tag{41}$$

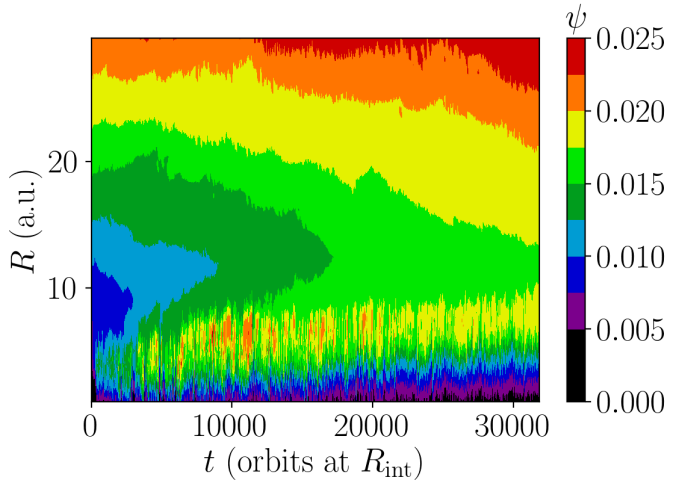

Fig. 15. Flux function $\psi(R,t)$ for the magnetic field, taking into account the flux at the surface of the seed and the radial flux. For radii larger than the one of the cavity, the field lines are advected toward the centre during the whole simulation. At $R \approx 13$, the flux accumulates and exhibits a striped structure for smaller radii.

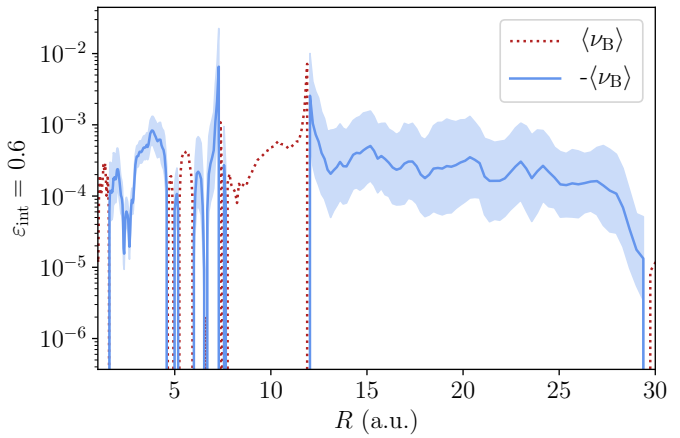

Fig. 16. Magnetic-field transport parameter $\nu_{\rm B}$ as a function of radius. We note that the outer disc is transporting magnetic field lines inwards ($\nu_{\rm B} < 0$).

where we defined the 'field advection velocity':

$$v_\psi = -\frac{\mathcal{E}_{\varphi,0}(R,t)}{B_{\theta,0}(R,t)}. \tag{42}$$

Eventually, we define a dimensionless advection parameter $\nu_{\rm B} = v_\psi/v_{\rm K,}$ which quantifies the advection speed (Bai & Stone 2017). In this framework, positive values of $\nu_{\rm B}$ imply an outward transport field, while negative values trace inward field transport.

We show the radial dependence of $\langle\nu_{\rm B}\rangle$ in Fig. 16. In the external disc, we find that the magnetic field is advected inwards with a velocity of $v_\psi = -2.6\times10^{-3}\,v_{\rm K}$. $\nu_{\rm B}$ changes its sign multiple times in the cavity, but it remains negative close to the cavity edge, between $R \approx 7$ and $R \approx 11$ au, where $v_\psi = +3.2\times10^{-3}\,v_{\rm K}$. Such a result is in accordance with Fig. 15 and indicates that field lines are converging at the transition radius with opposite vertical polarity. In the external parts, $\nu_{\rm B}$ is negative and $v_\psi = -2.6\times10^{-3}\,v_{\rm K}$ so that vertical magnetic field pointing upwards is advected. We note that this inwards advection of the outer disc field lines is in sharp contrast to other work that focused

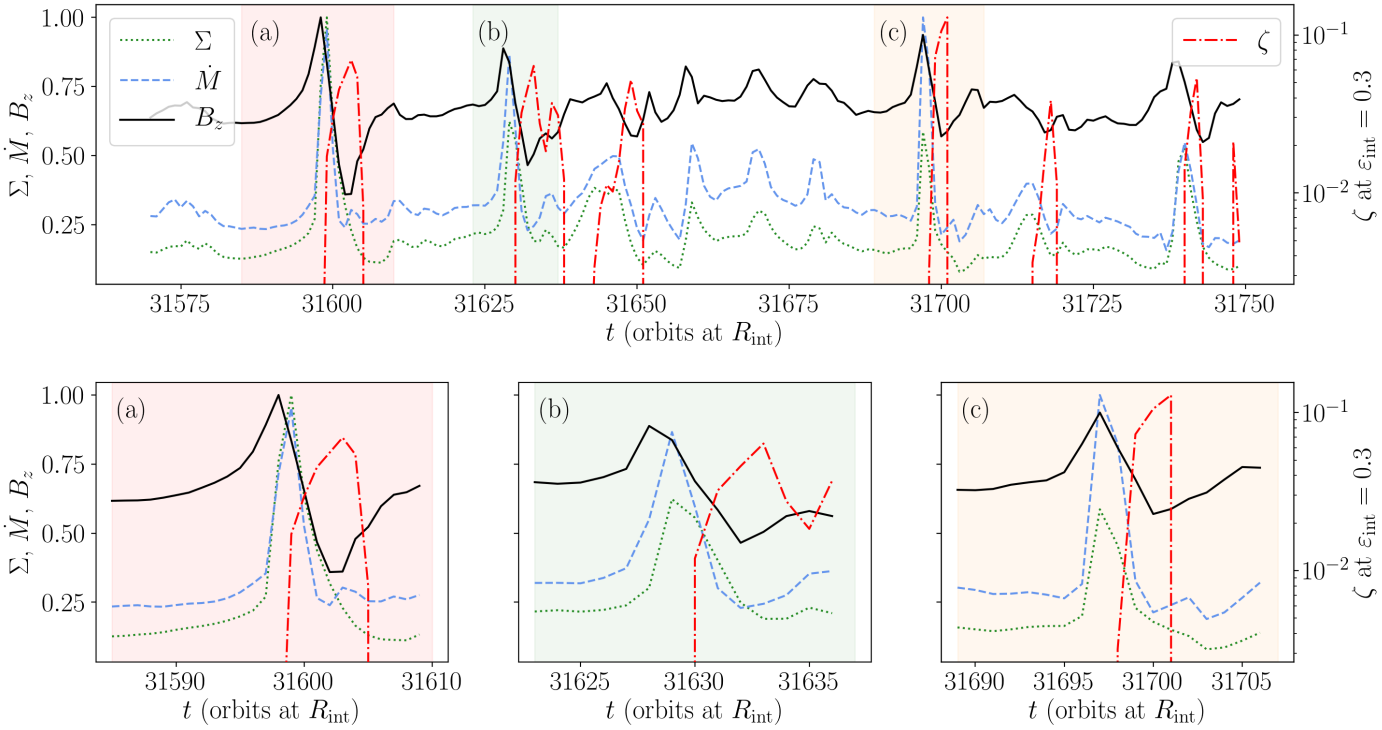

Fig. 17. Temporal evolution of Σ in dotted green, $\dot{M}$ in dashed blue, and B_z (vertically averaged) in black (full line) at $R = 3$ au for the fiducial simulation. ζ is calculated at $\varepsilon_{\rm int} = 0.3$ and shown by a semi-dashed red line with a logarithmic scale on the right of the panels. Apart from ζ, all the profiles are given in arbitrary units and divided by their maximum value reached during the timescale of the top panel.

on 'full' discs (Bai & Stone 2017; Lesur 2021b). We revisit this discrepancy in the discussion.

3.5.3. Fast variability of the cavity

Up to this point, we mostly considered time-averaged quantities and ignored fast variability. While our numerical solutions are quasi-steady if one looks at averages on 100s of orbits, they also exhibit a fast time variability (see the temporal stripes in Fig. 3), the origin of which requires clarification.

Figure 17 shows such a temporal evolution of Σ, $\dot{M}$, and B_z at $R = 3$. These profiles encounter sharp fluctuations chaotically distributed over time. Therefore, the cavity is subject to bursts of matter that quickly falls onto the star (the typical width of a peak is ∼5 orbits at $R_{\rm int}$, which is still far larger than our temporal resolution). This variability explains the stripes seen in the spatio-temporal diagram (Fig. 3).

We focus on a few of these bursts in the bottom panels of Fig. 17, while instantaneous pictures of the density corresponding to the (b) panel are given in Fig. 18. For these bursts, we see that the local maximum values of B_z, Σ, and $\dot{M}$ are correlated. When an inflow of matter crosses the cavity, Σ peaks as well as $\dot{M}$, which in turn increases ζ. In terms of temporal sequence, it seems that B_z increases slightly before Σ and $\dot{M}$, which would indicate that B_z is the driver of these bursts, but we cannot be definitive on this sequence because of the lack of temporal resolution. Finally, we observe that ζ is always clearly delayed compared to the other quantities, indicating that the wind inside the cavity ejects more material once the bubble of material has passed.

For a more precise insight on accretion and temporal variability, we refer the reader to Fig. 18, which shows the density and poloidal magnetic field lines at different times. In the first panel, we see a filament of matter located above the disc that extends from ($R = 10$, $Z = 5$) to ($R = 15$, $Z = 10$). This structure is cut in two on the second panel, revealing two bubbles of matter, one being about to fall, while the other is about to be ejected and leave the disc in the wind. Concerning the filament and the bubble formation, we detect a current sheet at the location of the filaments, where the total magnetic field cancels out ($B_\varphi = 0$ at the edge of the magnetic loop and $B_{\rm p} = 0$, because two anti-parallel poloidal field lines meet at the elbow-shaped structure location). It is therefore a possibility that these structures form due to magnetic reconnection. Focusing on the falling material, we see it reaching the edge of the cavity on the third panel before crossing it on the next one. When the gas crosses the cavity, the disc oscillates locally above and below the midplane and is therefore highly dynamical. With a slight delay (last three panels), we see an outflow emerging from the cavity, and the wind density increases. Such an observation exhibits the link between wind and accretion (see Fig. 10). The ejection of gas from the cavity is not constant with respect to time and occurs occasionally with burst events for which ζ eventually peaks at 0.1. This explains why the effective value of $\langle\zeta\rangle$ is lower than the one predicted by self-similar models for which the ejection is continuous with a higher mass-loss rate parameter.

Combining 6 and 18, we unveil a general scheme for feeding the cavity. First, the gas located inside the outer disc elevates from the midplane up to approximately two local disc heights and organises itself in a filamentary way. Then, bubbles of matter fall and cross the cavity, forming the elbow-shaped structure on the time-averaged profile.

3.5.4. Magnetic Rayleigh Taylor instability

To account for the formation and stability of the bubbles of matter at the cavity edge, we explored the possibility of having a

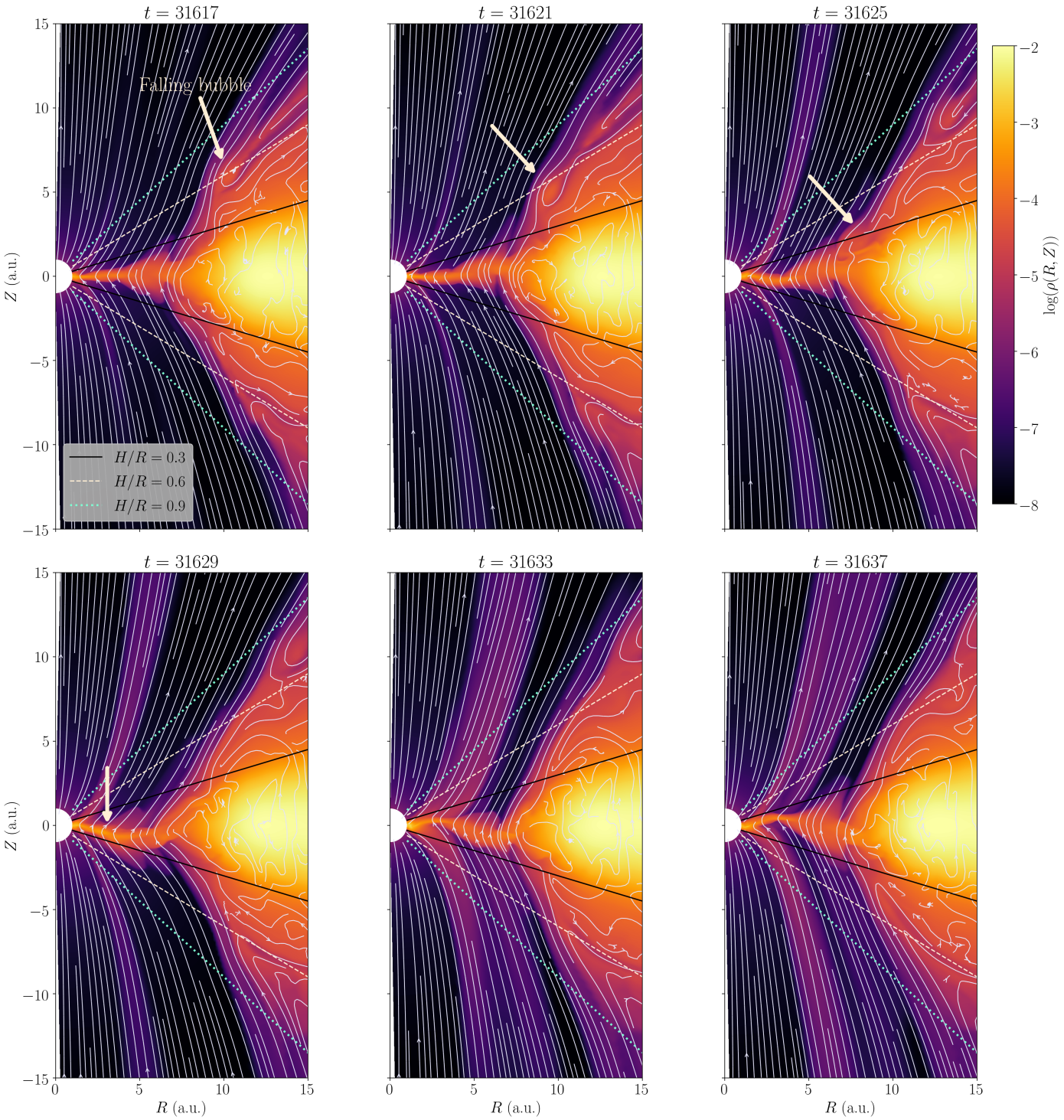

Fig. 18. Density and magnetic field lines at different times showing the advection of a bubble of material (arrow) from the outer disc through the cavity.

magnetic Rayleigh Taylor instability (RTI; or interchange instability) in the cavity. The disc is geometrically thin inside the cavity and the density is relatively continuous radially. Under these conditions, we referred to the analyses of Spruit & Taam (1990), Spruit et al. (1995) and Stehle & Spruit (2001), which assume an infinitely thin disc. We reformulated the instability criterion of Spruit et al. (1995) (see their Eq. (59)) in terms of the plasma parameter in Appendix C. The resulting criterion C.9 states that a necessary condition for the occurrence of the RTI is $\overline{\beta} < \beta_{\rm crit.} \simeq 0.0355$. Figure 3 shows that $\overline{\beta}$ is of the order of 0.1 in the cavity and rarely goes beyond this value, except for very short periods of time, for instance during the accretion 'bursts'. We conclude that the cavity β plasma parameter is too large to sustain the RTI on average, but we cannot exclude that it could be triggered in the rare excursions where the cavity reaches $\overline{\beta} < 0.1$, as it does during some of the bursts.

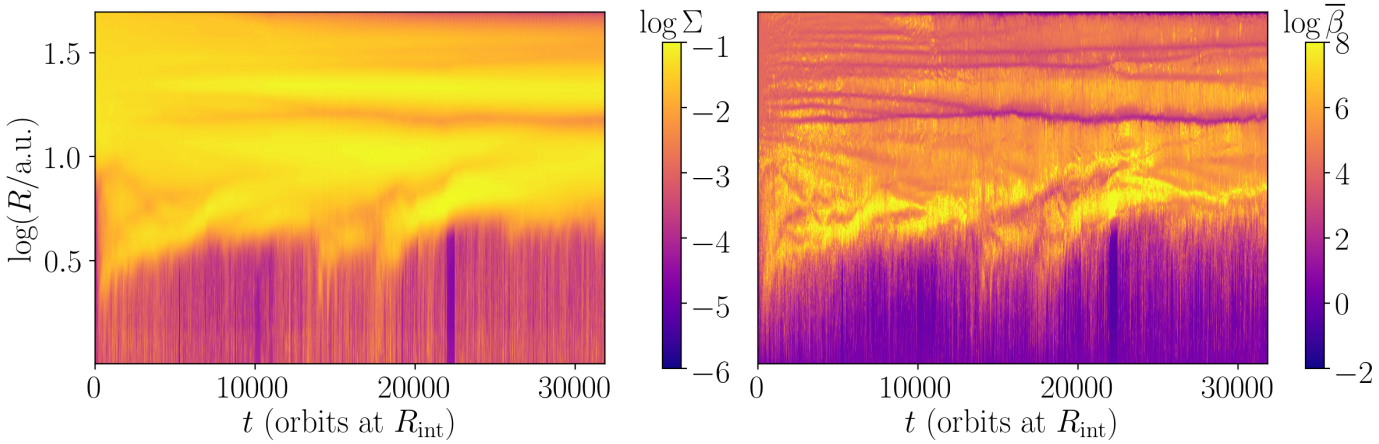

Fig. 19. $\Sigma(R, t)$ and $\overline{\beta}(R, t)$ of B4Bin0Am1. The cavity stands throughout the simulation, though its edge falls down to $R \approx 2$ au during the transient, before broadening up to $R \approx 4$ au in a few thousands of orbits at $R_{\rm int}$. The profile of $\overline{\beta}$ is characterised by the presence of gaps in the external disc.

4. Parameter space exploration

4.1. Ambipolar Diffusion

We checked the influence of $\Lambda_{\rm A,0}$ in the simulation B4Bin0Am1. This simulation is the same as the fiducial one, except for the initial value of $\Lambda_{\rm A,}$ which is set to 10.

4.1.1. General structure of the disc and gaps

The spatio-temporal evolution of Σ and β are shown in Fig. 19 for $\Lambda_{\rm A} = 10$. During the transient state, the cavity edge falls down to $R \lesssim 2$ au before expanding back up to $R \gtrsim 4$ au in a few thousands of orbits at $R_{\rm int}$. Overall, the transient state lasts for a shorter period of time than in the fiducial run, and the cavity extension is smaller.

We observe the apparition of gaps in both the profiles of Σ and $\overline{\beta}$ (Fig. 19) located in the external disc and broadening with time. Such structures are observed in numerous occasions in protoplanetary discs simulations either with ideal (Jacquemin-Ide et al. 2021) or non-ideal MHD (Béthune et al. 2017; Suriano et al. 2019; Riols et al. 2020; Cui & Bai 2021). We observe that gaps are associated with low β regions and are localised relatively far from the disc's inner boundary. Some gaps merge with one another, meaning that only three of them remain after 15 000 orbits at $R_{\rm int}$, similarly to what was found by Cui & Bai (2021). We reserve the study of the interaction between these gaps and the cavity for a future paper.

Figure 20 shows the flow and field topology for $\Lambda_{\rm A} = 10$ as well as the time-averaged magnetic structure of the disc. The main features of the fiducial simulation are recovered, namely the elbow-shaped structure and the associated magnetic loop. These are, however, located closer to the star, the cavity radius being smaller in this simulation.

In contrast to the fiducial simulation, the outer disc is this time top down asymmetric, which has an impact on the shape of the elbow above and below the disc plane. The elbow is prominent above the disc but almost disappears below it, except for a small set of streamlines close to the cavity. The magnetic field lines exhibit a local slanted symmetry in the external disc at the gaps location. This is similar to the topology observed in ambipolar-dominated discs (Riols & Lesur 2018, 2019). The gaps seem to be characterised by small vortices in the (r, θ) plane, located at the disc surface at the corresponding radii, indicating a meridional circulation.

4.1.2. Transport coefficients and wind invariants

The accretion rate remains constant in the whole disc with a value close to $1.2 \times 10^{-7}\, M_\odot\, {\rm yr}^{-1}$ and an accretion velocity that is still subsonic in the outer disc and peaks up to $2\, c_{\rm s}$ at the internal radius. Therefore, the accretion picture is identical to the one for the fiducial run with an internal transsonic regime connecting through the cavity edge to a weakly magnetised wind.

Regarding the wind, we obtain a highly mass-loaded field line in the external disc that removes little angular momentum ($\lambda_{\rm ext} = 1.5$ and $\kappa_{\rm ext} = 5.0$) and a lighter one in the internal disc that carries a massive load of angular momentum ($\lambda_{\rm in} = 4.9$ and $\kappa_{\rm in} = 0.24$). We note that the disc wind is overall less magnetised and more massive, while the general picture of the fiducial run remains. The rotational invariant contrast is higher than in the fiducial simulation, its internal value being three times lower and the external one three times higher.

4.2. Influence of the initial plasma parameter

We studied the impact of the plasma parameter by varying both its internal $\beta_{\rm in}$ and external $\beta_{\rm out}$ initial value.

4.2.1. Role of the external initial plasma parameter

We explored how the outer disc magnetisation impacts the general properties of the system. We varied the initial value of β between $\beta_{\rm out} = 10^3$ (run B3Bin0Am0) and $\beta_{\rm out} = 10^5$ (run B5Bin0Am0).

With regard to B5Bin0Am0, the spatio-temporal evolutions of Σ and $\overline{\beta}$ are shown in the left panels of Fig. 21. Right at the beginning of the simulation, a burst of matter appears in the cavity, which is subsequently refilled. Its radius then remains fixed at ~4 au until other bursts happen at ~17 400 and ~27 000 orbits at $R_{\rm int}$. Such local events do not dramatically change the general properties of the disc, which is similar to the fiducial one overall.

The bursts of matter (at ~17 400 and ~27 000 orbits at $R_{\rm int}$, assuming the first one is due to the initial transient) give the illusion that some gas might be created inside the cavity, challenging

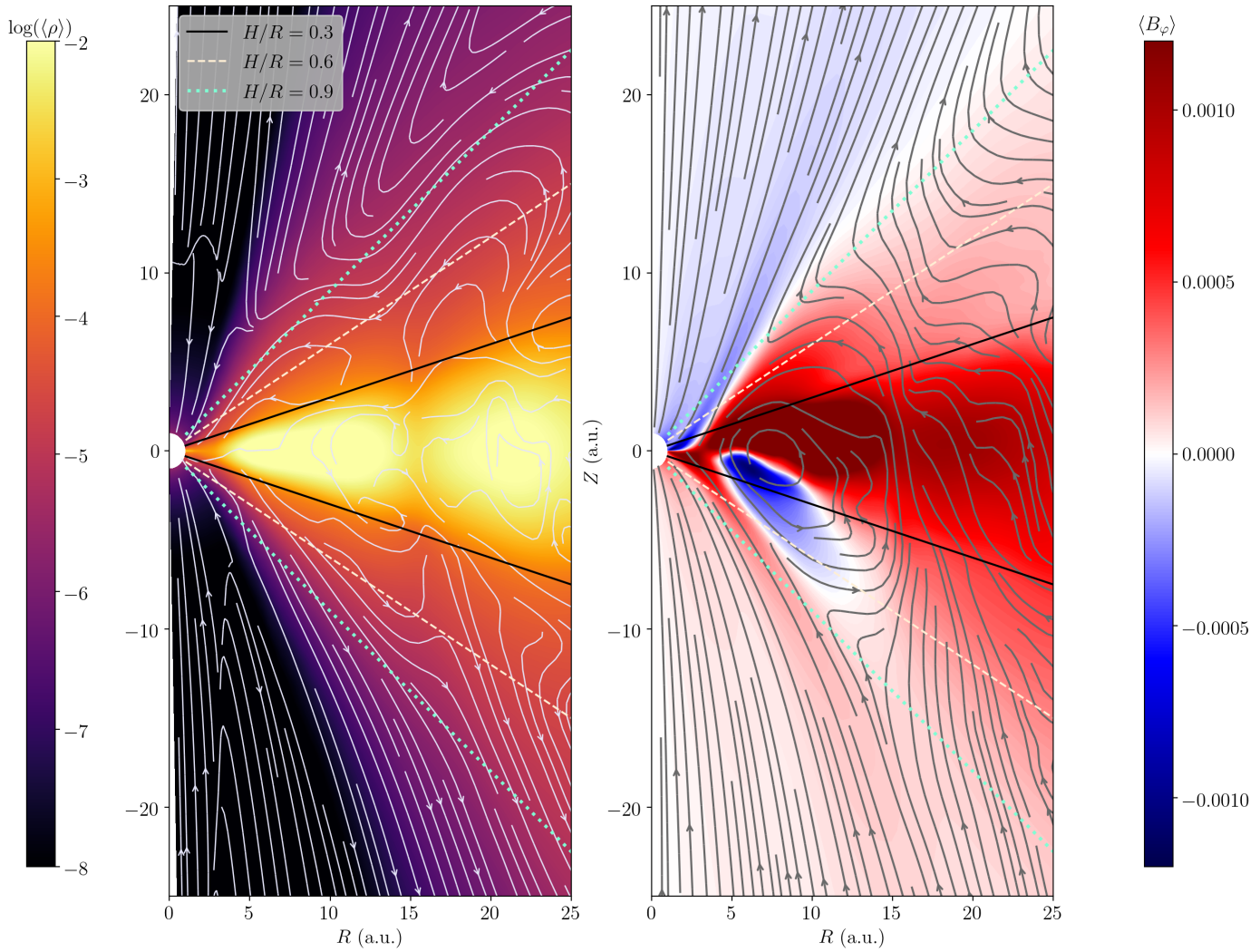

Fig. 20. Time-averaged structure of the disc for B4Bin0Am1. *Left panel*: poloidal streamlines and density. *Right panel*: magnetic structure of the disc with magnetic poloidal field lines and $\langle B_\varphi \rangle$.

mass conservation. These bursts are actually due to gas accumulating at the boundary of an accretion 'barrier'. We refer the reader to Appendix B for a more detailed description of these bursts. For now, we point out that these bursts highlight a limitation of our model regarding the implementation of the inner boundary conditions, but they only occur in the weakly magnetised ($\beta_{\rm out} = 10^5$) simulations. Lastly, we add that estimating $\dot{R}_0$ for this simulation is too difficult, since the cavity edge barely moves during the entire simulation.

In contrast to the run B5Bin0Am0, the cavity in the simulation B3Bin0Am0 quickly expands up to $R \approx 15$ au and keeps growing throughout the simulation, faster than in the fiducial run (see the right panels of Fig. 21). We estimate its velocity as $\dot{R}_0 \approx 3.0 \times 10^{-5}$ c.u., which is about three times faster than the fiducial run. We obtain $\delta\dot{M} \approx 2.3 \times 10^{-4}$ and $\delta\Sigma \approx 4.2 \times 10^{-2}$ (both in code units), so Eq. (38) gives $\dot{R}_0 \approx 4.2 \times 10^{-5}$ c.u., where we chose $R_0 \approx 20$. The simple model we used seems to overestimate the widening velocity of the cavity but still gives the correct order of magnitude.

The time-averaged surface density from the fiducial run, B3Bin0Am0, and B5Bin0Am0 are shown in Fig. 22, which demonstrates that the size of the cavity is ruled by the initial external plasma parameter. The lower $\beta_{\rm out}$ is, the wider the cavity gets when the disc reaches a steady state. On the contrary, the plasma parameter inside the cavity does not depend on its external structure and converges to $\beta_{\rm in} \lesssim 1$ in all of these simulations (Sect. 4.2.2 tackles this observation in depth). Once the transient state is gone, we note that the cavity expands faster for lower $\beta_{\rm out}$. This can be understood using Eq. (38), which can be recast as

$$\dot{R}_0 = v_{\rm acc.,\,in} \left(\frac{\Sigma_{\rm in}}{\Sigma_{\rm out}} - \frac{v_{\rm acc.,\,out}}{v_{\rm acc.,\,in}} \right), \tag{43}$$

where we defined the accretion velocities $v_{\rm acc.} \equiv \dot{M}/2\pi R_0 \Sigma$, and assumed $\Sigma_{\rm out} \gg \Sigma_{\rm in}$. The expansion speed is then controlled by the term in parenthesis, since the accretion velocity in the cavity is always sonic (see 4.2.2). It is well known that the accretion velocity in the outer 'standard' disc is a decreasing function of β. Writing $v_{\rm acc.} \propto \beta^{-\sigma}$ with $\sigma > 0$, Lesur (2021b) proposes $\sigma = 0.78$ and Bai & Stone (2013) $\sigma = 0.66$, which indicates that $0 < \sigma < 1$. Assuming that a value $\tilde{\beta}$ exists for which $\dot{R}_0 = 0$, we obtain the following scaling:

$$\dot{R}_0 = v_{\rm acc.,\,in} \frac{1}{\beta_{\rm out}} \left[1 - \left(\frac{\beta_{\rm out}}{\tilde{\beta}} \right)^{1-\sigma} \right], \tag{44}$$

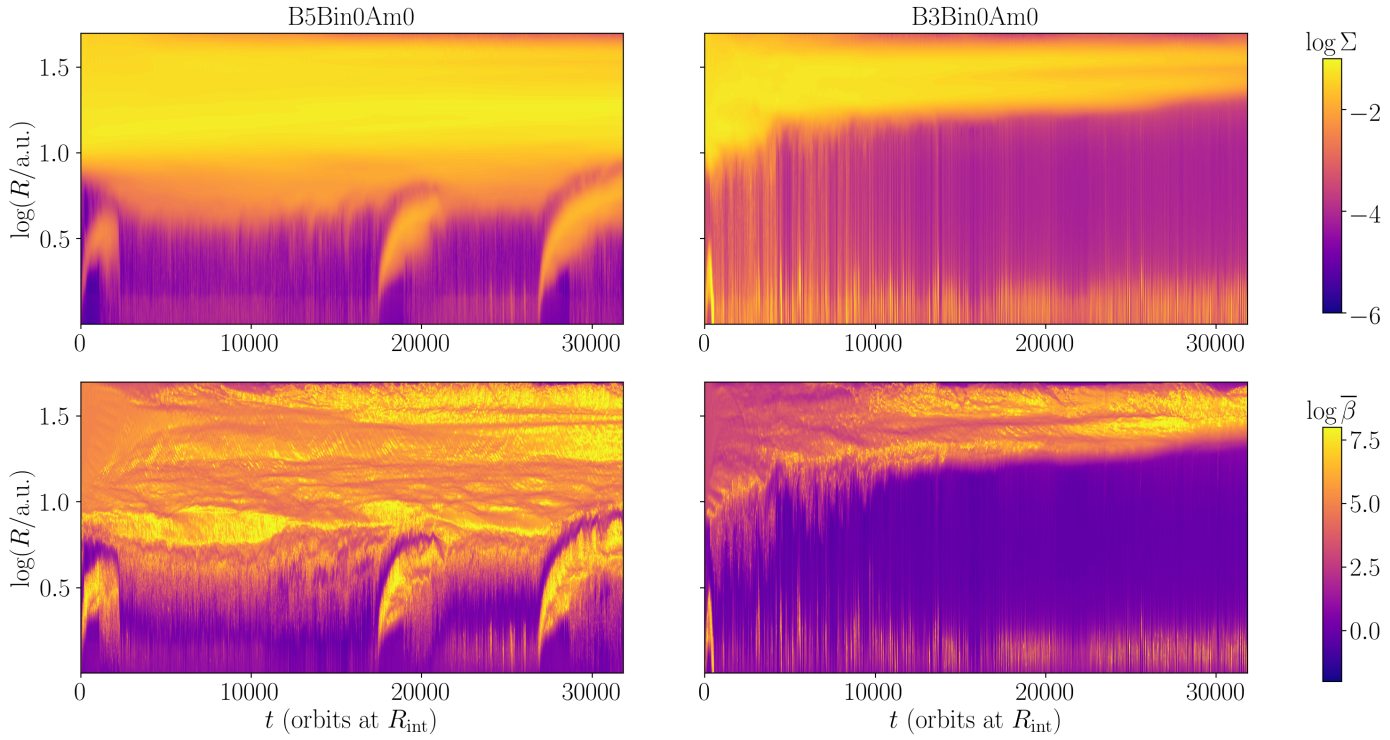

Fig. 21. Spatio-temporal diagrams for Σ and $\overline{\beta}$ for B5Bin0Am0 and B3Bin0Am0. The cavity expands more in B3Bin0Am0 but shrinks in B5Bin0Am0. Bursts of matter occur in B5Bin0Am0 (see main text for more explanations).

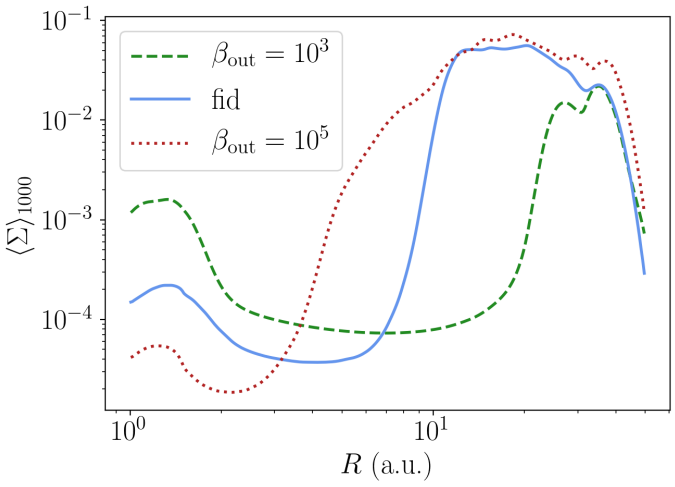

Fig. 22. Impact of initial external magnetisation on the surface density. We average the profile on the last 1000 orbits at $R_{\rm int}$. For B5Bin0Am0, we average on 1000 orbits at $R_{\rm int}$ occurring between the 2 burst events seen in Fig. 21.

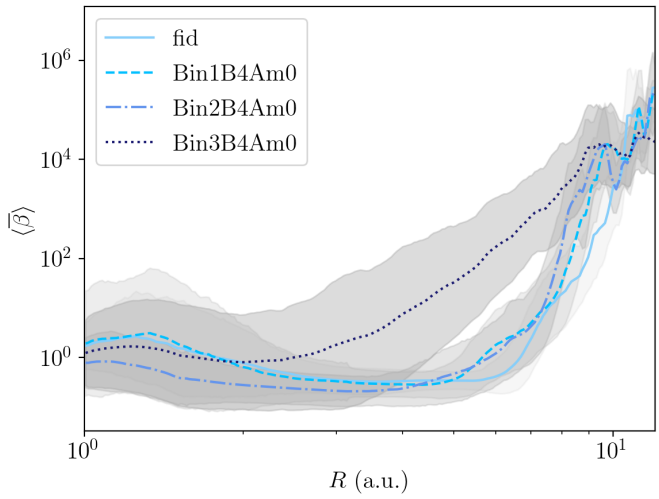

Fig. 23. Impact of internal initial magnetisation on the plasma parameter for $\beta_{\rm out} = 10^4$.

where we used the fact that $\Sigma_{\rm in}/\Sigma_{\rm out} = \beta_{\rm in}/\beta_{\rm out} = \beta_{\rm out}^{-1}$ in our setup. The relation (44) shows that for $\beta_{\rm out} \ll \tilde{\beta}$, we have approximately $\dot{R}_0 \approx v_{\rm acc.,in}\beta_{\rm out}^{-1}$, indicating that the cavity expansion speed should increase as $\beta_{\rm out}$ decreases, which is precisely what we observe for B3Bin0Am0. For $\beta_{\rm out} \gg \tilde{\beta}$, we obtain, on the contrary, $\dot{R}_0 \approx -v_{\rm acc.,in}\tilde{\beta}^{\sigma-1}\beta_{\rm out}^{-\sigma}$, showing a change of sign (hence a contraction of the cavity), albeit with a reduced speed. This regime might correspond to B5Bin0Am0, indicating that $\tilde{\beta} \simeq 10^4$.

4.2.2. Role of the internal initial plasma parameter

To study the impact of $\beta_{\rm in}$, we ran a set of simulations that cover all the possible initial gaps $\beta_{\rm in}/\beta_{\rm out}$ where $\log\beta_{\rm out} \in \{3, 4, 5\}$ and $\log\beta_{\rm in} \in [\![0; \log\beta_{\rm out}[\![$. We compared each result to the one obtained with $\beta_{\rm in} = 1$ and the corresponding value of $\beta_{\rm out}$. A striking result is the fact that the disc's inner structure does not depend on $\beta_{\rm in}$. No matter which $\beta_{\rm in}$ we initially choose, a transition occurs in the cavity in order to impose $\beta_{\rm in} \approx 1$. Interestingly, this threshold value is the one required to achieve transsonic accretion, which is mentioned in Wang & Goodman (2017). We illustrate this statement with Fig. 23 for the particular case of $\beta_{\rm out} = 10^4$. We focus on the transient state of B4Bin3Am0 in

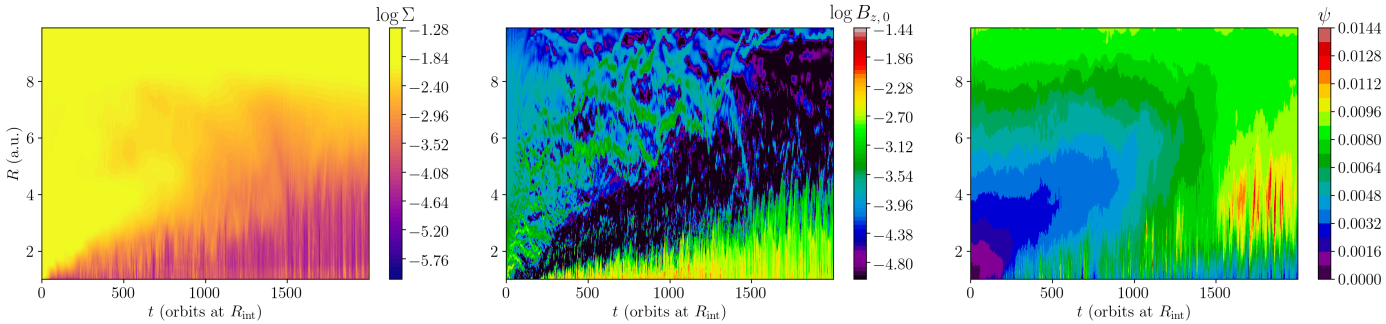

Fig. 24. Spatio-temporal diagrams of Σ (first panel), $B_{z,0}$, the vertical magnetic field at the midplane, and ψ, the flux function defined in Eq. (39). These profiles focus on the first orbits of the run B4Bin3Am0.

Fig. 24. The transition is due to matter leaving the cavity because of the fast accretion at stake after a sharp increase of the magnetic field (and therefore a decrease of β). This reorganisation of the cavity is a consequence of a rapid advection of magnetic flux from the cavity onto the seed, which initially has low magnetisation because of our initial setup. Due to the total magnetic flux conservation, there is a shortage of magnetic flux inside the cavity, up until the inner seed reaches a state where its magnetisation is almost constant. The magnetic field then accumulates at the inner boundary and β decreases accordingly so that accretion is enhanced. At this point, matter leaves the cavity as it is accreted onto the star. It is then clear that the cavity converges towards the same overall structure as the fiducial simulation one.

We note that taking $\beta_{\rm in}$ equal to $\beta_{\rm out}$ would simulate a full disc with no cavity. Hence, a threshold should exist regarding the value of $\beta_{\rm in}$, above which no cavity is able to form. Considering Fig. 23, it seems that this threshold is $\gtrsim 10^3$.

From these observations, we deduce that the cavity is regulated by the value of the plasma parameter, which must take a value close to 1. The reason for this regulation is not entirely clear, and we add a word of caution regarding the role of the inner radial boundary condition, especially with respect to the magnetic field transport at $R_{\rm int}$. We discuss this influence in Appendix B. Referring to Sects. 3.5.3 and 3.5.4, we suggest that the RTI may be responsible for this regulation, but a dedicated study would be required to ascertain this claim.

4.3. Zoom with a larger cavity radius

We performed a simulation with a double-sized cavity (R_0 = 20 au) in order to check the impact of the cavity size. The simulation was integrated for 1000 orbits at R = 10 au so that it reaches 355 orbits at R = 20 au The general observations are confirmed, such as the elbow-shaped structure, the magnetic loop, the magnetic field advection in the outer disc, as well as the conclusions regarding the accretion. While the cavity size is identical to B3Bin0Am0, the behaviour of the disc is exactly the same as the fiducial one (see Fig. 25), indicating that $\beta_{\rm out}$ is the main parameter regulating the cavity expansion. This means that the global picture where two types of discs are connected is robust and not linked to limitations in the cavity size or artefacts due to the inner boundary condition.

5. Discussion and comparison with previous work

We modelled TDs sustained by MHD winds by performing 2.5D global simulations. This model acts as a proof of concept, showing that steady-state discs with both a cavity and a wind can be obtained. The resulting simulated discs are characterised by two different zones with contrasted dynamics.

First, our 'outer disc' behaves like a standard, weakly magnetised, ambipolar-dominated protoplanetary disc (Lesur 2021b; Cui & Bai 2021). In particular, we find mass and angular-momentum transport coefficients, wind properties, and accretion rates comparable to those found in the literature for 'full' discs. We also find weak gaps, which are characteristic of non-ideal MHD discs (Riols & Lesur 2019; Riols et al. 2020). However, the magnetic field transport in the outer disc differs from previous studies: we find that magnetic field lines are advected inwards in the outer disc, in contrast to measurements in full discs which always show outwards transport (Bai & Stone 2017; Gressel et al. 2020; Lesur 2021b). This discrepancy is likely due to the fact that the field lines in the cavity are more collimated (i.e. less opened), which results in a lower pressure on the magnetic surfaces in the outer disc, but it is possibly also connected to the peculiar elbow-shaped magnetic surfaces at the transition radius. In any case, it points to the fact that magnetic field transport is a non-local phenomenon: it depends on the global disc structure.

In contrast to the outer disc, the cavity (or inner disc) is strongly magnetised ($\beta \approx 1$) because of its low surface density. We emphasise here that the absolute magnetic field strength in the cavity is not stronger than standard protoplanetary disc models. In practice, and given our set of units, we have $B_0 \approx 0.13$ G (see Eq. (17), with $\beta_{\rm out} = 10^4$), so, initially, $B_z \approx 1.25$ mG at R = 42 au in our simulations, which is of the same order of magnitude as the upper limit of $B_z(R = 42\ {\rm au}) = 0.8$ mG found in Vlemmings et al. (2019), for example. Hence, while the cavity is strongly magnetised, its field strength is compatible with observational constraints.

Compared to the outer disc, the mass and angular-momentum transport coefficients in the cavity are all of the order of unity, resulting in transsonic accretion velocities and faster wind with large lever arms ($\lambda \gtrsim 10$). Overall, this picture quantitatively matches the inner jet-emitting disc proposed by Combet & Ferreira (2008). Interestingly, in all of our models, the cavity manages to reach an accretion rate close to the outer disc one by self-regulating the magnetic stresses. We find that most of the angular-momentum transport is due to the laminar stress (Appendix D) indicating that turbulent transport (possibly MRI-driven) is unimportant in the cavity. This is not surprising since our discs are dominated by ambipolar diffusion, which mostly suppresses MRI turbulence (Bai 2011).

We find a significant deviation of the rotation profile in the cavity as a result of the strong magnetic stress due to the wind and typical rotation velocities of the order of 70–80% of the Keplerian velocity. This fact, combined with the transsonic

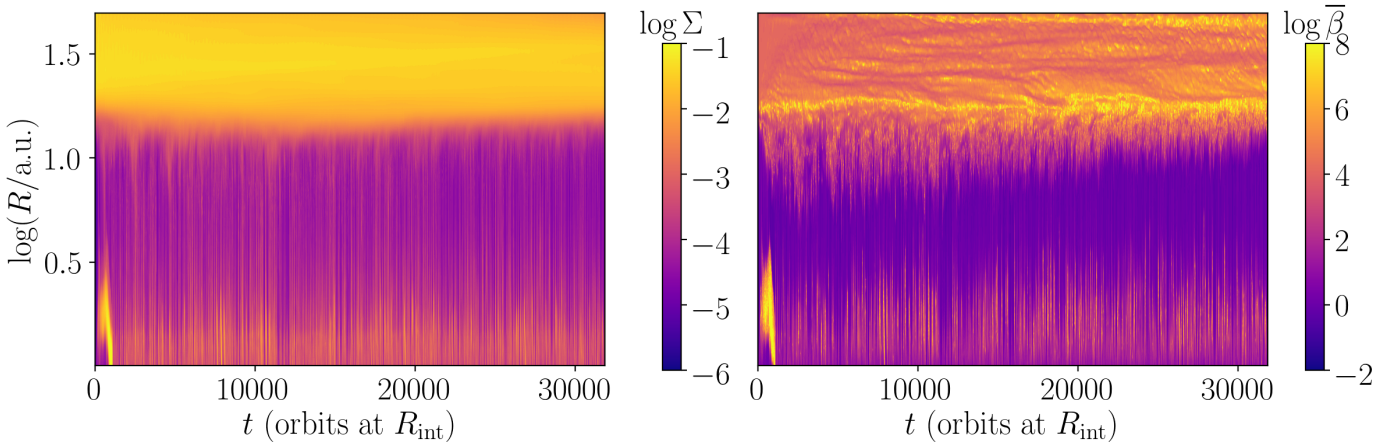

Fig. 25. Spatio-temporal diagrams for $\langle\Sigma\rangle$ and $\langle\beta\rangle$ for R20FID.

accretion, implies that the kinematics of these cavities have singular observational signatures. Fast accretion kinematics have been observed in some TDs (Rosenfeld et al. 2014), but we note that these signatures might also be due to a warped circumbinary disc (Casassus et al. 2015).

As a result of the stress balance mentioned above, we obtain accreting cavities that survive thousands of orbits and that are slowly expanding or contracting, depending on the outer-disc magnetisation. This result suggests that a cavity could be carved spontaneously if the magnetisation of the outer disc is high enough. There are already hints of such a process in global simulations; for instance, Cui & Bai (2021) show a gas-depleted cavity forming in the inner profile of Σ (see their Fig. 5, first row and first column panel). While this is by no means proof, since the boundary conditions are probably unrealistic, it shows that the secular evolution of wind-driven discs should be investigated systematically to check whether or not cavities could spontaneously form in these models.

The temporal analysis of the disc reveals the appearance of dynamical structures. In particular, we highlight the formation of gas filaments above the disc surface that end up forming two bubbles of gas each, one being ejected, while the other one falls down onto the cavity before crossing it. At some point, the falling matter has to cross the poloidal magnetic field lines at the magnetic field loop location, resembling, to some extent, the magnetospheric accretion observed in young stars (Bouvier et al. 2007, 2020b,a; Pouilly et al. 2020) and magnetospheric ejection events (Zanni & Ferreira 2013; Čemeljić et al. 2013). However, there is no magnetosphere in our simulations, so the magnetic topology is quite different from that of magnetospheric interaction.

By analogy with magnetospheric accretion, we checked whether the time variability seen in our simulations could be due to a magnetic RTI. We have studied two criteria for the RTI, in the form of a radial interchange of poloidal field lines (see Sect. 3.5.4 and Appendix C). We found, however, that the RTI requires magnetisations stronger than the ones found in our simulations, ruling out the RTI in the form we have assumed. It is, however, still possible that another branch of this instability is present. It is also possible that the non-axisymmetric version of the RTI could be triggered in 3D simulations. We therefore defer this study to a future publication.

On longer timescales, averaging out the fast variability, the magnetic field strength appears to be self-regulated with $0.1 \lesssim \beta \lesssim 1$ in the cavity, independently of the initial field strength. As a result, the cavity is strongly magnetised and rotates at sub-Keplerian velocities, indicating a substantial magnetic support against gravity in this region. In essence, the regime of our cavity is similar to the magnetically arrested disc (MAD) proposed by Narayan et al. (2003) in the context of black hole accretion discs. McKinney et al. (2012) showed that MADs could be regulated by magnetic RTI, leading to magnetically chocked accretion flows (MCAF). The MAD model is also associated with the formation of plasmoids by reconnection events (Ripperda et al. 2022). These features are recovered in our models of TDs, despite the fact that we used Newtonian dynamics (MADs are usually found in GRMHD simulations) and the presence of a strong ambipolar diffusivity in our models. Hence, our models could be interpreted as non-ideal, non-relativistic models of MADs.

The time variability of the cavity is likely to be related to the axisymmetric approximation used in this work since it suppresses non-axisymmetric instabilities, which seem to play a key role in MADs simulations (e.g. McKinney et al. 2012; Liska et al. 2022). Additionally, we note that the question of non-axisymmetric hydrodynamical instabilities such as the Rossby wave instability (RWI) (Lovelace et al. 1999; Li et al. 2000) at the cavity edge is still open to debate in a magnetised environment (Bajer & Mizerski 2013). We will address these points using full 3D simulations in a follow-up paper.

Regarding the caveats of our simulations, we remark that the inner radial boundary is probably the most stringent caveat of our numerical model. In particular, we found that this inner boundary condition sometimes expels some poloidal magnetic flux, resulting in the bursts seen in Fig. 21. However, the weakly magnetised simulations (such as B5Bin0Am0) are the only ones exhibiting these events, and once the transient state is over, all the simulations reach comparable steady states. So, the inner boundary condition is likely not affecting the long-term evolution of our models. Future models should nevertheless try to include either an inner turbulent disc, or possibly the magnetospheric interaction with the central star.

A possible limitation of our model concerns the role of the MRI. Our simulated discs are dominated by ambipolar diffusion, and as such, subject to MRI quenching by the non-linearity embedded in the ambipolar diffusivity ($\eta \propto B^2$). This saturation is different from the saturation by 3D turbulence observed in the ideal MHD regime. It is suggested that the MRI saturates in very similar ways in 3D and 2D under strong ambipolar diffusion (see e.g. Béthune et al. 2017; Cui & Bai 2021). This is also confirmed

by our own 3D simulations, which will be published in a forthcoming paper. Hence, the fact that our simulations are 2.5D has a very limited impact on the turbulent transport one may observe.

We note that our simulations used a simplified treatment of thermodynamics and ionisation chemistry. More numerically involved models, such as that of Wang & Goodman (2017), use a refined computation of the ionisation fraction and Λ_A inside the cavity of a TD, including several chemical species. This work highlights, in particular, the influence of the X-ray luminosity of the star L_X (see their Fig. 2, panels 2 and 3) as well as the role of the temperature T_0 at 16 au (Fig. 2, panels 6 and 7). Regarding our profile of $\Lambda_A \approx 1$–10, our work is similar to their models 2 (with $L_X = 10^{29}$ erg s^{-1}) and 6 (where $T_0 = 30$ K). Therefore, we anticipate that an increase of two orders of magnitude for L_X would lead to $\Lambda_A > 10^2$ in most of our cavity. Such a change would greatly alter the dynamical regime of the cavity since MRI would then play a significant role see Appendix A and Blaes & Balbus (1994) and Bai (2011). However, the role of the temperature is less straightforward and seems to have little impact on Λ_A.

Additionally, dust plays a significant role in the work of Wang & Goodman (2017) regarding the ionisation of the disc. As a matter of fact, only their models with dust reach low values of Λ_A. The effect of dust in TDs is a major subject that is not addressed in our work. Dust can modify the ionisation fraction but also create peculiar structures at the interface between the disc and cavity. We mention in particular the interplay between dust and the radiation pressure, which is known to create non-axisymmetric structures at the cavity edge (Bi & Fung 2022) or an inner rim with an accumulation of matter due to photophoresis (Cuello et al. 2016).

6. Conclusions

We performed 2.5D global numerical simulations of TDs in the context of non-ideal MHD with MHD wind launching. Our simulation design is initialised with a cavity in the gas surface density profile, and a power-law distribution for the vertical magnetic field strength, resulting in a strongly magnetised cavity surrounded by a standard weakly magnetised disc.

The main results are summarised in the following points:

1. We modelled strongly accreting TDs that reach a quasi-steady state that lasts for at least thousands of years. The accretion rate inside the cavity connects smoothly to the accretion rate in the external part of the disc;
2. The cavity itself is characterised by a strong sub-Keplerian rotation and a transsonic accretion velocity. These kinematic signatures could potentially be verified observationally;
3. The magnetic field is advected inwards in the outer disc, in contrast to full disc simulations. This points to the possible non-locality of large-scale field transport;
4. The cavity structure (density and field strength) is self-regulated. In particular, it is insensitive to a change in the initial internal magnetisation and is characterised by $0.1 \lesssim \beta_{\rm int} \lesssim 1$;
5. The temporal analysis of the cavity dynamics highlights the formation and accretion of bubbles of gas above the disc which cross the cavity at sonic speeds. The magnetic Rayleigh–Taylor instability might be responsible for this unsteadiness;
6. The physics of the cavity (accretion speed, wind lever arm, and mass loading) match previously published jet-emitting disc solutions (Ferreira 1997; Combet & Ferreira 2008). The presence of a strong radial magnetic support and possible regulation by the RTI is also reminiscent of MADs in black hole physics (Narayan et al. 2003; McKinney et al. 2012). These resemblances suggest that TDs could be an instance of MADs applied to protoplanetary discs.

Transition discs with strong accretion rates and arbitrarily large cavities can be achieved by magnetic winds emitted from the cavity. This model is promising and should be tested with observations.

Acknowledgements. The authors would like to thank the anonymous referee for constructive comments that have greatly improved the quality of this work. They wish to thank Jonatan Jacquemin-Ide, Andrés Carmona, Antoine Riols, Ileyk El Mellah and Jonathan Ferreira for fruitful discussions and comments. This work is supported by the European Research Council (ERC) European Union Horizon 2020 research and innovation programme (Grant agreement no. 815559 (MHDiscs)). This work was granted access to the HPC resources of TGCC under the allocation 2021-A0100402231 made by GENCI. A part of the computations presented in this paper were performed using the GRICAD infrastructure (`https://gricad.univ-grenoble-alpes.fr`), which is supported by Grenoble research communities. This work makes use of matplotlib (Hunter 2007) for graphics, NumPy (Harris et al. 2020), SciPy (Virtanen et al. 2020) and Pickle (Van Rossum 2020). This article has been typeset from a TEX/ LATEX file prepared by the authors.

References

Alexander, R., Pascucci, I., Andrews, S., Armitage, P., & Cieza, L. 2014, in Protostars and Planets VI, eds. H. Beuther, R. S. Klessen, C. P. Dullemond, & T. Henning, 475
Bai, X.-N. 2011, ApJ, 739, 50
Bai, X.-N., & Goodman, J. 2009, ApJ, 701, 737
Bai, X.-N., & Stone, J. M. 2013, ApJ, 769, 76
Bai, X.-N., & Stone, J. M. 2017, ApJ, 836, 46
Bajer, K., & Mizerski, K. 2013, Phys. Rev. Lett., 110, 104503
Balbus, S. A., & Hawley, J. F. 1991, ApJ, 376, 214
Béthune, W., Lesur, G., & Ferreira, J. 2017, A&A, 600, A75
Bi, J., & Fung, J. 2022, ApJ, 928, 74
Blaes, O. M., & Balbus, S. A. 1994, ApJ, 421, 163
Blandford, R. D., & Payne, D. G. 1982, MNRAS, 199, 883
Bouvier, J., Alencar, S. H. P., Boutelier, T., et al. 2007, A&A, 463, 1017
Bouvier, J., Alecian, E., Alencar, S. H. P., et al. 2020a, A&A, 643, A99
Bouvier, J., Perraut, K., Bouquin, J.-B. L., et al. 2020b, A&A, 636, A108
Carmona, A., Pinte, C., Thi, W. F., et al. 2014, A&A, 567, A51
Carmona, A., Thi, W. F., Kamp, I., et al. 2017, A&A, 598, A118
Casassus, S., Marino, S., Pérez, S., et al. 2015, ApJ, 811, 92
Čemeljić, M., Shang, H., & Chiang, T.-Y. 2013, ApJ, 768, 5
Clarke, C. J., Gendrin, A., & Sotomayor, M. 2001, MNRAS, 328, 485
Combet, C., & Ferreira, J. 2008, A&A, 479, 481
Combet, C., Ferreira, J., & Casse, F. 2010, A&A, 519, A108
Cuello, N., Gonzalez, J.-F., & Pignatale, F. C. 2016, MNRAS, 458, 2140
Cui, C., & Bai, X.-N. 2021, MNRAS, 507, 1106
Dong, R., & Dawson, R. 2016, ApJ, 825, 77
Dullemond, C. P., & Dominik, C. 2005, A&A, 434, 971
Espaillat, C., Muzerolle, J., Najita, J., et al. 2014, in Protostars and Planets VI, eds. H. Beuther, R. S. Klessen, C. P. Dullemond, & T. Henning, 497
Evans, C. R., & Hawley, J. F. 1988, ApJ, 332, 659
Fang, M., Kim, J. S., van Boekel, R., et al. 2013, ApJS, 207, 5
Ferreira, J. 1997, A&A, 319, 340
Fromang, S., Terquem, C., & Balbus, S. A. 2002, MNRAS, 329, 18
Gammie, C. F. 1996, ApJ, 457, 355
Gárate, M., Delage, T. N., Stadler, J., et al. 2021, A&A, 655, A18
Gressel, O., Ramsey, J. P., Brinch, C., et al. 2020, ApJ, 896, 126
Guilet, J., & Ogilvie, G. 2014, MNRAS, 441, 852
Harris, C. R., Millman, K. J., van der Walt, S. J., et al. 2020, Nature, 585, 357
Hunter, J. D. 2007, Comput. Sci. Eng., 9, 90
Igea, J., & Glassgold, A. E. 1999, ApJ, 518, 848
Jacquemin-Ide, J., Lesur, G., & Ferreira, J. 2021, A&A, 647, A192
Kane, Y., 1966, IEEE Trans. Antennas Propag., 14, 302
Lesur, G. R. J. 2021a, J. Plasma Phys., 87, 205870101
Lesur, G. R. J. 2021b, A&A, 650, A35
Lesur, G., Kunz, M. W., & Fromang, S. 2014, A&A, 566, A56
Li, H., Finn, J. M., Lovelace, R. V. E., & Colgate, S. A. 2000, ApJ, 533, 1023
Liska, M. T. P., Musoke, G., Tchekhovskoy, A., Porth, O., & Beloborodov, A. M. 2022, ApJl, 935, L1

Lovelace, R. V. E., Li, H., Colgate, S. A., & Nelson, A. F. 1999, ApJ, 513, 805
Manara, C. F., Testi, L., Natta, A., et al. 2014, A&A, 568, A18
Marsh, K. A., & Mahoney, M. J. 1992, ApJ, 395, L115
McKinney, J. C., Tchekhovskoy, A., & Blandford, R. D. 2012, MNRAS, 423, 3083
Mignone, A., Bodo, G., Massaglia, S., et al. 2007, ApJS, 170, 228
Mishra, B., Begelman, M. C., Armitage, P. J., & Simon, J. B. 2020, MNRAS, 492, 1855
Morishima, R. 2012, MNRAS, 420, 2851
Najita, J. R., Strom, S. E., & Muzerolle, J. 2007, MNRAS, 378, 369
Narayan, R., Igumenshchev, I. V., & Abramowicz, M. A. 2003, PASJ, 55, L69
Nelson, R. P., Gressel, O., & Umurhan, O. M. 2013, MNRAS, 435, 2610
Perez-Becker, D., & Chiang, E. 2011, ApJ, 735, 8
Pouilly, K., Bouvier, J., Alecian, E., et al. 2020, A&A, 642, A99
Riols, A., & Lesur, G. 2018, A&A, 617, A117
Riols, A., & Lesur, G. 2019, A&A, 625, A108
Riols, A., Lesur, G., & Menard, F. 2020, A&A, 639, A95
Ripperda, B., Liska, M., Chatterjee, K., et al. 2022, ApJ, 924, L32
Rosenfeld, K. A., Chiang, E., & Andrews, S. M. 2014, ApJ, 782, 62
Shakura, N. I., & Sunyaev, R. A. 1973, A&A, 24, 337
Simon, J. B., Bai, X.-N., Stone, J. M., Armitage, P. J., & Beckwith, K. 2013, ApJ, 764, 66
Simon, J. B., Lesur, G., Kunz, M. W., & Armitage, P. J. 2015, MNRAS, 454, 1117
Spruit, H. C., & Taam, R. E. 1990, A&A, 229, 475
Spruit, H. C., Stehle, R., & Papaloizou, J. C. B. 1995, MNRAS, 275, 1223
Stehle, R., & Spruit, H. C. 2001, MNRAS, 323, 587
Suriano, S. S., Li, Z.-Y., Krasnopolsky, R., Suzuki, T. K., & Shang, H. 2019, MNRAS, 484, 107
Suzuki, T. K., Ogihara, M., Morbidelli, A., Crida, A., & Guillot, T. 2016, A&A, 596, A74
Thi, W. F., Lesur, G., Woitke, P., et al. 2019, A&A, 632, A44
Umebayashi, T., & Nakano, T. 1980, PASJ, 32, 405
Umebayashi, T., & Nakano, T. 2008, ApJ, 690, 69
van der Marel, N., van Dishoeck, E. F., Bruderer, S., Pérez, L., & Isella, A. 2015, A&A, 579, A106
van der Marel, N., van Dishoeck, E. F., Bruderer, S., et al. 2016, A&A, 585, A58
Van Rossum, G. 2020, The Python Library Reference, release 3.8.2 (Python Software Foundation)
Virtanen, P., Gommers, R., Oliphant, T. E., et al. 2020, Nature Methods, 17, 261
Vlemmings, W. H. T., Lankhaar, B., Cazzoletti, P., et al. 2019, A&A, 624, A7
Wang, L., & Goodman, J. J. 2017, ApJ, 835, 59
Wardle, M. 2007, Astrophys. Space Sci., 311, 35
Wardle, M., & Koenigl, A. 1993, ApJ, 410, 218
Zanni, C., & Ferreira, J. 2013, A&A, 550, A99
Zhang, K., Isella, A., Carpenter, J. M., & Blake, G. A. 2014, ApJ, 791, 42
Zhu, Z., & Stone, J. M. 2018, ApJ, 857, 34
Zhu, Z., Nelson, R. P., Hartmann, L., Espaillat, C., & Calvet, N. 2011, ApJ, 729, 47

Appendix A: Ambipolar diffusivity for a transition disc - a simple model

The aim of this appendix is to model the ambipolar diffusivity spatial dependence in both a TD and a standard protoplanetary disc (i.e. without cavity). The general procedure to reach such a result follows and adapts the main calculation steps that are presented in Combet et al. (2010). As assumed in Eq. 4, only the ambipolar diffusivity does appear in the MHD equations, which we assume is the dominant non-ideal effect in the regime of discs we used at $R \geq 10$ (Riols et al. 2020; Simon et al. 2015). Therefore, the only momentum exchange that occurs between particles happens exclusively between ions and neutrals. In a plasma made of molecular ions, electrons and neutrals, the ambipolar diffusivity is given by

$$\eta_{\rm A} = \frac{\boldsymbol{B}^2}{4\pi\,\gamma_{\rm in}\,\rho_{\rm n}\,\rho_{\rm i}} \tag{A.1}$$

(Wardle 2007), where $\rho_{\rm n}$ and $\rho_{\rm i}$ are, respectively, the density of the neutrals (the gas so $\rho_{\rm n} = \rho$) and of the ions and $\gamma_{\rm in} = \langle\sigma v\rangle_{\rm in}/(m_{\rm n} + m_{\rm i})$ with $\langle\sigma v\rangle_{\rm in}$ is the ion-neutral collision rate whose value is

$$\langle\sigma v\rangle_{\rm in} = 2{,}0 \times 10^{-9} \left(\frac{m_{\rm H}}{\mu}\right)^{1/2} {\rm cm^3 s^{-1}} \tag{A.2}$$

(Bai 2011), with $m_{\rm H}$ being the atomic mass and $\mu = 2{,}34\,m_{\rm H}$ the mean molecular weight. Introducing the ionisation fraction $\xi = \rho_{\rm i}/\rho_{\rm n}$, one obtains

$$\eta_{\rm A} = 1{,}6{\times}10^{16} \left(\frac{\xi}{1\times10^{-13}}\right)^{-1} \left(\frac{\boldsymbol{B}}{1\,{\rm G}}\right)^{2} \left(\frac{\rho}{1\times10^{14}\,{\rm cm^{-1}}}\right)^{-2} {\rm cm^2 s^{-1}}. \tag{A.3}$$

Ambipolar diffusion is usually evaluated with the dimensionless ambipolar Elsasser number $\Lambda_{\rm A}$ defined in Eq. 13. To obtain this number, we have to evaluate the ionisation fraction. Let us consider a simple chemical lattice with no metals nor grains:

$$\mathrm{m} + \text{ionising radiation} \longrightarrow \mathrm{m^+} + \mathrm{e^-} \qquad \zeta_{\rm i}, \tag{A.4}$$

$$\mathrm{m^+} + \mathrm{e^-} \longrightarrow \mathrm{m} \qquad \delta, \tag{A.5}$$

with $\zeta_{\rm i}$ being the ionisation rate and δ the dissociative recombination rate. Following Fromang et al. (2002), we take

$$\delta = 3\times10^{-6}\,T^{-1/2}\,{\rm cm^3 s^{-1}}. \tag{A.6}$$

In this toy model, we then have

$$\xi = \sqrt{\frac{\zeta_{\rm i}}{\delta\,\rho}} + \xi_{\rm FUV} \tag{A.7}$$

(Lesur et al. 2014), where $\xi_{\rm FUV}$ accounts for the far-UV photon contribution that we modelled following Perez-Becker & Chiang (2011) as

$$\xi_{\rm FUV} = 2\times10^{-5}\,\exp\left[-\left(\Sigma_\star/0{,}03\,{\rm g\,cm^{-2}}\right)^4\right], \tag{A.8}$$

with $\Sigma_\star$ the column density computed from the star to the point of interest.

To calculate $\zeta_{\rm i}$, we considered several ionisation sources. We modelled the X-ray ionisation from the protostar by two bremsstrahlung-emitting corona (following Bai & Goodman 2009 and Igea & Glassgold 1999):

$$\zeta_{\rm X} = L_{\rm X,29}\left(\frac{R}{1\,{\rm au}}\right)^{-2,2}\left[\zeta_1\left(e^{-(N_{\rm H1}/N_1)^\alpha} + e^{-(N_{\rm H2}/N_1)^\alpha}\right) + \zeta_2\left(e^{-(N_{\rm H1}/N_2)^\beta} + e^{-(N_{\rm H2}/N_2)^\beta}\right)\right], \tag{A.9}$$

with $L_{\rm X,29} \equiv L_{\rm X}/10^{29}{\rm erg\,s^{-1}}$ and $L_{\rm X}$, ζ_1, ζ_2, α, β, N_1, N_2 being the numerical values defined in Bai & Goodman (2009), while $N_{\rm H1}$ and $N_{\rm H2}$ are the column densities of hydrogen vertically computed above and below the calculation point.

We modelled the cosmic-ray ionisation rate following Umebayashi & Nakano (1980) so that:

$$\zeta_{\rm CR} = \zeta_{\rm CR,0}\,e^{-\Sigma_{\rm col.}/96\,{\rm g\,cm^{-2}}}\,{\rm s^{-1}}, \tag{A.10}$$

where $\zeta_{\rm CR,0} = 10^{-17}\,{\rm s^{-1}}$ and $\Sigma_{\rm col.}$ is the matter column density above and below the point of interest.

Lastly, we added the radioactive decay that is assumed constant (Umebayashi & Nakano 2008) with a ionisation rate given by

$$\zeta_{\rm rad.} = 10^{-19}\,{\rm s^{-1}}. \tag{A.11}$$

Combining the Eqs. A.9, A.10, and A.11, we obtain $\zeta_{\rm i} = \zeta_{\rm X} + \zeta_{\rm CR} + \zeta_{\rm rad.}$, paving the way to finally reach $\Lambda_{\rm A}$ using Eqs. 13, A.6, and A.7. We note that due to the dependency of $\eta_{\rm A}$ and $v_{\rm A}$ on the norm of the magnetic field, this latter is cancelled out and does not need to be computed to obtain $\Lambda_{\rm A}$. The previous calculations can be performed either for a standard protoplanetary disc or for a TD. The only thing that needs to be changed to account for such discs is the surface density profile, where Eq. 18 allows us to consider (or not) the effects of the cavity.

The results of such calculations are displayed in Fig. A.1, which represents the spatial dependency of $\Lambda_{\rm A}$ in both a standard protoplanetary disc and a TD. Though these two profiles look different at first glance, a deeper investigation reveals that the values taken by $\Lambda_{\rm A}$ in the discs remain quite close to unity in both cases, while the general trend of $\Lambda_{\rm A}$ in a standard protoplanetary disc is recovered even in the case of a TD (Thi et al. 2019).

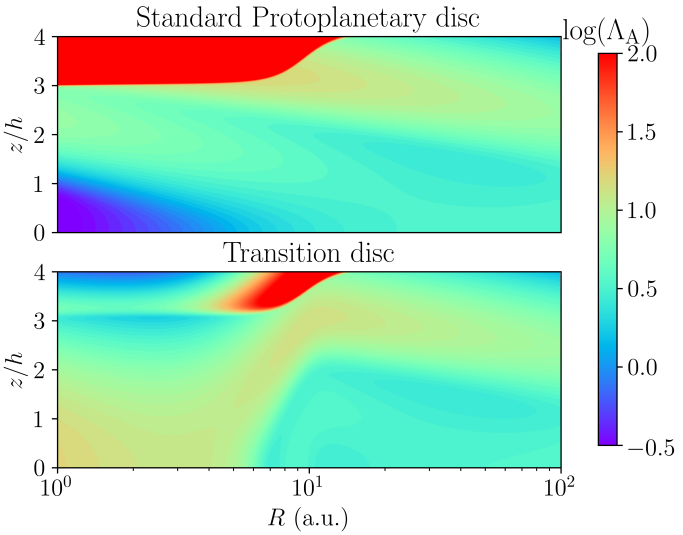

Fig. A.1. Ambipolar Elsasser number $\Lambda_{\rm A}$ in a standard protoplanetary disc (top panel) and in a TD (bottom panel). In spite of these 2 profiles being slightly different, no major changes occur from one kind of disc to another around the midplane.

Moreover, Λ_A remains fairly below the critical value $\Lambda_{A,\,crit.} = 10^2$ with or without a cavity. Λ_A must stay below $\Lambda_{A,\,crit.}$ so that the MRI effects are negligible (Blaes & Balbus 1994; Bai 2011). Therefore, assuming a characteristic value of $\Lambda_{A,0} = 1$ captures, with a reasonable level of accuracy, the physics of ambipolar diffusion, and the cavity does not alter the ambipolar Elsasser number profile. The results we achieve from this simple toy model are to be compared to the more detailed work of Wang & Goodman (2017), in which many chemical species were taken into account to compute the ambipolar Elsasser number inside the cavity of a wind-driven TD.

Following Lesur (2021b) and Thi et al. (2019), we implemented the profile of Λ_A so that

$$\Lambda_A(z,R) = \Lambda_{A,0}\,\exp\left(\frac{z}{\lambda\,h}\right)^4, \tag{A.12}$$

where λ is a parameter that controls the height where a transition between non-ideal and ideal MHD occurs (the non-ideal MHD part being the inside of the disc) and is chosen as constant and equal to $3\,h$. $\Lambda_{A,0}$ remains a free parameter (see Section 1 for more details). Additionally, a cut-off is used for the η_A profile so that if $\eta_A > \eta_{A,\,max}$, the value of η_A is replaced by $\eta_{A,\,max} \equiv 10\,\varepsilon^2$ in code units, such a choice being reflected in the Λ_A profile with Eq. 13.

Appendix B: Poloidal velocity relaxation and inner boundary condition

We aim to address the influence of the poloidal velocity relaxation on our results to test our control on the inner boundary condition. Two additional simulations were conducted with the same setup as B4Bin0Am0 (fiducial run) and B5Bin0Am0, respectively, but without the relaxation procedure. The results are given in Fig. B.1, where we show the surface density $\langle\Sigma\rangle_{4000}$ time averaged on the first 4000 orbits at the internal radius (when the differences are enhanced), with a focus on the innermost radii. We highlight that these differences do not increase for $t > 4000$ orbits at R_{int}. For B5Bin0Am0, the right panel of Fig.B.1 suggests that the relaxation procedure influences how the initial burst is evacuated since we detect differences between the surface-density profiles at $R > 1.5$. However, releasing this inner constraint reduces the inner peak of the profile of Σ, but it does not prevent the initial accumulation of matter from appearing. In particular, the bursts of matter seen in Fig. 21 are not due to this condition (and are probably due to the inner boundary condition; see next paragraph). For the fiducial simulation, we estimate differences of 15% until $R = 2$, 7% until $R = 10$, and less than 2% until $R = 50$, and we conclude that the slight accumulation described in Section 3.1 is due to this procedure, contrary to the occurrence of bursts as seen in Fig. 21.

Regarding the bursts of B5Bin0Am0 (see Fig. 21), we focus on one of them in Fig. B.2. The first panel displays the spatio-temporal diagram of the surface density on which the burst is clearly detected at 17435 orbits at R_{int} and localised by the red dashed line. The accumulation of matter is correlated with a decrease of the vertical magnetic field at the midplane (second panel of Fig. B.2). This magnetic field is not lost but is expelled outwards, as is evident from the magnetic flux function (third panels of Fig. B.2). Such a shortage of magnetic field leads to an increase of β and blocks accretion (we recall that the accretion speed is $v_{acc.} \propto \beta^{-\sigma}$ with $\sigma > 0$). As a result, $\dot{M}$ falls from 0,25 down to $0{,}1 \times 10^{-7}\,M_\odot\,\mathrm{yr}^{-1}$ in the region between the inner radial boundary and the burst, and matter piles up in the cavity. This episode ends when the magnetic flux is eventually re-accreted, leading to an increase of the mass-accretion rate and the disappearance of the density excess in the cavity. At some point, the magnetic flux is advected back onto the seed until it saturates so that B_z can accumulate again close to the inner boundary condition before accretion is enhanced back to normal. The reason why such magnetic flux evacuates from the seed from time to time remains unclear, and these occurrences close to the inner boundary suggest that these might be a boundary condition artefact. However, we mention that the total magnetisation of the seed eventually saturates with a roughly constant value, so a sharp increase of magnetic field (as is the case for this burst; see the middle panel of Fig. B.2, a few orbits before the location of the red dashed line) could force the seed to lose magnetic flux to ensure its conservation. We finish by adding that these bursts are only detected for the weakly magnetised simulations (the ones with $\beta_{out} = 10^5$).

Regarding the inner radial boundary condition for the magnetic field, we tried several configurations (an outflow condition, which is the one we eventually chose, and a perfect conductor). Both of these conditions lead to the same steady states.

We also ran a simulation with a stronger magnetic field close to the inner boundary condition, but no significant changes were noticed. The additional magnetic field was chosen so that the magnetisation of the seed is set close to its saturation value in the fiducial run. However, in any case, the same transient state occurs and leaves the stage to a similar steady state (the magnetisation of the seed reaches the same saturation value and the same stripes are observed in the spatio-temporal diagram of ψ).

We therefore conclude that our setup is robust regarding the initial state and the boundary conditions. The inner boundary still plays a role because of its magnetisation and the fact that only a given amount of magnetic field can be advected. This probably leads to the burst events seen in simulation B5Bin0Am0.

Appendix C: Interchange instability criterion calculations

We express the instability criterion for the interchange instability (or RTI) calculated in Spruit et al. (1995) (Eq. 59) in terms of the plasma parameter. This criterion reads

$$g_m\,\partial_R \ln\frac{\Sigma}{B_z} > 2\left(r\frac{\mathrm{d}\Omega}{\mathrm{d}r}\right)^2 \equiv 2\,S^2, \tag{C.1}$$

where S is the shear that we approximate with $S^2 = 9/4\,\Omega^2$, and g_m is

$$g_m \equiv \frac{B_R^+\,B_z}{2\pi\,\Sigma}. \tag{C.2}$$

B_R^+ is the radial component of the magnetic field at the disc surface. Let us rewrite the previous expression in terms of β, q (defined with $B_R^+ = q\,B_z$) and δ (defined as $\delta = -\mathrm{d}\ln\Sigma/\mathrm{d}\ln R$):

$$\frac{B_R^+\,B_z}{2\pi\,\Sigma}\partial_R \ln\frac{\Sigma}{B_z} = \frac{B_R^+\,B_z}{2\pi\,\Sigma}\frac{\Sigma'}{\Sigma} - \frac{B_R^+\,B_z}{2\pi\,\Sigma}\frac{B_z'}{B_z}, \tag{C.3}$$

$$= \frac{q\,B_z^2}{2\pi\,\Sigma}\frac{-\delta}{R} - \frac{q}{4\pi\,\Sigma}\left(B_z^2\right)', \tag{C.4}$$

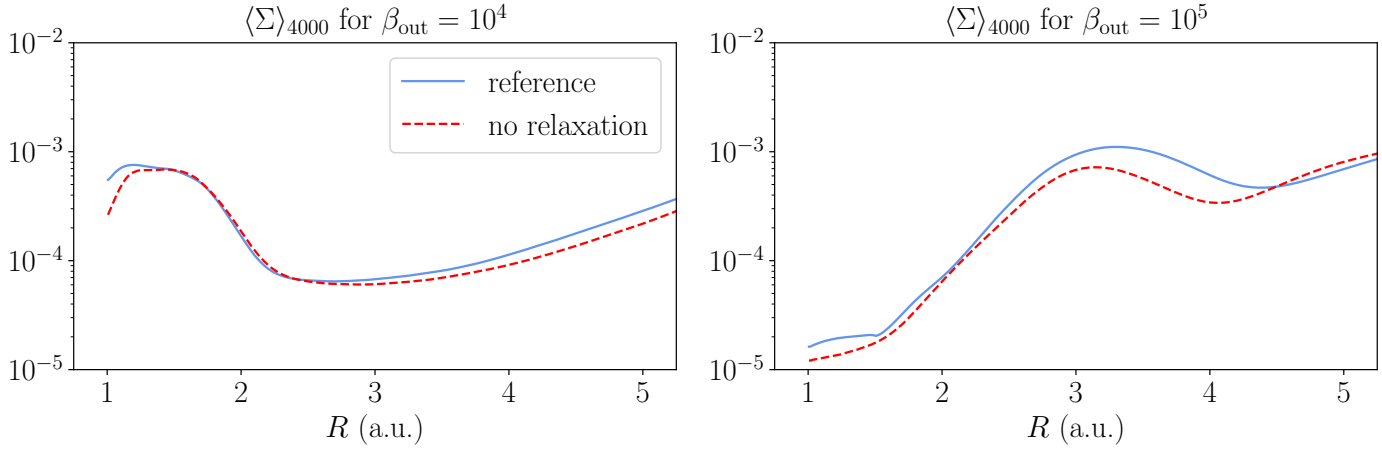

Fig. B.1. Surface density time-averaged on the first 4000 orbits at $R_{\rm int}$. The blue lines are the reference runs (left panel: fiducial run, right panel: B5Bin0Am0), and the red-dashed mines are the corresponding runs without the relaxation.

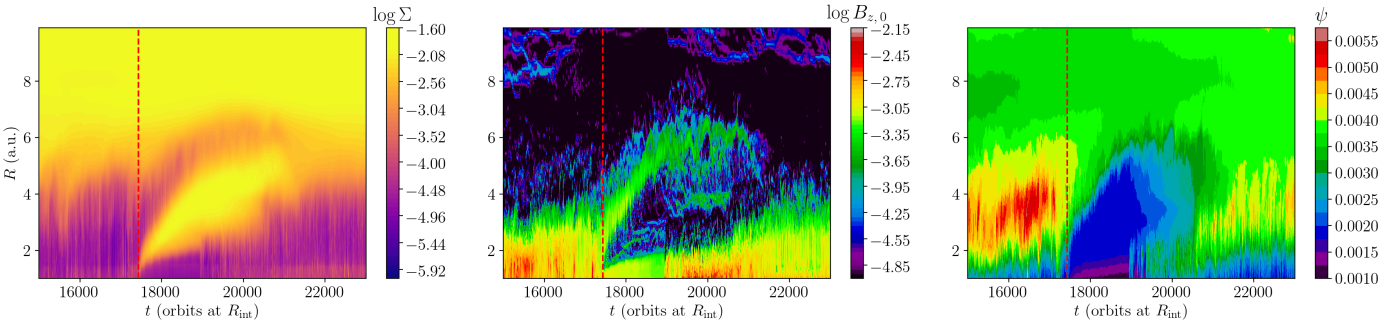

Fig. B.2. Spatio-temporal diagrams of Σ (first panel), $B_{z,0}$ the vertical magnetic field at the midplane and ψ the flux function defined in Eq. 39, for simulation B5Bin0Am0. These profiles focus on the second burst detected in the left panels of Fig. 21. The red dashed line marks the beginning of the burst when detected using Σ.

where X' denotes the derivative of X with respect to R. With $P = c_s^2\,\rho = (h\,\Omega_{\rm K})^2\,\Sigma/(\sqrt{2\pi}\,h)$, we obtain

$$\beta = \frac{4\sqrt{2\pi}\,R\,\varepsilon\,\Omega_{\rm K}^2\,\Sigma}{{B_z}^2}. \tag{C.5}$$

Therefore, the instability criterion becomes

$$S^2 < -\frac{4\,\varepsilon\,\Omega_{\rm K}^2\,q\,\delta}{\sqrt{2\pi}\,\beta} - \frac{q}{4\pi\,\Sigma}\partial_R\left(\frac{4\sqrt{2\pi}\,R\,\varepsilon\,\Omega_{\rm K}^2\,\Sigma}{\beta}\right), \tag{C.6}$$

ε being constant in the disc as well as β inside the cavity. $\Omega_{\rm K}$ varies as $R^{-3/2}$ and Σ as $R^{-\delta}$ so that

$$S^2 < \frac{4\,\varepsilon\,\Omega_{\rm K}^2}{\sqrt{2\pi}\,\beta}\,q\,(-\delta + 1 + \delta/2). \tag{C.7}$$

By taking $S^2/\Omega_{\rm K}^2 = 9/4$, the RTI can be triggered when

$$\beta < \frac{16\,\varepsilon}{9\,\sqrt{2\pi}}\,q\left(1 - \frac{\delta}{2}\right). \tag{C.8}$$

If we now assume that $\delta = q = 1$ for simplicity, we finally obtain

$$\beta < \frac{8\,\varepsilon}{9\,\sqrt{2\pi}} \approx 0.355\,\varepsilon = 0.0355 \equiv \beta_{\rm crit.}, \tag{C.9}$$

where $\varepsilon = 0.1$.

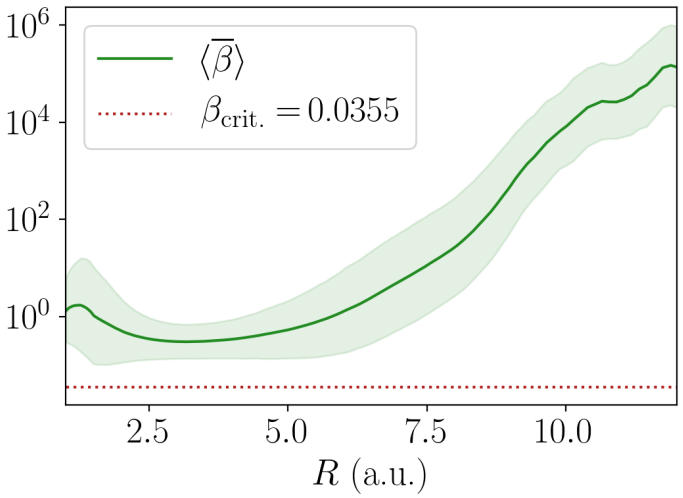

Fig. C.1. Interchange instability criteria. The red dotted line shows the critical value of $\beta_{\rm crit.}$, while the green solid line is obtained with Eq. C.8.

Figure C.1 compares the time-averaged values of $\overline{\beta}$ with the criterion given in Eq. C.9. The value of $\beta_{\rm crit.}$ is below the time-averaged values of $\overline{\beta}$. Though this simple analysis makes it difficult to make definitive conclusions on this subject, it seems that the interchange instability is not triggered inside the cavity.

Appendix D: Laminar transport coefficients

In order to discuss the role of the MRI, we must highlight the impact of the laminar stress and its contribution to the transport coefficients. In this article, we focus on the total stresses, defined in Eq. 29. To compare the turbulent effects, we decompose the stresses with a turbulent and a laminar part. In this prospect, we introduce the deviation to the temporal mean such that

$$\delta X \equiv X - \langle X \rangle. \tag{D.1}$$

Focusing on $W_{r\varphi}$, we expand the magnetic term as

$$\overline{\langle B_r\, B_\varphi \rangle} = \underbrace{\overline{\langle B_r \rangle \langle B_\varphi \rangle}}_{\text{laminar}} + \underbrace{\overline{\langle \delta B_r\, \delta B_\varphi \rangle}}_{\text{turbulent}}. \tag{D.2}$$

Concerning the turbulent stresses, we referred to Jacquemin-Ide et al. (2021) (see their Appendix A) as we only computed the laminar ones and compared the laminar transport coefficients to the ones studied in the article. Therefore, we adopted the following definition for the laminar radial stress:

$$\langle W_{r\varphi}^{\text{lam.}} \rangle \equiv -\frac{1}{4\pi} \overline{\sin\theta \langle B_r \rangle \langle B_\varphi \rangle}, \tag{D.3}$$

and for the laminar surface stress

$$\langle W_{\theta\varphi}^{\text{lam.}} \rangle \equiv -r \left[\sin^2\theta \, \frac{\langle B_\theta \rangle \langle B_\varphi \rangle}{4\pi} \right]_{\theta_+}^{\theta_-}. \tag{D.4}$$

These definitions are coherent with previous works (Béthune et al. 2017; Mishra et al. 2020; Jacquemin-Ide et al. 2021). Hence, the laminar transport coefficients are given by

$$\begin{cases} \langle \alpha^{\text{lam.}} \rangle \equiv \dfrac{\langle W_{r\varphi}^{\text{lam.}} \rangle}{\langle \overline{P} \rangle} \\ \langle \upsilon_{\text{W}}^{\text{lam.}} \rangle \equiv \dfrac{\langle W_{\theta\varphi}^{\text{lam.}} \rangle}{r \langle P_0 \rangle} \end{cases},$$

while we define their turbulent counterparts as

$$\begin{cases} \langle \alpha^{\text{turb.}} \rangle \equiv \langle \alpha \rangle - \langle \alpha^{\text{lam.}} \rangle \\ \langle \upsilon_{\text{W}}^{\text{turb.}} \rangle \equiv \langle \upsilon_{\text{W}} \rangle - \langle \upsilon_{\text{W}}^{\text{lam.}} \rangle \end{cases}.$$

The results are shown in Fig. D.1. The laminar contribution is the major one for $\langle \upsilon_{\text{W}} \rangle$ in the whole disc, so we only show its laminar contribution with respect to the full coefficient, as they take essentially the same values. Nevertheless, despite the laminar term being high for $\langle \alpha \rangle$, a strong turbulent term is at stake, especially in the external part of the disc where it is dominant. Inside the cavity, $\langle \alpha \rangle$ is fairly distributed between the laminar and turbulent contributions. However, we recall that the wind may act also on the turbulent component of $\langle \alpha \rangle$ since the magnetic field also appears in Eq. D.2. We finally conclude that the MRI is probably acting on the disc outer parts in the $\langle \alpha \rangle$ coefficient, while the surface stress embodied by $\langle \upsilon_{\text{W}} \rangle$ is definitely dominated by the laminar part and due to the wind.

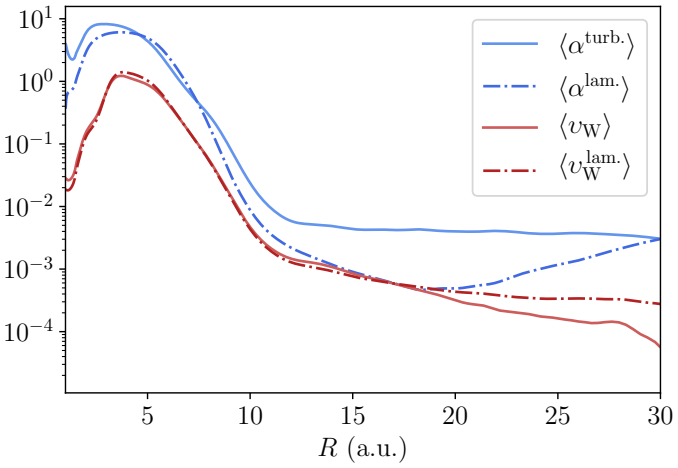

Fig. D.1. Time-averaged transport coefficients and their laminar and turbulent contributions. We give the laminar and turbulent contributions for $\langle \alpha \rangle$ and the total profile with its laminar contribution for $\langle \upsilon_{\text{W}} \rangle$.

BIBLIOGRAPHY

[1]R. D. Alexander, C. J. Clarke, and J. E. Pringle, "Photoevaporation of protoplanetary discs – I. hydrodynamic models," MNRAS **369**, 216–228 (2006) (cit. on pp. 19, 65).

[2]R. Alexander, I. Pascucci, S. Andrews, P. Armitage, and L. Cieza, "The dispersal of protoplanetary disks," in *Protostars and planets* VI (Jan. 1, 2014), pp. 475–496 (cit. on p. 19).

[3]J. M. Anderson, Z.-Y. Li, R. Krasnopolsky, and R. D. Blandford, "Locating the launching region of T tauri winds: the case of DG tauri," ApJ **590**, L107 (2003) (cit. on p. 185).

[4]S. M. Andrews, D. J. Wilner, A. M. Hughes, C. Qi, and C. P. Dullemond, "Protoplanetary disk structures in ophiuchus," ApJ **700**, 1502–1523 (2009) (cit. on pp. 42, 43).

[5]S. M. Andrews et al., "The disk substructures at high angular resolution project (DSHARP). I. motivation, sample, calibration, and overview," ApJL **869**, L41 (2018) (cit. on pp. xiv, 8, 9, 193).

[6]M. Ansdell et al., "ALMA survey of lupus protoplanetary disks. II. gas disk radii," ApJ **859**, 21 (2018) (cit. on p. 196).

[7]P. J. Armitage, "Physical processes in protoplanetary disks," Nov. 30, 2017 (cit. on pp. 12, 67).

[8]X.-N. Bai, "Magnetorotational instability driven accretion in protoplanetary disks," ApJ **739**, 50 (2011) (cit. on pp. 68, 70).

[9]X.-N. Bai and J. Goodman, "Heat and dust in active layers of protostellar disks," ApJ **701**, 737–755 (2009) (cit. on p. 65).

[10]X.-N. Bai and J. M. Stone, "Effect of ambipolar diffusion on the nonlinear evolution of magnetorotational instability in weakly ionized disks," ApJ **736**, 144 (2011) (cit. on pp. 13, 214, 217).

[11]X.-N. Bai and J. M. Stone, "Local study of accretion disks with a strong vertical magnetic field: magnetorotational instability and disk outflow," ApJ **767**, 30 (2013) (cit. on p. 145).

[12]X.-N. Bai and J. M. Stone, "Wind-driven accretion in protoplanetary disks. I. suppression of the magnetorotational instability and launching of the magnetocentrifugal wind," ApJ **769**, 76 (2013) (cit. on pp. 65, 125).

[13]X.-N. Bai and J. M. Stone, "Hall effect–mediated magnetic flux transport in protoplanetary disks," ApJ **836**, 46 (2017) (cit. on pp. 110, 111, 213).

[14]K. Bajer and K. Mizerski, "Elliptical flow instability in a conducting fluid triggered by an external magnetic field," Phys. Rev. Lett. **110**, 104503 (2013) (cit. on p. 215).

[15]S. A. Balbus and J. F. Hawley, "A powerful local shear instability in weakly magnetized disks. I. linear analysis," ApJ **376**, 214 (1991) (cit. on p. 12).

[16]S. A. Balbus and C. Terquem, "Linear analysis of the hall effect in protostellar disks," ApJ **552**, 235 (2001) (cit. on p. 13).

[17]S. A. Barenfeld, J. M. Carpenter, A. I. Sargent, A. Isella, and L. Ricci, "Measurement of circumstellar disk sizes in the upper scorpius OB association with ALMA," ApJ **851**, 85 (2017) (cit. on p. 196).

[18]C. Baruteau, A. Crida, S.-J. Paardekooper, F. Masset, J. Guilet, B. Bitsch, R. P. Nelson, W. Kley, and J. C. B. Papaloizou, "Planet-disc interactions and early evolution of planetary systems," in *Protostars and planets* VI (2014) (cit. on p. 19).

[19]C. Baruteau, G. Wafflard-Fernandez, R. Le Gal, F. Debras, A. Carmona, A. Fuente, and P. Rivière-Marichalar, "Observational signatures of eccentric jupiters inside gas cavities in protoplanetary discs," MNRAS **505**, 359–376 (2021) (cit. on pp. 194, 217).

[20]M. R. Bate, "Stellar, brown dwarf and multiple star properties from hydrodynamical simulations of star cluster formation," MNRAS **392**, 590–616 (2009) (cit. on p. 6).

[21]M. C. Begelman, N. Scepi, and J. Dexter, "What really makes an accretion disc MAD," MNRAS **511**, 2040–2051 (2022) (cit. on p. 154).

[22]W. Béthune, G. Lesur, and J. Ferreira, "Global simulations of protoplanetary disks with net magnetic flux - I. non-ideal MHD case," A&A **600**, A75 (2017) (cit. on pp. 14, 73, 118, 146, 216, 233).

[23]J. Bi and J. Fung, "Dust dynamics in transitional disks: clumping and disk recession," ApJ **928**, 74 (2022) (cit. on p. 217).

[24]T. Birnstiel, S. M. Andrews, and B. Ercolano, "Can grain growth explain transition disks?" A&A **544**, A79 (2012) (cit. on p. 28).

[25]T. Birnstiel and S. M. Andrews, "On the outer edges of protoplanetary dust disks," ApJ **780**, 153 (2013) (cit. on p. 197).

[26]O. M. Blaes and S. A. Balbus, "Local shear instabilities in weakly ionized, weakly magnetized disks," ApJ **421**, 163 (1994) (cit. on pp. 13, 70, 217).

[27]R. D. Blandford and D. G. Payne, "Hydromagnetic flows from accretion discs and the production of radio jets," MNRAS **199**, 883–903 (1982) (cit. on pp. 13, 29, 30, 68, 104, 108, 186).

[28]A. Boccaletti et al., "Possible evidence of ongoing planet formation in AB aurigae - a showcase of the SPHERE/ALMA synergy," A&A **637**, L5 (2020) (cit. on pp. xiv, 15, 16).

[29]C. S. Borlina, B. P. Weiss, J. F. J. Bryson, and P. J. Armitage, "Lifetime of the outer solar system nebula from carbonaceous chondrites," Journal of Geophysical Research: Planets **127**, e2021JE007139 (2022) (cit. on p. 45).

[30]J. Bouvier, S. H. P. Alencar, T. J. Harries, C. M. Johns-Krull, and M. M. Romanova, "Magnetospheric accretion in classical T tauri stars," in *Protostars and protoplanets v* (Apr. 14, 2006) (cit. on pp. 10, 112, 214).

[31]J. Bouvier, K. Perraut, J.-B. L. Bouquin, G. Duvert, C. Dougados, W. Brandner, M. Benisty, J.-P. Berger, and E. Alécian, "Probing the magnetospheric accretion region of the young pre-transitional disk system DoAr 44 using VLTI/GRAVITY," A&A **636**, A108 (2020) (cit. on p. 214).

[32]J. Bouvier et al., "Investigating the magnetospheric accretion process in the young pre-transitional disk system DoAr 44 (v2062 Oph) - a multiwavelength interferometric, spectropolarimetric, and photometric observing campaign," A&A **643**, A99 (2020) (cit. on p. 214).

[33]S. I. Braginskii, "Transport processes in a plasma," Rev. Plasma Phys. **1**, 205 (1965) (cit. on pp. 56, 61).

[34]a. C. L. Brogan et al., "The 2014 ALMA long baseline campaign: first results from high angular resolution observations toward the HL tau region," ApJL **808**, L3 (2015) (cit. on pp. xiv, 8, 11).

[35]J. M. Brown, G. A. Blake, C. Qi, C. P. Dullemond, D. J. Wilner, and J. P. Williams, "Evidence for dust clearing through resolved submillimeter imaging," ApJ **704**, 496–502 (2009) (cit. on p. 17).

[36]S. Bruderer, N. van der Marel, E. F. van Dishoeck, and T. A. van Kempen, "Gas structure inside dust cavities of transition disks: ophiuchus IRS 48 observed by ALMA," A&A **562**, A26 (2014) (cit. on pp. 17, 24).

[37]J. Calcino, V. Christiaens, D. J. Price, C. Pinte, T. M. Davis, N. van der Marel, and N. Cuello, "Are the spiral arms in the MWC 758 protoplanetary disc driven by a companion inside the cavity?" MNRAS **498**, 639–650 (2020) (cit. on pp. 27, 74).

[38]J. Calcino, T. Hilder, D. J. Price, C. Pinte, F. Bollati, G. Lodato, and B. J. Norfolk, "Mapping the planetary wake in HD 163296 with kinematics," ApJL **929**, L25 (2022) (cit. on p. 191).

[39]N. Calvet, L. Hartmann, and S. E. Strom, *Evolution of disk accretion* (eprint: arXiv:astro-ph/9902335, May 1, 2000), p. 377 (cit. on p. 11).

[40]X. Cao and H. C. Spruit, "Instability of an accretion disk with a magnetically driven wind," A&A **385**, 289–300 (2002) (cit. on p. 208).

[41] A. Carmona et al., "Constraining the structure of the transition disk HD 135344b (SAO 206462) by simultaneous modeling of multiwavelength gas and dust observations," A&A **567**, A51 (2014) (cit. on pp. 17, 62).

[42] A. Carmona et al., "A gas density drop in the inner 6 AU of the transition disk around the herbig ae star HD 139614 - further evidence for a giant planet inside the disk?" A&A **598**, A118 (2017) (cit. on p. 17).

[43] S. Casanova, T. Montmerle, E. D. Feigelson, and P. Andre, "ROSAT X-ray sources embedded in the rho ophiuchi cloud core," ApJ **439**, 752 (1995) (cit. on p. 65).

[44] S. Casassus et al., "Accretion kinematics through the warped transition disk in HD 142527 from resolved CO(6–5) observations," ApJ **811**, 92 (2015) (cit. on pp. 24, 191, 214).

[45] P. Cazzoletti et al., "\Textsc{alma} survey of class II protoplanetary disks in corona australis: a young region with low disk masses," A&A **626**, A11 (2019) (cit. on p. 6).

[46] B. Cerutti, G. R. Werner, D. A. Uzdensky, and M. C. Begelman, "Simulations of particle acceleration beyond the classical synchrotron burnoff limit in magnetic reconnection: an explanation of the crab flares," ApJ **770**, 147 (2013) (cit. on p. 73).

[47] Y. Chachan, R. A. Booth, A. H. M. J. Triaud, and C. Clarke, "Dust accretion in binary systems: implications for planets and transition discs," MNRAS **489**, 3896–3904 (2019) (cit. on p. 27).

[48] S. Chandrasekhar, *Hydrodynamic and hydromagnetic stability* (Jan. 1, 1961) (cit. on pp. 12, 163).

[49] S. Chapman and T. G. Cowling, *The mathematical theory of non-uniform gases. an account of the kinetic theory of viscosity, thermal conduction and diffusion in gases* (Jan. 1, 1970) (cit. on p. 46).

[50] Y.-X. Chen, Z. Wang, Y.-P. Li, C. Baruteau, and D. N. C. Lin, "Wide dust gaps in protoplanetary disks induced by eccentric planets: a mass-eccentricity degeneracy," ApJ **922**, 184 (2021) (cit. on p. 194).

[51] M. Chevance, M. R. Krumholz, A. F. McLeod, E. C. Ostriker, E. W. Rosolowsky, and A. Sternberg, "The life and times of giant molecular clouds," Mar. 17, 2022 (cit. on p. 6).

[52] T.-C. Ching, D. Li, C. Heiles, Z.-Y. Li, L. Qian, Y. L. Yue, J. Tang, and S. H. Jiao, "An early transition to magnetic supercriticality in star formation," Nature **601**, 49–52 (2022) (cit. on p. 6).

[53] C. Combet and J. Ferreira, "The radial structure of protostellar accretion disks: influence of jets," A&A **479**, 481–491 (2008) (cit. on pp. 29, 34, 108, 214, 218).

[54]C. Combet, J. Ferreira, and F. Casse, "Dead zones in protostellar discs: the case of jet emitting discs," A&A **519**, A108 (2010) (cit. on pp. 29, 64).

[55]J. Contopoulos and R. V. E. Lovelace, "Magnetically driven jets and winds: exact solutions," ApJ **429**, 139 (1994) (cit. on p. 32).

[56]A. F. Cook and F. A. Franklin, "Rediscussion of maxwell's ADAMS prize essay on the stability of saturn's rings. II," ApJ **71**, 10 (1966) (cit. on p. 46).

[57]R Courant, K Friedrichs, and H Lewyt, "On the partial difference equations of mathematical physics," Math. Ann., 32–74 (1928) (cit. on p. 72).

[58]T. G Cowling, *Magnetohydrodynamics*. (Interscience Publishers, New York, 1957) (cit. on p. 56).

[59]A. Crida and A. Morbidelli, "Cavity opening by a giant planet in a protoplanetary disc and effects on planetary migration," MNRAS **377**, 1324–1336 (2007) (cit. on p. 26).

[60]B. Crinquand, B. Cerutti, and G. Dubus, "Kinetic modeling of the electromagnetic precursor from an axisymmetric binary pulsar coalescence," A&A **622**, A161 (2019) (cit. on p. 73).

[61]R. M. Crutcher and A. J. Kemball, "Review of zeeman effect observations of regions of star formation," Frontiers in Astronomy and Space Sciences **6** (2019) (cit. on p. 6).

[62]N. Cuello, J.-F. Gonzalez, and F. C. Pignatale, "Effects of photophoresis on the dust distribution in a 3D protoplanetary disc," MNRAS **458**, 2140–2149 (2016) (cit. on p. 217).

[63]N. Cuello, M. Montesinos, S. M. Stammler, F. Louvet, and J. Cuadra, "Dusty spirals triggered by shadows in transition discs," A&A **622**, A43 (2019) (cit. on p. 193).

[64]C. Cui and X.-N. Bai, "Global three-dimensional simulations of outer protoplanetary discs with ambipolar diffusion," MNRAS **507**, 1106–1126 (2021) (cit. on pp. 14, 68, 118, 145, 213, 214, 216).

[65]A. de Valon, C. Dougados, S. Cabrit, F. Louvet, L. A. Zapata, and D. Mardones, "ALMA reveals a large structured disk and nested rotating outflows in DG tauri B," A&A **634**, L12 (2020) (cit. on pp. 13, 185).

[66]F. Debras, C. Baruteau, and J.-F. Donati, "Revisiting migration in a disc cavity to explain the high eccentricities of warm jupiters," MNRAS **500**, 1621–1632 (2021) (cit. on p. 194).

[67]A. Dedner, F. Kemm, D. Kröner, C. D. Munz, T. Schnitzer, and M. Wesenberg, "Hyperbolic divergence cleaning for the MHD equations," Journal of Computational Physics **175**, 645–673 (2002) (cit. on p. 72).

[68]J.-F. Donati, F. Paletou, J. Bouvier, and J. Ferreira, "Direct magnetic field detection in the innermost regions of an accretion disc," Nature **438**, 466–469 (2005) (cit. on p. 14).

[69]R. Dong and R. Dawson, "Stability and occurrence rate constraints on the planetary sculpting hypothesis for "transitional" disks," ApJ **825**, 77 (2016) (cit. on p. 26).

[70]R. Dong et al., "The sizes and depletions of the dust and gas cavities in the transitional disk J160421.7-213028," ApJ **836**, 201 (2017) (cit. on p. 17).

[71]B. T. Draine, *Physics of the interstellar and intergalactic medium* (Sept. 1, 2011) (cit. on p. 61).

[72]C. P. Dullemond and C. Dominik, "The effect of dust settling on the appearance of protoplanetary disks," A&A **421**, 1075–1086 (2004) (cit. on p. 43).

[73]C. P. Dullemond, A. Juhasz, A. Pohl, F. Sereshti, R. Shetty, T. Peters, B. Commerçon, and M. Flock, "RADMC-3D: a multi-purpose radiative transfer tool.," (2012) (cit. on p. 189).

[74]C. P. Dullemond, A. Natta, and L. Testi, "Accretion in protoplanetary disks: the imprint of core properties," ApJ **645**, L69 (2006) (cit. on p. 10).

[75]W. M. Elsasser, "The hydromagnetic equations," Phys. Rev. **79**, 183–183 (1950) (cit. on p. 56).

[76]R. F. Elsner and F. K. Lamb, "Accretion by magnetic neutron stars. II - plasma entry into the magnetosphere via diffusion, polar cusps, and magnetic field reconnection," ApJ **278**, 326 (1984) (cit. on p. 116).

[77]A. Emsenhuber, C. Mordasini, R. Burn, Y. Alibert, W. Benz, and E. Asphaug, "The new generation planetary population synthesis (NGPPS) - II. planetary population of solar-like stars and overview of statistical results," A&A **656**, A70 (2021) (cit. on p. 17).

[78]B. Ercolano and I. Pascucci, "The dispersal of planet-forming discs: theory confronts observations," Royal Society Open Science **4**, 170114 (2020) (cit. on pp. xiv, 18, 22, 23, 28, 34).

[79]B. Ercolano, G. Picogna, K. Monsch, J. J. Drake, and T. Preibisch, "The dispersal of protoplanetary discs – II: photoevaporation models with observationally derived irradiating spectra," MNRAS **508**, 1675–1685 (2021) (cit. on p. 21).

[80]C. Espaillat, P. D'Alessio, J. Hernández, E. Nagel, K. L. Luhman, D. M. Watson, N. Calvet, J. Muzerolle, and M. McClure, "Unveiling the structure of pre-transitional disks," ApJ **717**, 441–457 (2010) (cit. on p. 19).

[81]C. R. Evans and J. F. Hawley, "Simulation of magnetohydrodynamic flows: a constrained transport model," ApJ **332**, 659 (1988) (cit. on p. 72).

[82]M. Fang, I. Pascucci, S. Edwards, U. Gorti, A. Banzatti, M. Flock, P. Hartigan, G. J. Herczeg, and A. K. Dupree, "A new look at T tauri star forbidden lines: MHD-driven winds from the inner disk," ApJ **868**, 28 (2018) (cit. on p. 186).

[83]E. D. Feigelson, L. Townsley, M. Güdel, and K. Stassun, "X-ray properties of young stars and stellar clusters," in *Protostars and planets v* (2007), pp. 313–328 (cit. on p. 65).

[84]J. Ferreira, "Magnetically-driven jets from keplerian accretion discs.," A&A **319**, 340–359 (1997) (cit. on pp. 32, 108, 186, 218).

[85]J. Ferreira, C. Dougados, and S. Cabrit, "Which jet launching mechanism(s) in T tauri stars?" A&A **453**, 785–796 (2006) (cit. on p. 185).

[86]J. Ferreira and G. Pelletier, "Magnetized accretion-ejection structures. III. stellar and extragalactic jets as weakly dissipative disk outflows.," A&A **295**, 807 (1995) (cit. on pp. 29, 68).

[87]J. Ferreira, "Theory of magnetized accretion discs driving jets," Nov. 28, 2003 (cit. on p. 33).

[88]K. M. Flaherty, A. M. Hughes, R. Teague, J. B. Simon, S. M. Andrews, and D. J. Wilner, "Turbulence in the TW hya disk," ApJ **856**, 117 (2018) (cit. on p. 13).

[89]K. Flaherty, A. M. Hughes, J. B. Simon, C. Qi, X.-N. Bai, A. Bulatek, S. M. Andrews, D. J. Wilner, and A. Kóspál, "Measuring turbulent motion in planet-forming disks with ALMA: a detection around DM tau and nondetections around VMWC 480 and V4046 sgr," ApJ **895**, 109 (2020) (cit. on p. 13).

[90]M. Flock, N. Dzyurkevich, H. Klahr, N. J. Turner, and T. Henning, "Turbulence and steady flows in three-dimensional global stratified magnetohydrodynamic simulations of accretion disks," ApJ **735**, 122 (2011) (cit. on p. 145).

[91]A. S. Font, I. G. McCarthy, D. Johnstone, and D. R. Ballantyne, "Photoevaporation of circumstellar disks around young stars," ApJ **607**, 890 (2004) (cit. on p. 21).

[92]L. Francis and N. van der Marel, "Dust-depleted inner disks in a large sample of transition disks through long-baseline ALMA observations," ApJ **892**, 111 (2020) (cit. on pp. xiv, 19, 20, 62, 193).

[93]S. Fromang, W. Lyra, and F. Masset, "Meridional circulation in turbulent protoplanetary disks," A&A **534**, A107 (2011) (cit. on p. 146).

[94]S. Fromang, C. Terquem, and S. A. Balbus, "The ionization fraction in α models of protoplanetary discs," MNRAS **329**, 18–28 (2002) (cit. on p. 67).

[95]R. R. Fu, M. W. R. Volk, D. Bilardello, G. Libourel, G. R. J. Lesur, and O. Ben Dor, "The fine-scale magnetic history of the allende meteorite: implications for the structure of the solar nebula," AGU Adv. **2**, e2021AV000486 (2021) (cit. on p. 45).

[96]R. R. Fu et al., "Solar nebula magnetic fields recorded in the semarkona meteorite," Science **346**, 1089–1092 (2014) (cit. on p. 45).

[97]R. L. Gal et al., "Molecules with ALMA at planet-forming scales (MAPS). XII. inferring the C/O and S/H ratios in protoplanetary disks with sulfur molecules," ApJS **257**, 12 (2021) (cit. on p. 67).

[98]C. F. Gammie, "Layered accretion in T tauri disks," ApJ **457**, 355 (1996) (cit. on pp. 13, 26, 64, 67).

[99]M. Gárate, T. N. Delage, J. Stadler, P. Pinilla, T. Birnstiel, S. M. Stammler, G. Picogna, B. Ercolano, R. Franz, and C. Lenz, "Large gaps and high accretion rates in photoevaporative transition disks with a dead zone," A&A **655**, A18 (2021) (cit. on p. 25).

[100]J. M. Girart, R. Rao, and D. P. Marrone, "Magnetic fields in the formation of sun-like stars," Science **313**, 812–814 (2006) (cit. on p. 15).

[101]S. K. Godunov and I. Bohachevsky, "Finite difference method for numerical computation of discontinuous solutions of the equations of fluid dynamics," Mat. Sb. **47(89)**, 271–306 (1959) (cit. on p. 72).

[102]J. P. H. Goedbloed and S. Poedts, *Principles of magnetohydrodynamics: with applications to laboratory and astrophysical plasmas* (Cambridge University Press, Cambridge, 2004) (cit. on pp. 51, 53).

[103]C. González-Ruilova et al., "A tale of two transition disks: ALMA long-baseline observations of ISO-Oph 2 reveal two closely packed nonaxisymmetric rings and a $\sim$2 AU cavity," ApJL **902**, L33 (2020) (cit. on pp. xiv, 23, 24, 27, 191).

[104]M. Gordovskyy, P. Browning, and R. F. Pinto, "Combining MHD and kinetic modelling of solar flares," Advances in Space Research, Advances in Solar Physics **63**, 1453–1465 (2019) (cit. on p. 47).

[105]U. Gorti and D. Hollenbach, "Photoevaporation of circumstellar disks by far-ultraviolet, extreme-ultraviolet and x-ray radiation from the central star," ApJ **690**, 1539–1552 (2008) (cit. on p. 21).

[106]O. Gressel, J. P. Ramsey, C. Brinch, R. P. Nelson, N. J. Turner, and S. Bruderer, "Global hydromagnetic simulations of protoplanetary disks with stellar irradiation and simplified thermochemistry," ApJ **896**, 126 (2020) (cit. on pp. 51, 111, 213).

[107]O. Gressel, N. J. Turner, R. P. Nelson, and C. P. McNally, "Global simulations of protoplanetary disks with ohmic resistivity and ambipolar diffusion," ApJ **801**, 84 (2015) (cit. on p. 68).

[108]J. Guilet and G. I. Ogilvie, "Global evolution of the magnetic field in a thin disc and its consequences for protoplanetary systems," MNRAS **441**, 852–868 (2014) (cit. on p. 109).

[109]S. Guilloteau, A. Dutrey, J. Pety, and F. Gueth, "Resolving the circumbinary dust disk surrounding HH 30," A&A **478**, L31–L34 (2008) (cit. on p. 42).

[110]R. E. Harrison, L. W. Looney, I. W. Stephens, Z.-Y. Li, R. Teague, R. M. Crutcher, H. Yang, E. G. Cox, M. Fernández-López, and H. Shinnaga, "ALMA CN zeeman observations of AS 209: limits on magnetic field strength and magnetically driven accretion rate," ApJ **908**, 141 (2021) (cit. on p. 15).

[111]R. E. Harrison, L. W. Looney, I. W. Stephens, Z.-Y. Li, H. Yang, A. Kataoka, R. J. Harris, W. Kwon, T. Muto, and M. Momose, "Dust polarization in four protoplanetary disks at 3 mm: further evidence of multiple origins," ApJL **877**, L2 (2019) (cit. on p. 15).

[112]D. Harsono, P. Bjerkeli, M. H. D. van der Wiel, J. P. Ramsey, L. T. Maud, L. E. Kristensen, and J. K. Jø rgensen, "Evidence for the start of planet formation in a young circumstellar disk," Nat Astron **2**, 646–651 (2018) (cit. on p. 191).

[113]L. Hartmann, N. Calvet, E. Gullbring, and P. D'Alessio, "Accretion and the evolution of T tauri disks," ApJ **495**, 385 (1998) (cit. on p. 10).

[114]J. F. Hawley and J. M. Stone, "Nonlinear evolution of the magnetorotational instability in ion-neutral disks," ApJ **501**, 758 (1998) (cit. on p. 13).

[115]C. Hayashi, "Structure of the solar nebula, growth and decay of magnetic fields and effects of magnetic and turbulent viscosities on the nebula," Progress of Theoretical Physics Supplement **70**, 35–53 (1981) (cit. on p. 42).

[116]R. M. Heath and C. J. Nixon, "On the orbital evolution of binaries with circumbinary discs," A&A **641**, A64 (2020) (cit. on p. 74).

[117]P. Hennebelle, B. Commerçon, G. Chabrier, and P. Marchand, "Magnetically self-regulated formation of early protoplanetary disks," ApJL **830**, L8 (2016) (cit. on p. 7).

[118]K. Hoadley, K. France, R. D. Alexander, M. McJunkin, and P. C. Schneider, "The evolution of inner disk gas in transition disks," ApJ **812**, 41 (2015) (cit. on p. 186).

[119]D. Hollenbach and U. Gorti, "Diagnostic line emission from extreme ultraviolet and x-ray-illuminated disks and shocks around low-mass stars," ApJ **703**, 1203–1223 (2009) (cit. on p. 65).

[120]A. M. Hughes, S. M. Andrews, C. Espaillat, D. J. Wilner, N. Calvet, P. D'Alessio, C. Qi, J. P. Williams, and M. R. Hogerheijde, "A spatially resolved inner hole in the disk around gm aurigae," ApJ **698**, 131–142 (2009) (cit. on p. 27).

[121]A. M. Hughes, C. L. H. Hull, D. J. Wilner, and R. L. Plambeck, "Interferometric upper limits on millimeter polarization of the disks around DG tau, GM aur, and MWC 480," ApJ **145**, 115 (2013) (cit. on p. 15).

[122] A. M. Hughes, D. J. Wilner, J. Cho, D. P. Marrone, A. Lazarian, S. M. Andrews, and R. Rao, "Stringent limits on the polarized submillimeter emission from protoplanetary disks," ApJ **704**, 1204–1217 (2009) (cit. on p. 15).

[123] J. Igea and A. E. Glassgold, "X-ray ionization of the disks of young stellar objects," ApJ **518**, 848 (1999) (cit. on p. 65).

[124] M. J. Ireland and A. L. Kraus, "The disk around coku tauri/4: circumbinary, not transitional*," ApJ **678**, L59 (2008) (cit. on p. 27).

[125] J. Jacquemin-Ide, G. Lesur, and J. Ferreira, "Magnetic outflows from turbulent accretion disks - I. vertical structure and secular evolution," A&A **647**, A192 (2021) (cit. on pp. 14, 77, 118, 233).

[126] J. H. Jeans and G. H. Darwin, "I. the stability of a spherical nebula," Philos. Trans. R. Soc. Lond. Ser. Contain. Pap. Math. Phys. Character **199**, 1–53 (1902) (cit. on p. 6).

[127] Kane Yee, "Numerical solution of initial boundary value problems involving maxwell's equations in isotropic media," IEEE Trans. Antennas Propag. **14**, 302–307 (1966) (cit. on p. 72).

[128] A. Kataoka, T. Muto, M. Momose, T. Tsukagoshi, M. Fukagawa, H. Shibai, T. Hanawa, K. Murakawa, and C. P. Dullemond, "Millimeter-wave polarization of protoplanetary disks due to dust scattering," ApJ **809**, 78 (2015) (cit. on p. 15).

[129] A. Kataoka, T. Tsukagoshi, A. Pohl, T. Muto, H. Nagai, I. W. Stephens, K. Tomisaka, and M. Momose, "The evidence of radio polarization induced by the radiative grain alignment and self-scattering of dust grains in a protoplanetary disk," ApJL **844**, L5 (2017) (cit. on p. 15).

[130] S. J. Kenyon and L. Hartmann, "Pre-main-sequence evolution in the taurus-auriga molecular cloud," ApJS **101**, 117 (1995) (cit. on p. 17).

[131] J. Kluska, H. V. Winckel, Q. Coppée, G.-M. Oomen, K. Dsilva, D. Kamath, V. Bujarrabal, and M. Min, "A population of transition disks around evolved stars: fingerprints of planets - catalog of disks surrounding galactic post-AGB binaries," A&A **658**, A36 (2022) (cit. on pp. 10, 19).

[132] A. Königl and M. Wardle, "A comment on the stability of magnetic wind-driving accretion discs," MNRAS **279**, L61–L64 (1996) (cit. on p. 208).

[133] A. Königl, "Accretion disks and jets in protostellar systems," in Accretion disks magn. fields astrophys. Edited by G. Belvedere, Astrophysics and Space Science Library (1989), pp. 165–178 (cit. on p. 68).

[134] A. Königl, "Are magnetic wind-driving disks inherently unstable?" ApJ **617**, 1267 (2004) (cit. on p. 208).

[135]J. H. Krolik and T. R. Kallman, "X-ray ionization and the orion molecular cloud.," ApJ **267**, 610–624 (1983) (cit. on p. 65).

[136]M. Kruskal and M. Schwarzschild, "Some instabilities of a completely ionized plasma," Proceedings of the Royal Society of London Series A **223**, 348–360 (1954) (cit. on p. 166).

[137]M. Kunitomo, T. K. Suzuki, and S.-i. Inutsuka, "Dispersal of protoplanetary discs by the combination of magnetically driven and photoevaporative winds," MNRAS **492**, 3849–3858 (2020) (cit. on pp. 23, 34).

[138]M. W. Kunz and S. A. Balbus, "Ambipolar diffusion in the magnetorotational instability," MNRAS **348**, 355–360 (2004) (cit. on p. 13).

[139]M. W. Kunz and G. Lesur, "Magnetic self-organization in hall-dominated magnetorotational turbulence," MNRAS **434**, 2295–2312 (2013) (cit. on pp. 13, 60).

[140]G. Laibe, J.-F. Gonzalez, L. Fouchet, and S. T. Maddison, "SPH simulations of grain growth in protoplanetary disks," A&A **487**, 265–270 (2008) (cit. on p. 74).

[141]A. Lazarian, "Tracing magnetic fields with aligned grains," Journal of Quantitative Spectroscopy and Radiative Transfer, IX Conference on Electromagnetic and Light Scattering by Non-Spherical Particles **106**, 225–256 (2007) (cit. on p. 15).

[142]C.-F. Lee, B. Tabone, S. Cabrit, C. Codella, L. Podio, J. Ferreira, and J. Jacquemin-Ide, "First detection of interaction between a magnetic disk wind and an episodic jet in a protostellar system," ApJL **907**, L41 (2021) (cit. on p. 185).

[143]J. Lequeux, *Le milieu interstellaire - cnrs editions* (2012) (cit. on p. 6).

[144]G. Lesur, J. Ferreira, and G. I. Ogilvie, "The magnetorotational instability as a jet launching mechanism," A&A **550**, A61 (2013) (cit. on pp. 33, 34, 68, 208).

[145]G. Lesur et al., "Hydro-, magnetohydro-, and dust-gas dynamics of protoplanetary disks," in *Protostars and planets* VII (Mar. 18, 2022) (cit. on p. 12).

[146]G. R. J. Lesur, "Magnetohydrodynamics of protoplanetary discs," JPP **87** (2021) (cit. on pp. 33, 56, 64, 67, 68, 76, 100, 104, 108).

[147]G. R. J. Lesur, "Systematic description of wind-driven protoplanetary discs," A&A **650**, A35 (2021) (cit. on pp. xxii, 14, 68, 101, 103, 111, 125, 186, 187, 213).

[148]G. Lesur, M. W. Kunz, and S. Fromang, "Thanatology in protoplanetary discs - the combined influence of ohmic, hall, and ambipolar diffusion on dead zones," A&A **566**, A56 (2014) (cit. on pp. 65, 67, 73).

[149]E. H. Levy, "Magnetic field in the primitive solar nebula," Nature **276**, 481–481 (1978) (cit. on p. 45).

[150]H. Li, S. A. Colgate, B. Wendroff, and R. Liska, "Rossby wave instability of thin accretion disks. III. nonlinear simulations," ApJ **551**, 874 (2001) (cit. on p. 163).

[151]H. Li, J. M. Finn, R. V. E. Lovelace, and S. A. Colgate, "Rossby wave instability of thin accretion disks. II. detailed linear theory," ApJ **533**, 1023 (2000) (cit. on pp. 132, 163, 165, 215).

[152]L.-X. Li and R. Narayan, "Quasi-periodic oscillations from rayleigh-taylor and kelvin-helmholtz instability at a disk-magnetosphere interface," ApJ **601**, 414 (2004) (cit. on p. 116).

[153]M. Li and L. Xiao, "Lifetimes and accretion rates of protoplanetary disks," ApJ **820**, 36 (2016) (cit. on p. 10).

[154]M. T. P. Liska, G. Musoke, A. Tchekhovskoy, O. Porth, and A. M. Beloborodov, "Formation of magnetically truncated accretion disks in 3D radiation-transport two-temperature GRMHD simulations," Jan. 14, 2022 (cit. on p. 215).

[155]F. Long et al., "Gaps and rings in an ALMA survey of disks in the taurus star-forming region," ApJ **869**, 17 (2018) (cit. on pp. 8, 193).

[156]R. V. E. Lovelace, H. Li, S. A. Colgate, and A. F. Nelson, "Rossby wave instability of keplerian accretion disks," ApJ **513**, 805–810 (1999) (cit. on pp. 132, 163, 164, 215).

[157]S. H. Lubow, J. C. B. Papaloizou, and J. E. Pringle, "On the stability of magnetic wind-driven accretion discs," MNRAS **268**, 1010–1014 (1994) (cit. on p. 208).

[158]D. Lynden-Bell, "Galactic nuclei as collapsed old quasars," Nature **223**, 690–694 (1969) (cit. on p. 10).

[159]D. Lynden-Bell, "On why discs generate magnetic towers and collimate jets," MNRAS **341**, 1360–1372 (2003) (cit. on p. 29).

[160]D. Lynden-Bell and J. E. Pringle, "The evolution of viscous discs and the origin of the nebular variables," MNRAS **168**, 603–637 (1974) (cit. on p. 196).

[161]W. Lyra and M.-M. M. Low, "Rossby wave instability at dead zone boundaries in three-dimensional resistive magnetohydrodynamical global models of protoplanetary disks," ApJ **756**, 62 (2012) (cit. on p. 164).

[162]E. E. Mamajek, "Initial conditions of planet formation: lifetimes of primordial disks," AIP Conf. Proc. **1158**, 3–10 (2009) (cit. on p. 17).

[163]P. Marchand, J. Masson, G. Chabrier, P. Hennebelle, B. Commerçon, and N. Vaytet, "Chemical solver to compute molecule and grain abundances and non-ideal MHD resistivities in prestellar core-collapse calculations," A&A **592**, A18 (2016) (cit. on p. 67).

[164]E. Martel and G. Lesur, "Magnetised winds in transition discs. I. 2.5D global simulations," A&A (2022) (cit. on pp. 88, 90, 239).

[165]J. Masson, G. Chabrier, P. Hennebelle, N. Vaytet, and B. Commerçon, "Ambipolar diffusion in low-mass star formation: I. general comparison with the ideal magnetohydrodynamic case," A&A **587**, A32 (2016) (cit. on pp. 7, 61).

[166]B. J. McCall et al., "An enhanced cosmic-ray flux towards ζ persei inferred from a laboratory study of the H3+–e- recombination rate," Nature **422**, 500–502 (2003) (cit. on p. 66).

[167]C. F. McKee and J. P. Ostriker, "A theory of the interstellar medium: three components regulated by supernova explosions in an inhomogeneous substrate.," ApJ **218**, 148–169 (1977) (cit. on p. 6).

[168]J. C. McKinney, A. Tchekhovskoy, and R. D. Blandford, "General relativistic magnetohydrodynamic simulations of magnetically choked accretion flows around black holes," MNRAS **423**, 3083–3117 (2012) (cit. on pp. 168, 215, 218).

[169]H. Meheut, F. Casse, P. Varniere, and M. Tagger, "Rossby wave instability and three-dimensional vortices in accretion disks," A&A **516**, A31 (2010) (cit. on p. 164).

[170]H. Meheut, R. Keppens, F. Casse, and W. Benz, "Formation and long-term evolution of 3D vortices in protoplanetary discs," A&A **542**, A9 (2012) (cit. on p. 164).

[171]J. Menu et al., "On the structure of the transition disk around TW hydrae," A&A **564**, A93 (2014) (cit. on p. 185).

[172]A. Mignone, "A simple and accurate riemann solver for isothermal MHD," Journal of Computational Physics **225**, 1427–1441 (2007) (cit. on p. 72).

[173]A. Mignone, G. Bodo, S. Massaglia, T. Matsakos, O. Tesileanu, C. Zanni, and A. Ferrari, "PLUTO: a numerical code for computational astrophysics," ApJS **170**, 228 (2007) (cit. on pp. 70–72).

[174]A. Mignone, C. Zanni, P. Tzeferacos, B. van Straalen, P. Colella, and G. Bodo, "The PLUTO code for adaptive mesh computations in astrophysical fluid dynamics," ApJS **198**, 7 (2011) (cit. on p. 71).

[175]K. Milliner, J. H. Matthews, K. S. Long, and L. Hartmann, "Disc wind models for FU ori objects," MNRAS **483**, 1663–1673 (2019) (cit. on p. 185).

[176]B. Mishra, M. C. Begelman, P. J. Armitage, and J. B. Simon, "Strongly magnetized accretion discs: structure and accretion from global magnetohydrodynamic simulations," MNRAS **492**, 1855–1868 (2020) (cit. on p. 233).

[177]R. Moll, "Shearing box simulations of accretion disk winds," A&A **548**, A76 (2012) (cit. on p. 208).

[178]R. Morishima, "Gap opening beyond dead zones by photoevaporation," MNRAS **420**, 2851–2858 (2012) (cit. on p. 25).

[179]J. R. Najita and E. A. Bergin, "Protoplanetary disk sizes and angular momentum transport," ApJ **864**, 168 (2018) (cit. on p. 196).

[180]R. Narayan, I. V. Igumenshchev, and M. A. Abramowicz, "Magnetically arrested disk: an energetically efficient accretion flow," Publications of the Astronomical Society of Japan **55**, L69–L72 (2003) (cit. on pp. 131, 215, 218).

[181]R. Narayan, A. Loeb, and P. Kumar, "Causality in strong shear flows," ApJ **431**, 359 (1994) (cit. on p. 46).

[182]R. P. Nelson, O. Gressel, and O. M. Umurhan, "Linear and nonlinear evolution of the vertical shear instability in accretion discs," MNRAS **435**, 2610–2632 (2013) (cit. on pp. 74, 76).

[183]W. A. Newcomb, "Lagrangian and hamiltonian methods in magnetohydrodynamics," Nucl. Fusion Suppl. Part 2 **2**, 451–463 (1961) (cit. on p. 54).

[184]K. I. Öberg, C. Qi, D. J. Wilner, and S. M. Andrews, "The ionization fraction in the DM tau protoplanetary disk," ApJ **743**, 152 (2011) (cit. on p. 64).

[185]G. I. Ogilvie and S. H. Lubow, "On the wake generated by a planet in a disc," MNRAS **330**, 950–954 (2002) (cit. on p. 15).

[186]T. Ono, H. Nomura, and T. Takeuchi, "Rotational instability in the outer region of protoplanetary disks," ApJ **787**, 37 (2014) (cit. on p. 163).

[187]J. Otter, A. Ginsburg, N. P. Ballering, J. Bally, J. A. Eisner, C. Goddi, R. Plambeck, and M. Wright, "Small protoplanetary disks in the orion nebula cluster and OMC1 with ALMA," ApJ **923**, 221 (2021) (cit. on pp. xiv, 6, 7).

[188]J. E. Owen, B. Ercolano, C. J. Clarke, and R. D. Alexander, "Radiation-hydrodynamic models of x-ray and EUV photoevaporating protoplanetary discs," MNRAS **401**, 1415–1428 (2010) (cit. on p. 65).

[189]J. E. Owen, "The origin and evolution of transition discs: successes, problems, and open questions," Publ. Astron. Soc. Aust. **33** (2016) (cit. on pp. 17, 23, 24, 34).

[190]J. E. Owen and C. J. Clarke, "Two populations of transition discs?" MNRAS **426**, L96–L100 (2012) (cit. on p. 24).

[191]J. E. Owen, C. J. Clarke, and B. Ercolano, "On the theory of disc photoevaporation," MNRAS **422**, 1880–1901 (2012) (cit. on p. 21).

[192]I. Pascucci, U. Gorti, and D. Hollenbach, "Free-free emission and radio recombination lines from photoevaporating disks," ApJL **751**, L42 (2012) (cit. on p. 186).

[193]I. Pascucci and M. Sterzik, "Evidence for disk photoevaporation driven by the central star," ApJ **702**, 724–732 (2009) (cit. on p. 185).

[194]I. Pascucci, M. Sterzik, R. D. Alexander, S. H. P. Alencar, U. Gorti, D. Hollenbach, J. Owen, B. Ercolano, and S. Edwards, "The photoevaporative wind from the disk of TW hya," ApJ **736**, 13 (2011) (cit. on p. 21).

[195]I. Pascucci, S. Cabrit, S. Edwards, U. Gorti, O. Gressel, and T. Suzuki, *The role of disk winds in the evolution and dispersal of protoplanetary disks*, Mar. 18, 2022 (cit. on pp. 186, 191).

[196]I. Pascucci et al., "The evolution of disk winds from a combined study of optical and infrared forbidden lines," ApJ **903**, 78 (2020) (cit. on p. 186).

[197]G. Pelletier and R. E. Pudritz, "Hydromagnetic disk winds in young stellar objects and active galactic nuclei," ApJ **394**, 117 (1992) (cit. on p. 186).

[198]D. Perez-Becker and E. Chiang, "Surface layer accretion in conventional and transitional disks driven by far-ultraviolet ionization," ApJ **735**, 8 (2011) (cit. on p. 65).

[199]L. M. Pérez et al., "Spiral density waves in a young protoplanetary disk," Science **353**, 1519–1521 (2016) (cit. on p. 193).

[200]A. Piel, *Plasma physics - an introduction to laboratory space, and fusion plasmas* (Springer, 2010), 398 pp. (cit. on p. 48).

[201]P. Pinilla, N. T. Kurtovic, M. Benisty, C. F. Manara, A. Natta, E. Sanchis, M. Tazzari, S. M. Stammler, L. Ricci, and L. Testi, "A bright inner disk and structures in the transition disk around the very low-mass star CIDA 1," A&A **649**, A122 (2021) (cit. on p. 216).

[202]P. Pinilla, M. Flock, M. d. J. Ovelar, and T. Birnstiel, "Can dead zones create structures like a transition disk?" A&A **596**, A81 (2016) (cit. on p. 25).

[203]C. Pinte et al., "Kinematic detection of a planet carving a gap in a protoplanetary disk," Nat Astron **3**, 1109–1114 (2019) (cit. on p. 191).

[204]K. M. Pontoppidan, G. A. Blake, and A. Smette, "The structure and dynamics of molecular gas in planet-forming zones: a crires spectro-astrometric survey," ApJ **733**, 84 (2011) (cit. on p. 186).

[205]K. Pouilly, J. Bouvier, E. Alecian, S. H. P. Alencar, A.-M. Cody, J.-F. Donati, K. Grankin, G. a. J. Hussain, L. Rebull, and C. P. Folsom, "Magnetospheric accretion in the intermediate-mass T tauri star HQ tauri," A&A **642**, A99 (2020) (cit. on p. 214).

[206]K. G. Powell, "An approximate riemann solver for magnetohydrodynamics," in *Upwind and high-resolution schemes*, edited by M. Y. Hussaini, B. van Leer, and J. Van Rosendale (Springer, Berlin, Heidelberg, 1997), pp. 570–583 (cit. on p. 72).

[207]D. J. Price et al., "Phantom: a smoothed particle hydrodynamics and magnetohydrodynamics code for astrophysics," Publ. Astron. Soc. Aust. **35** (2018/ed) (cit. on p. 73).

[208]E. Quataert and E. I. Chiang, "Angular momentum transport in particle and fluid disks," ApJ **543**, 432–437 (2000) (cit. on p. 46).

[209]R. R. Rafikov, "Protoplanetary disks as (possibly) viscous disks," ApJ **837**, 163 (2017) (cit. on p. 47).

[210]R. Rao, J. M. Girart, D. P. Marrone, S.-P. Lai, and S. Schnee, "IRAS 16293: a "magnetic" tale of two cores," ApJ **707**, 921–935 (2009) (cit. on p. 15).

[211]J. Rax, *Physique des plasmas: cours et applications*, Physique (Dunod, 2005) (cit. on p. 48).

[212]T. Rembiasz, M. Obergaulinger, P. Cerdá-Durán, M.-A. Aloy, and E. Müller, "On the measurements of numerical viscosity and resistivity in eulerian MHD codes," ApJS **230**, 18 (2017) (cit. on p. 223).

[213]L. Ricci, S. K. Harter, B. Ercolano, and M. Weber, "Testing photoevaporation and MHC disk wind models through future high-angular resolution radio observations: the case of TW hydrae," ApJ **913**, 122 (2021) (cit. on p. 185).

[214]M. Rieke, T. Trost, and R. Grauer, "Coupled vlasov and two-fluid codes on GPUs," Journal of Computational Physics **283**, 436–452 (2015) (cit. on p. 73).

[215]A. Riols and G. Lesur, "Spontaneous ring formation in wind-emitting accretion discs," A&A **625**, A108 (2019) (cit. on pp. 120, 213).

[216]A. Riols, G. Lesur, and F. Menard, "Ring formation and dust dynamics in wind-driven protoplanetary discs: global simulations," A&A **639**, A95 (2020) (cit. on pp. 68, 73, 96, 118, 120, 146, 152, 213).

[217]B. Ripperda, M. Liska, K. Chatterjee, G. Musoke, A. A. Philippov, S. B. Markoff, A. Tchekhovskoy, and Z. Younsi, "Black hole flares: ejection of accreted magnetic flux through 3D plasmoid-mediated reconnection," ApJL **924**, L32 (2022) (cit. on pp. 168, 215).

[218]C. M. T. Robert, H. Méheut, and F. Ménard, "Dynamical signatures of rossby vortices in cavity-hosting disks," A&A **641**, A128 (2020) (cit. on p. 164).

[219]P. J. Rodenkirch, H. Klahr, C. Fendt, and C. P. Dullemond, "Global axisymmetric simulations of photoevaporation and magnetically driven protoplanetary disk winds," A&A **633**, A21 (2020) (cit. on p. 21).

[220]D. Rodgers-Lee, T. P. Ray, and T. P. Downes, "Global multifluid simulations of the magnetorotational instability in radially stratified protoplanetary discs," MNRAS **463**, 134–145 (2016) (cit. on p. 51).

[221]M. M. Romanova, A. K. Kulkarni, and R. V. E. Lovelace, "Unstable disk accretion onto magnetized stars: first global three-dimensional magnetohydrodynamic simulations," ApJ **673**, L171 (2008) (cit. on p. 168).

[222]T. Rometsch, P. J. Rodenkirch, W. Kley, and C. P. Dullemond, "Migration jumps of planets in transition discs," A&A **643**, A87 (2020) (cit. on p. 217).

[223]K. A. Rosenfeld, E. Chiang, and S. M. Andrews, "Fast radial flows in transition disk holes," ApJ **782**, 62 (2014) (cit. on pp. 24, 190, 191, 214).

[224]D. Ruíz-Rodríguez, M. Ireland, L. Cieza, and A. Kraus, "The frequency of binary star interlopers amongst transitional discs," MNRAS **463**, 3829–3847 (2016) (cit. on p. 27).

[225]E. Sanchis et al., "Measuring the ratio of the gas and dust emission radii of protoplanetary disks in the lupus star-forming region," A&A **649**, A19 (2021) (cit. on p. 196).

[226]Y. M. Seo, C. D. Dowell, P. F. Goldsmith, J. L. Pineda, and L. Majumdar, "Probing polarization and the role of magnetic fields in cloud destruction in the keyhole nebula," ApJ **917**, 57 (2021) (cit. on p. 15).

[227]N. I. Shakura and R. A. Sunyaev, "Black holes in binary systems. observational appearance.," A&A **24**, 337–355 (1973) (cit. on pp. 10, 103, 196).

[228]F. H. Shu, D. Johnstone, and D. Hollenbach, "Photoevaporation of the solar nebula and the formation of the giant planets," Icarus **106**, 92–101 (1993) (cit. on pp. 19, 21).

[229]J. B. Simon, X.-N. Bai, J. M. Stone, P. J. Armitage, and K. Beckwith, "Turbulence in the outer regions of protoplanetary disks. I. weak accretion with no vertical magnetic flux," ApJ **764**, 66 (2013) (cit. on pp. 26, 145).

[230]J. B. Simon, G. Lesur, M. W. Kunz, and P. J. Armitage, "Magnetically driven accretion in protoplanetary discs," MNRAS **454**, 1117–1131 (2015) (cit. on p. 68).

[231]M. N. Simon, I. Pascucci, S. Edwards, W. Feng, U. Gorti, D. Hollenbach, E. Rigliaco, and J. T. Keane, "Tracing slow winds from T tauri stars via low-velocity forbidden line emission," ApJ **831**, 169 (2016) (cit. on p. 186).

[232]H. C. Spruit, "Magnetohydrodynamic jets and winds from accretion disks," **477**, 249–286 (1996) (cit. on p. 33).

[233]H. C. Spruit, R. Stehle, and J. C. B. Papaloizou, "Interchange instability in and accretion disc with a poloidal magnetic field," MNRAS **275**, 1223–1231 (1995) (cit. on pp. 116, 166, 221).

[234]H. C. Spruit and R. E. Taam, "Mass transport in a neutron star magnetosphere," A&A **229**, 475–493 (1990) (cit. on pp. 116, 166).

[235]K. R. Stapelfeldt, J. E. Krist, F. Ménard, J. Bouvier, D. L. Padgett, and C. J. Burrows, "An edge-on circumstellar disk in the young binary system HK tauri," ApJ **502**, L65–L69 (1998) (cit. on p. 42).

[236]R. Stehle and H. C. Spruit, "Stability of accretion discs threaded by a strong magnetic field," MNRAS **323**, 587–600 (2001) (cit. on pp. 116, 166).

[237]I. W. Stephens, L. W. Looney, W. Kwon, M. Fernández-López, A. M. Hughes, L. G. Mundy, R. M. Crutcher, Z.-Y. Li, and R. Rao, "Spatially resolved magnetic field structure in the disk of a T tauri star," Nature **514**, 597–599 (2014) (cit. on p. 13).

[238]I. W. Stephens et al., "ALMA reveals transition of polarization pattern with wavelength in HL tau's disk," ApJ **851**, 55 (2017) (cit. on p. 15).

[239]K. M. Strom, S. E. Strom, S. Edwards, S. Cabrit, and M. F. Skrutskie, "Circumstellar material associated with solar-type pre-main-sequence stars: a possible constraint on the timescale for planet building," AJ **97**, 1451 (1989) (cit. on pp. 8, 17).

[240]S. S. Suriano, Z.-Y. Li, R. Krasnopolsky, T. K. Suzuki, and H. Shang, "The formation of rings and gaps in wind-launching non-ideal MHD discs: three-dimensional simulations," MNRAS **484**, 107–124 (2019) (cit. on p. 118).

[241]T. K. Suzuki, T. Muto, and S.-i. Inutsuka, "Protoplanetary disk winds via magnetorotational instability: formation of an inner hole and a crucial assist for planet formation," ApJ **718**, 1289–1304 (2010) (cit. on p. 34).

[242]T. K. Suzuki, M. Ogihara, A. Morbidelli, A. Crida, and T. Guillot, "Evolution of protoplanetary discs with magnetically driven disc winds," A&A **596**, A74 (2016) (cit. on p. 195).

[243]B. Tabone, S. Cabrit, G. P. des Forêts, J. Ferreira, A. Gusdorf, L. Podio, E. Bianchi, E. Chapillon, C. Codella, and F. Gueth, "Constraining MHD disk winds with ALMA - apparent rotation signatures and application to HH212," A&A **640**, A82 (2020) (cit. on p. 185).

[244]B Tabone, G. P. Rosotti, G Lodato, P. J. Armitage, A. J. Cridland, and E. F. van Dishoeck, "Mhd disc winds can reproduce fast disc dispersal and the correlation between accretion rate and disc mass in lupus," MNRAS **512**, L74–L79 (2022) (cit. on pp. 194, 196).

[245]B. Tabone, G. P. Rosotti, A. J. Cridland, P. J. Armitage, and G. Lodato, "Secular evolution of MHD wind-driven discs: analytical solutions in the expanded α-framework," MNRAS **512**, 2290–2309 (2022) (cit. on pp. 34, 194, 195).

[246]M. Tagger and R. Pellat, "An accretion-ejection instability in magnetized disks," A&A **349**, 1003–1016 (1999) (cit. on p. 166).

[247]M. Tazzari et al., "Physical properties of dusty protoplanetary disks in lupus: evidence for viscous evolution?" A&A **606**, A88 (2017) (cit. on p. 196).

[248]M Tazzari et al., "The first ALMA survey of protoplanetary discs at 3 mm: demographics of grain growth in the lupus region," MNRAS **506**, 5117–5128 (2021) (cit. on pp. 6, 28).

[249]A. Tchekhovskoy, R. Narayan, and J. C. McKinney, "Efficient generation of jets from magnetically arrested accretion on a rapidly spinning black hole," MNRAS **418**, L79–L83 (2011) (cit. on p. 154).

[250]W. F. Thi, G. Lesur, P. Woitke, I. Kamp, C. Rab, and A. Carmona, "Radiation thermo-chemical models of protoplanetary disks. grain and polycyclic aromatic hydrocarbon charging," A&A **632**, A44 (2019) (cit. on pp. 69, 76).

[251]H. B. Throop and J. Bally, "Can photoevaporation trigger planetesimal formation?" ApJ **623**, L149–L152 (2005) (cit. on p. 22).

[252]D. Thun, W. Kley, and G. Picogna, "Circumbinary discs: numerical and physical behaviour," A&A **604**, A102 (2017) (cit. on p. 27).

[253]E. Toro, "Riemann solvers and numerical methods for fluid dynamics: a practical introduction," in *Riemann solvers and numerical methods for fluid dynamics* (Jan. 1, 2009) (cit. on p. 72).

[254]L. Trapman, B. Tabone, G. Rosotti, and K. Zhang, "Effect of MHD wind-driven disk evolution on the observed sizes of protoplanetary disks," ApJ **926**, 61 (2022) (cit. on p. 194).

[255]L. Trapman, K. Zhang, M. L. R. van 't Hoff, M. R. Hogerheijde, and E. A. Bergin, "A novel way of measuring the gas disk mass of protoplanetary disks using N2H$\mathplus$ and C18O," ApJL **926**, L2 (2022) (cit. on p. 44).

[256]Y. T. Tsap, A. V. Stepanov, and Y. G. Kopylova, "Ambipolar diffusion and magnetic reconnection," Astronomy Reports **56**, 138–145 (2012) (cit. on p. 112).

[257]T. Umebayashi and T. Nakano, "Recombination of ions and electrons on grains and the ionization degree in dense interstellar clouds," Publ. Astron. Soc. Jpn. **32**, 405 (1980) (cit. on p. 66).

[258]T. Umebayashi, "The densities of charged particles in very dense interstellar clouds," Progress of Theoretical Physics **69**, 480–502 (1983) (cit. on p. 64).

[259]T. Umebayashi and T. Nakano, "Effects of radionuclides on the ionization state of protoplanetary disks and dense cloud cores," ApJ **690**, 69–81 (2008) (cit. on p. 66).

[260]T. Uyama, G. Ruane, K. Lawson, T. Muto, C. Beichman, and N. van der Marel, "A spatially-resolved large cavity of the J0337 protoplanetary disk in perseus," ApJ **163**, 204 (2022) (cit. on p. 193).

[261]N. van der Marel, P. Cazzoletti, P. Pinilla, and A. Garufi, "Vortices and spirals in the HD 135344b transition disk," ApJ **832**, 178 (2016) (cit. on p. 193).

[262]N. van der Marel, E. F. van Dishoeck, S. Bruderer, S. M. Andrews, K. M. Pontoppidan, G. J. Herczeg, T. van Kempen, and A. Miotello, "Resolved gas cavities in transitional disks inferred from CO isotopologs with ALMA," A&A **585**, A58 (2016) (cit. on pp. 17, 19, 29, 62, 191).

[263]N. van der Marel, T. Birnstiel, A. Garufi, E. Ragusa, V. Christiaens, D. J. Price, S. Sallum, D. Muley, L. Francis, and R. Dong, "On the diversity of asymmetries in gapped protoplanetary disks," ApJ **161**, 33 (2020) (cit. on pp. 19, 62).

[264]N. van der Marel, J. P. Williams, G. Picogna, S. van Terwisga, S. Facchini, C. F. Manara, A. Zormpas, and M. Ansdell, "High-resolution ALMA observations of transition disk candidates in lupus," Apr. 18, 2022 (cit. on pp. 19, 191).

[265]E. P. Velikhov, "Stability of an ideally conducting liquid flowing between cylinders rotating in a magnetic field," Sov. Phys. JETP **36**, 995–998 (1959) (cit. on p. 12).

[266]F. Verbunt, "Accretion disks in stellar x-ray sources," Space Sci Rev **32**, 379–404 (1982) (cit. on p. 10).

[267]M. Villenave et al., "Spatial segregation of dust grains in transition disks - SPHERE observations of 2MASS J16083070-3828268 and RXJ1852.3-3700," A&A **624**, A7 (2019) (cit. on p. 19).

[268]W. H. T. Vlemmings et al., "Stringent limits on the magnetic field strength in the disc of TW hya: ALMA observations of CN polarisation," A&A **624**, L7 (2019) (cit. on pp. 15, 213).

[269]G. Wafflard-Fernandez and C. Baruteau, "Intermittent planet migration and the formation of multiple dust rings and gaps in protoplanetary discs," MNRAS **493**, 5892–5912 (2020) (cit. on p. 194).

[270]L. Wang and J. J. Goodman, "Wind-driven accretion in transitional protostellar disks," ApJ **835**, 59 (2017) (cit. on pp. 29, 34, 65, 68, 70, 75, 127, 189, 217).

[271]M. Wardle, "The balbus-hawley instability in weakly ionized discs," MNRAS **307**, 849–856 (1999) (cit. on p. 12).

[272]M. Wardle, "Magnetic fields in protoplanetary disks," Astrophysics and Space Science **311**, 35–45 (2007) (cit. on p. 64).

[273]M. Wardle and A. Koenigl, "The structure of protostellar accretion disks and the origin of bipolar flows," ApJ **410**, 218 (1993) (cit. on pp. 29, 68).

[274]G. M. Webb and S. C. Anco, "Conservation laws in magnetohydrodynamics and fluid dynamics: lagrangian approach," AIP Conf. Proc. **2153**, 020024 (2019) (cit. on p. 54).

[275]M. L. Weber, B. Ercolano, G. Picogna, L. Hartmann, and P. J. Rodenkirch, "The interpretation of protoplanetary disc wind diagnostic lines from x-ray photoevaporation and analytical MHD models," MNRAS **496**, 223–244 (2020) (cit. on p. 186).

[276]S. J. Weidenschilling, "Aerodynamics of solid bodies in the solar nebula," MNRAS **180**, 57–70 (1977) (cit. on p. 27).

[277]E. T. Whelan, I. Pascucci, U. Gorti, S. Edwards, R. D. Alexander, M. F. Sterzik, and C. Melo, "Evidence for an MHD disk wind via optical forbidden line spectroastrometry," ApJ **913**, 43 (2021) (cit. on pp. 13, 185).

[278]K. Willacy, "The chemistry of multiply deuterated molecules in protoplanetary disks. I. the outer disk," ApJ **660**, 441 (2007) (cit. on p. 64).

[279]J. P. Williams and L. A. Cieza, "Protoplanetary disks and their evolution," Annu. Rev. Astron. Astrophys. **49**, 67–117 (2011) (cit. on p. 6).

[280]R. M. Winglee, "Multi-fluid simulations of the magnetosphere: the identification of the geopause and its variation with IMF," Geophys. Res. Lett. **25**, 4441–4444 (1998) (cit. on p. 51).

[281]P. Woitke, I. Kamp, and W.-F. Thi, "Radiation thermo-chemical models of protoplanetary disks - I. hydrostatic disk structure and inner rim," A&A **501**, 383–406 (2009) (cit. on p. 67).

[282]S. G. Wolff, G. Duchêne, K. R. Stapelfeldt, F. Ménard, C. Flores, D. Padgett, C. Pinte, M. Villenave, G. van der Plas, and M. D. Perrin, "The anatomy of an unusual edge-on protoplanetary disk. I. dust settling in a cold disk," ApJ **161**, 238 (2021) (cit. on p. 43).

[283]H. Yang and X.-N. Bai, "Global non-ideal magnetohydrodynamic simulations of protoplanetary disks with outer truncation," ApJ **922**, 201 (2021) (cit. on pp. 196–198, 205).

[284]C. Yu and D. Lai, "Rossby wave instability in accretion discs with large-scale poloidal magnetic fields," MNRAS **429**, 2748–2754 (2013) (cit. on p. 163).

[285]F. Zagaria, G. P. Rosotti, C. J. Clarke, and B. Tabone, "Modelling the secular evolution of protoplanetary disc dust sizes – a comparison between the viscous and magnetic wind case," MNRAS **514**, 1088–1106 (2022) (cit. on pp. 194, 196).

[286]C. Zanni, A. Ferrari, R. Rosner, G. Bodo, and S. Massaglia, "MHD simulations of jet acceleration from keplerian accretion disks - the effects of disk resistivity," A&A **469**, 811–828 (2007) (cit. on p. 68).

[287]C. Zanni and J. Ferreira, "MHD simulations of accretion onto a dipolar magnetosphere. II. magnetospheric ejections and stellar spin-down," A&A **550**, A99 (2013) (cit. on pp. 112, 214).

[288]Y. Zhou, "Variational integration for ideal magnetohydrodynamics and formation of current singularities," Aug. 28, 2017 (cit. on p. 54).

[289]Z. Zhu, L. Hartmann, and C. Gammie, "Long-term evolution of protostellar and protoplanetary disks. ii. layered accretion with infall," ApJ **713**, 1143–1158 (2010) (cit. on p. 25).

[290]Z. Zhu, R. P. Nelson, L. Hartmann, C. Espaillat, and N. Calvet, "Transitional and pre-transitional disks: gap opening by multiple planets?" ApJ **729**, 47 (2011) (cit. on p. 26).

[291]Z. Zhu and J. M. Stone, "Global evolution of an accretion disk with a net vertical field: coronal accretion, flux transport, and disk winds," ApJ **857**, 34 (2018) (cit. on p. 77).

[292]M. Čemeljić, H. Shang, and T.-Y. Chiang, "Magnetospheric accretion and ejection of matter in resistive magnetohydrodynamic simulations," ApJ **768**, 5 (2013) (cit. on p. 214).